Characterising the gas and dust in protoplanetary discs around Herbig stars

UNIVERSITY OF LEEDS

James Miley

University of Leeds

School of Physics & Astronomy

A thesis submitted for the degree of

Doctor of Philosophy

5 June, 2020

Declaration

The candidate confirms that the work submitted is his own, except where work which has formed part of jointly authored publications has been included. The contribution of the candidate and the other authors to this work has been explicitly indicated below. The candidate confirms that appropriate credit has been given within the thesis where reference has been made to the work of others.

Chapter 2 is based on the published article "Asymmetric mid-plane gas in ALMA images of HD100546". This work was published in volume 485 of Monthly Notices of the Royal Astronomical Society, pages 7239-752, May 2019. Co-authors were O. Panić, T.J. Haworth, I. Pascucci, M. Wyatt, C. Clarke, A.M.S. Richards, T. Ratzka. This work is based on data from ALMA project 2015.1.01600.S, P.I. O. Panić. T.J. Haworth provided scripts for the calculation of disc gas mass. A. M. S. Richards advised on the astrometric accuracy of ALMA imaging. All co-authors contributed feedback on the manuscript and discussion on the analysis.

Chapter 3 is based on the published article "Unlocking the secrets of the midplane gas and dust distribution in the young hybrid disc HD141569". This work was published in volume 615 of Astronomy &. Astrophysics, letter 10 in July 2018. Co-authors were O. Panić, M. Wyatt and G. M. Kennedy. All co-authors contributed feedback on the manuscript and discussion on the analysis.

For Edwin Maxwell, who was guided by the stars.

Acknowledgements

First of all I would like to say a massive thank you to Olja Panić for guiding, teaching and supporting me throughout years of PhD study. From the very first days you've inspired me to be the best researcher I can possibly be and I'll forever be grateful for all the time you've invested in me. Thank you also to my second supervisor René Oudmaijer for wise words and support when it was needed.

Thank you to John Ilee, Tom Haworth and Richard Booth, each of whom have provided expert technical knowledge and scientific insight. I would have taken a lot longer to get here without vital contributions and discussions from each of you at the right times. Thank you also for setting the best example of what a scientist should be like.

A special thanks also to Tom Hartquist who throughout my seven and a half years in Leeds has guided me through physics as a teacher, a mentor and a friend. Thank you also to the School of Physics & Astronomy, and to Leeds University Union for providing a home away from home for all this time. I loved my time at Leeds.

I owe an enormous debt of gratitude to every single PhD student who has been through room 9.64; for sharing food, films, football and an awful lot of time in the Fenton. It has been a pleasure and a privilege to know you all.

Gracias Alice Pérez and Miguel Vioque for keeping the journey fun and for being great friends. Part of me is still partying in Madrid. A big mention to the other half of Disco Inferno and my disc-wife from day one, Alice Booth, best of luck in Leiden!

Thank you especially to Abi Frost with whom over the past three years I've shared all the highs and lows of a PhD, and of life. I hope to share a great deal more of them with you in the future, wherever that takes us.

Finally, I'm eternally grateful to my fantastic friends and family outside of the astrophysics bubble. To Sam, Ash and Meghan who became my second family in Leeds, thank you for everything from drinking cans of lager in university halls of residence, to Sunday dinners and *attempting* to tackle the big bad world. To my friends for life the boys from Hitchin, who despite going on to do great and amazing things with their lives have still not changed one bit.

My greatest thanks are to Mum and Dad for consistent and unwavering support in every possible way, at every juncture of my life. I'm a very lucky person and couldn't have done this without you.

Abstract

This thesis contains a study of the circumstellar discs around intermediate mass stars. Through observational data and protoplanetary disc modelling, the physical structure and composition of protoplanetary discs are investigated with regards to their capacity for planet formation.

In-depth analysis of millimetre-wavelength interferometric observations are carried out on the circumstellar environment of two Herbig stars. Firstly, the distribution of gas and dust in the gas-rich, potentially planet-hosting disc of HD100546 is characterised. Using ALMA observations of 1.3mm continuum and CO isotopologues tracing the disc midplane, estimates of disc mass are calculated, constraints on the size of dust grains inferred and evidence for midplane counterparts to scattered light features are identified.

Secondly, an analysis of the more evolved circumstellar disc around Herbig star HD141569 is made in order to investigate the mass content of the disc and inform the debate as to its evolutionary stage. New ALMA observations presented in this thesis find new midplane structures in the gas and dust that support an intermediary stage of evolution between the protoplanetary disc and debris disc regimes.

Finally, modelling of the pre-main sequence evolution of stars across the stellar mass range at which exoplanet detections peak is combined with Monte Carlo radiative transfer and modelling of the evolution of midplane gas and dust in order to study the impact of stellar evolution on the midplanes of protoplanetary discs. Variations in midplane temperature profiles result in different locations of key snowlines in the disc, which in turn produces variations in the molecular composition of the local disc. The results quantify how snowline locations depend on stellar luminosity evolution. This modelling procedure is applied to the system of HR8799 in order to put constraints on the time and location within the disc at which wide-orbit planets could have formed based on their atmospheric C/O ratio. The results support an early formation time, within around 1 Myr, for the carbon-rich exoplanet HR8799b.

Abbreviations

ALMA	Atacama Large Millimetre/Sub-millimetre Array
AO	Adaptive Optics
APEX	Atacama Pathfinder EXperiment
ARIEL	Atmospheric Remote-sensing Infrared Exoplanet Large-survey
ATCA	Australia Telescope Compact Array
au	Astronomical Unit
CASA	Common Astronomy Software Applications
ESA	European Space Agency
ESO	European Southern Observatory
EUV	Extreme Ultra-Violet
FUV	Far Ultra-Violet
FWHM	Full-Width at Half-Maximum
HAeBe	Herbig Ae/Be
HST	Hubble Space Telescope
IR	Infra-red
ISM	Inter-Stellar Medium
JWST	James Webb Space Telescope
MESA	Modules for Experiments in Stellar Astrophysics
MIST	MESA Isochrones and Stellar Tracks
MS	Main Sequence
MYSO	Massive Young Stellar Object
NASA	National Aeronautics and Space Administration
NOEMA	NOrthern Extended Millimeter Array
PA	Position Angle

PdBI	Plataue de Bure Interferometer
PMS	Pre-Main Sequence
PSF	Point Source Function
SED	Spectral Energy Distribution
SKA	Square Kilometre Array
SMA	Sub-Millimetre Array
SPHERE	Spectro-Polarimetric High- contrast Exoplanet REsearch instrument
VISIR	VLT Imager and Spectrometer for mid-Infrared
VLA	Very Large Array
VLT	Very Large Telescope
YSO	Young Stellar Object
ZAMS	Zero Age Main Sequence

Contents

List of Figures

Chapter 1

Introduction

1.1 Protoplanetary Discs

Protoplanetary discs are the astrophysical environment in which exoplanets are built and born. Comprised of gas and dust orbiting a young star, these discs simultaneously feed the growing star and mark the beginning of the planet formation process. Characterising these objects through observational evidence and theoretical study reveals to astronomers the properties of the local environment in which planet formation can take place. The physical structures of discs are imprinted with the signatures of mechanisms for planet formation, the signs of interactions with other nearby systems and clues as to the stage of evolution the environment has reached. Astronomers can use these hints to reconstruct a disc's past in order to learn how much of an impact a planet can have in perturbing the disc that hosts it, and to what extent the initial conditions in the local environment dictate the properties of the planets that form there.

Remarkable progress has been made in both the theoretical and observational efforts of the field, meaning that protoplanetary discs and the physics within them can now be constrained with unprecedented detail. Meanwhile missions launched to detect new worlds around distant stars provide a wealth of information on the properties of exoplanets and the architecture of planetary systems. But there is a long way still to go and many big questions still awaiting an answer. How exactly do the discs we observe, and the planet formation mechanisms we define, produce the 'zoo' of over 4000 exoplanets that have been detected?

This thesis explores the physical properties of discs around intermediate mass stars at various stages of evolution through observations and disc modelling. In the rest of Chapter 1 this thesis is put into context with the progress in the field so far. Chapter 2 focuses on characterising the distribution of gas and dust in a massive, gas-rich protoplanetary disc believed to be hosting embedded planets through millimetre-wavelength interferometric observations. In Chapter 3 a similar approach is applied to a disc showing a markedly different stage of evolution; one that is more advanced and approaching the end of the protoplanetary disc phase. In Chapter 4, radiative transfer modelling is combined with models of pre-main sequence stellar evolution and with modelling of midplane evolution in protoplanetary discs to explore why the discs hosted by intermediate mass stars differ from those around their lower mass counterparts. The impact of stellar evolution on the conditions in the midplane are quantified and applied to the system of intermediate mass star HR8799, host to four giant planets. In Chapter 5 the conclusions of this thesis are summarised and promising opportunities for future work are discussed.

1.1.1 Star formation

Protoplanetary discs originate as a byproduct of the star formation process. In order to understand how protoplanetary discs form, and to provide a context within the wider cosmos, we must first understand the processes by which stars are formed.

At the beginning are giant molecular clouds; massive ($\geq 10^4$ $M_\odot$) dense regions of 10-100pc in size. Molecular clouds obscure their inner regions from exterior starlight leading to a very cool environment with temperatures of ∼10 K. In order to form a star, these giant clouds must fragment into progressively smaller, concentrated clumps of dense material.

Molecular clouds collapse due to gravity, and in doing so form dense clumps (Williams et al., 2000) and elongated filamentary structures. The latter appears to be ubiquitous in giant molecular clouds (GMCs) and can be seen in observations of gas (e.g. in Orion Bally et al., 1987) and dust (e.g. in the Gould Belt André et al., 2010). These filaments have an average length of around 0.1pc (Arzoumanian et al., 2014).

The densest filaments go on to form protostellar cores. Gravitational collapse of a filament occurs when the mass per unit length exceeds the critical mass of isothermal structure. The final collapse of a 'pre-stellar' core, with density of around n$\sim 10^4 - 10^5$ cm^{-3}, produces a protostellar object. Often stars are formed in multiple systems, through the growth of two separate fragments from the same molecular cloud, or through the fragmentation of a massive circum-primary disc to form companions (e.g. simulations of protobinary systems by Bate, 2000). The majority of stars are in multiple systems, massive stars in particular are more likely to have companions (Raghavan et al., 2010, and references therein) and this has a significant influence on the future of a system. For example binary interaction dominate the evolution of higher mass stars (Sana et al., 2012) and dynamical interactions between partners in a system can result in truncation or complete dispersal of the circum-primary/circum-secondary discs. This thesis focuses mainly on single star systems. Conservation of angular momentum in the collapsing material leads to the formation of an accretion disc comprised of gas and dust from the pre-stellar core, orbiting the protostar. The accretion disc simultaneously feeds the central object and provides the environment in which planet formation begins, and so its formation marks the birth of the 'protoplanetary' disc.

1.1.2 Observational evidence for protoplanetary discs

Striking early images of protoplanetary discs came from the Hubble Space Telescope (HST). At optical wavelengths dark silhouettes were identified around young stars indicating an increase in opacity due to the circumstellar material (Figure 1.1). Images show discs with a range of sizes and inclinations relative to the line of sight. Some discs also exhibit 'flaring', an increase in vertical height above the midplane of gas and the dust coupled to it (Bell et al., 1997). As well as providing sharp optical images of the geometry of protoplanetary discs, the Orion 'proplyds' give direct evidence of external photoevaporation of discs, a process which results in rapid mass loss (Johnstone et al., 1998). The observations were made of systems in Orion; where massive O-stars are more frequent than in other star forming regions meaning the discs that reside there are subject to unusually high photoevaporative mass-loss rates. Evidence of this photoevaporation can be seen in Figure 1.1 as bright limbs on the edge of the discs, where strong incident flux from neighbouring massive stars is incident upon the disc.

In the years to follow imaging of discs would be attempted in the infrared to detect warm dust with instruments such as VISIR (e.g. Pascucci and Sterzik, 2009; Verhoeff et al., 2011), hot-dust at near-infrared wavelengths (MillanGabet et al., 2001; Monnier et al., 2006) and via scattered light observations on the HST (e.g. Augereau et al., 1999, 2001). Following these breakthroughs advanced adaptive optic systems capable of hunting for planets were developed and implemented

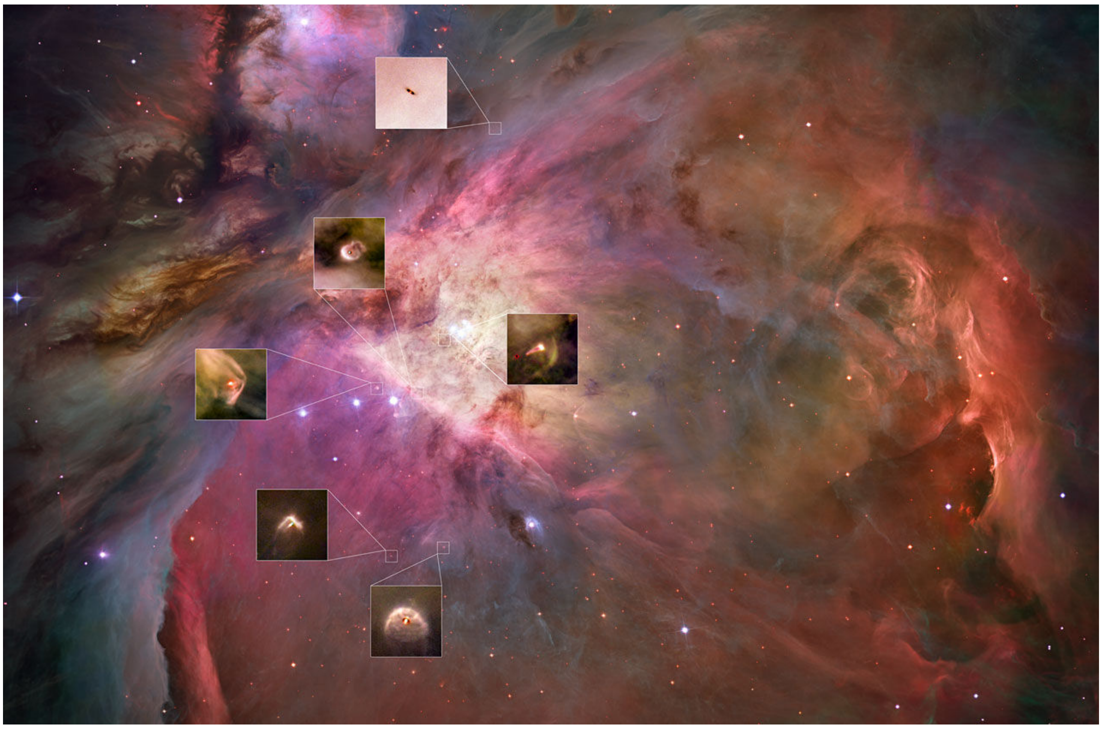

Figure 1.1: Examples of some of the first direct imaging of protoplanetary disc with the HST. This HST image of protoplanetary discs in the Orion nebula, with a magnified view of six discs appearing in silhouette and displaying signs of evidence of photoevaporation from external sources. Credit: NASA, ESA, M. Robberto (Space Telescope Science Institute/ESA), the Hubble Space Telescope Orion Treasury Project Team and L. Ricci (ESO)

on the Keck and Gemini telescopes (e.g. the four giant planets in HR8799, Marois et al., 2008) and later with SPHERE on the VLT (e.g. two planets within the gap of transition disc PDS 70, Haffert et al., 2019). With this observing technique 'backlit' images of protoplanetary discs are produced from light that has been scattered or reflected into the line of site of the observer. Analysis of the images allows for characterisation of the inner dust disc in individual systems (e.g. HD141569 with MagAO/GPI Follette et al., 2017) of for wider surveys as done in the SEEDS survey with SUBARU (Dong et al., 2012). Modern instruments such as SPHERE and NACO on the VLT are used for probing disc structure present in the upper layers of the disc, which often take the form of spiral arms and gaps

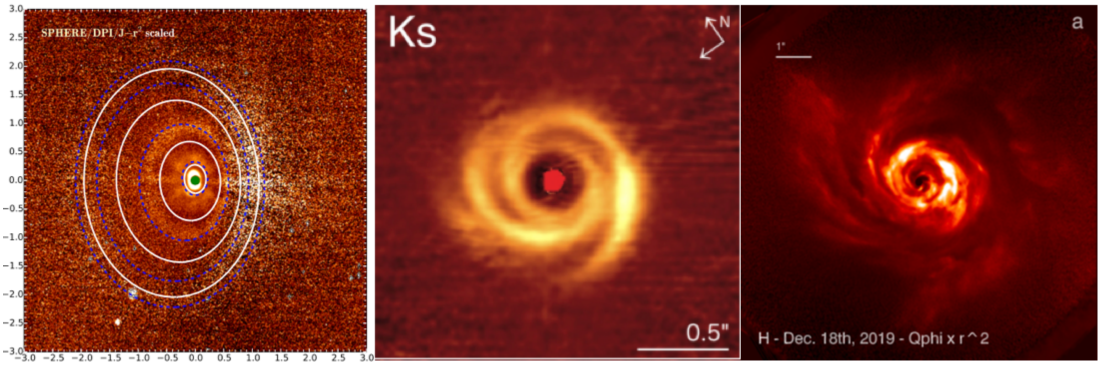

Figure 1.2: **Left:** Near IR SPHERE/IRDIS DPI image of the disc HD 97048, overlaid with the best fitting ellipses corresponding to ring (dashed blue lines) and gaps (white lines). Image and fits from (Ginski et al., 2016). **Middle:** Spiral arms revealed in the Ks band VLT/NACO image of HD 135344B (Garufi et al., 2013) . **Right:** Polarised light obsverd by SPHEER in the H band shows clumpy spiral arms over a range of spatial scales in the disc AB Aur (Boccaletti et al., 2020). All images have their brightness scaled with r^2.

in the disc as demonstrated in Figure 1.2. Boccaletti et al. (2020); Garufi et al. (2013); Ginski et al. (2016).

Imaging of protoplanetary discs requires angular resolution only achieved by a handful of leading modern day instruments, but evidence of circumstellar gas and dust can also be found from analysing the photometry of a disc over a range of wavelengths, known as its spectral energy distribution (SED). Infrared wavelengths are particularly useful for alerting observers to not only the presence of protoplanetary discs, but also their structure (Dullemond and Dominik, 2004a; Hillenbrand et al., 1992; Natta et al., 2001). Starlight absorbed by solid dust grains is re-emitted at longer wavelengths, resulting in an excess of infrared (IR) emission relative to the blackbody of the star. The presence of an IR excess in a young star's SED therefore provides indirect evidence of circumstellar material.

The greatest leap in observations of protoplanetary discs came through millimetre interferometry (Section 1.4.1). Continuum emission at millimetre wavelengths traces thermal emission from cool dust that resides within the midplane and in the outer regions of the disc. The midplane is a dense, sheltered environment that remains cool as a result of this shield from radiation. The midplane is also where giant planets are expected to form. Unlike observations made in the infra-red, millimetre emission is usually optically thin meaning that variations in the intensity of continuum emission from dust alerts observers to changes in dust density within the disc. Millimetre emission therefore plays a vital role in weighing protoplanetary discs (although not without uncertainties; see Section 1.1.6). A further benefit is that millimetre continuum emission originates mostly from grains of around millimetre sizes, i.e. dust on the verge of becoming 'pebbles'. Dust grains of this size are at a critical juncture in dust evolution and planet formation models as they demonstrate that dust has grown significantly from typical ISM grains of around micron sizes. Further growth beyond mm- or cm-sizes is however very difficult due to fragmentation barriers and increasingly rapid inward radial drift (Section 1.1.6). Confirming the location and structure of millimetre grains in the disc is therefore crucial in characterising the potential sites of planet formation. It is not just studies of dust that benefit from mm wavelengths; low-level rotational transitions of key mass tracer carbon monoxide and its less abundant isotopologues fall within millimetre wavelengths. This provides the opportunity to study the structure and temperature of gas in the disc whilst simultaneously investigating the dust (Section 1.1.5).

Facilities such as Australia Telescope Compact Array (ATCA) in the southern hemisphere and the Sub-Millimetre Array (SMA) and Plateau de Bure Interferometer (PdBI, later renamed NOEMA), in the northern hemisphere led the way in producing interferometric images of continuum emission from dust and molecular emission from gas in protoplanetary discs. The arrival of the Atacama Large Millimetre Array (ALMA) provided unprecedented sensitivity and angular resolution at millimetre and sub-millimetre wavelengths. Protoplanetary discs can be probed with incredible accuracy by sub-au angular resolution, and as a result a wide range of sub-structures have been unveiled within discs including rings, gaps, spirals and asymmetric density clumps. In fact, sub-structure within discs appears to be ubiquitous amongst high resolution observations to date, especially in the case of gaps and rings. Figure 1.3 shows 35 milliarcsecond resolution images from the ground-breaking Disk Substructures at High Angular Resolution Project (DSHARP) survey (Andrews et al., 2018), in which the full range of

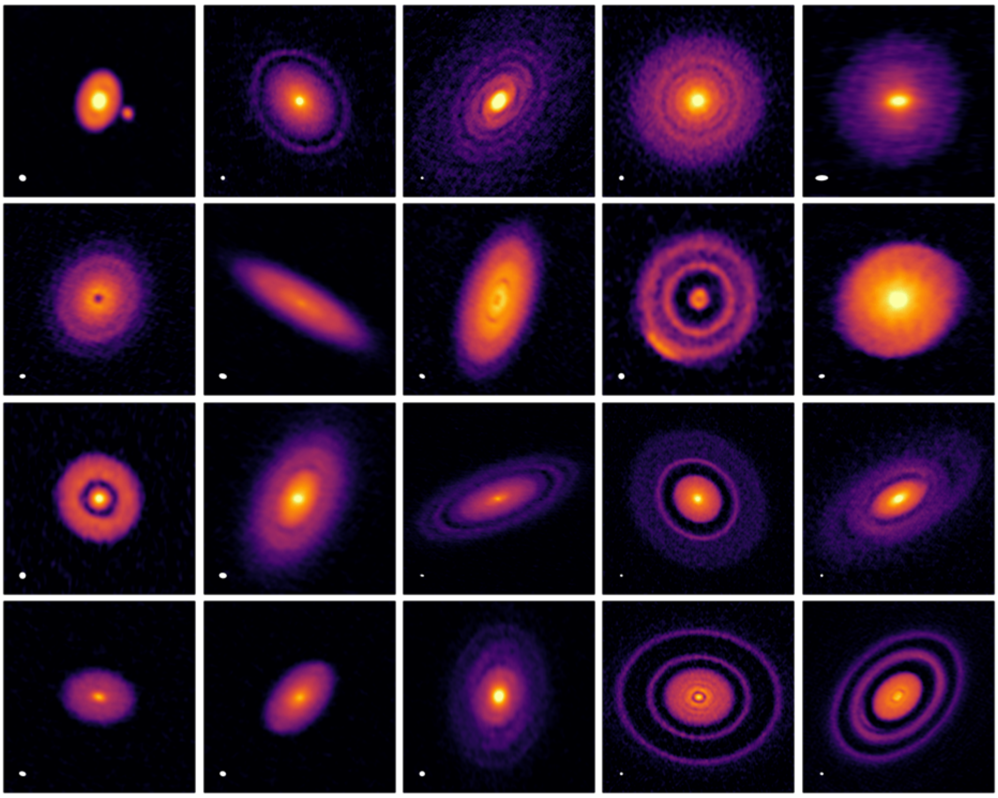

Figure 1.3: The modern view of protoplanetary discs - ALMA continuum images at 1.25mm from the DSHARP survey of protoplanetary discs (Andrews et al., 2018). High resolution mm observations such as these have unveiled a range of substructures in protoplanetary discs, including rings, gaps, spirals and asymmetric density clumps.

protoplanetary disc substructure is exhibited with state-of-the-art sensitivity and resolution.

1.1.3 Protoplanetary disc structure

Protoplanetary discs are comprised of a mixture of gas and dust inherited from the parent molecular cloud. The gas is mainly H_2 (~90%) and He (~10%), unfortunately the spectral lines of these species are weak and difficult to detect. The next most abundant molecule, carbon monoxide (less-abundant than H_2 by a factor of $\sim$ 10,000 in the ISM), has numerous bright spectral lines over a range of wavelengths making it the most useful astronomical tracer of density in molecular clouds and protoplanetary discs.

Dust properties are deduced from observing spectral features of continuum emission, particularly in the infrared. Dust in the ISM is mostly sub-micron sized amorphous silicate grains enriched with elements including O, Fe, Mg, Ca and Al, some crystalline silicates have also been observed in protoplanetary discs (Kemper et al., 2004; Malfait et al., 1998). Millimetre observations can be used to calculate opacities in the dust or protoplanetary discs (Isella et al., 2010; Natta et al., 2006), which are strongly sensitive to grain composition and a_{max}, the largest grain size in the distribution (Draine, 2006).

Gas is far more abundant than dust in protoplanetary discs. Typically a canonical ratio of gas to dust mass (g/d) of 100 is adopted based on values from the ISM. This value does an adequate job in modelling of discs, however significant evolution of dust and gas occurs over the lifetime of a disc and g/d is unlikely to remain constant radially, or with time. The uncertainties in estimating total disc mass from observations of gas and dust emission are significant (discussed in Sections 1.1.5 and 1.1.6), and prevent a critical verification of this assumption.

Radial structure

Protoplanetary discs are first and foremost accretion discs feeding the central star, and so to describe their structure we must consider the transport of angular momentum through the disc. Lynden-Bell and Pringle (1974) were the first to suggest that a viscous accretion disc could explain known properties of T Tauri stars. Angular momentum transport in discs is assumed to be driven by turbulence within the disc on length scales that are small in comparison to the disc scale height. It is still somewhat of a puzzle as to what the specific physical origin of this turbulence is. However in order to proceed, many parametric models adopt the Hartmann et al. (1998) description of viscosities in the disc as a time-independent power law $\nu \propto R^{\gamma}$. Shakura and Sunyaev (1973) introduced a way to write the 'effective' or turbulent viscosity as $\nu = \alpha c_s h$ still regularly utilised to this day. This prescription allows for viscosity to be defined only in terms of the local disc quantities sound speed c$_s$, scale height h and the dimensionless alpha parameter α, a constant which describes the efficiency of angular momentum transport independent of a specific physical origin.

Building from these seminal works and the disc modelling that followed them, Andrews et al. (2011) define a global surface density radial profile based on millimetre observations of protoplanetary discs and modelling of their SEDs as

$$\Sigma_g = \Sigma_c \left(\frac{R}{R_c}\right)^{-\gamma} \exp\left[-\left(\frac{\mathrm{R}}{\mathrm{R_c}}\right)^{2-\gamma}\right], \tag{1.1}$$

where Σ_g is the surface density of the gas, R$_c$ is a characteristic scaling radius and Σ_c the surface density at that radius. This model includes a tapered exponential decay in the outer disc, necessary for reproducing the extended gas and dust emission regularly detected in outer regions (Hughes et al., 2008).

Vertical structure

The vertical profile of a protoplanetary disc is a balance between the vertical pressure gradient in the gas, and the vertical component of gravity. This gravitational component is a result of rotation around the central star, i.e. not the gravitational field of the disc, which is assumed to be negligible unless $\mathrm{M_{disc}} \approx \mathrm{M_*}$ in which case disc self-gravity leads to the disc becoming unstable to the formation of spiral waves in the disc. Assuming the disc to be vertically isothermal and that pressure in the midplane is defined by $P = \rho c^2$, this gives

$$\frac{1}{\rho}\frac{dP}{dz} = \frac{c^2}{\rho}\frac{d\rho}{dz}. \tag{1.2}$$

The solution to Equation 1.2 for a thin disc $z \ll r$ in Keplerian rotation gives a vertical density profile of

$$\rho = \rho_0 e^{-\frac{z^2}{2h^2}}, \tag{1.3}$$

where h is the disc scale height and ρ_0 is the midplane density. The midplane of a disc is dense, resulting in an increased optical depth to starlight meaning that it becomes an obscured environment that cools to temperatures of around 20 K even at 10s of au. It is in this environment that giant planets are expected to form. The ratio h/r increases with radius due to the flared disc surface; outer regions are heated mainly through the capture and reprocessing of starlight from the surface layers. Dust grains coupled to the gas are suspended vertically above the midplane in a balance between gas pressure and gravity. The largest grains settle towards the dense midplane of the disc (Dullemond and Dominik, 2004b). Close to the inner wall of the disc temperature gradients are steeper and subsequently viscous heating becomes a dominant factor in determining disc temperature. The size of the regions over which viscous heating is significant varies depending on the spectral type of the star and the disc properties, but typically does not stretch much further than a few au.

An isothermal vertical temperature profile is often adopted in modelling following Chiang and Goldreich (1997), this approximation only holds for regions close to the midplane, where heating from reprocessed starlight is negligible.

1.1.4 Results from observational surveys

High resolution observations with long integration times are useful in characterising individual discs to a great degree of accuracy such as those in Figure 1.3. In order to determine fundamental properties of discs across statistically significant sample sizes, a slightly different approach is required. Large demographic surveys take snapshots of complete populations within known star forming regions to determine fundamental properties of discs. Furthermore the different star forming regions span a range in ages, and so comparisons between regions can also give an indication as to expected trends in disc evolution.

One key property constrained in surveys such as these is disc mass. Typical gas masses for the young discs in Lupus are $< \ 1$ M_J (Miotello et al., 2017), whilst most dust masses range between $10^{-4} - 10^{-6}$ $M_\odot$. Figure 1.4 compares the disc dust mass cumulative distribution for star forming regions of different ages. Between the ~1 Myr Orion Nebular cluster and 5-10 Myr Upper Sco, dust masses generally decrease as the discs evolve (See Section 1.2 for discussion of disc evolution).

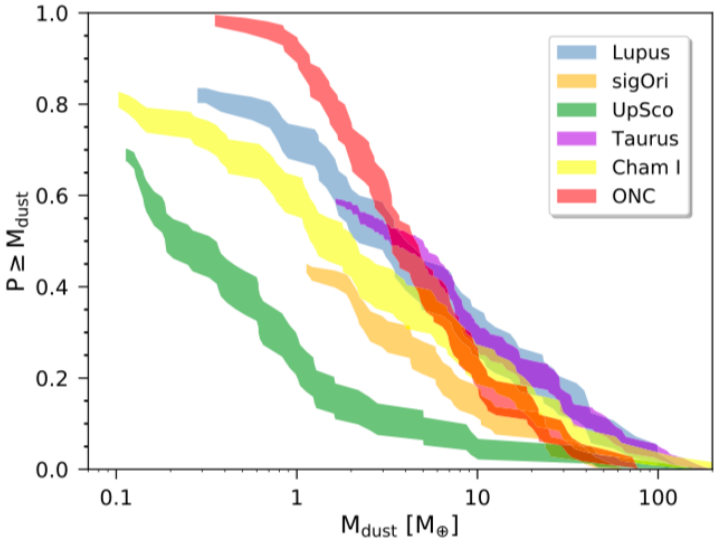

Figure 1.4: Disc dust mass cumulative distribution in Orion Nebular Cluster (ONC) (1 Myr, Eisner et al., 2018), Taurus (2 Myr, Andrews et al., 2013), Lupus (1-3 Myr, Ansdell et al., 2016), Chameleon 1 (2 Myr, Pascucci et al., 2016), σ Orionis (3-5 Myr, Ansdell et al., 2017), and Upper Sco (Barenfeld et al., 2016). The distributions and the 1 confidence intervals (shaded regions) were calculated using the KaplanMeier estimator. Figure originally in Eisner et al. (2018).

The other fundamental property well constrained by these surveys is disc size. Gas discs are universally more extended than the millimetre dust discs (Ansdell et al., 2018) and there is evidence that this is because of inward radial drift of solids, rather than optical depth effects (Trapman et al., 2019). The size of dust discs also appears to decrease with time when comparing across star forming regions. Dust discs in Upper Sco are around three times smaller than in Taurus (1-3 Myr) (Barenfeld et al., 2017).

1.1.5 Gas in discs

Molecular line emission

Gas in discs is studied by the observation of emission lines from molecules within the disc. Different molecules trace different regions of the disc or act as useful tracers of chemical processes. Emission lines broaden through the Doppler effect if the gas is moving along the line of sight of the observer, and as a result spectrally resolved lines also provide kinematic information. In the case of protoplanetary discs this can be used to constrain the inclination of the disc relative to the observers line of sight and its position angle on the sky.

CO is an abundant molecule with well studied chemistry making it a useful observational tool. It also has a number of less abundant isotopologues that are readily detectable at similar frequencies. These species are useful tracers of gas density structure and, through spectral resolution of their emission lines, gas kinematics in the disc. CO is also the molecule most regularly used to make estimates of disc mass; a property that is vital to observational and modelling efforts in the field, but one that is still not accurately measured easily.

Mass estimates

The mass of gas in the disc can be estimated from observations by integrating the flux received from a molecular emission line and then for an assumed temperature, calculating how many molecules are required to produce such a flux. This is done with Equation 1.4

$$M_{\rm gas} = \frac{4\pi}{h\nu_{u,l}} \frac{F_{u,l}\ m\ d^2}{A_{u,l}\ X}, \tag{1.4}$$

where $\mathrm{F}_{u,l}$ is the integrated line flux resulting from a transition from upper energy level u to lower level l, $\nu_{u,l}$ is the rest frequency of the transition, d the distance to the source, m is the mass of the CO molecule and $A_{u,l}$ is the appropriate Einstein coefficient. X_u is the fractional population of the upper level, assuming that all energy levels are populated through a Boltzmann distribution

$$X_u = \frac{N_u}{N_{total}} = \frac{g_u}{Z} e^{\frac{-E_u}{kT_k}}, \tag{1.5}$$

where g_u is the degeneracy of level u, E_u is the energy of that level, T_k is the kinetic (i.e. disc) temperature and Z is the partition function

$$Z = \sum_i g_i\ e^{\frac{-E_i}{kT_k}}. \tag{1.6}$$

Equation 1.4 provides a direct method for computing disc mass which is not dependent on any model. This method does however make a number of assumptions which introduce large uncertainties into the result it produces.

CO remains in the gas phase until its freezing temperature, which in a protoplanetary disc is ≈20 K (Öberg et al., 2011) , meaning unlike other molecules it remains in the gas phase for a large fraction of the protoplanetary disc's radial extent. At a certain radial separation from the host star, the midplane temperature profile drops below this critical value. CO that is radially interior to the so-called ‘snowline’ will remain in the gas phase whereas beyond the snowline CO molecules stick to icy solid grains, a process known as ‘freeze-out’. As a result, beyond the snowline any CO or CO isotopologues will not be detectable and so the disc mass estimate is likely to be an underestimate. Molecules of the chosen tracer can exist in various radial and vertical locations in the disc, and so local disc temperature is unlikely to be the same across the whole emitting population. In this thesis, the density tracers used for mass estimates are CO isotopologues that are assumed to be tracing the column down to the midplane. In the cold, dense midplane and in the outer disc (where a large proportion of disc mass is stored) temperatures can drop to levels of around 20K. If temperature is any lower than this, CO will be frozen out and undetectable. By assuming a minimum temperature of 20 K, this method provides a firm lower limit on the estimate of gas mass.

Figure 1.5 shows the regions of the disc in which carbon resides in different forms. UV absorption lines of ^{12}CO become optically thick at a column density of 10^{15} cm^{-2} (van Dishoeck and Black, 1988), reached in the warm molecular layers towards the surface of the disc as shown in Figure 1.5. In this case, the optically thick ^{12}CO emission is not useful for tracing density in the disc as the observed emission originates only from a thin layer of the disc above the $\tau = 1$ surface. This means that variations in the observed intensity can originate either from variations in density or in temperature of the local disc in emitting regions.

The optical depth issues can be solved with observations of less abundant CO isotopologues such as ^{13}CO and C^{18}O, because these species do not become optically thick until much deeper in the disc, if at all. In discs with optically thick ^{12}CO emission, optically thin CO isotopologue emission is a powerful tool

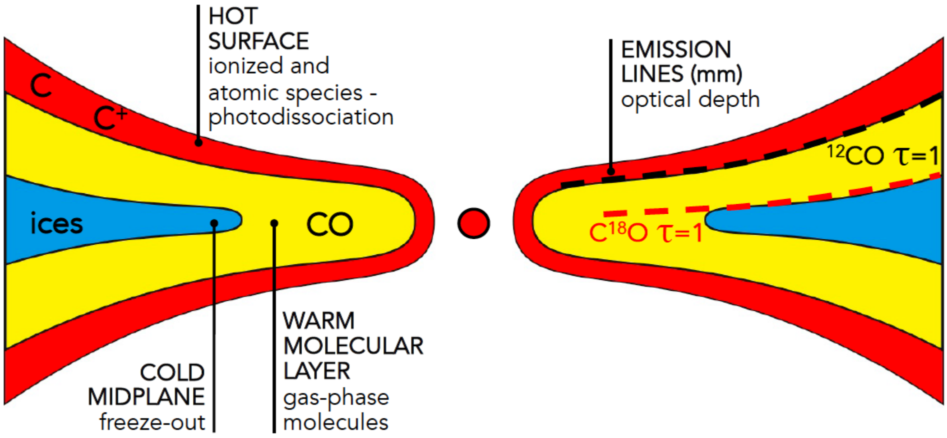

Figure 1.5: Diagram showing the thermo-chemical structure of carbon in a protoplanetary disc as a result of the radial and vertical temperature profile. Figure from PhD thesis of Miotello (2018)

.

in tracing column density down to the dense midplane of the disc. In this case, the derived disc mass must be scaled up to reflect the relative abundance of, for example, $C^{18}O$ compared to ^{12}CO, by assuming the ratio $C^{18}O/^{12}CO$ follows the elemental isotopic ratio $[^{18}O]/[^{16}O]$ in the ISM ≈560 (Wilson and Rood, 1994). Again we must be careful with the assumption of a constant abundance ratio. ^{12}CO, ^{13}CO and $C^{18}O$ are sensitive to photodissociation by UV photons, but at high column density can also self-shield and mutually shield (Visser et al., 2009). Due to their different abundances photodissociation occurs at different depths within the disc, meaning large relative abundances of e.g. ^{12}CO and ^{13}CO will arise in dense regions where $C^{18}O$ is affected by dissociation. Miotello et al. (2014) show that isotope selective photodissociation effects such as these can lead to underestimation of disc masses by up to an order of magnitude.

A final consideration in relation to disc mass is the depletion of volatile carbon budget in the disc. Although H_2 emission cannot aid with the determination of disc mass, a handful of HD detections have been made in bright protoplanetary discs. Mass estimates using HD are producing values greater than that obtained from CO, suggesting the latter may not be as strong a tracer of density as previously thought (Bergin et al., 2013; Favre et al., 2013; Kama et al., 2016). Removal of carbon may occur through the conversion of CO into more complex molecules (Yu et al., 2016), locked up in solids towards the midplane (Du et al., 2015) or through depletion as a result of chemical evolution in the disc driven by X-rays and cosmic rays (Eistrup et al., 2016).

1.1.6 Dust in discs

Radial Drift

Dust in protoplanetary discs orbits the central star in a Keplerian fashion. The gas however is affected by a centrally peaked pressure gradient. Assuming viscosity and magnetic fields to be negligible, in a stationary axisymmetric flow where the star dominates the potential, the radial component of the momentum equation gives

$$\frac{v_{\phi,gas}^2}{r} = \frac{GM_*}{r^2} + \frac{1}{\rho}\frac{dP}{dr}, \tag{1.7}$$

as given in (Armitage, 2009) where the second term on the right hand side is negative, because pressure decreases with radius from the star for a centrally peaked density profile such as in Equation 1.1. This means that gas will always orbit at a slightly sub-Keplerian velocity, slower then the dust. This creates a headwind for orbiting dust grains, decelerating their orbital velocity from Keplerian and introducing a radial velocity that carries the dust grain towards the central star in a process known as radial drift (Weidenschilling, 1977). Radial drift results in a radial size-sorting of particles because the drag force increases for grains of larger surface area. The smallest grains remain in the outer disc, whereas larger grains approaching mm sizes drift inwards. Radial drift timescales for particles in the outer regions of the disc (>100 au) are of order 10^5 years, however disc lifetimes are of order $10^6 - 10^7$ years, meaning the particles in the outer disc should have already drifted onto the star.

Retention of large grains in the outer disc, or alternatively some form of continuous replenishment, therefore seems to be essential in order to explain the observational data (Birnstiel and Andrews, 2013; Klahr and Bodenheimer, 2006). Local maxima in gas density due to pressure bumps can prevent radial drift and create ideal locations for further growth of dust (Pinilla et al., 2012b; Weidenschilling, 1977; Whipple, 1972). Massive planets capable of opening a cavity in the gas distribution create a large pressure bump at the edge of the orbit, resulting in radial dust traps that produce ring shaped dust accumulation (2012a). All of the rings analysed in the high resolution ALMA observations in the DSHARP survey are consistent with the predictions of dust trapping (Dullemond et al., 2018). Pressure maxima can occur azimuthally as well as radially. If a massive orbiting body causes a large perturbation, azimuthal dust traps can have an influential role on the dust distribution in the disc, producing a crescent or banana shaped dust structure. This theory has been successful in explaining the highly asymmetric dust emission observed in IRS 48 (van der Marel et al., 2015). Evidence of crescent-shaped dust asymmetries in systems such as V1247 Orionis (Kraus et al., 2017) and HD135344B (Cazzoletti et al., 2018) point towards the gravitational interaction of orbiting massive planets as the cause of the dust traps. Radial drift can also be inhibited by magnetic dead-zones where turbulence and angular momentum transport reduce to a minimum, allowing solid material and planetary embryos to be efficiently trapped at the inner edge of the dead zone (Dzyurkevich et al., 2010).

Dust evolution

Dust in the ISM is found with a grain size distribution that follows a power law,

$$dn/da \propto a^{-p}, \tag{1.8}$$

a distribution described by a power law such as this with index p=3.5 is known as an MRN power law, after the authors of the paper in which it was derived, and describes a typical size distribution in interstellar grains (Mathis et al., 1977). The index in Equation 1.8 changes as the dust population evolves, a flatter power law means more of the mass in the total dust population is contained within the larger grains. Dust grains orbiting in the disc stick together as a result of collisions. If the collisional velocity in the disc is high, the grains can bounce off each other or fragment into smaller grains (see Testi et al., 2014, and references therein).

Models suggest the competing growth and fragmentation processes will settle towards a steady state solution. The resulting distribution is usually a power-law or broken power-law, which does not necessarily match the MRN distribution seen in the ISM (Birnstiel et al., 2011). Growth of grains tends to lower p, whereas fragmentation will re-introduce small particles and raise p.

Birnstiel et al. (2012) present a simple model comprised of just two populations: small grains that are well coupled to the gas and large grains that feel the effects of radial drift and contain most of the dust mass. The results of the model agree very well with the results of full simulations from dust evolution codes and can describe the radial evolution of dust surface density and the evolution of largest grain sizes (Birnstiel et al., 2012). This approach provides the basis for much of the dust modelling in the field.

Continuum emission

We can probe dust content of a protoplanetary disc through observations of continuum emission from the dust. Solid grains emit as a blackbody, and as temperature in protoplanetary discs decreases with radial separation from the star, different regions of the disc will contribute to different parts of the SED as illustrated in Figure 1.6. For example the inner wall of the protoplanetary disc and the hottest regions closest to the star contribute at near-IR wavelengths, whereas the outer disc and the cool, sheltered mid-plane contribute to millimetre wavelengths.

Continuum emission also depends on particle size; millimetre continuum emission comes most efficiently from a narrow range of grain sizes between 1 mm and 1 cm (Takeuchi and Lin, 2005). If grains have grown beyond $a_{max} \approx 3\lambda$, where λ is the wavelength of observation, they emit less efficiently (Draine, 2006).

Tracing mass

Continuum emission at mm-wavelengths is a diagnostic tool for tracing the coolest dust in a protoplanetary disc, which is contained in the mid-plane and in the outer disc, where the majority of solid mass is expected to be contained. This makes millimetre fluxes the most useful for estimating disc mass.

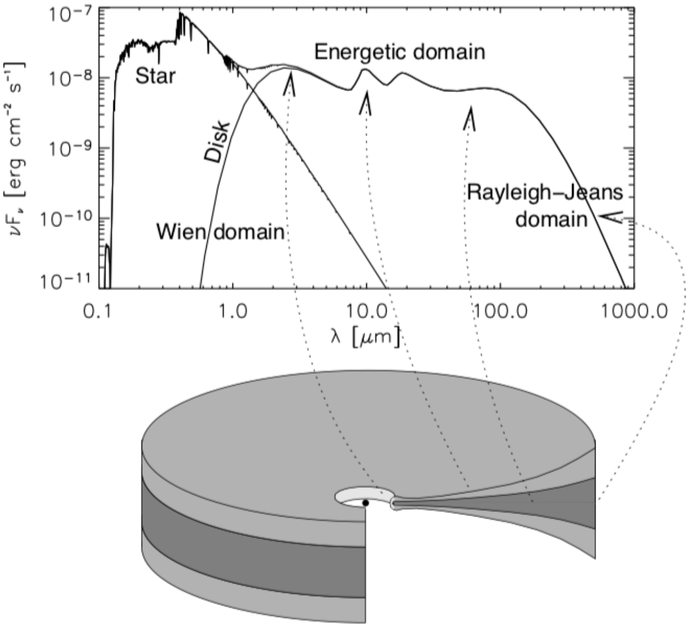

Figure 1.6: A diagram showing the cross section of a protoplanetary disc and the regions of the disc that contribute to difference components of the SED, from (Dullemond et al., 2007).

Measured flux can be related to the mass of emitting particles by assuming optically thin emission and using

$$F_\nu = \frac{\kappa_\nu B_\nu(T) M_{dust}}{d^2}, \tag{1.9}$$

where F$_\nu$ is the continuum flux measured at frequency ν, κ_ν is the specific opacity, d is the distance to the source from the observer and $B_\nu(T)$ the Planck function at temperature T. This method also assumes that millimetre flux is from thermal emission; in some more massive Herbigs free-free emission can be non-negligible, but remains a small fraction of total flux (e.g. HD100546 Wright et al., 2015).

Estimating disc mass directly from millimetre continuum flux does not tell the full story however. Manara et al. (2018) compared the masses of known exoplanets with the masses of protoplanetary discs in young regions of 1-3 Myr. It was expected that discs would be much more massive, as current theories of planet formation assert that it is not a particularly efficient process in terms of converting disc material into planets. The authors found protoplanetary dust disc masses to be lower, or at best comparable to, the amount of mass in heavy elements in the exoplanetary systems discovered to date. Either disc dust masses are systematically, significantly underestimated, or the cores of planets are forming very quickly (0.1-1 Myr) and disc are continuously replenished throughout their lifetime. In both scenarios, we are far from understanding the puzzle of solid mass in discs.

The largest uncertainty in estimates made of dust mass using Equation 1.9, and a likely source for the discrepancy highlighted by (Manara et al., 2018), is due to the opacity term. Opacity has a power law dependence on frequency $\kappa_\nu \propto \nu^\beta$ where β is the opacity spectral index β,

$$\beta(\lambda) \equiv \frac{d\ ln\ \kappa}{d\ ln\ \nu}. \tag{1.10}$$

In an optically thin disc under the Rayleigh-Jeans approximation, the opacity index can be related to the spectral index by $\alpha_{\mathrm{mm}} = \beta_{\mathrm{mm}} + 2$ (Draine, 2006) . At millimetre wavelengths the dust being traced in the outer disc and midplane is often cool enough that the Rayleigh-Jeans approximation does not apply. Draine (2006) shows that in this case, for power law size distributions of $dn/da \propto a^{-p}$, where $a \leq a_{\mathrm{max}}$, $3 < p$ <4 and $\mathrm{a}_{\mathrm{max}} \geq 3\lambda_{\mathrm{obs}}$, then

$$\beta \approx (p - 3)\ \beta_s, \tag{1.11}$$

where β_s is the opacity spectral index of solid material in the Rayleigh limit (Draine, 2003, 2006). Figure 1.7 shows calculations of the opacity of amorphous spheres as a function of both frequency and the maximum grain size in the dust distribution.

Figure 1.7 calculates κ and β for a single grain type, in a real disc the dust will be a mixture of compositions in which optical constants, and as a result κ will vary (e.g. carbonaceous grains, Jäger et al., 1998).

At millimetre wavelengths it is clear that simplifications of opacity based on the Rayleigh-Jeans approximation cannot be relied upon, and without robust information on the distribution and composition of dust grains, constraining opacity is difficult observationally. However, even if the absolute opacity cannot be

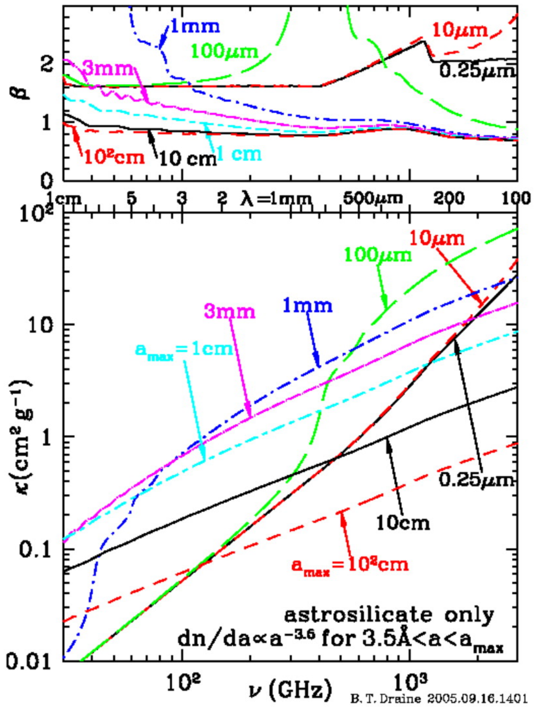

Figure 1.7: From Draine (2006). Lower panel: Opacity of amorphous silicate spheres with size distribution dn/da $\propto a^{-3.5}$ for 3.5Å$\leq a \leq a_{max}$. Curves are labelled by a_{max}. Upper panel: $\beta \equiv d\ \ln\kappa / d\ \ln\nu$ for selected a_{max}; β(1mm)≤ 1 is found for $a_{max} \geq$ 3mm.

determined, multi-wavelength observations can be used to measure the opacity spectral index. Using fluxes measured at observing frequencies ν_1 and ν_2, the opacity index can be calculated by

$$\beta_{\rm mm}(R) = \frac{{\rm dlog}F_\nu(R) - {\rm dlog}B_\nu}{{\rm dlog}\nu} = \frac{\log\left(\frac{{\rm F}_{\nu,1}}{{\rm F}_{\nu,2}}\right) - \log\left(\frac{{\rm B}_{\nu,1}}{{\rm B}_{\nu,2}}\right)}{\log\left(\frac{\nu_1}{\nu_2}\right)}. \tag{1.12}$$

In diffuse clouds $\beta \approx 1.7$ (Finkbeiner et al., 1999; Li and Draine, 2001). A lower value is found for unresolved measurements of continuum flux in protoplanetary discs, Beckwith and Sargent (1991) fit models to a sample of 29 pre-main sequence objects finding a median value of $\beta_{\rm disc}$=0.92 . The arrival of ALMA has resulted in the resolved images of discs and as a result β can now be calculated as a function or radius. Guidi et al. (2016) calculate β(R) in HD163926 and find its value to increase with radial separation from the star from ≈0.5 - 2.3. A radially increasing β agrees with the predictions of size sorting by radial drift as larger grains will give a lower value of β.

The most reliable dust mass estimates through Equation 1.9 will make a good choice of T by constraining it through modelling of the dust disc. Alternatively a minimum dust mass can be calculated by assuming all emitting dust is at a low temperature representative of the outer disc or midplane ($\approx$ 20 K). A good estimate of κ can be made from Figure 1.7 using the observing frequency and an estimate of $a_{\max}$ in the dust distribution of the disc. All of the above assumes optically thin emission, which is not necessarily the case, particularly in inner regions where $\tau > 1$ can be reached even at millimetre wavelengths.

Spectral index

The spectral index of emission from a protoplanetary disc shows the dependence of flux on frequency.

$$\alpha = \frac{d \log \mathrm{F}_\nu}{d \log \nu} \tag{1.13}$$

The spectral index is related to the opacity index, and so is still affected by the caveats described above. Variations in spectral index between different discs, or indeed between different regions in a single disc, alert observers to differences in the properties of the emitting solid material. Surveys of star forming regions find that disc-averaged spectral indices can lie in the range $1.5 \leq \alpha_{\mathrm{mm}} \leq 3.5$ (Pinilla et al., 2014; Ricci et al., 2012). Using α and dust modelling to constrain the index p of the dust grain size distribution can demonstrate the level of dust evolution in a disc, offering insight as to the evolutionary state of the system (e.g. in HD141569 White et al., 2018).

Radial drift and grain growth predict the largest solid particles to be concentrated toward the star, leaving the smaller ones behind. As emission brightness is related to grain size we can therefore expect a variation in observed disc size at different observing wavelengths, but also a variation in spectral index, α_{mm}, across the disc. Spatially resolved continuum images of discs at multiple wavelengths allow for a calculation of a position-dependent α_{mm}, where, for optically thin emission, $S_\nu \propto \nu^{\alpha_{\rm mm}}$. If the size of grains in the disc varies with radius then so will the spectral index. Guidi et al. (2016) find a spectral index that increases radially $2.5 < \alpha(R) < 3.9$.

2D mapping of the spectral index from high-resolution images of protoplanetary discs can shows how α varies throughout the disc, which can be useful for identifying local concentrations of, for example, large grains trapped in a pressure trap (e.g. IRS 48; HD135344B, Cazzoletti et al., 2018; van der Marel et al., 2015). Spectral index of the trapped dust can be used as a diagnostic tool for exploring the properties of the vortex causing the trap, and the efficiency of the dust trapping (Hammer et al., 2019).

1.2 Disc Evolution

1.2.1 Classical view of isolated low-mass star formation

Characterisation and modelling of a system's SED gives a good first order approximation of a protoplanetary discs evolutionary state because the shape of the SED is related to properties such as disc mass and the radial distribution of gas and dust in the disc. Great care must be taken with SED modelling of protoplanetary discs however; there is no unique solution to any individual SED. Modelling of a disc's emission includes a number of degenerate properties, the effects of which are impossible to distinguish on the basis of photometry alone.

Nevertheless, broad conclusions can be drawn from the shape of an SED, in particular from the form of the observed IR excess. As discussed at the beginning of this chapter, protoplanetary discs initially result from the process of star formation. Figure 1.8 shows the observational stages of protostar formation in the evolutionary sequence proposed to explain the changes to their spectra known as the 'Lada Sequence' (Adams et al., 1987; Lada, 1987). These epochs set the context for disc evolution and provide useful points of reference for the processes of disc evolution and planet formation.

The **Class 0** stage represents the embedded processes of star formation described in Section 1.1.1. The star is obscured from view by the cold material which surrounds it, the latter produces cold blackbody emission at millimetre wavelengths as seen in the top panel of Figure 1.8. By the **Class I** stage, circumstellar material has settled into a vertically thin accretion disc. Accretion luminosity from the central star heats the inner disc and the flared outer disc absorbs a large amount of stellar radiation, which is re-emitted at infrared wavelengths resulting in the large IR excess in the Class I panel of Figure 1.8, peaking at far-IR wavelengths.

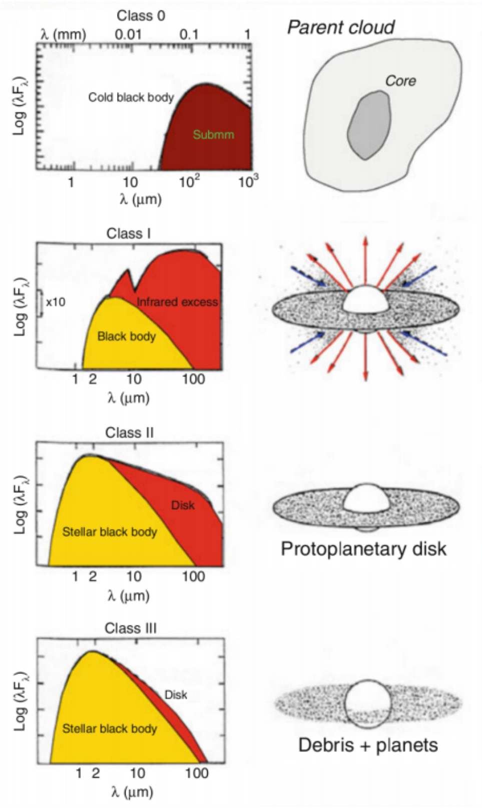

Figure 1.8: An illustration of the stages of star formation and disc evolution. On the right is a sketch of the physical geometry of the system at each stage, and the left is a typical spectral energy distribution at each stage, where yellow represents the contribution from the star, and red the contribution from the surrounding material. Figure originally from Mulders (2013).

It was unclear at first whether disc structures existed in the obscured regions around the cold core. Surveys of protostellar discs at mm and cm wavelengths with large sample sizes have now begun to detect discs around Class 0/I objects and provide information on their demographics. ALMA observed 330 protostars in Orion as part of the VANDAM survey, from which disc radii were approximated through a Gaussian fit to emission maps, and disc masses were estimated by assuming a dust temperature of 30 K and a canonical gas-to-dust ratio in the disc of 100. For non-binary, Class 0 objects a median disc radii of ≈34 au was found and a median disc mass estimate of $\approx 0.029\mathrm{M}_{\odot}$. Class I discs were systematically more compact with a median radius of 25 au, and a disc mass of $\approx$0.019 $\mathrm{M}_{\odot}$ (Tobin et al., 2020). It is increasingly believed that planet formation processes must begin during these early Class 0 and I stages when disc masses are expected to be larger (see Figure 1.4) and when fewer of the larger grains that are important for forming cores have drifted inward to be accreted by the star.

This thesis focuses mainly on discs in the Class II and III stage; after the circumstellar envelope has dispersed, settled into the disc or been accreted onto the star, leaving a star-disc system behind. Although strict divisions between these classes are difficult to determine, **Class II** is often considered the first instance of a 'protoplanetary' disc. Protoplanetary discs are described as being geometrically thin, following the settling of circumstellar material, and optically thick, meaning class II objects still exhibit strong emission throughout IR wavelengths due to re-radiation of absorbed starlight. The SED peaks at optical wavelengths however, as less stellar flux is obscured by surrounding material. It is within these discs that the mechanisms for planet formation operate. The physical structure of Class II discs is described in detail in Section 1.1.3.

Class III discs are the last stage in a classical view of disc evolution. Through a combination of photoevaporation, planet formation, accretion onto the central star and dispersal into the ISM, disc material is depleted over timescales of a few million years. When inner regions are cleared of material, accretion can no longer continue. This leads to the outer gas disc viscously draining onto the central star rapidly, bringing about a swift end to the protoplanetary stage (e.g. see models of X-ray photoevaporation by Alexander et al., 2006). All planet formation has already occured by now. In this heavily gas-depleted disc there is no longer any vertical support for dust, leading to a thin, discontinous disc of solids. Collisions between larger bodies result in fragmentation into smaller grains. These Class III systems are hence given the name 'debris' discs. Most debris discs have an SED

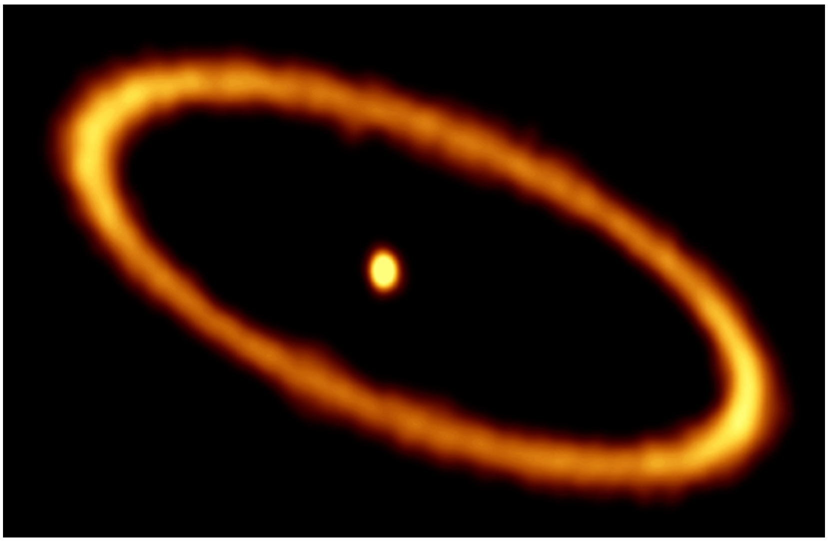

Figure 1.9: ALMA image of the debris ring around Fomalhaut. This images was produced though a mosaic of images observed at a wavelength of 1.3mm. Image from (Macgregor et al., 2017)

that can be described with emission at two different temperatures, which is likely to suggest the presence of multiple rings/belts in a disc (Kennedy and Wyatt, 2014). This two-temperature structure may be analogous to the remaining disc of the Solar System; comprised of the Asteroid belt and Edgeworth-Kuiper belt. A two-temperature profile can in some instances be reproduced from a single belt containing a variation in grain sizes due to the degeneracies in SED modelling. As the mass of remaining disc material is low, debris discs are often faint and have been difficult to detect in the past. Modern facilities are now capable of detecting and even spatially resolving debris discs, confirming the proposed ring-like structure as can be seen in the image of Fomalhaut in Figure 1.9 (MacGregor et al., 2016).

1.2.2 Transition Discs

SED modelling of T Tauri stars helped to reveal the process by which class II discs evolve into class III discs. So called "transition discs" were first identified by Strom et al. (1989) and Skrutskie et al. (1990) as PMS stars hosting discs with inner holes. The absence of dust towards inner regions was inferred from a lack of IR excess in the SED even though a strong mid- and far- IR excess was still present. This prediction was later confirmed by SMA imaging that revealed discs with inner holes (e.g. Brown et al., 2009). Transition discs provided significant observational evidence for evolutionary processes in protoplanetary discs to occur from the inside-out, as opposed to a homogeneous depletion of circumstellar material or the exterior photo evaporation of the Orion proplyds.

Some discs with inner gaps have been found to contain small dust components interior to this gap at very short separation (e.g. HD100546 Panić et al., 2014), and were labelled 'pre-transition' discs (Espaillat et al., 2007). As the nomenclature suggests, initially these systems were thought to be showing a transitional phase between a transition disc and a gas-poor, ringed debris disc.

Clearing of inner regions can be achieved through photoevaporation, planet formation or dynamical influences of inner companions/exoplanets. A decrease in near-IR flux can also be achieved if dust situated in the inner regions of the disc has grown into larger bodies such as km-sized planetesimals, which emit at longer wavelengths. In this case low optical depth at IR or mm observing wavelengths can give the impression of a cleared gap.

Photoevaporation models for inner clearing are unable to reproduce the large cavity sizes, accretion rates and disc masses observed in transition discs. Analysis of 12 resolved transition disc cavities with the SMA by Andrews et al. (2011) found dynamical clearing due to either low mass companions, giant planets on long orbits, or young brown dwarfs to be the most likely explanation in order to fit the observed disc density profiles. Within the dust gaps, gas is usually present but with decreased surface density (Carmona et al., 2017). High resolution ALMA imaging of ^{13}CO and C^{18}O revealed gas cavities within the dust cavities of four transition discs, where the cavity in gas was up to three times smaller than that of the dust (van der Marel et al., 2016). The observed structures agree with models of planet-disc interactions in which giant planetary companions sculpt the inner gap (van der Marel et al., 2016).

As a result of the growing library of high resolution ALMA data, gaps and rings have become frequently observed structural features. Some transition discs have been shown to consist of multiple dust rings (Fedele et al., 2018; van der Plas et al., 2019) and some systems previously categorised as transition discs such as MY Lup (Tazzari et al., 2017; van der Marel et al., 2018) have shown a centrally peaked surface density profile when imaged with high resolution (Huang et al., 2018) - contradicting the predictions from SED analysis. Indeed many of the substructures associated with transitional discs can be reproduced by invoking a single binary partner (Ireland and Kraus, 2008). Through 3D hydrodynamical models of 'transition' disc HD142527, Price et al. (2018) reproduced all the structural features identified in the disc through observations including spiral arms, inner cavity, shadows, fast radial flows, streamers and a 'horseshoe' structure in the dust.

Due to the multiple mechanisms or scenarios for creating an inner gap, the role of transition discs in protoplanetary disc evolution is not completely clear. Not every gap or cavity in a disc should be assumed to be one that is planet driven (Dong et al., 2017; Gonzalez et al., 2015; Ndugu et al., 2019). Nevertheless, transition discs are likely to play a vital role in the modelling of embedded exoplanets and their interaction with the host disc. In recent years the first evidence of directly imaged planets within the cavity of a transitional disc has been achieved (Haffert et al., 2019; Keppler et al., 2018; Wagner et al., 2018, PDS 70) and more cases are expected to follow.

1.2.3 Gaseous Debris Discs

Debris discs are widely presumed to be dusty, gas-free environments governed by collisional dynamics of the large, rocky bodies that comprise the debris belts. There is no well defined distinction between protoplanetary discs and debris discs, but a good indication is given by considering dust mass in the disc and the age of the host star.

Figure 1.10 plots sub-mm emission from protoplanetary and debris discs over a range of ages. Although there is some overlap, and stellar ages are characteristically uncertain, 'protoplanetary' discs mainly occupy the region of the plot where age is less than 10 Myr and dust mass is greater than $\sim 10\mathrm{M}_{\oplus}$.

Many of these discs are older than the typical lifetimes predicted for lower mass stars through photoevaporation models (4 Myr, Gorti et al. (2009)) or inferred

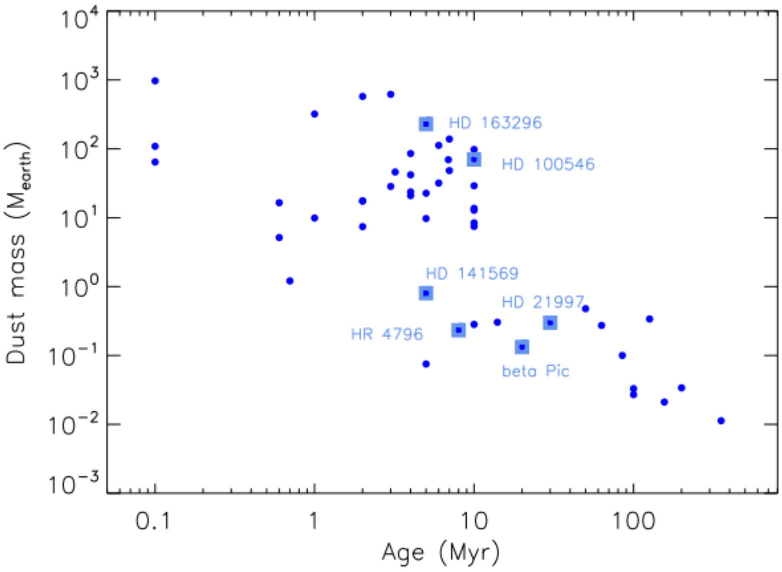

Figure 1.10: Dust mass estimates made from sub-mm observations as function of stellar age stars of spectral type A and B-type. Figure from Wyatt et al. (2015), in original form from Panić et al. (2013). Highlighted with blue squares are two Herbig discs: HD100546 and HD163296, two hybrid discs: HD141569 and HD21997, and two debris discs: HR4796 and Beta Pic.

from measurements of accretion (3 Myr, Fedele et al. (2010)). Near infrared observations of star clusters by Haisch et al. (2001) found that half of the disc population had lost their discs by 3 Myr, and virtually all had lost them by 6 Myr.

Observational evidence at millimetre wavelengths suggests that these lifetimes are underestimates. Some of the brightest, and most well studied Herbig discs are older than 4 Myr, yet maintain a strong $C^{18}O$ flux (e.g. HD97048 Panić et al. (in prep), HD100546 Miley et al. (2019), HD163296 Boneberg et al. (2016)). Even T Tauri disc TW Hydra is ~8 Myr (Donaldson et al., 2016). There is not yet a complete model of photoevaporation in Herbig disc to compare with.

Wyatt et al. (2015) proposed the distinction lies in the existence of large quantities of primordial gas in the disc. Specifically, enough gas so that small dust grains remain well coupled, so that the gas can damp collisions and suspend grains vertically above the midplane.

However, recent observations have begun to detect significant amounts of gas in systems previously categorised as debris discs. Analysing mm-wavelength observations, Moór et al. (2017) found that 11 of the 16 discs in their sample of A type had ^{12}CO detections, and 3 of the 7 discs studies with ALMA observations had optically thick ^{12}CO emission; masking the true density through optical depth effects. Less abundant molecular tracers are therefore crucial in making accurate mass estimates from these discs, previously thought to be very gas poor. There is now significant amounts of gas detected in over 16 'debris' systems, a number likely to rise as more ALMA observations are executed.

There are two leading theories as to how gas can remain at such late stages of disc evolution. The first proposes that the gas we observe is of a secondary origin. In a secondary scenario, after the primordial disc has dispersed collisions between large, rocky planetesimals result in fragmentation and the release of any gas that was trapped within them. This secondary generation of gas is immediately vulnerable to photodissociation and it is believed that neutral carbon within the inner disc plays an important role in shielding the CO to avoid its rapid removal (Kral et al., 2019). A prime example of a secondary scenario is in debris disc β Pic. Figure 1.11 shows the ALMA data in which CO gas was detected at the same location as the planetesimal belt in the system, but only on one side of the disc.

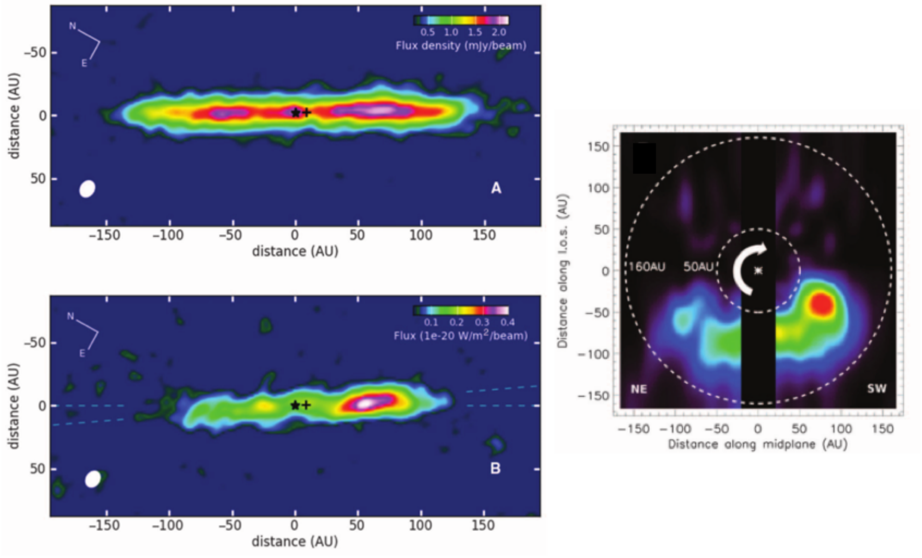

Figure 1.11: ALMA observations of dust continuum (top left) and CO gas rotational emission from the β Pic disc, viewed here almost edge-on. On the right hand side is a deprojection of the gas emission, reconfigured so as to give a pole-on view. Figure adapted from Dent et al. (2014).

The de-projected view on the right of Figure 1.11 is interpreted as a site of origin for the gas towards the southwest followed by a tail pointing in the direction of rotation (Dent et al., 2014). The gas is believed to have been released due to a collision of objects with mass similar to that of the planet Mars. Kral et al. (2017a) applied a numerical secondary gas model to 13 known debris discs with gas detections and were able to reproduce the observed fluxes for all but three cases, suggesting that the majority of currently known gas bearing debris discs agree with a secondary gas scenario. The gas in the remaining three systems (HD 21997, HD 131835 and HD 138813) is likely to be primordial.

The alternative theory is of ‘hybrid’ discs. In a hybrid scenario, the dust in the disc is of a secondary generation resulting from growth and fragmentation as a result of collisions of solids. The gas however is still primordial, lingering from the protoplanetary disc stage of evolution.

In Figure 1.12, Péricaud et al. (2017) demonstrate a correlation between CO gas emission and continuum emission for sources from a range of evolutionary

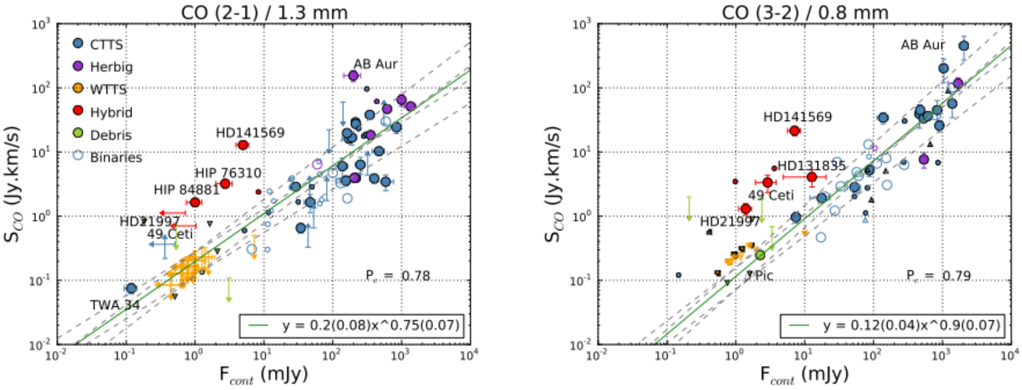

Figure 1.12: ^{12}CO rotational emission plotted against continuum emission in two different ALMA wavelength bands for T Tauri, Herbig, debris and hybrid discs. Binaries are plotted as open circles. Hybrid discs lie above the general trend at both wavelengths. Figure from Péricaud et al. (2017).

stages. The hybrid discs in red appear as outliers from the main population of the plot due to their increased gas flux relative to the dust flux. The straight line fit to data in Figure 1.12 is interpreted as showing a concurrent reduction of both gas and dust from the disc as time goes on. The hybrid discs do not follow this behaviour, perhaps suggesting that their dust population is evolving faster than the gas. The rarity of detected hybrid discs may be a result of the speed of disc dispersal mechanisms, making hybrids difficult to catch observationally (Péricaud et al., 2017).

All currently proposed hybrid discs are found around A type stars, and as of yet there is no equivalent around T Tauri stars (Lieman-Sifry et al., 2016). All hybrid discs are either isolated, or in loose associations, perhaps aiding with their detection as their discs are likelier to be more massive and more luminous, unaffected by the dynamics or radiation fields of neighbours.

1.3 Herbig Stars

Herbig Ae/Be (HAeBe) stars are pre-main sequence intermediate mass stars that host massive accretion discs (Hillenbrand et al., 1992). First considered as a distinct grouping of objects by Herbig (1960), the author set out three key criteria for the sample: the star must be of spectral type A or earlier with emission lines, it must lie in an obscure region and it must illuminate a fairly bright nebulosity in the immediate vicinity. The et al. (1994) produced a comprehensive catalogue of 287 sources meeting this criteria which forms the basis of modern lists defining the category. In the modern day, only the first of the main criteria is regularly upheld, and even this has been relaxed somewhat to include some F-type stars (e.g. Chen et al., 2016; Vioque et al., 2018).

Herbig stars have mass between 2-8 $M_\odot$, bridging the gap between low mass T Tauri stars and embedded MYSOs. The division between high and low mass stars is a result of the internal structure of the star. Low mass stars have a radiative interior and a convective envelope, leading to strong magnetic fields that control accretion from the disc (Bouvier et al., 2007). Massive stars on the other hand have a convective interior and a radiative envelope, the corresponding mechanism for accretion is still unknown. As a result of the differing internal structure, the stars take different paths on the HR diagram as they evolve towards the main sequence. Low mass stars contract on to the main sequence taking a nearly vertical path, whereas intermediate- and high- mass stars increase in effective temperature more drastically and so they move to the left on the HR diagram before joining the main sequence. Massive stars are still embedded when they reach the main sequence and continue to accrete strongly. Figure 1.13 gives an indication of how pre-main sequence evolution varies over the stellar mass range.

The terms intermediate mass star, A type star and Herbig star are used somewhat interchangeably in the remainder of this thesis when comparisons are made between discs hosted by stars with similar properties. For clarity, the main difference in the usage here is that 'Herbig stars' is used as shorthand for Herbig AeBe stars, and will strictly refer to pre-main sequence objects. 'Intermediate mass' stars will be used to refer stars of mass $\approx 2-8 M_\odot$ ignoring their age so as to include stars with debris discs or naked planetary systems. 'A type stars' will sometimes loosely incorporate stars of early K or late B type as well as spectral type A stars, but is always broadly referring to the lower mass Herbig stars of $\approx$2-3 $M_\odot$ and their older main-sequence counterparts of similar mass.

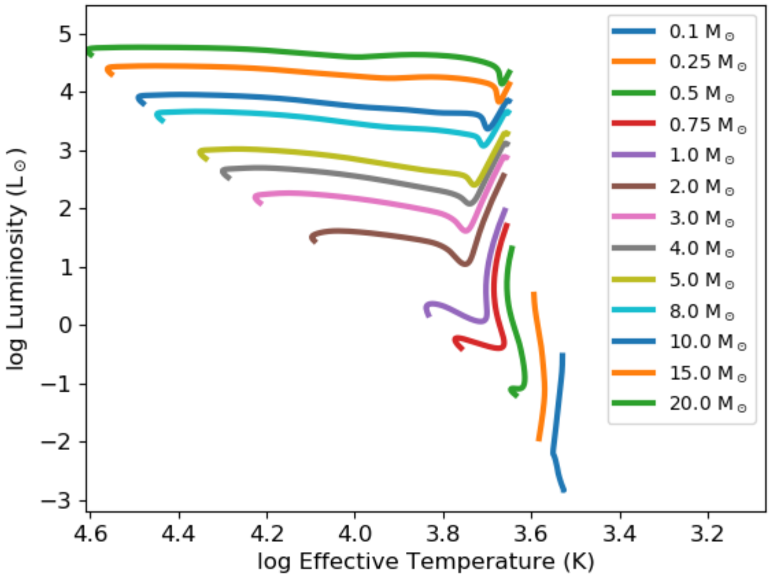

Figure 1.13: Pre-main sequence evolutionary tracks using the results of the MIST project (Choi et al., 2016; Paxton et al., 2010) on a Hertzsprung-Russel diagram. Tracks are plotted for a range of stellar masses from 0.1–20 $M_{\odot}$. Low mass stars descend vertically onto the main sequence whereas high mass stars travel further horizontally on the plot. The tracks are plotted until the point at which the star joins the main sequence.

1.3.1 Discs around Herbig Stars

Herbig stars are particularly useful for studying planet formation because the discs they host are bright, massive and extended, making them relatively easy to detect and resolve. Herbig discs have masses 1-10 M_J (Panić et al. in prep), with the most massive being of order 10s M_J. These are large masses in comparison to T Tauri discs in the ALMA Lupus survey where $M_{gas} \leq M_J$ (Ansdell et al., 2016). Gas discs in Herbigs can extend for 100s of au, an extreme example being HD 97048 in which CO gas extends up to $\approx$ 750 au (Walsh et al., 2016) (c.f. median disc radii in the Lupus survey = 102 au).

The embedded nature of massive stars and their strong radiative pressure make disc studies very difficult; only recently was the first Keplerian disc around an O-type star imaged (Johnston et al., 2015). Low mass T Tauris on the other hand host cool, small discs that require high resolution and sensitivity to study in detail. Consequently Herbigs have played an instrumental role in studies of disc structure. Their bright discs make them ideal targets for interferometric observations and as a result some of the most famous and well-studied discs are hosted by Herbigs (e.g. HD163296, HD100546). Furthermore due to the more massive, more luminous host stars compared to their T Tauri counterparts, Herbigs are ideal targets for studying gas in protoplanetary discs. A more luminous star results in a warmer disc that is capable of sustaining key molecules in the gas-phase for a greater radial extent. As a result the disc's temperature and chemical structure is different to those of lower mass stars, with the latter possessing inner regions that are more carbon-rich (Walsh et al., 2014a).

Intermediate-mass stars and their discs have played a large role in observational breakthroughs in planet formation, and it seems they may well hold the keys to a number of remaining open questions. Results from radial velocity surveys suggest that A type stars are the most likely to host giant planets (Johnson et al., 2010; Reffert et al., 2014), and the majority of debris discs detected to contain large amounts of gas are also around A type stars (Moór et al., 2017; Péricaud et al., 2017). Characterising the dust and gas in their discs is therefore crucial for developing our understanding of planet formation processes and disc evolution.

1.4 Methods

1.4.1 Millimetre Interferometry

As illustrated in Figure 1.6, the midplane of the dust disc and the outer regions contribute to the SED of a protoplanetary disc with emission mainly at millimetre wavelengths. For mapping dust structure or tracing density (caveats permitting, Section 1.1.6) millimetre observations are ideal. Furthermore the useful gas tracer CO and its isotopologues have low level rotational transitions at frequencies in the (sub-)mm regime, and so characterisation of gas in discs also requires millimetre observations.

Unfortunately, many promising objects are far away and difficult to spatially resolve. Furthermore high spatial resolution is inversely proportional to observing wavelength, an inconvenience for millimetre continuum and molecular lines. The solution to these problems is millimetre interferometry. This is where multiple antennas work in conjunction to simulate one large aperture. The angular resolution of the array, rather than being dictated by the diameter of a single antenna's dish, is proportional to the maximum baseline between two antennas in the array.

Rather than measuring brightness and position on the sky as in most other forms of imaging, interferometry measures the interference pattern between two apertures, measuring instead amplitude and phase. The brightness and position that we see in the 'image plane' are related to the raw interferometric data, known as visibilities $V(u, v)$ following van Cittert-Zernicke theorem (Thompson et al., 2017).

The fidelity of an image reconstructed from interferometric measurements, i.e. the degree to which it is faithful to the original brightness distribution of the source on the sky, is limited by 'uv-coverage'. uv-coverage refers to how well the Fourier transforms of the set of baselines for a particular array fills the uv plane. The more baselines employed, the more baseline vectors a configuration of antenna pairs covers, and the greater the coverage of the uv-plane for the observation.

Long exposure times benefit observations in two ways. The first is that an increased number of photons can be captured relative to a 'snapshot' observation, thereby improving the signal-to-noise ratio. The second relates to the uv coverage; the rotation of the Earth during the period of observation means that the position of the target source will change relative to the observing array, which means a greater amount of uv space is covered. Increasing the number of antennas in an array increases the number of baselines which will also improve uv coverage, for example the Australia Telescope Compact Array (ATCA) observes at mm and cm wavelengths using six antennas, which means it has 15 individual baselines and relatively low uv-coverage. Whereas the Atacama Large Millimetre/submillimetre Array (ALMA) observing with 50 antennas has 1225 baselines. ALMA offers unprecedented uv-coverage at millimetre wavelengths, along with unprecedented angular resolution achieved through the maximum baseline of up to 16km.

A further consideration is the configuration in which the antennas are arranged. Antenna configuration is related to the uv coverage achieved and so careful design of the antenna array can maximise uv coverage in observations to improve fidelity as shown in Figure 1.14. A linear configuration of antennas in the top panel of Figure 1.14 samples only a very specific part of the uv space in one direction, and so the image represents a 1-dimensional projection of the brightness distribution. The second row achieves much better uv coverage by simulating a long integration time, thereby utilising the Earth's rotation and producing an image that resolves key features in the image which has become recognisable. The final panel uses the ALMA extended configuration which was designed to maximise angular resolution. Finer details in the image are recovered and the image looks very similar to the brightness distribution of the science target, which in this case means that the image of Jafar the lion is very clear and his main features can be easily identified and analysed.

1.4.2 Data reduction

The reduction of millimetre interferometric data can be broadly summed up by the following sequence:

$$\text{Calibrate } V(u,v) \xrightarrow{\text{Fourier Transform}} \text{Dirty beam \& image} \xrightarrow{\text{Deconvolution}} \text{Clean beam \& image.}$$

The first step is calibration of the observed visibilities, $V(u,v)$. Calibration is achieved by utilising observations of calibrator objects that were observed alongside the science target. Flux is calibrated using an object of known magnitude at millimetre wavelengths, often a bright quasar in the same region of sky as the science target. Also required are real-time calibrations of phase in order to discern the effects from the atmosphere with those originating from the target. Good phase calibrators should be a point source as a true point source should have zero phase in the visibilities. Phase calibration is the most important for final image quality, removing atmospheric effects and variation with time throughout the observation. A final important step is the bandpass, or frequency, calibration which

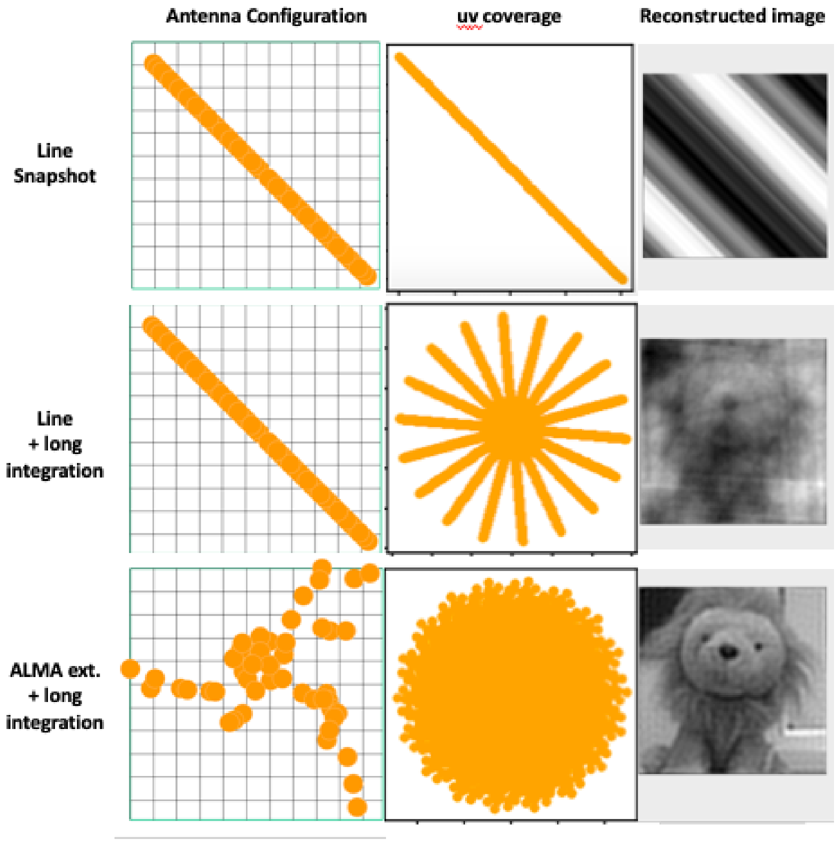

Figure 1.14: Demonstrating the importance of the sampling function and good uv-space coverage. The panels show three synthetic images of Jafar the Leeds Lion generated using three different observing set ups. In each row the configuration of antennas is shown on the left, the uv coverage is shown in the middle and on the right is the final ‘image’. The top row simulates a snapshot integration with 50 antennas in a linear configuration. The second row uses the same antenna configuration as the top row, but with a much longer integration time that utilises the rotation of the Earth to maximise uv coverage. The bottom row uses the ALMA extended configuration with 50 antennas and a long integration time. Synthetic observations visualised using Pynterferomter, available at: www.jb.man.ac.uk/pynterferometer/

removes noise introduced due to instrumental effects and non-physical variations in frequency. The calibration process is becoming increasingly automated with the development of high quality calibration pipelines that can be applied to a data set.

Once visibilities have been calibrated, a Fourier transform converts the sampling function into a 'dirty beam' and the observed visibilities into a dirty image. Mathematically the dirty beam is described by the inverse Fourier transform $\mathcal{F}^{-1}$ of the sampling function S:

$$S(u,v) = \begin{cases} 1 & \text{where visibilities are measured} \\ 0 & \text{where they are not} \end{cases}$$

$$B_{\text{dirty}} = \mathcal{F}^{-1}(S(u,v)),$$

and the dirty image is described by

$$I_{\text{dirty}} = \mathcal{F}^{-1}(S \times V),$$

where V is the measured visibilities, defined as

$$V = \mathcal{F}(B_{\text{primary}} \cdot I_{\text{source}}).$$

The CLEAN algorithm (Högbom, 1974; Rau and Cornwell, 2011) is then used to convert the dirty map as measured by the array into an image compatible with the brightness distribution on the sky via deconvolution. Deconvolution is a process that attempts to discern 'real' emission from artefacts that have been introduced as a side effect of the image reconstruction process. It does so by building a model of the emission by iteratively subtracting the brightest emission and inserting it into the model until the noise levels of the dirty image are reached.

Aside from using data that has been taken with a greater number of antennas or a more appropriate layout of antennas (i.e. decisions made before the observations are taken), the deconvolution process can be optimised by choosing the weighting scheme for the sampling function. The basic, and most regularly used weighting schemes are (Remijan et al., 2019):

- **Natural:** Visibilities are weighted using the inverse noise variance on that visibility. This scheme typically produces images with the best signal-to-noise at the expense of angular resolution.

- **Uniform:** Regrids the data in the uv plane, and then gives equal weighting to all uv cells, increasing the contribution of visibilities that would be given low weighting by the 'natural' scheme. This sharpens the angular resolution of the final image and helps to reduce sidelobe artefacts, but in doing so increases rms noise.

- **Briggs:** A flexible weighting scheme controlled by a robust parameter, R, to achieve a trade-off between sensitivity and resolution. R=-2 gives a result similar to 'uniform' weighting and R=2 is similar to 'natural'. R=0.5 is regularly adopted as a useful compromise.

Line emission

Line emission occurs over much narrower frequency intervals than continuum emission. Line profiles are best detected and characterised when using fine spectral resolution (ALMA Cycle 7 channel widths could be as narrow as 3.8 kHz). An important consideration in reducing data of molecular emission lines is removing the contribution from continuum flux. If the line emission is not brighter than the continuum within its frequency range, there will be no detection at all. By fitting a polynomial to the continuum data, a model of the emission's dependence on frequency is created and subtracted from the spectral windows containing line emission to leave behind only the emission from the line.

Self-calibration

As part of the deconvolution process, a model of the observed emission is built by the CLEAN algorithm. If the source is bright enough, this model can be used to calibrate the data and produce an image with increased signal to noise. Self-calibration takes advantage of time averaging of the data and can be used iteratively to continually improve signal to noise in the image (Pearson and Readhead, 1984).

1.4.3 Radiative Transfer Modelling

In order to understand the temperature structure within protoplanetary discs, and to subsequently model their emission, the passage of stellar photons through the mixture of gas and dust in protoplanetary discs must be addressed. When passing through a medium photons can be absorbed, scattered, or continue onward unimpeded. The mean free path of a photon in such a scenario depends upon both frequency and the distance travelled through the attenuating medium. The reciprocal of the mean free path defines the extinction coefficient, κ, often referred to as the opacity. The optical depth of a ray of light travelling between two points (s_0, s_1) in this medium can be expressed as:

$$\tau_\nu = \int_{s_0}^{s_1} \kappa_\nu(s) ds \tag{1.14}$$

where ds is an infinitesimal path length through the medium. Optical depth is used to construct the radiative transfer equation, which describes how the intensity of light alters as it travels through a medium:

$$\frac{dI_\nu}{d\tau_\nu} = -I_\nu + \frac{j_\nu}{\rho\kappa_\nu}, \tag{1.15}$$

where j_ν is the emissivity of the medium. The first term on the right hand side represents absorption within the medium whereas the second term represents emission and is sometimes written as S_ν, the source function.

Monte Carlo Methods - MCMax

Solving the equations of radiative transfer for a specific geometry and containing a variety of matter is very difficult and cannot be achieved analytically. In this thesis the code MCMax (Min et al., 2009) is employed, which performs 3D Monte Carlo radiative transfer in a 2D axisymmetric geometry. The code calculates dust temperature, vertical structure and contains disc physics including dust sublimation and viscous heating.

A Monte Carlo code solves the equation of radiative transfer through probability. Radiation from the star is represented as photon packages travelling through a disc model, propogating as described by Equation 1.15 in order to set the temperature. Photons take a random walk and at each grid cell they are either absorbed, scattered or do not interact at all. Absorption of a photon adds its energy to that of the grid cell, increasing its temperature. A new photon with a spectrum corresponding to the temperature in the cell and the local dust opacity is then emitted.

If the cell has absorbed and emitted before, then the new photon is emitted with the difference spectrum between before and after the energy absorption, this procedure is known as immediate temperature correction (Bjorkman and Wood, 2001). The random walk of each photon continues from cell to cell until the photon leaves the disc. When all photon packages have propagated through the disc, the final temperature structure is been calculated. An infinite number of photons would explore all possible paths and produce an exact temperature structure. In reality stochastic errors on temperature occur in each cell, but these errors can be reduced by increasing the number of photons used in the calculations.

The vertical structure is then calculated iteratively, assuming the gas to be in hydrostatic equilibrium and that the gas temperature is equal to the dust temperature (a good approximation below the surface layer of the disc as shown in modelling by Kamp and Dullemond, 2004). The initial structure is calculated using Equation 1.3. The vertical structure of the dust is then calculated under the influence of dust settling and turbulent mixing, which requires an update to dust temperature. This dust temperature is in turn used to update the vertical structure of the gas which is likely to deviate from the guess made with Equation 1.3, meaning the temperature and density structure in the disc are not currently self-consistent. Dust temperature and vertical structure calculations of the dust and gas are iterated until a self-consistent solution is converged upon.

The run time for a model increases with the number of photon packages used and is proportional to τ^2. Certain models can therefore lead to significant computational costs. MCMax includes two approximations that reduce the overall run time and improve the calculated temperature structure in regions of high optical depth. The first deals with regions of high optical depth, where photons can have many interactions within a small region of the disc, using up a disproportionate amount of computation time. This time can be reduced however by treating all interactions with a single computational step using a modified random walk (Fleck and Canfield, 1984). A second key optimisation improves the accuracy of the temperature structure in regions of high optical depth where photon statistics are low. In these environments energy transport occurs mainly through radiative diffusion and so the issue can be solved using a partial diffusion approximation. MCMax reduces the temperature in such regions by using the diffusion equation from Wehrse et al. (2000) with the Monte Carlo temperature immediately outside of the optically thick region as boundary conditions. This reduces the number of photons requires to get an accurate midplane temperature by orders of magnitude.

MCMax uses a multi-wavelength approach accounting for the full energy spectrum of photons leaving the disc, which leads to smoother predicted SEDs. The formal solution to the radative transfer equation along the line of sight to the disc can also be used to create a synthetic image of the disc at a given observing wavelength.

1.4.4 Midplane Evolution and Chemical Models

In Chapter 4 midplane conditions are modelled by including the dominant physical mechanisms acting in this region of the disc. The disc evolution code presented in (Booth et al., 2017) is employed to calculate the transport of gas and dust in the disc in 1D. It combines viscous evolution of the gas with diffusion and radial drift of solids. Dust evolution is calculated with a model containing two populations of dust: one of sub-micron sized ‘small’ grains that are well coupled to the gas and a ‘large’ grain population where maximum grain size is determined by the competition between growth and fragmentation processes following Birnstiel et al. (2012). The total dust mass is dominated by the contribution from the large grains, whereas the surface area is dominated by the small grains.

Temperature structure in the disc controls whether grains are icy or ice-free, which in turn sets the collision velocity at which grains fragment, and determines the state of volatiles in the midplane. In this thesis a simple chemical model is applied in order to trace the abundance of major molecular carriers of carbon and oxygen in both the gas and solid phase. The model adopted is that of Öberg et al. (2011), also implemented as 'case 2' in Booth et al. (2017); Madhusudhan et al. (2014, 2017). It contains the major C-, N- and O- carrying species observed in protoplanetary discs and giant exoplanet atmospheres; H_2O, CO, CO_2, NH_3, N_2, silicates, refractory O components, organics and carbon grains. Initial solar abundances are adopted: C/H= 2.7×10^{-4} , N/H= 6.8×10^{-5}, O/H= 4.9×10^{-4}, and Si/H= 3.2×10^{-5} and the binding energies for the key molecules are the same as those used by Piso et al. (2016) and Booth et al. (2017). Equilibrium ice abundances are found by balancing thermal adsorption and desorption rates in the midplane. Drift will act to alter the chemical abundances as a function of radius, an assumption of our model is that chemical reactions act to restore equilibrium abundances. Abundances of the gas and ice phase molecular species are updated close to snowlines but the amount of material in carbon grains and silicates is assumed to be constant (Booth et al., 2017).

Chapter 2

Asymmetric midplane gas in ALMA images of HD 100546

2.1 Context

In this chapter new ALMA observations of the Herbig transition disc HD100546 are presented. These data include the first detection of $C^{18}O$ in the disc and the first ALMA imaging at 1.3 mm, a crucial wavelength regime for tracing mass in the outer disc and dense midplane in which a significant proportion of disc mass resides. This system is investigated through characterisation of its gas and dust emission. Estimates of mass in both the gas and dust are calculated in order to assess the remaining planet-building budget within the disc. By utilising observations at shorter wavelengths, the spectral index of disc emission is used to constrain the maximum size to which dust grains have grown in the disc giving an indication as to the state of the dust's evolution. The detailed analysis of these ALMA observations provide a valuable characterisation of a massive disc around an intermediate mass, pre-main sequence star thought to be hosting embedded planets within its disc.

2.1.1 HD 100546

This chapter focuses on a fascinating example of planet formation; the well-studied disc around Herbig Ae/Be star HD 100546. The star is located at a distance of 110pc (Lindegren et al., 2018) with a mass reported by van den Ancker et al. (1997) of 2.4 $M_\odot$ from pre-main sequence (PMS) track fitting and more recently 1.9 $M_\odot$ by Fairlamb et al. (2015) derived through X-shooter spectroscopy and PARSEC PMS tracks (Bressan et al., 2012). Although previously thought to be as old as $\geq$10Myr (van den Ancker et al., 1997), Fairlamb et al. (2015) calculate an age for the star of 7.02±1.49 Myr and using the updated parallax from GAIA data release 2, Vioque et al. (2018) find a younger age of $5.5^{+1.4}_{-0.7}$ Myr.

2.1.2 Evidence for proto-planet(s)

The system has been long associated with active planet formation and so is well studied. Direct imaging of a protoplanet has been claimed at ~50 au via direct imaging by Quanz et al. (2015) and there has been some evidence of an inner companion as well. This includes SED modelling and mid-IR interferometry (Mulders et al., 2013; Panić et al., 2014), ALMA observations (Walsh et al., 2014a), near IR spectroscopy (Brittain et al., 2014, 2013) and a point source in GEMINI Planet Imager (GPI) data at 10 au (Currie et al., 2015) supporting the proposed planet at the inner disc wall. However this predicted companion has alluded detection in more recent GPI and Magellan Adaptive Optics System observations by Follette et al. (2017). The position of the potential inner companion coincides with the position of the rim of the inner gap at $\sim 11 \pm 1$ au, interior to which is a small inner dust disc of $\leq$0.7 au (Panić et al., 2014) and a recently detected bar-like structure reaching across the inner gap in both continuum and Hα emission (Mendigutía et al., 2017).

2.1.3 Structure in the disc

Observing with ATCA, 7mm continuum emission from HD100546 can be fit by a Gaussian with FWHM between 50 and 60 au (Wright et al., 2015), and the authors assert that grains in the disc are well-processed and have grown as large as 5cm and possibly further. Walsh et al. (2014a) are able to detect a significant amount of weak, extended continuum emission beyond this and find a best-fit model for the dust in the uv plane comprised of two rings with a Gaussian profile; one centred at 26 au with a FWHM of 21 au and one at 190 au with FWHM 75 au. Pineda et al. (2014) find that mm-sized grains are trapped within a similar inner ring and note brightness asymmetries in the dust between the South-East and North-West of the disc. All three of these studies at (sub-)millimetre wavelengths favour arguments of at least one giant planet orbiting within the disc. The disc does not appear to be axi-symmetric; scattered light studies routinely observe multiple asymmetric features and spiral arms within the dust disc (Follette et al., 2017; Garufi et al., 2016), including a 'dark lane' observed by Avenhaus et al. (2014) in the same direction as the horse-shoe shaped asymmetry identified in 7 mm images of (Wright et al., 2015). A selective summary of imaging of HD100546 across the wavelength range is presented in Figure 2.1. The exact nature of corresponding features at millimetre wavelengths has until now remained largely undefined.

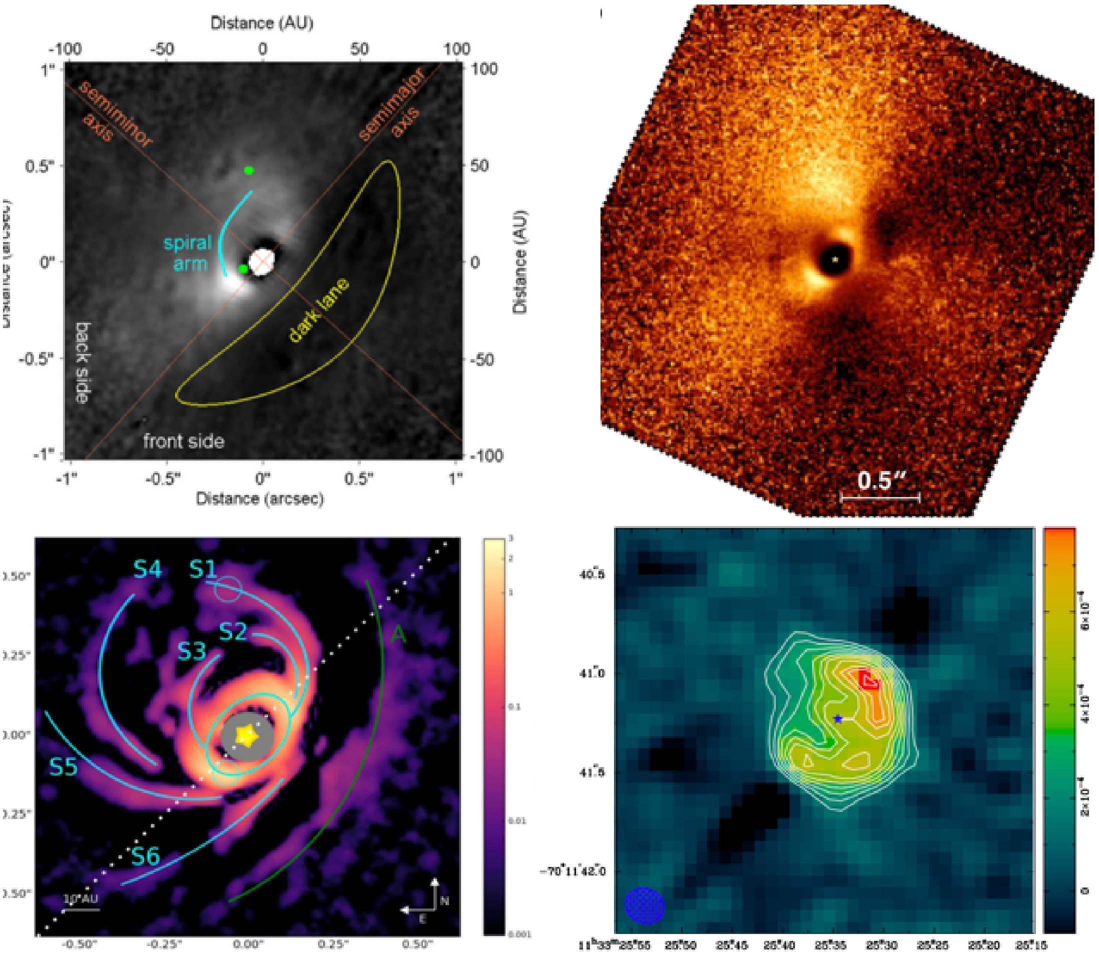

Figure 2.1: Previous multi-wavelength imaging of HD100546 on shorter spatial scales within the ~0.9 arcsec synthesized beam of the ALMA images presented here. **Top left:** Near-IR polarised scattered light image created by Avenhaus et al. (2014), image shown is a K_s filter PDI image of HD100546 annotated with detected features. Green dots show the proposed locations of planets. **Top right:** SPHERE/ZIMPOL Q_ϕ polarized light image of HD 100546 at visible wavelengths from (Garufi et al., 2016). **Bottom left:** Sum of GPI and MagAO imaging presented in (Follette et al., 2017) annotated with identified features. **Bottom right:** Radio interferometry image from data taken with ATCA at ~7 mm and presented in Wright et al. (2015). Contour levels are at 5, 7, 9, 11, 13, 15, 18, 21, 23, 25.7 times the RMS of 0.03 mJy/beam. The synthesized beam is 0.200.18 arcsec.

The gas in the disc is much more spatially extended than the dust, CO has been measured out to ∼400au (Walsh et al., 2014a). Very little is known about the gas mass of this uniquely interesting disc due to a lack of data observing optically thin gas lines. Gas mass calculations based on optically thick ^{12}CO emission can lead to underestimations of as large as two orders of magnitude in comparison to those using optically thin CO isotopologues (e.g. Kospal et al., 2013).

In Section 2.2 the observations are described and the initial results and measurements are presented in Section 2.3. In Section 2.4 the gas and dust mass in the disc are calculated and apparent asymmetry in the images is analysed. The deprojected, azimuthally averaged flux profiles are utilised to determine the radial extent of the emission for each of the observed tracers and calculate β_{mm} to infer levels of grain growth. The main results are summarised in Section 2.5.

2.2 Observations & Data Reduction

New ALMA observations of HD 100546 were made using band 6 receivers across 4 unique spectral windows (SPWs); project ID 2015.1.01600.S, PI: O. Panić. The two continuum windows, SPW0 and SPW1, both contain 128 channels of width 15625 kHz to give a total bandwidth of 2 GHz, SPW0 has a central frequency of 232 GHz, with SPW1 at 234 GHz. SPW2 contains 1920 channels of width 61.035 kHz, which at central frequency 220398 MHz gives resolution of 0.083kms^{-1} for the window containing the ^{13}CO (2-1) emission line. The C^{18}O (2-1) line is in SPW3, this window has 3840 channels of 0.166 kms^{-1} at central frequency 219560 MHz. Observations were made on the 28th March 2016 for a total time of 625s on source, employing 43 antennas with a baseline range of 15-460 metres giving a maximum angular scale of $10\farcs6$. The flux calibrator was J1107-4449 and the phase calibrator was J1136-6827, the latter is found at the position 11:36:02.09787 -68:27:05821, which is ($0\farcs22$, $1\farcs73$) degrees offset from the target.

Calibration and reduction was carried out using CASA version 4.7.0. and imaging was performed using CASA tasks and the CLEAN algorithm (Rau and Cornwell, 2011). Line-free continuum channels were used to construct image models to be used for self-calibration with reference antenna DA59 and the minimum solution interval length for phase calibration. The resulting solutions were then applied to all channels. After applying self-calibration, images were created with Briggs weighting and robust=0.5, giving a synthesized beam of $1''.05$ x $0''.77$, P.A. = -160° for the continuum image. Source emission is contained within the inner third of the primary beam and so primary beam correction was not applied to images. Data cubes were created for the line emission by subtracting the continuum from SPWs containing the line emission using CASA task *uvcontsub*. Images of the lines have beam sizes of $1''.08$ x $0''.82$, P.A. = -161° for ^{13}CO and $1''.10$ x $0''.83$, P.A. = -160° for C^{18}O. Integrated intensity, from which fluxes are measured, and intensity weighted velocity maps were created with CASA task *immoments* by summing all emission in channels containing significant ($> 3\sigma$) signal; in the case of ^{13}CO this corresponds to a range between -0.62 and 11.4 kms^{-1} and for C^{18}O between -2.0 and 10.8 kms^{-1}.

In addition to the data presented here, archival cycle 0 ALMA observations of HD 100546 in band 7 as described by Walsh et al. (2014a) are utilised (Project ID: 2011.0.00863.S, PI: C. Walsh). This data is re-reduced and imaged, applying self calibration as described above to obtain continuum emission observed at a wavelength of 867μm. The cycle 0 data used J1147-6753 as a phase calibrator, offset from the primary target by ($1''.2$, $2''.3$). The continuum image has a synthesized beam of dimensions $0''.95$ x $0''.42$, 38°. The minimum baseline of 21 m results in a maximum angular scale of $5''.3$.

2.3 Results

The integrated continuum flux in the 1.3 mm image of 492 mJy is measured with an image rms of 0.5 mJy/beam. The ^{13}CO (2-1) integrated flux is measured at 12.872 Jy kms^{-1} and the first detection of C^{18}O in the disc gives an integrated flux of 2.948 Jy kms^{-1} for the (2-1) transition, with rms noise 0.033 Jy/beam kms^{-1} and 0.027 Jy/beam kms^{-1} respectively. The 2σ contour reaches a maximum separation of $2''.5$ in the 1.3 mm image, $3''.6$ in ^{13}CO and $3''.0$ in C^{18}O. Asymmetry and the radial extent of the emission maps are thoroughly discussed in Section 2.4.2.

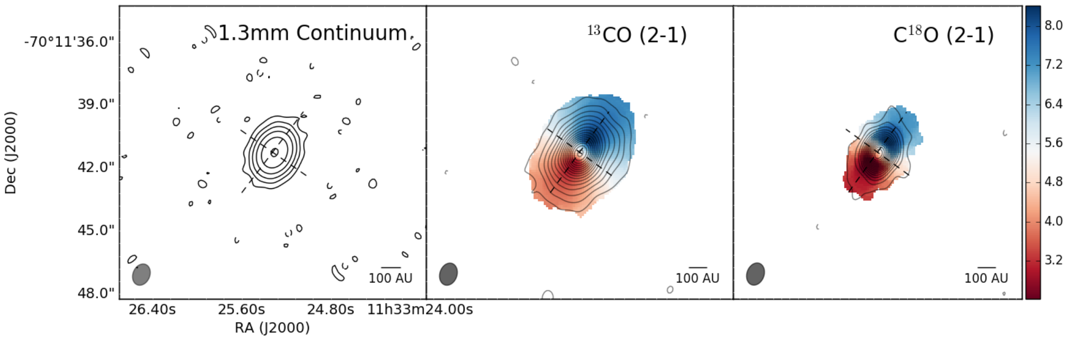

Figure 2.2: On the left is the contour map of the continuum emission, contours increase in base 3 logarithms from 3σ to 729σ. Intensity weighted velocity maps of the two isotopologue transitions are shown overlaid with contours of the integrated line emission. For ^{13}CO(2-1), contours start at 3σ and rise in steps of 5σ to 78σ, for C^{18}O(2-1) contours start at 3σ, and rise in steps of 3σ up to 45σ. Dashed contours are negative. Beam ellipses and a scale bar of 100 au are shown in each image. North is up and West is right, dashed lines follow the major and minor axis of the disc, assuming a position angle of 144° and join at the stellar position given by GAIA.

To find a position angle for the disc, the data cubes from the CO isotopologue emission are used to identify the minor axis of the disc by locating the channel at the systemic velocity, $v_{\rm sys}$, of the source by eye, which can be identified by the symmetry of the map as at $v_{\rm sys}$ there will be no Doppler shifting. Channel maps show the minor axis of ^{13}CO in the channel at 5.51±0.08 kms^{-1} and for C^{18}O at 5.33±0.17 kms^{-1}. An average of these two velocities is adopted as $v_{\rm sys}$ from this data set, giving 5.42±0.19 kms^{-1}, shown in Figure 2.3 along with the minor axis channel of each isotopologue. This average is consistent with the two $v_{\rm sys}$ determined from the channel maps within the uncertainties (which is assumed to be represented by the channel widths). Figure 2.4 plots the observed spectrum of each of the two lines. Both lines display a double peaked spectrum, where each of the C^{18}O peaks is broader than the peaks of ^{13}CO. The mid-point of the ^{13}CO spectrum is consistent with the average $v_{\rm sys}$. The mid-point of the C^{18}O spectrum is harder to determine due to its shape. The local minimum at the centre of the double peak profile is offset from the adopted $v_{\rm sys}$ by 0.33 kms^{-1}.

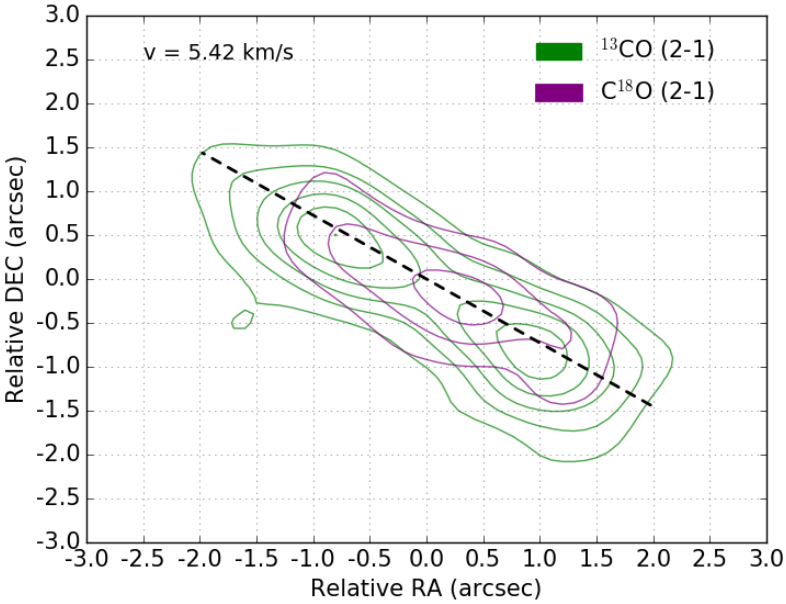

Figure 2.3: Overlaid contour maps of the isotopologue channels at system velocity for determining disc position angle. Contours increase in multiples of 3 from 3σ, where for individual channels, σ= 23 mJy kms^{-1} /beam for ^{13}CO and 11 mJy kms^{-1} /beam for C^{18}O. The dashed black line represents the adopted minor axis corresponding to a position angle of 144°.

Walsh et al. (2014a) constrain a system velocity of 5.7 kms^{-1} from their ALMA observations of ^{12}CO(3-2).

The orientation of the disc minor axis is used to determine the position angle of the disc. The constrained position angle is used as an a priori estimate for a Gaussian fit of the data, in order to determine the inclination of the source. Any asymmetry in the emission map will influence the fitting of a Gaussian, by using this observationally determined a priori estimate for position angle, the accuracy of the fitted inclination is ensured.

For ^{13}CO the position angle of the major axis, measured East of North, is determined to be $142 \pm 0.8°$ and for C^{18}O, $146 \pm 2.3°$. The average value of the two is $144 \pm 2.4°$ which is adopted henceforth. Uncertainties give the variation in position angle when measured from the adjacent spectral channels. Keeping

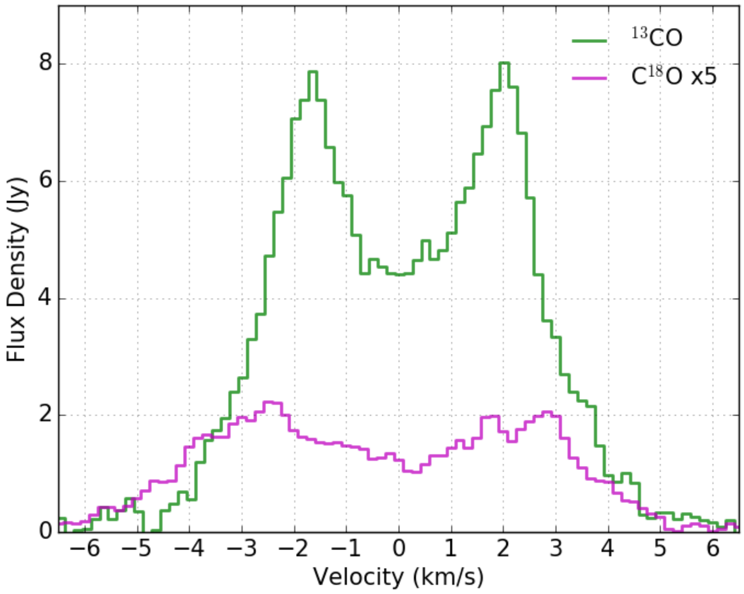

Figure 2.4: Spectrum from the spectral windows centred on the CO isotopologue lines. The C^{18}O line flux densities have been multiplied by a factor of 5 in order to make the profile easily visible in the plot. The x axis is measured relative to the system velocity of 5.42 kms^{-1}.

this position angle fixed, an elliptical Gaussian is fitted to each of the CO isotopologue integrated emission maps to determine inclinations of 42.6° and 43.7° for ^{13}CO and C^{18}O respectively via a Chi squared test with UVMODELFIT. An average inclination of 43° is adopted for all further analysis. For comparison with the continuum data, a simple Gaussian fit on the continuum emission returns a position angle of 157±1.

These values are consistent with most reported position angles from previous sub-mm observations of the disc with ALMA; Walsh et al. (2014a) find a position angle of 146° ± 4° and inclination 44° ± 3°, whilst Pineda et al. (2014) find 145.14° ± 0.04° and 41.94° ± 0.03°. Panić et al. (2014) observed the disc with the MID-infrared Interferometric instrument (MIDI) on the VLT and find a position angle of 145±5°, their inclination is considerably higher however because their observations probe the inner wall of the disc at 11 au. There is growing evidence for a warp in the disc (Panić et al., 2010; Quillen, 2006; Walsh et al., 2017) which would cause inclination to deviate radially.

Asymmetry in the ^{12}CO line profile is detected in both APEX and ALMA observations (Panić and Hogerheijde, 2009; Walsh et al., 2017). Images of the ALMA observations of ^{12}CO achieve a synthesizing beam of $0\farcs92$x$0\farcs38$ (Pineda et al., 2014). This asymmetry is not detected in the less abundant ^{13}CO or C^{18}O lines, finding instead double-peaked line profiles symmetric to within uncertainties (Figure 2.4). ^{12}CO emission traces higher scale heights in the disc, meaning that the asymmetry could be restricted to the upper vertical layers of the disc. There already exists evidence for asymmetry of the disc surface in the scattered light images that identify spiral arms and other structures (Ardila et al., 2007; Avenhaus et al., 2014; Follette et al., 2017; Garufi et al., 2016). The APEX observations have a larger beam and therefore the results may be affected by the extended envelope of the disc as detected by scattered light as far as $\sim$ 1000 au (Ardila et al., 2007; Grady et al., 2001).

The GAIA data release 2 (2018) position of HD 100546 was adjusted taking into account proper motion between the dates of the ALMA and GAIA observations, giving a position of 11h33m25.3209s -70d11m41.2432s, within an accuracy of (0.04, 0.05) mas (Lindegren et al., 2018). The centre of emission for each of the tracers observed is found to be offset from this position.

Table 2.1 gives the coordinates of the centre of emission for the continuum and CO isotopologues, accompanied by its offset from the GAIA coordinates. A 2D Gaussian is fitted to the emission maps in Figure 2.2, the positions of these fits are taken to be the centre of emission. A similar analysis is undertaken here by fitting a uniform, elliptical disc geometry in the uv plane using CASA task *uvcontsub*. This is repeated for each tracer, giving the position of the best-fit disc model in Table 2.1. The benefit of uv-analysis is that it avoids being misled by spurious artefacts that can be introduced into images during the image reconstruction process. In each case the uv-fitted position is very similar to that determined in the image plane. The uniform-disc fits give a position angle of 146° and inclination of 42°, values which are within a few degrees of those constrained above, and those from previous ALMA observations (Pineda et al., 2014; Walsh et al., 2014a).

	Coordinates of best fitting model	Offset from Stellar Position ("), P.A.
Cont. (Im.)	11:33:25.305 -70.11.41.258	0.082, 79°
^{13}CO (Im.)	11:33:25.310 -70.11.41.291	0.073, 49°
C^{18}O (Im.)	11:33:25.305 -70.11.41.300	0.098, 55°
Cont. (uv)	11:33:25.305 -70.11.41.257	0.082, 80°
^{13}CO (uv)	11:33:25.308 -70.11.41.276	0.072, 63°
C^{18}O (uv)	11:33:25.300 -70.11.41.280	0.110, 71°

Table 2.1: Sexadecimal positions of central emission in the 1.3 mm continuum and CO isotopologues as determined by fitting a Gaussian to integrated emission maps in the image plane ('Im.' above), and a uniform disc in the uv plane ('uv'). Positions are rounded to the nearest milliarcsecond. The angular separation between these positions and the GAIA position of HD 100546, corrected for proper motion between GAIA and ALMA observations, is given in the final column.

The uncertainty in an astrometric position in an ALMA image depends on a number of factors. The signal-to-noise based target position-fitting error is 1.3 mas. This is consistent with the ALMA technical handbook Section 10.6.6 . The dominating factor in positional uncertainty is introduced when the phase corrections are transferred from the phase calibrator to the target. The phase calibrator is 1.7 degrees in separation from HD 100546, and from the phase drift between scans a total uncertainty on the astrometric position is estimated to be ~10 mas. This is relatively low as a result of a stable phase in the observations. Other factors such as antenna position errors can degrade astrometry; the ALMA technical handbook cautions that with reasonable phase stability, positional accuracy is ~1/20 of resolution, which in this case would correspond to a maximum of 50 mas. This greater value of 50 mas is adopted as a conservative uncertainty on coordinate positions in the image. Each of the best-fit centres of emission in Table 2.1 have a separation from the central star that exceeds the 50 mas uncertainty in ALMA image positions. An offset of emission from the stellar position may indicate an over-density of disc material towards one side of the disc. Asymmetry in disc emission is discussed in more detail in Section 2.4.2.

2.4 Analysis and Discussion

2.4.1 Disc Mass

Dust Mass

In order to estimate the mass of dust in the disc the flux within a 3σ contour of the 1.3 mm continuum image is measured. The opacity depends on the maximum grain size, for which there are only loose constraints in any individual protoplanetary discs. A minimum dust mass estimation can be made by assuming a dust grain size distribution $dn/da \propto a^{-3.5}$ (Mathis et al., 1977). Assuming a maximum grain size $a_{\max} = 1$ mm yields $\kappa_{1.3\mathrm{mm}} = 1.15\ \mathrm{cm}^2\mathrm{g}^{-1}$ (Draine, 2006). Midplane temperature of the dust is difficult to constrain from observations, however a firm handle on the midplane disc mass can be found by assuming a sensible temperature range for this dense, cool environment, and so a temperature range of 20K – 40K is adopted here. In this transition disc, gas and dust are likely to be well coupled, and our strong gas line detections suggest that the disc temperature must be over the CO freeze-out temperature of ∼20 K. Herbigs host more luminous, warmer discs than their T Tauri counterparts, and so the temperature is likely to be above this 20 K lower bound. The upper bound is taken to be 40K. In the radiative transfer models of A type stars by Panić and Min (2017), gas mass in the disc must be increased by over two orders of magnitude to increase midplane disc temperatures from 20 to 40 K at ∼40 au from the star, so this can safely be considered as a generous upper limit.

The assumptions above give a minimum total dust mass of $4.1{\times}10^{-4}$ M$_\odot$ for T= 40 K, and $9.6{\times}10^{-4}$ M$_\odot$ for T= 20 K. Figure 2.5 shows how this dust mass can vary with midplane temperature or if the assumed level of grain growth varies, thereby changing $a_{\max}$ and the emissivity of the dust in turn. Between $a_{\max}$= 1 mm and 10 mm, the most likely values in a protoplanetary disc at this stage of evolution, the masses remain almost constant and are less sensitive to temperature. This indicates that for reasonable assumptions of $a_{\max}$ and midplane temperature, the dust mass is $\approx 10^{-3}$ M$_\odot$.

The mass range calculated is comparable with the estimate of Wright et al. (2015) who employ the accretion disc models of d 'Alessio et al. (2005) to find

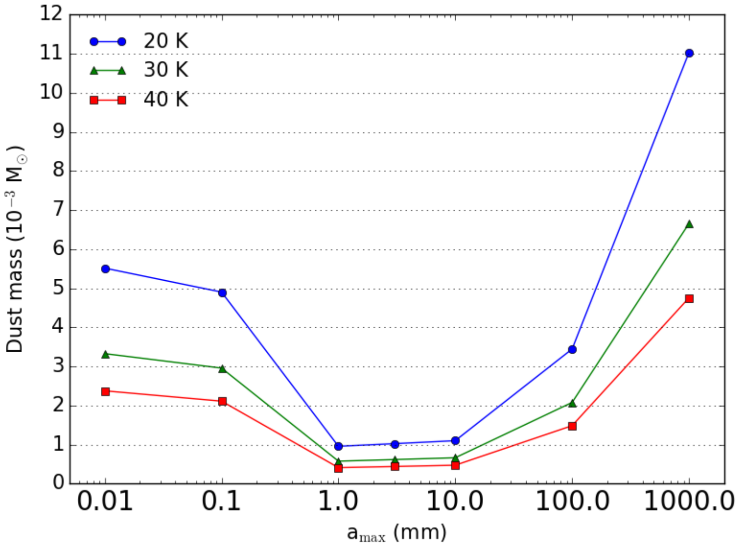

Figure 2.5: Dust mass calculated over a range of temperatures and maximum grain sizes assuming optically thin emission measured at 1.3 mm.

M_dust of order 1.0×10^{-3} $M_\odot$. Repeating the calculation above using instead the ALMA measured flux at 867μm from Walsh et al. (2014a) with a temperature of 30K and $a_\text{max} = 1$ mm, a disc mass of 0.7×10^{-3} $M_\odot$ is found, similar to the results between 1mm and 10mm in Figure 2.5.

This is more massive than most discs around low-mass stars, which fall in the range $10^{-6} - 10^{-4}M_\odot$ (Manara et al., 2018). This dust mass is also at the higher end of the range found for Herbig Ae stars $10^{-4} < M_\text{dust}(M_\odot) < 10^{-3}$ (Panić at al., in prep). Given the age of the star this is quite exceptional, suggesting a prime object to study longevity of dust in discs.

Gas Mass

From the integrated line flux of $C^{18}O$ above 3σ, assuming optically thin emission and local thermodynamic equilibrium, the total gas mass is calculated similarly to Hughes et al. (2008); Matrà et al. (2015); White et al. (2016),

$$M_\text{gas} = \frac{4\pi}{h\nu_{21}} \frac{F_{21} m d^2}{A_{21} x_2}, \tag{2.1}$$

where F_{21} is the integrated line flux, ν_{21} is the rest frequency of the transition, d the distance to the source, m is the mass of the CO molecule, A_{21} is the appropriate Einstein coefficient, and x is the fractional population of the upper level. ISM fractional abundances for CO and its isotopologues are adopted, specifically $CO/H_2 \sim 10^{-4}$, and the abundance of $C^{18}O$ relative to the main isotope $CO/C^{18}O \sim 550$ (Wilson and Rood, 1994). A gas mass is calculated in this way over a range of temperatures. The minimum gas mass was calculated with a temperature of 20 K, giving a minimum disc gas mass of 0.018 $M_{\odot}$. This estimated gas mass is around 1% of the stellar mass, corresponding to around 18 Jupiter masses. For comparison, in an ALMA survey of Lupus, most low-mass discs have a gas disc mass of $\leq 10^{-3} M_{\odot}$. In this case Ansdell et al. (2016) determine gas mass using the ^{13}CO and $C^{18}O$ measured flux for each disc and comparing to a grid of models including isotope selective photo-dissociation. Such disc masses are large even for Herbig stars, where the majority have discs within the range $(1\text{-}10)\times10^{-3} M_{\odot}$ when calculated from midplane tracing CO isotopologues (Panić at al., in prep). HD100546 therefore appears to still possess enough disc mass to form Jupiter mass planets, a very significant amount for a disc that has reached the transition disc stage of its evolution and shows detections of active planet formation (Quanz et al., 2015).

The calculated gas mass assumes ISM abundances of $C^{18}O$ relative to CO. Isotope-selective photodissociation can alter these ratios significantly in some discs, which can lead to underestimates of disc mass by up to an order of magnitude (Miotello et al., 2014). The CO line luminosities measured in this data are unable to conclusively determine the extent of any isotope-selective photodissociation when compared to the models of Miotello et al. (2016), and so our calculation represents a lower limit. Carbon freeze-out beyond the snowline can also result in low measured gas masses; T Tauri discs appear to have significant levels of carbon freeze-out, for example in TW Hya (Schwarz et al., 2016). Herbig discs such as HD 100546 on the other hand remain warmer for a greater radial extent due to the more massive host star (Panić and Min, 2017). This pushes the CO snowline to a greater radial separation allowing carbon to remain in the gas phase for a greater radial extent of the disc. In the disc of HD 100546 freeze-out is not expected to play a significant role; fitting physical-chemical models to observations, Kama et al. (2016) find that within the disc of TW Hydra, C and O are strongly under-abundant, whereas in HD 100546, the depletion of gas-phase carbon appears quite low, in part due to the relatively warm disc.

In light of the discussion above, our calculated gas estimate represents a firm lower limit, but a very large one in comparison to other Herbig discs. The gas mass estimated here is similar to that achieved through line modelling of another bright Herbig disc, HD 163296 (Boneberg et al., 2016), and shows there is still a large budget remaining in the disc for giant planet building in comparison to discs that are in a more advanced stage of their evolution towards a debris disc, e.g. HD 141569 (White et al., 2016).

Gas To Dust Ratio

Taking the dust mass calculated with T=20K and the minimum gas mass calculated at the same temperature results in a calculated g/d for HD 100546 of $\approx$ 19. Low g/d (< 100) is observed in the majority of sources in recent surveys of discs in star forming regions (Ansdell et al., 2016; Long et al., 2017). Studies of individual Herbig discs suggest g/d is generally low in these larger, brighter discs too (Boneberg et al., 2016; Meeus et al., 2010). The g/d affects disc evolution because gas dynamics dominate the behaviour of the dust in gas-rich protoplanetary discs. The uncoupling of these two populations when gas densities drop sufficiently low is a signpost for the transition to a debris disc.

Low observed g/d can mean a great amount of gas has been lost, or it can be the result of carbon depletion in the disc through sequestration into large icy bodies or the conversion of CO into more complex molecules. This ratio is indicative only of regions within the CO snowline where freeze out is avoided. In the similar Herbig disc HD 163296, the snowline is calculated to be at around 90 au (Qi et al., 2015), in cooler discs the snowline will be at a lesser separation, e.g. TW Hydra, 30 au (Qi et al., 2013).

2.4.2 Disc Asymmetry

Evidence in ALMA Images

Asymmetry in the disc has previously been reported with evidence in asymmetric ^{12}CO line profiles (Panić and Hogerheijde, 2009), horse-shoe structures in cm-wavelength observations (Wright et al., 2015) and the identification of multiple scattered light features (e.g. Ardila et al., 2007; Follette et al., 2017; Garufi et al., 2016). Unfortunately higher resolution imaging by (Pérez et al., 2019) resolves only the most inner regions within the first synthesized beam, and so direct comparison is inconclusive. These high resolution images show a brighter side of the inner wall on the opposite side to the asymmetry in the outer disc emission we identify here. Asymmetric features can form in the disc as a result of mechanisms such as planet-disc interactions (Baruteau et al., 2014), interactions between binary companions (Price et al., 2018) or particle traps within the disc (Van Der Marel et al., 2016; van der Marel et al., 2013). Such features are therefore particularly interesting in a disc such as that of HD 100546 which is proposed to host two embedded protoplanets and exhibits a range of observed structures across different spatial scales.

In the data presented here a striking match is seen between the extended emission in the C^{18}O map and the structures in HST scattered light observations of the disc. The low-level bulges in C^{18}O emission (Figure 2.6) persist in images created using different weighting parameters in the image reconstruction process, and are present both before and after applying self-calibration. Using the Advanced Camera for Surveys (ACS) on board the Hubble Space Telescope (HST) Ardila et al. (2007) identify 3 structures in the outer disc which are attributed to the known spiral arms in the disc. The authors name these structures 1, 2 and 3 and this convention is adopted here as well. Figure 2.6 displays the HST image in the F435W band presented by Ardila et al. (2007). Each of the low-level bulges in the extended C^{18}O (2-1) emission is found in the same region of the disc as one of the 3 scattered light structures. This provides tentative evidence of a midplane gas equivalent to the scattered light features. The C^{18}O emission is optically thin, and can therefore be interpreted as an increase in local midplane density. An increased local gas density will increase the scale height of the

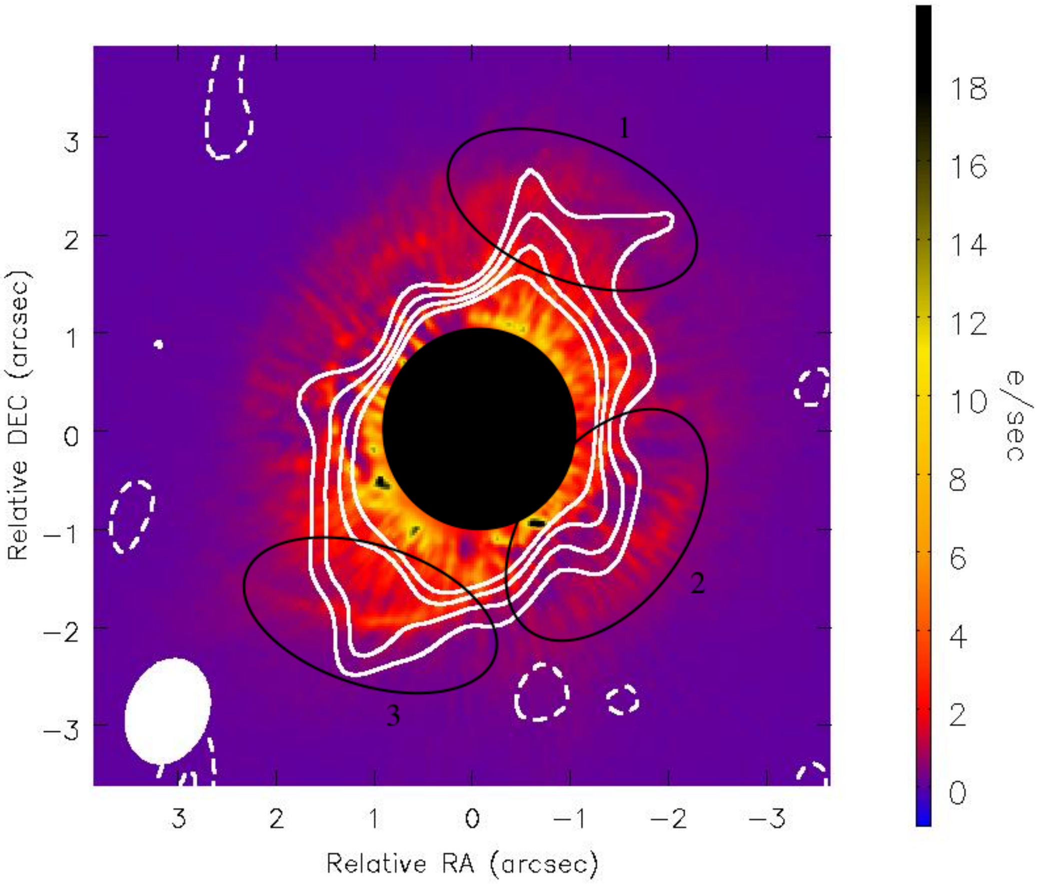

Figure 2.6: The colour image shows the PSF deconvolved HST ACS image of HD 100546 in the F435W band. Overlaid in white contours is the integrated C^{18}O (2-1) emission observed by ALMA, with contours at (-2,2,3,4,5)$\times\sigma_{18}$, dashed lines are negative contours. Structures in the scattered light image initially identified by Ardila et al. (2007) are indicated with black ellipses. The black circle of radius $1\farcs0$ represents the HST coronograph.

disc, the subsequent elevation of small particles towards the scattering surface will result in a stronger scattered light flux, as seen in the HST data. The C^{18}O emission bulges towards the outer disc may therefore be signalling the midplane density features that correspond with the disc's spiral arms. In this section a general analysis is made of any observational evidence for asymmetry in the disc, within the limits of the angular resolution of our ALMA observations.

In Section 2.3 the inclination and position angle of the disc is accurately measured, both of which are very close to values derived from previous sub-millimetre ALMA observations of the disc (Pineda et al., 2014; Walsh et al., 2014a). This geometry is used to construct an ellipse with a semi-major axis equivalent to 100 au in the disc. An initial visual assessment of asymmetry in the disc is made by plotting this ellipse over the emission maps in Figure 2.2 centred at the stellar position. The midplane tracing 1.3 mm continuum and $C^{18}O$ (2-1) emission in particular show evidence of an offset disc in Figure 2.7, on scales larger than that the offsets listed in Table 2.1. In both panels high level contours internal to the inner ellipse are omitted for clarity. Towards the northwest in the panels of Figure 2.7, the 75σ contour (in the 1.3 mm image) and the 15σ contour ($C^{18}O$) overlap with the 100 au ellipse, whereas to the southeast there is a significant offset. $C^{18}O$ in particular shows azimuthal asymmetry in the outer disc, with low level emission extending much further out as previously highlighted in Figure 2.6.

The largest asymmetry in the disc is along the minor axis (Figure 2.7) with the brighter region found towards the position of Structure 2 in Figure 2.6. Evidence for this also appears in Figure 2.8, which shows slices from the emission maps taken along the minor axis in both directions, centered at the stellar position.

$C^{18}O$ (bottom panel) is brighter in the southwest for the majority of the disc, and emission extends further by $\sim 0\farcs3$ in comparison to that in the northeast. In the continuum (top panel) the southwest side is brighter than the northeast throughout the disc. The greatest difference between the two sides is at an angular separation of $0\farcs7$, where the southwest is brighter by 50σ. A low-level bump in the continuum emission just beyond $2\farcs0$ occurs at the same radial location as the extended $C^{18}O$ emission and scattered light emission in Figure 2.6. ^{13}CO emission (middle panel) is also brighter in the southwest for as far as $\sim 2\farcs8$, beyond which the northeast of the disc is brighter.

Comparison to previously detected asymmetries in HD 100546

Figure 2.6 displays how the low-level, extended emission towards the edge of the gas disc is spatially coincident with structures identified by Ardila et al.

(2007), potentially linking observed scattered light features with the midplane gas above which the small, scattering grains are suspended. In other scattered light observations, Avenhaus et al. (2014) see a dark lane that extends from $\sim 0\overset{\prime\prime}{.}2 - 0\overset{\prime\prime}{.}6$ along the minor axis. The authors attribute this to effects due to the polarised scattering function, rather than any physical feature in the disc. However Wright et al. (2015) also observe an arc of millimetre emission in the same direction, at the same separation as the scattered light dark lane, but not quite as extended.

Mid-IR interferometry is able to resolve the inner disc, where asymmetry is found close to the inner gap of the disc at 9 au (Panić et al., 2014). Features in the inner disc can have a strong effect on the outer disc. For example there has been recent evidence of warps from ALMA observations, e.g. this disc (Walsh et al., 2017) and T Tauri star AA Tau (Loomis et al., 2017). A warp of the inner disc can lead not only to shadowing of the outer disc but potentially even a break of the disc into two distinct planes. Substructure can then develop as a result of this geometry; a misaligned disc can result in shadows that create asymmetric illumination of the disc, whilst a ‘broken’ disc can contain dust streamers that cross gaps in the disc (Dutrey et al., 2014; Loomis et al., 2017). Recent very high angular resolution ($0\overset{\prime\prime}{.}05$) ALMA observations of the disc resolve the very inner regions of the disc, revealing an asymmetric circumstellar ring in the continuum, brightest towards the North East (Pineda et al., 2019). The authors attribute this asymmetry to another scattered light spiral feature, this time identified by SPHERE (Garufi et al., 2016), on angular scales much less than that of the synthesized beam achieved in the observations presented here.

Many of these disc structures can arise through interactions with a central companion as shown by 3D hydrodynamic simulations of the transition disc HD 142527 (Price et al., 2018), this is particularly interesting in regard to any asymmetries found in the HD 100546 disc when bearing in mind the evidence found in recent years for a further companion at smaller separation.

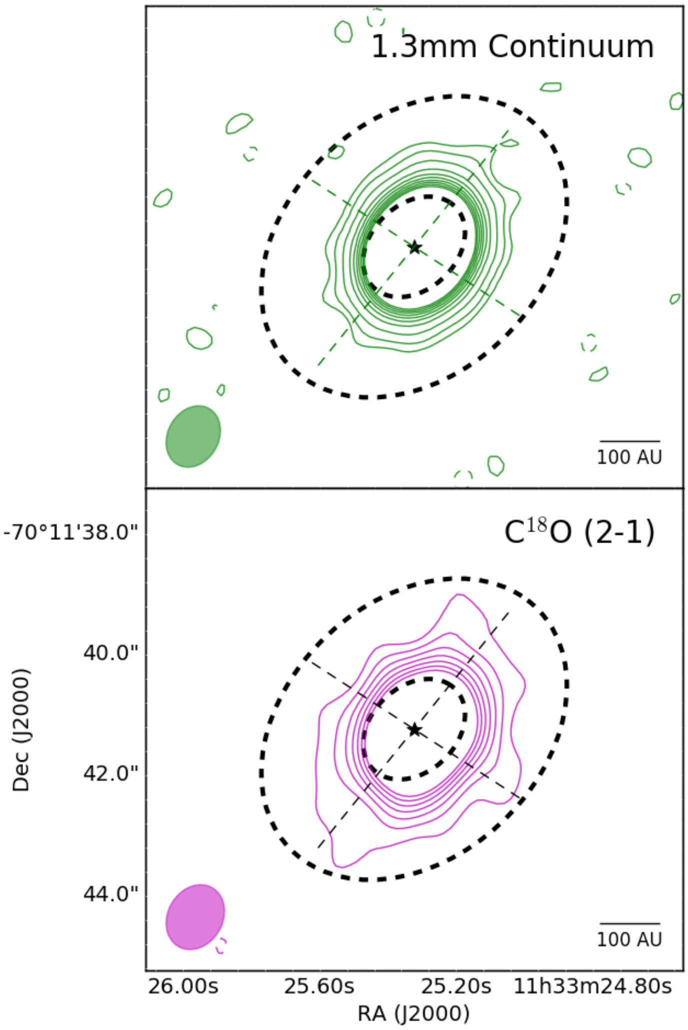

Figure 2.7: Emission maps of 1.3mm continuum and C^{18}O (2-1) with overlaid dashed ellipses with a position angle of 144° and inclination of 43°. These correspond to rings with a deprojected radius of 100 au and 300 au. The star marks the GAIA position of HD 100546 on which the ellipses are centered. Contours in the top panel range from (5-75)$\times\sigma$ in steps of 10σ and in the bottom panel from (3-15)$\times\sigma$ in steps of 2σ. Dashed contours are negative. High level contours internal to the ellipse are omitted for clarity.

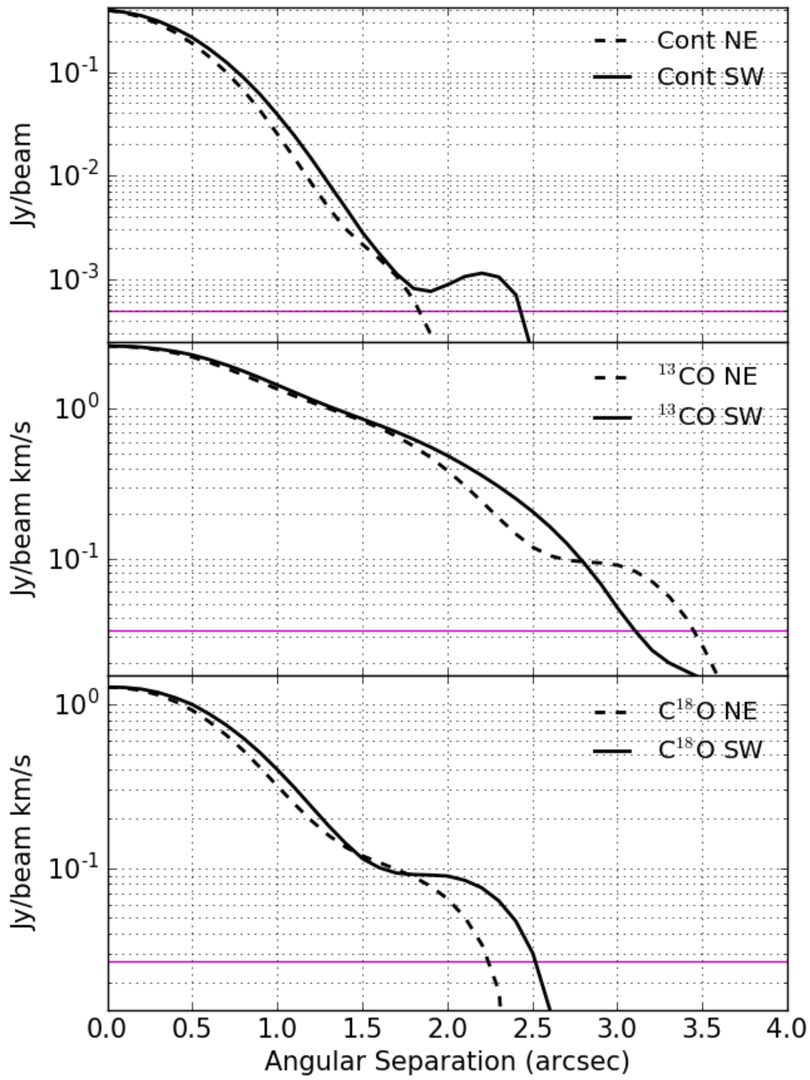

Figure 2.8: Slice are extracted from the emission maps of each tracer along the minor axis. Solid lines show the slice towards the southwest, dashed lines show the slice to the northwest. The horizontal purple line indicates the rms measured in each image.

2.4.3 Asymmetry Analysis

Asymmetry in the surface brightness of the gas emission can occur from increased temperature, increased density or a combination of the two.

In 3D hydrodynamic simulations, spiral arms launched by planets observed at 1.3 mm have been shown to induce azimuthal variation in gas surface density of approximately 50-60% (Juhász and Rosotti, 2018), and should also be observable in optically thin gas observations. In this scenario, a large spiral arm could increase gas density locally, thereby elevating the scale height of micron-sized grains to produce the scattered light features. Alternatively a local density increase of 30% over a length scale approximately equal to the disc scale height is enough to provide the conditions for dust trapping of larger particles in the outer disc (Pinilla et al., 2012b). Another explanation for local increase in density is a gravitationally unstable disc, where clumping occurs due to gravitational forces if the free fall time scale is short compared to sound speed crossing time scales and shearing time scales (Toomre, 1964). This is generally found in discs at an earlier stage in their evolution whilst discs are still very massive ($\mathrm{M_{disc}/M_\star} > 10\%$), which is not the case here.

Brightness asymmetry can also result from varying temperature in the disc. Azimuthal variation in disc temperature may result from an inner warp that obscures sections of the disc or azimuthal variation of density.

Density Scenario

In this scenario it is assumed that the difference in observed brightness is due solely to changes in gas density. The disc is bisected along the major axis and then each half is divided into three 60° degree segments, the flux for each segment is then summed. By calculating the brightness ratio between two segments on opposite sides of the disc, the increase in surface density required to produce the difference in flux can be readily calculated. The intensity of integrated line emission is given by

$$I = \frac{h\nu A_{J,J-1} N(J)}{4\pi}, \tag{2.2}$$

where $A_{J,J-1}$ is the Einstein coefficient for spontaneous emission from level J to level J-1, and N(J) is the column density in a specific level. The intensity is therefore proportional to the density of molecules in the N(J) level.

The largest brightness difference is between the two segments along the minor axis; the southwest is brighter than the northeast by a factor of 1.10 ± 0.15 . The asymmetry identified in Section 2.4.2 is most obvious in the outer disc. The brightness ratio of outer regions, summing only the emission beyond a deprojected radius of 100 au is found to be 1.27 ± 0.18 . The angular resolution of the current observations limits comparisons of brightness across regions of the disc. Local density increases on smaller scales can alert us to certain physical mechanisms in the disc, some of which are discussed below.

Given the $1\farcs0$ resolution of the data, it is feasible that there are much larger azimuthal density variations for a given radial separation that are diluted by the beam. This might arise due to a local increase in density due to, for example, a spiral arm. Ardila et al. (2007) associate the three structures in Figure 2.6 with spiral arms, and it is towards each of these structures that the outer disc of $C^{18}O$ emission seems least symmetric.

From this data the possibility of an unresolved vortex capable of trapping particles at large separation in the HD 100546 disc cannot be ruled out, as the observed density variation is similar to that predicted by Pinilla et al. (2012b). High resolution data across multiple wavelengths would help to identify any such feature (e.g. Cazzoletti et al., 2018). Such dust trapping vortices have not yet been found at such a large radial separation from the host star however, as densities in outer disc regions are typically not large enough to create the required pressure jump.

Calculation of the Toomre parameter, Q, based on the radial profile of $C^{18}O$ rules out gravitational instability in the disc. Assuming $C^{18}O$ traces total disc mass, Q(R) for this disc reaches a minimum of 24 at 80 au confirming that the disc is stable against gravitational collapse. However a clump in the outer disc will experience relatively long orbital timescales, meaning it will take longer to break up. Fragments of the disc that were previously unstable might linger at the outer edges of the disc as they dissipate.

Temperature Scenario

To test the possibility of temperature variation as the cause of asymmetry in the outer $C^{18}O$ disc, the average flux in different segments of the disc is measured as in the previous section, and the temperature variation that would be required to reproduce such a flux difference is calculated. Through a comparison of the average fluxes in opposite segments, the increase in temperature required if this was to be due to temperature alone (i.e. no density increase) can be determined.

Column density of $C^{18}O$ gas in the J=2 level is calculated using

$$N_J = N(total)\frac{2J+1}{Z}\frac{1}{exp\left(\frac{hB_eJ(J+1)}{kT}\right)}, \tag{2.3}$$

where T is the midplane temperature and B_e is the rotation constant. The partition function, Z, is calculated using

$$Z = \sum_{J=0}^{\infty}(2J+1)\ exp\left(\frac{-hB_eJ(J+1)}{kT}\right), \tag{2.4}$$

Substituting for Z and N(J), Equation 2.2 becomes

$$I = \frac{h\nu A_{J,J-1}}{4\pi}\frac{N_{\text{total}}\ (2J+1)}{exp\left(\frac{hB_eJ(J+1)}{kT}\right)}\frac{1}{\sum_{J=0}^{\infty}(2J+1)\ exp\left(\frac{-hB_eJ(J+1)}{kT}\right)}. \tag{2.5}$$

ΔT required to produce the observed brightness ratio of 1.27 from Section 2.4.3 is plotted against a range of potential midplane temperatures in Figure 2.9.

Figure 2.9 shows that even for a midplane temperature as cool as 20K (below which CO is no longer in the gas phase), a 75% increase in average temperature is required. From 24K and above, the average temperature of the outer disc midplane must increase by greater than 200%. There are no known physical processes expected within the disc midplane which could produce such a large change in temperature, especially when averaged over such a large proportion of the disc. Assuming that inner parts of the disc dominate the flux in each segment, temperatures may be larger than in the cool outer disc. However, the radiative transfer models of Panić and Min (2017) show that in reality an increase in disc temperature from 20 to 32K (comparable to the 20-35K increase in Figure 2.9), requires an increase in gas density of order 10, far greater than what is

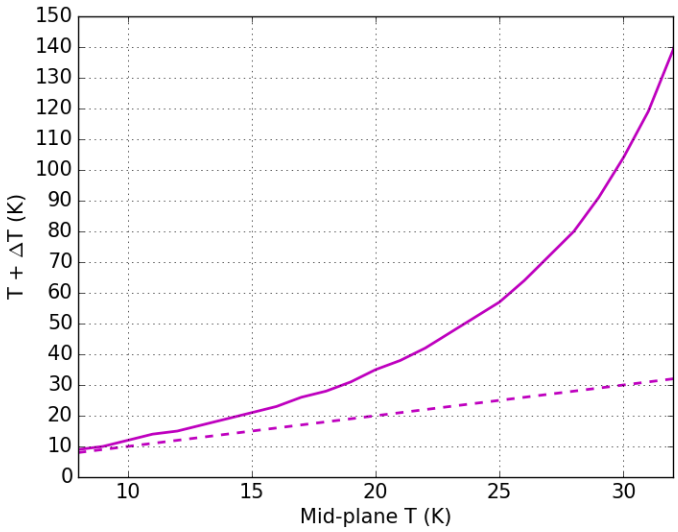

Figure 2.9: Calculated temperature, T+TΔT, required to produce the observed variation in flux in segments of the disc from the $C^{18}O$ moment 0 map, over a range of assumed midplane temperatures. The dashed line indicates ΔT=0.

detected here. These calculations rule out temperature as a sole cause of any flux asymmetry. In order to explain the difference in brightness between the two regions of the disc, some form of density increase must be invoked as well.

2.4.4 Radial Flux Profiles

Ignoring azimuthal variations in disc emission, flux changes in the radial direction are considered by de-projecting and then azimuthally averaging, around the mm continuum centre, the emission from images in Figure 2.2. The resultant average profiles are shown in Figure 2.10.

Taking advantage of the high signal to noise in the data, the following method is adopted to obtain an accurate uncertainty estimate for the radial flux profiles. Each image is averaged off-source in ‘empty’ sky locations at 45° position angle intervals at a separation that does not include any significant emission from the central source, but is also well within the primary beam. The resultant radial profile gauges the level of fluctuations due to background noise in that part of the image (shown as grey lines in Figure 2.10, more visible in the insets). The

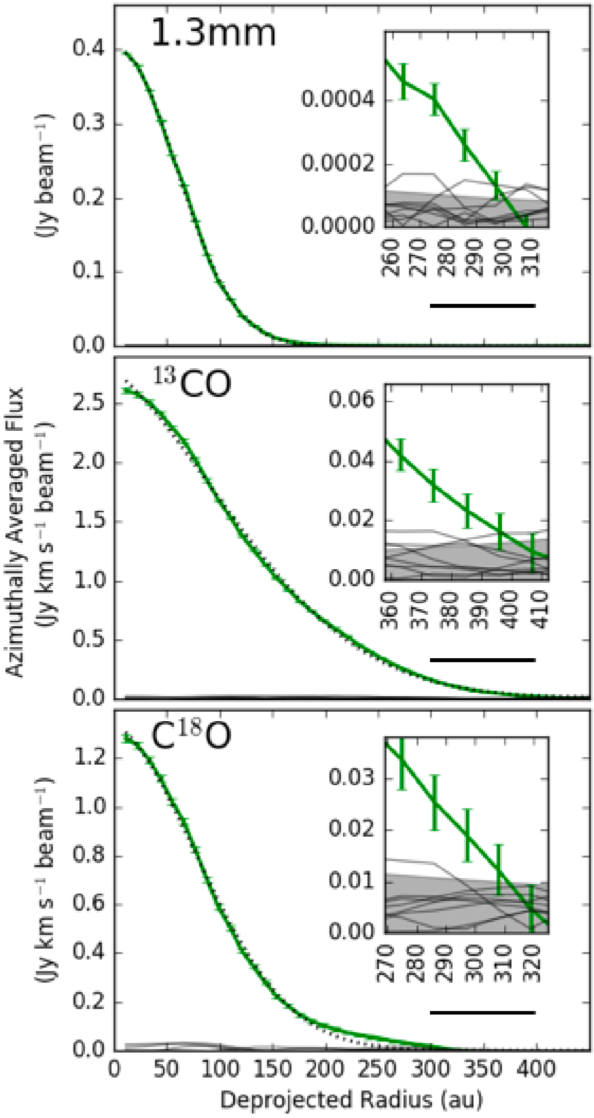

Figure 2.10: Azimuthally averaged flux plotted against radius in green for both the continuum and line emission. Grey lines show the averages obtained for regions off-source (no emission). The shaded area represents the 2σ level computed from these off-source averages. Dotted black lines are least-squares fitted Gaussians to the flux profiles. Horizontal black lines give the spatial scale corresponding to the deprojected FWHM of the synthesized beam.

amplitudes of these fluctuations as a function of radius are fitted with polynomials, the polynomials are then averaged over the different off-source locations. The resulting final polynomial gives the average level of off-source fluctuations in the image as a result of the azimuthal averaging process, which is used for error bars on the average flux curve. This method also allows for a determination of average outermost detection radius that does not rely on a pre-defined function or model; taken to be the point at which the average flux becomes less than 2 times the average noise fluctuations at that radius. In Figure 2.10 this corresponds to the error bars reaching the grey shaded area.

Figure 2.10 plots the azimuthally averaged continuum flux and integrated line emission against deprojected radius (using inclination=43° and PA=144° as determined in Section 2.3). The 1.3 mm continuum is detected as far as an average deprojected radial separation of 286±11 au. The ^{13}CO profile shows us that the gas in the disc is significantly more extended; detected as far out as 385±11 au, a comparable distance to the 390±20 au extent of ^{12}CO in the disc reported by Walsh et al. (2014a). The less abundant molecule C^{18}O is detected out to a shorter separation of 297±11 au.

A large amount of mass spread over large radial separations is important for planet formation in the outer disc. Giant planets grow more massive in discs of higher initial disc (gas) mass (Mordasini et al., 2012). Furthermore, population synthesis models suggest that significant amounts of giant planets migrate into the central star after formation (See review Mordasini, 2018). In order to survive, some cores accrete late in the disc lifetime and grow as they migrate inward (Baruteau et al., 2014). These results suggest the disc of HD 100546 is well placed to support such late survivors, because a large amount of planet building material ($\sim$18 M_J) still exists over a large region of the disc (297 au outermost detection of C^{18}O). This is particularly relevant in the case of this disc, where a proto-planet detection is claimed towards the outer disc at a radial separation of $\sim$50 au (Quanz et al., 2015).

The difference in the outer radius at which the discs are detected may be a true physical difference, or could be a result of the different sensitivity between the continuum and the line emission. In Figure 2.11 the surface density profile of each tracer is plotted in order to assess how it changes with radial separation. Here

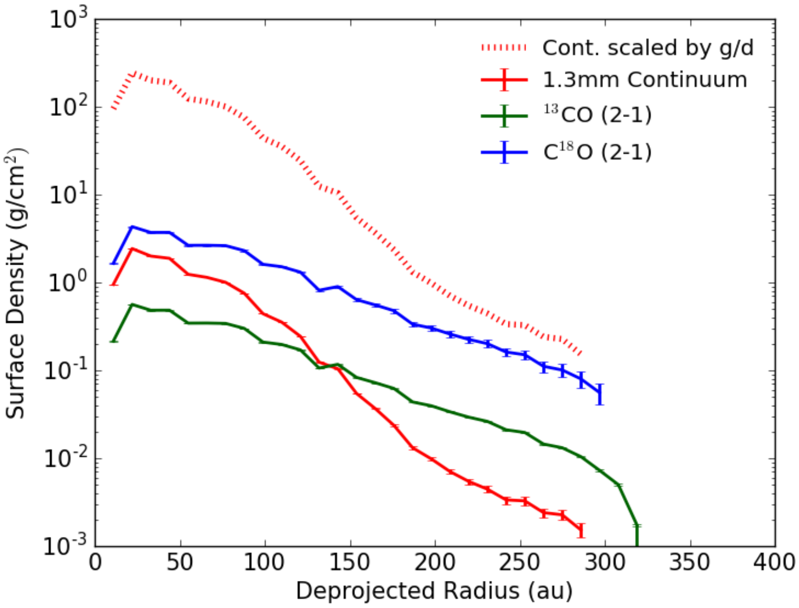

Figure 2.11: Surface density profiles calculated form the radial profiles in Figure 2.10. The dotted line represents the surface density of the 1.3 mm continuum image scaled up by a factor g/d=100.

surface density has been calculated by converting azimuthally averaged intensity from the images at each radial location into mass using the same parameterised temperature profile for each tracer, T$\propto R^{\frac{1}{2}}$ and adopting the opacity assumptions used in the mass calculations. If the emission were to be deconvolved from the synthesized beam, or observed with higher resolution a steeper gradient would be expected. The ^{13}CO curve represents a lower bound because the emission is optically thick for most of the disc. The continuum surface density profile is scaled by an assumption that g/d in the disc is the canonical value of 100, giving an upper bound to compare to the gas profile. The profiles in Figure 2.11 tend to show a steady decline towards the outer disc, rather than a sharp fall that might signify a definitive outer edge of the disc. Variations in slope may also be influenced by differences in temperature profile between the tracers if the emission originates from different scale height in the disc.

The surface density of mm particles, as calculated from the 1.3 mm emission, is fairly large to begin with but begins to drop sharply after ∼100 au. The $C^{18}O$ surface density declines over the extent of the disc on the log scale in Figure 2.11, converging with the g/d scaled continuum curve. The mass calculations in Section 2.3 result in a disc g/d lower than 100. If values of <100 are used to scale the 1.3 mm surface density curve, in the outer disc $C^{18}O$ would soon have a greater surface density than the scaled dust, suggesting there is sufficient sensitivity in the gas line observations to confirm that the gas is more extended than the dust. Determining the outer radius of a disc in either gas or dust is complex, but Facchini et al. (2017) use thermo-chemical models to find that the observed difference between dust and gas disc radii is largely down to optical depth effects. The effect of radial drift is shown by a sharp outer edge to the dust disc. Such a feature is absent from the dust surface density profile in Figure 2.11 due to the ∼100 au resolution in these observations.

Evidence of optical depth effects in this data set are seen in the CO isotopologues; throughout the disc ^{13}CO has a lower surface density than the much less abundant $C^{18}O$. Optical depth is estimated by adopting the method as used by Schwarz et al. (2016) through Equation 2.6,

$$\frac{S(^{13}\mathrm{CO})}{S(\mathrm{C}^{18}\mathrm{O})} = \frac{\nu_{^{13}\mathrm{CO}}}{\nu_{\mathrm{C}^{18}\mathrm{O}}} \frac{T_{ex,^{13}\mathrm{CO}}}{T_{ex,\mathrm{C}^{18}\mathrm{O}}} \frac{1-e^{\tau_{^{13}\mathrm{CO}}}}{1-e^{\tau_{\mathrm{C}^{18}\mathrm{O}}}}. \tag{2.6}$$

The integrated flux ratio from the observations of $^{13}CO/C^{18}O=4$, half the isotopic value of 8 in the ISM (Wilson, 1999), giving a strong indication that ^{13}CO is optically thick. The ISM isotopic ratio is adopted for this calculation and the ratio of excitation temperatures of the two isotopologues is assumed to be ≈ 1. Figure 2.12 shows the resulting τ(R) as well as the flux ratio from the two isotopologues.

At the outer edge of $C^{18}O$ detection, the ratio of isotopologue emission rises up to ∼7, with a steep increase towards the ISM ratio of 8 from ∼250 au as the edge of the $C^{18}O$ disc is approached. $C^{18}O$ is found to be optically thin for the full radial distance over which it is detected, with $\tau \leq 0.68$ as shown in Figure 2.12. This optical depth result can help to explain the isotopic ratio curve, which rises as the optical depth decreases. Assuming the intrinsic isotopic abundance ratio within the disc remains constant, the ^{13}CO optical depth will decrease as the

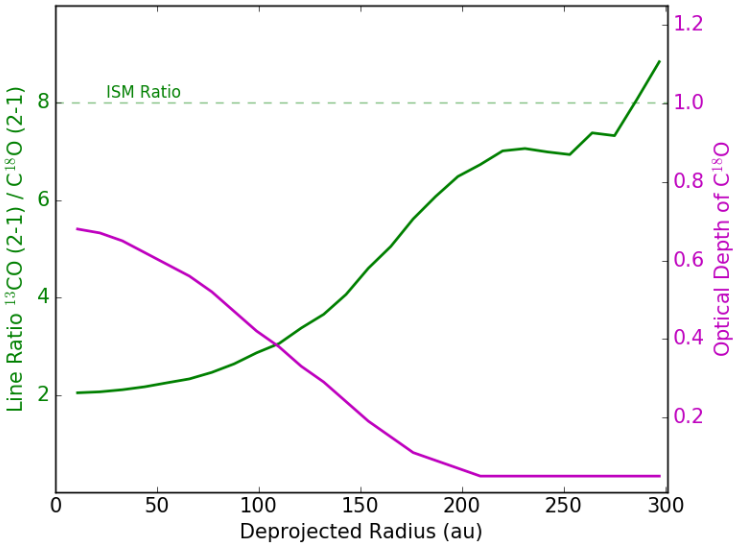

Figure 2.12: The ratio ^{13}CO/C^{18}O is plotted against de-projected radius and coloured in green, the calculated optical depth of C^{18}O as a function of radius is plotted in purple.

C^{18}O does with separation from the star. As ^{13}CO becomes increasingly optically thin, the observed abundance ratio will tend towards its true value.

Spectral Index

The 867 μm continuum data from the ALMA band 7 data on this source (Walsh et al., 2014a) is here utilised to calculate the spectral index of the dust. The data is imaged using the same beam as the 1.3mm continuum. Using azimuthal averaged profiles of each continuum image a radially dependent spectral index for the disc is calculated and plotted as the central green line in Figure 2.13. In the upper panel of Figure 2.13, $\alpha_{\rm mm}$(R) begins in the inner disc with a value of 2.1 and steadily rises with radius by $\Delta\alpha_{\rm mm} \approx 0.3$.

$\alpha_{\rm mm}$(R) remains within the range typically seen in protoplanetary discs (Pinilla et al., 2014; Ricci et al., 2012), covering a range of values that are low in comparison to that of the ISM. Low spectral index at millimetre wavelengths can be down to one of two reasons; grain growth has lead to larger dust particles ($a_{\rm max} \geq 3\lambda$) which emit less efficiently and reduce the calculated α, or optically thick emis-

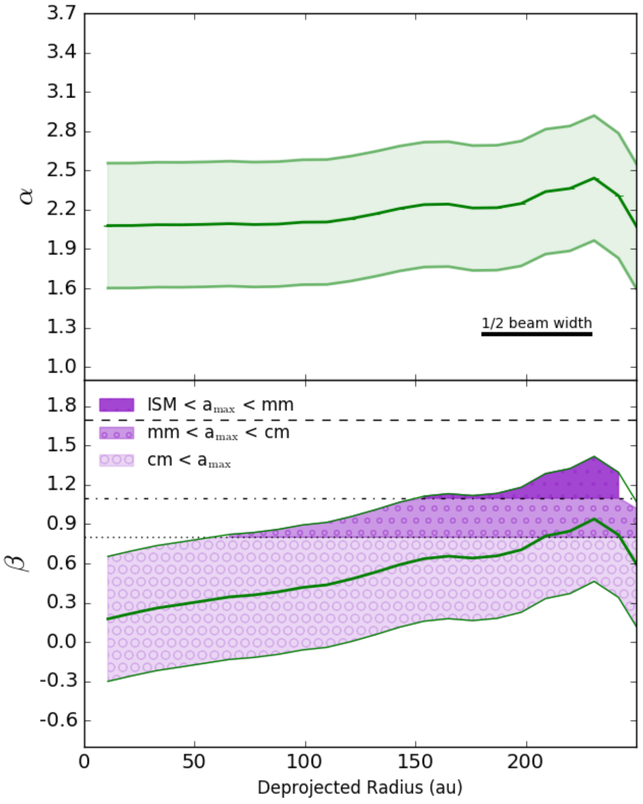

Figure 2.13: Upper panel : Radially dependent spectral index, α, calculated using ALMA continuum observations at 867 μm and 1.3 mm for the disc of HD 100546. The upper and lower green lines give the maximum and minimum curve considering flux calibration uncertainties. The bar indicates a length of 50 au, approximately half the beam width. Lower panel: Radially dependent opacity index, β, over-plotted with horizontal lines that show the opacity calculated by Draine (2006) for a dust population with $a_{\rm max}$ of cm- (dotted), mm- (dash-dot) and ISM grains (dashed), assuming a grain size distribution of $dn/da \propto a^{-3.5}$. Where the lower-bound curve crosses these lines, the area under the curve is coloured according to the key. Error bars are propagated from noise in the image (insets of Figure 2.10), and are barely visible. The x-axis is shown up to 230 au, the detected size of the 867 μm disc (Walsh et al., 2014a).

sion. As there is no robust information on the sizes of grains present in the disc, optical depth of 1.3 mm continuum emission is calculated as a function of radius using the surface density profiles calculated above and a range of emissivities at 1.3 mm corresponding to different particle sizes from Draine (2006). The surface density profiles presented in Figure 2.11 necessarily assume optically thin emission, and so τ given in Figure 2.14 represent the τ values if this assumption is correct. Future high resolution observations of HD100546's dust disc will confirm the radial surface density profile with greater accuracy. Through comparing spectral indices calculated from previous mm observations, Walsh et al. (2014a) find that at sub-mm wavelengths the continuum emission may be approaching the optically thick regime however.

In order to constrain what the size of the emitting grains are the opacity index $\beta_{\rm mm}$ is calculated. In an optically thin disc under the Rayleigh-Jeans approximation, this can be related to the spectral index by $\alpha_{\rm mm} = \beta_{\rm mm} + 2$. At $\lambda \approx 1$ mm cool dust in the disc is traced, where the Rayleigh-Jeans approximation does not hold, and so an approach similar to that of Guidi et al. (2016) is adopted, calculating $\beta_{\rm mm}$ with

$$\beta_{\rm mm}(R) = \frac{{\rm dlog}F_\nu(R) - {\rm dlog}B_\nu}{{\rm dlog}\nu}, \tag{2.7}$$

adopting a temperature profile that obeys a power law, $T(R) = T_{100}\;(R/100\;au)^{0.5}$, and taking T_{100}=25K. Figure 2.15 demonstrates how temperature affects the calculated $\beta_{\rm mm}$(R). Although temperatures in the midplane and the outer disc are cool and relatively stable, Figure 2.15 shows that an inaccurate temperature prescription can alter the β significantly; a difference of 20K in T_{100} changes β at $\sim$200 au by 0.32. For comparison, this difference is larger than the difference between the characteristic β for $a_{\rm max}$=1mm and $a_{\rm max}$=1cm. Under-estimating disc temperature increases the inferred size of grains in the cooler outer disc, meaning the radial size sorting of grain sizes is of a lesser degree and that grain sizes thoughout the disc are of large ($\sim$mm) sizes.

In the lower panel of Figure 2.13 $\beta_{\rm mm}$ is plotted as a function of radius compared with opacity indexes calculated by Draine (2006). Coloured areas on the plot show radii at which $\beta_{\rm mm}$ indicates a particular $a_{\rm max}$ has been achieved through grain growth, determined by when the lower bound of the calculation crosses the indicative horizontal lines. The curve takes a similar form to that in the top panel, except for a larger variation of $\Delta\beta_{\rm mm}(R) \approx 0.8$ over the extent of the disc.

The main result from Figure 2.13 is that $\beta_{\rm mm}(R)$ calculated between 867μm and 1.3 mm indicates grain growth to cm-sizes throughout the disc. In fact, the characteristic β for $a_{\rm max} = 1, 10, 10^2$ cm, at millimetre wavelengths are all ≈ 0.8 (see Draine, 2006, Figure 2), so dust could be growing even larger than cm sizes without us being able to detect it. Within the uncertainties due to flux calibration, this result is consistent with grain growth to cm-size for the full extent of the disc detected at both continuum wavelengths, where α is calculated over the shorter $\sim$ 230 au band 7 continuum radius (Walsh et al., 2014a). $\beta_{\rm mm}(R)$ for the disc inward of $\sim$200 au is consistent with pebble (>cm) sized dust. The upper curve remains below the top dashed line for the full extent of the disc, confirming that grains have evolved from an ISM-like β throughout the disc. Overall, midplane dust has grown substantially from ISM levels within the disc.

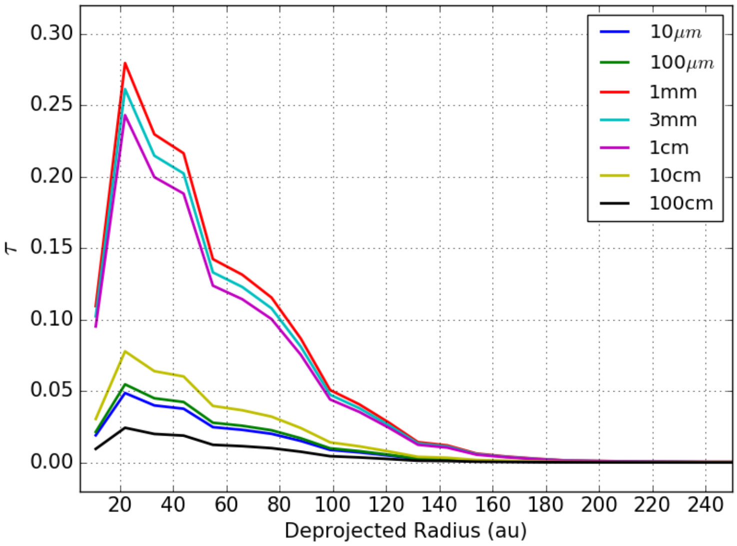

Figure 2.14: Optical depth of the 1.3 mm emission as a function of de-projected radius calculated for a range of maximum grain sizes ($a_{\rm max}$) in the MRN grain size distribution.

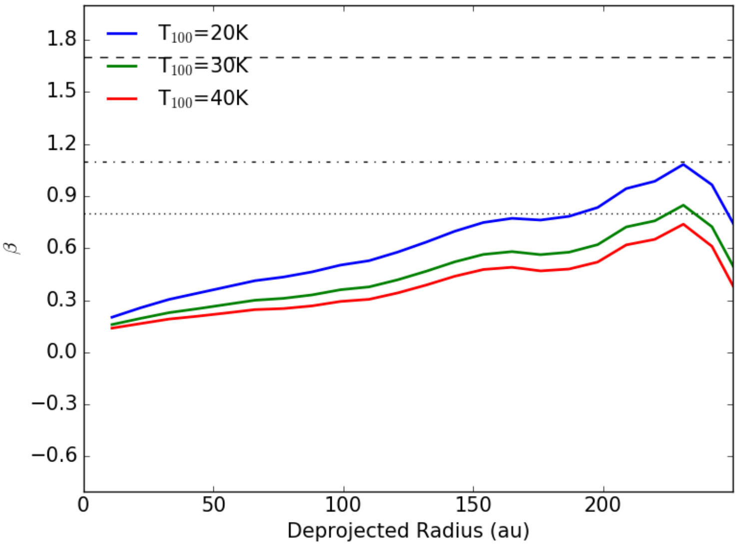

Figure 2.15: $\beta_{\rm mm}$ calculated using temperature profiles calculated with a power law with varying T_{100}. Horizontal lines are the same as in the lower panel of Figure 2.13.

Radially increasing $\beta_{\rm mm}$ in the outward direction has been predicted by dust evolution models that include realistic coagulation and fragmentation (Birnstiel et al., 2010; Brauer et al., 2008). Radially increasing β also agrees with past studies that fit multi-wavelength observations with parametric models of discs in the uv-plane, where only those with a radially increasing β could reproduce observed emission (Banzatti et al., 2011; Pérez et al., 2012; Tazzari et al., 2016; Trotta et al., 2013).

Guidi et al. (2016) use high resolution data from ALMA and the VLA to observationally confirm a radially increasing dust opacity in the disc of intermediate mass star HD 163296, a bright disc around a Herbig star that has been found to have a series of dust-depleted rings (Isella et al., 2016). This is confirmed here for HD 100546, adding further evidence for the prediction of Wright et al. (2015) who suggest grains may have grown to at least 5 cm. Walsh et al. (2014a) compare their measured flux with previous mm observations by Henning et al. (1994); Wilner et al. (2003) in order to calculate disc-averaged $\beta_{\rm 3mm-1mm}$=0.7-0.8, and $\beta_{1{\rm mm}-870\mu{\rm m}}$=-0.4, values that lie within the range found here over the extent of the disc in Figure 2.13.

This analysis assumes that dust grains in the disc have a size distribution of $dn/da \propto a^{-p}$, where p=3.5, an index typical of the ISM (Mathis et al., 1977) that is canonically adopted when modelling discs. As grains grow, the overall distribution of mass between grain sizes is likely to evolve. Birnstiel et al. (2011) showed that when both coagulation and fragmentation are included within a disc grain growth model, the size distribution will deviate from p=3.5; growth of grains tends to lower p, whereas fragmentation will re-introduce small particles and raise p. Draine (2006) demonstrates how β decreases with index p for a constant $a_{\rm max}$ in Figure 6 of that paper. ISM-like grains are expected at the outer edge of the disc, yet this is not shown in Figure 2.13. Either these observations lack the sensitivity to detect the full extent of the dust, or the dust in the disc would be better suited to an alternative value of p. The latter would corroborate with the results of Wright et al. (2015) when studying HD 100546, where the authors find that only d 'Alessio et al. (2005) disc models with p=2.5 fit their data. Tighter constraints could be achieved by comparing against an extensive grid of opacity calculations at millimetre wavelengths over a range of p values.

2.5 Conclusions

New ALMA observations of the HD 100546 protoplanetary disc are presented here including the first detection of $C^{18}O$ in the disc.

An integrated flux of 492 mJy is measured from the 1.3 mm continuum image. An outer-most detection of the dust disc is determined at a radial separation from the star of 290±10 au at 1.3 mm and the lower limit on dust disc mass was calculated to be 4.1-9.6 $\times 10^{-4}$ $M_\odot$.

Line emission is detected from CO isotopologue transitions ^{13}CO (2-1) and $C^{18}O$ (2-1). ^{13}CO has an integrated flux of 12.872 Jy kms^{-1} and extends out to 390±10 au, a size comparable with previous observations of ^{12}CO in the disc. The optically thinner, midplane tracing isotopologue $C^{18}O$ is detected for the first time in the disc, giving an integrated flux of 2.948 Jy kms^{-1} with emission detected as far as 300±10 au.

These detections correspond to a considerable gas mass of 0.018 $M_{\odot}$, around 1% of the stellar mass. Freeze-out is not expected in this warm Herbig disc. If carbon sequestration is efficient the total gas mass may be larger, but not lower, by these calculations. The ALMA observations of continuum and CO isotopologue emission presented here suggest the lower limit of the gas to dust ratio for the HD 100546 disc is 19. This calculation assumes ISM abundances of $C^{18}O$ relative to H_2 in the disc and so the gas to dust ratio in the disc will be larger in the event that $C^{18}O$ is significantly depleted relative to other species.

Low-level extended $C^{18}O$ emission is observed that is spatially coincident with spiral arm structures identified in scattered light observations by the HST. The extended $C^{18}O$ emission may be tracing the midplane density variation that creates the scattered light features. In each of the observed tracers, the disc is seen to have a puzzling offset from the known stellar position of between ≈70-110 milliarcseconds.

Spectral index, $\alpha_{\rm mm}$, is derived as a function of radius in the disc and rises with separation from the star suggesting a decrease of maximum dust grain size in the outward direction. The opacity index, $\beta_{\rm mm}$ gives results consistent with the growth of grains beyond mm-sizes throughout the disc, and to larger cm-sized 'pebbles' within ∼200 au. A shallower dust grain size distribution is the alternative explanation, suggesting a larger proportion of the solid mass is contained within the largest grains in comparison to the ISM, or indeed optically thick dust at 867μm.

Chapter 3

Unlocking the secrets of the midplane gas and dust distribution in the young hybrid disc HD 141569

3.1 Context

Understanding the evolution from protoplanetary to debris discs (Dominik and Dullemond, 2002; Wyatt et al., 2015) requires an understanding of their structures. How do the many gaps, dust traps and asymmetries seen in protoplanetary discs evolve into dusty debris discs that typically host one or two rings, and what is the role of gas in this process? The 'hybrid' discs (Péricaud et al., 2017), are believed to probe this step in evolution because of detectable amounts of gas in the disc despite otherwise appearing to have evolved beyond the protoplanetary disc limit in dust mass. Whilst some molecular gas remains in the disc from the protoplanetary stage, the dust in hybrids is of a second generation meaning it is the product of dust evolution via grain growth and fragmentation processes.

In Chapter 2 there was evidence of large sized dust grains in transitional disc HD 100546, suggesting a certain degree of evolution in the disc's composition. But what is the next stage? Herbig star HD 141569 hosts the only known hybrid disc amongst pre-main sequence stars to date, a B9-A0 type, 5 Myr old star at a GAIA distance of 111±1 pc (Lindegren et al., 2016; Weinberger et al., 2000)[1]. Its SED and IR excess luminosity of 0.0084 (Sylvester et al., 1996) were the first indicators of this unique status. Figure 3.1 shows that HD 141569 has an SED which appears as a scaled-down version of a protoplanetary disc's SED in the sense that it is comprised by multiple radial (temperature) components. This is not the case in known debris and hybrid discs as both these types show, at most, two radial (temperature) components (e.g., 49 Ceti, HD 131835, Kennedy and Wyatt, 2014; Moór et al., 2015; Roberge et al., 2013). Although its SED seems protoplanetary, the disc dust mass of 0.7 $M_\oplus$ (Panić et al., 2013; Sandell et al., 2011) places HD 141569 in between the protoplanetary and debris-disc regimes (Wyatt et al., 2015). First detected by Dent et al. (2005), CO gas in the disc extends up to 200 au (Flaherty et al., 2016; White et al., 2016) and is nested inside the two outermost rings detected by Hubble Space Telescope NICMOS at 234 and 388 au (Augereau et al., 1999; Biller et al., 2015; Weinberger et al., 1999). Wide dusty belts are more typically associated with debris discs. Reported gas masses for

---

[1] In this work all previously reported length scales are updated using the latest GAIA distance for the source

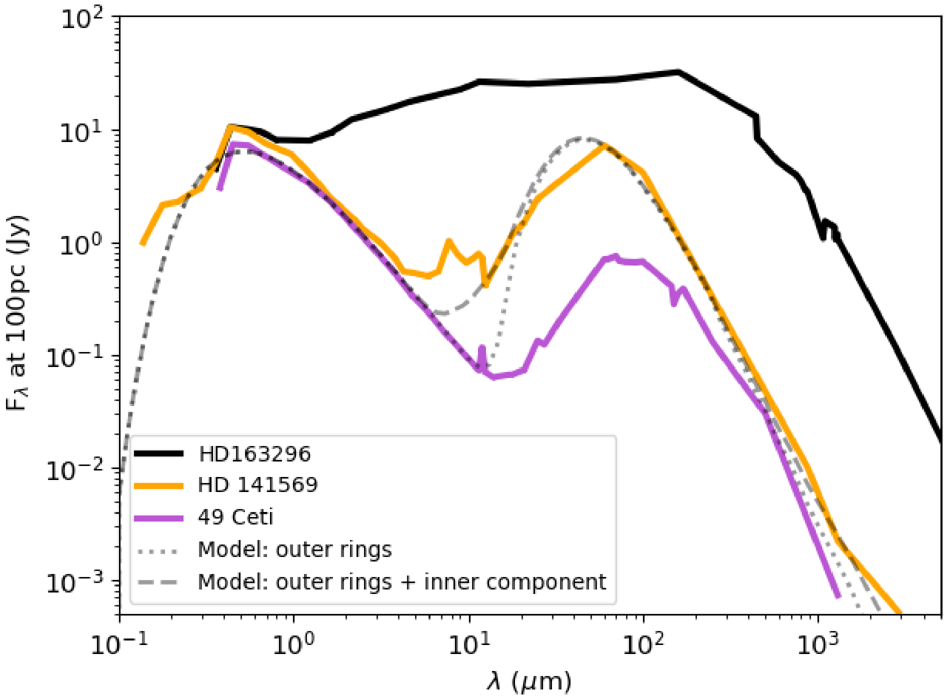

Figure 3.1: SEDs of typical protoplanetary disc HD163296, the youngest hybrid disc HD141569 and 40Myr hybrid disc 49 Ceti. Fluxes have been scaled to a distance from Earth of 100pc. Grey lines show SEDs from radiative transfer models of HD141569 built using the outer ring properties from Biller et al. (2015),and dust masses calculated here.

HD 141569 range between 4.5×10^{-6} $M_\odot$ derived from ^{12}CO (White et al., 2016) and 5×10^{-4} $M_\odot$ derived from SED model fits to Herschel line observations (Thi et al., 2014). None of these estimates employed optically thin CO isotopologue emission, which until now remained undetected in this disc. The estimated gas mass range for HD 141569 is below the typical protoplanetary disc gas masses of 10^{-3} $M_\odot$ to 10^{-1} $M_\odot$ but above the hybrid discs gas masses which are mainly $< 10^{-6}$ $M_\odot$ (Péricaud et al., 2017).

Insight into the innermost regions comes from SED fitting, with an inner radius set at 30 au (Marsh et al., 2002), and CO ro-vibrational emission placing gas as close as 11 au from the star (Goto et al., 2006). These regions have recently been imaged with SPHERE on the Very Large Telescope (VLT), detecting a series of concentric, but discontinuous, scattered light ‘ringlets’ at separations of 45, 61 and 89 au (Perrot et al., 2016). Inside these ringlets is a dust disc component within $0\farcs2$, detected in 8.2μm imaging with the VLT’s VISIR instrument (Perrot et al., 2016). A central, unresolved component of millimetre continuum emission peaks at the stellar location (Marsh et al., 2002; White et al., 2018). Beyond the gas-rich region are the two scattered light rings at 234 and 388 au, with inclination and PA similar to that of the inner rings seen with SPHERE (Perrot et al., 2016), but showing more complex structures and spirals, possibly due to planets within the disc (Wyatt, 2005) or a fly-by (Reche et al., 2009).

Using new ALMA observations this chapter investigates to what extent the midplane gas and dust of HD 141569 exhibit protoplanetary and debris disc characteristics, in the context of increasing evidence for a hybrid class of discs.

3.2 Observations and results

ALMA observations in Band 6 were taken on 16th May 2016 (PI Panić, ID 2015.1.01600.S). 39 antennas of 12 m diameter were employed in a configuration providing baseline lengths ranging from 16 m to 640 m. The velocity resolution is 0.166 km/s for ^{13}CO and 0.333 km/s for C^{18}O, providing optimal sensitivity to the tenuous and previously undetected midplane gas emission. The total effective continuum bandwidth was 4 GHz. The data were flagged and calibrated following the ALMA-pipeline data reduction. Titan was used as the flux calibrator, J1550+0527 and J1733-1304 were used as the bandpass and phase calibrators respectively. In addition to these new observations archival data from ALMA Band 7 published by White et al. (2016) is also employed here, taking advantage of the ^{12}CO(3-2) observations. Using CASA 4.7.1, continuum emission is subtracted from the uv plane. Images were created using the clean algorithm (Rau and Cornwell, 2011); as no a priori knowledge of the distribution of ^{13}CO, or indeed of the dust emission at 1.3mm exists, a natural weighting is adopted in image reconstruction in order to prioritise the collection of signal, rather than the increased resolution that could be achieved with other baseline weightings. This produced a synthesized beam size of $0\farcs65$ (72 au) for the continuum and $0\farcs71$ (79 au) for ^{13}CO and C^{18}O.

Rms noise level in the continuum image is 0.11 mJy/beam, and in the ^{13}CO and C^{18}O channel maps rms was 0.04 and 0.03 Jy km/s/beam respectively. In the continuum imaging an unresolved point source of 1.7 mJy is detected. ^{13}CO does not show a firm detection in the individual channel maps, but the integrated intensity map over the known range of velocities in which ^{12}CO is seen (Flaherty et al., 2016; White et al., 2016) shows a 6σ detection in ^{13}CO. C^{18}O is not detected >3σ in either the channels or the integrated intensity map.

Azimuthal averaging was performed in radial bins of $0\farcs12$ for the ^{13}CO and 1.3mm maps, and $0\farcs15$ for ^{12}CO. Neither the strongly asymmetric ^{13}CO nor the unresolved central 1.3mm emission can provide reliable constraints on the position angle and inclination of the disc, so for deprojection of coordinates the values of the ^{12}CO disc are adopted, PA=-9° and inclination=55° (White et al., 2016). Figure 3.2 shows the averaged profiles. At 220 au a thin concentration of millimetre grains is detected in a ring. ^{13}CO(2-1) emission is detected as far as 220±10 au.

To derive uncertainties for the radial flux profile, azimuthal averaging is applied centered on emission-free regions of the image that are sufficiently far from the central emission, yet within the primary beam of the observation. The mean value across emission-free regions from different parts of the image gives a flux profile that describes the background noise in the image as a result of the averaging process. This method is more robust than simply taking the variation in an elliptical bin and does not rely on any predefined disc models. The resultant noise curves are shown in Figure 3.2 for each tracer. The outer belt is detected at $\sim 6\sigma_{\rm mm}$ in contiguous radial bins (comparing the 1.3 mm curve to the blue dashed noise line), with a peak at 220±10 au.

3.3 Discussion

3.3.1 Dust emission

The comparison of the radial profile of 1.3 mm flux with the known disc structures shows that some of the flux in the central unresolved component may be arising from the rings detected by SPHERE (Perrot et al., 2016). A minimum dust

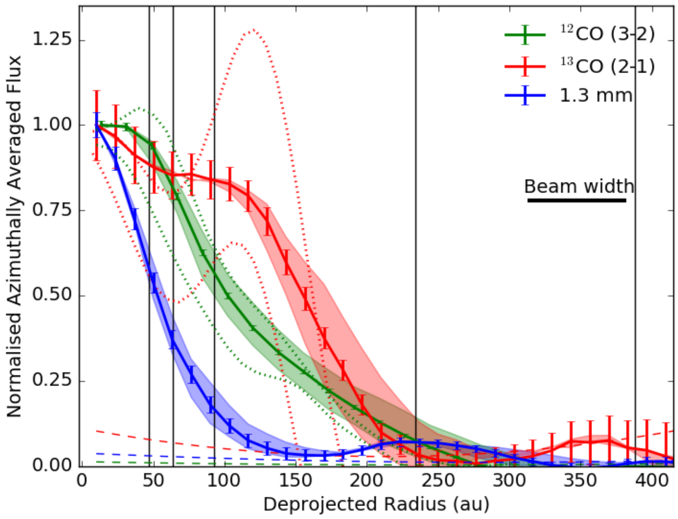

Figure 3.2: Azimuthally averaged flux profile following the deprojection of coordinates from the 1.3 mm image of HD 141569 (blue), ^{12}CO (green) and ^{13}CO (red). Vertical black lines show the radial locations of rings identified in scattered light. Peak intensities for 1.3 mm continuum, ^{12}CO and ^{13}CO are 1.74 mJy/beam, 1.06 and 0.25 Jy km/s/beam respectively. Coloured dotted lines show NW (upper) and SE (lower) cuts of the ^{12}CO and ^{13}CO maps along the position angle of the ^{13}CO peak. The shaded regions show the variation of the profile when changing inclination of the source by +/-10°. Error bars are calculated as described in the text, the coloured dashed lines represent the noise level after averaging for each curve.

mass is calculated for the inner disc by assuming optically thin emission, using $M_{dust} = \frac{F_\nu \ d^2}{\kappa_\nu \ B_\nu(T)}$, taking a midplane disc temperature of 20 K, an opacity, κ_ν, corresponding to mm size grains of 1.15 cm^{2}g^{-1} (Draine, 2006) and a distance to the star, d, of 111 pc. The minimum dust mass for the inner disc is calculated in this way to be $(3.6\pm0.5)\times10^{-6}$ M$_\odot$ = 1.2±0.2 M$_\oplus$. This calculation assumes that all emission is thermal. A maximum opacity has been chosen to derive a minimum dust mass, the uncertainties correspond to a ±15% flux calibration uncertainty applied to all ALMA observations. This mass depends on disc temperature, 20 K is a good assumption for cool material in the midplane and outer disc, increasing the assumed midplane temperature to 50 K would give a mass of 0.04 $M_\oplus$.

An alternative explanation for the origin of this flux may be free-free emission, rather than thermal emission originating from rings of dust within the inner disc. In fact, a typical mm contribution from free-free emission in Herbig discs at a similar distance to HD 141569 is a few mJy (e.g., Wright et al., 2015), similar to the 1.7 mJy integrated flux measured for the unresolved peak. Non-thermal, free-free emission can be detected through a characteristically low spectral index, as is seen towards inhomogeneous ultracompact Hii regions for example (de Muizon et al., 1988; Rodríguez et al., 1989). Optically thin free-free emission has spectral slope ≈-0.1 above the break frequency with the value increasing as high as 2 at shorter wavelength or higher optical depth (Condon and Ransom, 2016). This value is considerably lower than that of thermal continuum emission in this regime and so its effect may be seen in the spectral index. Protoplanetary discs typically show $\alpha_{\rm mm} \approx 2 - 3$, transition discs tend to show slightly higher values than this (Pinilla et al., 2014), whilst debris discs have $\alpha_{\rm mm} \approx 2.5 - 3$ (MacGregor et al., 2016). ALMA (0.87mm and 2.9mm) and VLA (9mm) observations derive a spectral index for the disc of $\alpha_{\rm mm} = 1.63$ (MacGregor et al., 2016; White et al., 2018), with which the 1.3 mm integrated flux of 1.8 mJy is consistent. $\alpha_{\rm mm}$ calculated between ALMA observations at 870μm and 2.9 mm also give a steeper, but still relatively low value of 1.81 (White et al., 2018). VLA observations show a significant variability in the continuum flux of the disc, varying by a factor of two to three on timescales of tens of minutes (White et al., 2018). Fluxes measured on integration times shorter than the variability timescale may therefore only offer a snapshot of flux emission. To make a conservative estimate of possible free-free contribution, VLA flux of 54 μJy (MacGregor et al., 2016) can be extrapolated using a characteristic spectral slope for optically thin free-free emission. From this estimate the free-free flux at 1.3mm would be just 3% of the total integrated flux measured, meaning the flux is predominantly thermal, potentially with small free-free contribution of order 10s of μJy at most.

In Figure 3.2 there is an increase in flux which peaks at a deprojected radial separation of 220±10 au. The ring is detected interior to the scattered light ring at 234 au (Biller et al., 2015) as is demonstrated by the ellipses in Figure 3.3. Taking the flux from the peak of the ring in Figure 3.2 and assuming the

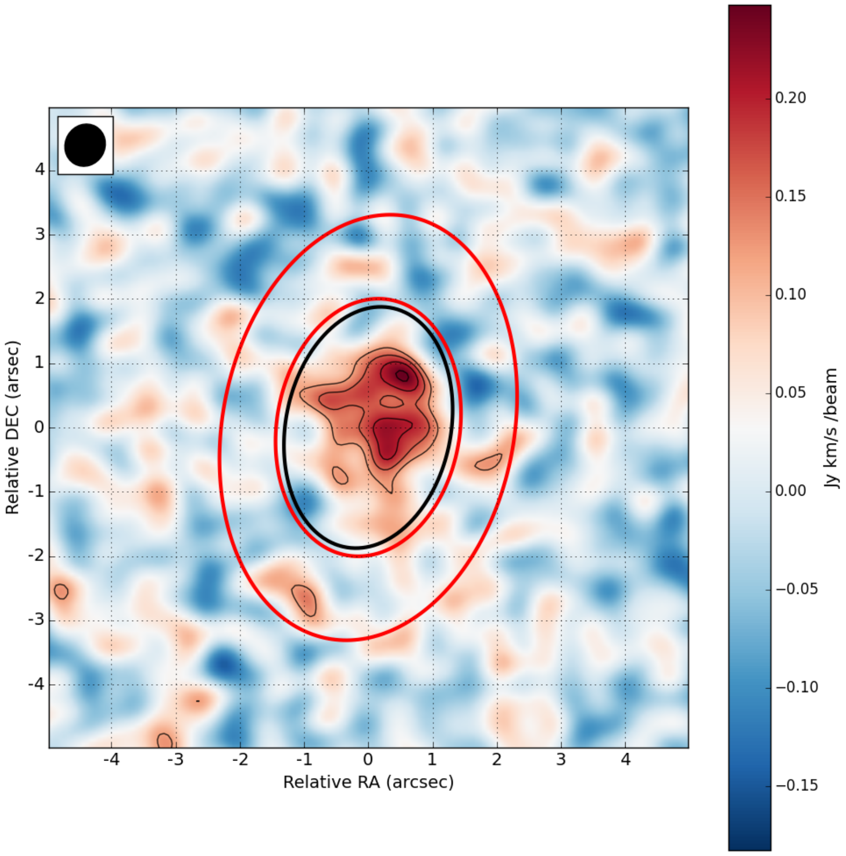

Figure 3.3: ^{13}CO emission is shown in the colour map and contoured at levels of (3,4,5,6)$\times\sigma_{13}$, with σ_{13}=0.040 Jy km/s /beam. The red ellipses show the position of the HST rings with parameters from Biller et al. (2015). The black ellipse shows the location of the mm ring detected in the 1.3 mm continuum image.

same temperature and opacity as before, a minimum dust mass of 0.13±0.02 $M_\oplus$ is calculated, firmly in the debris disc regime < 1 $M_\oplus$. An upper limit can be placed on the outermost scattered light ring at 388 au from the non-detection in the continuum. Making the same assumptions as before, the maximum mass of the outer ring at which it could still avoid detection in azimuthal averaging is ∼0.11±0.02 $M_\oplus$.

The position of the millimetre ring relative to the gas disc hints at potential formation mechanisms. A continuum ring at the edge of the gas disc is a morphology that can be compared with models of a primordial, but depleted gas disc.

In this case radiation pressure overcomes radial drift to push dust particles of <100 μm outwards to the edge of the gas disc (Takeuchi and Artymowicz, 2001). The ring emission detected is likely to come from larger grain sizes; millimetre continuum is emitted most efficiently by a narrow range between 1mm and 1cm (Takeuchi and Lin, 2005). If blow-out from radiation pressure formed the ring, the small grains collecting up at the edge of the gas disc would have to collide and grow into mm-sized grains. This seems unlikely; some small grains will acquire an eccentricity from this process, resulting in collisions that would occur at higher velocity leading to fragmentation rather than grain growth (Takeuchi and Artymowicz, 2001, see Figure 7). Given these results, a more detailed application of this model to HD 141569 is required, but the level of necessary grain growth seems extremely difficult to achieve. An alternative scenario might be the sculpting of grains into a ring as a result of an unseen planet or perhaps a flyby. Two M dwarfs in a binary system are located less than $9\overset{''}{.}0$ away from HD 141569 and previous studies of the disc considering a flyby have been able to reproduce global disc features such as the wide gap in the dust and spiral structures (Ardila et al., 2005; Augereau and Papaloizou, 2004; Reche et al., 2009). The caveat on this explanation is that the statistical likelihood of such a flyby is still low and the relationship, both present and past, between HD 141569 and the binary is not completely understood (Reche et al., 2009).

3.3.2 Gas emission

The ^{13}CO emission is strongly asymmetrical (Figure 3.3). The emission peak is measured at $6\sigma_{13}$ off centre from the stellar position, located at a deprojected separation of $1\overset{''}{.}1$ (120±10 au) at a position angle of -33°. Whilst at the same separation towards the south-east direction, emission is measured $< 2\sigma_{13}$. The emission detected from ^{13}CO is roughly co-spatial with the scattered light emission of the eccentric dust ring found at a separation of 89 au (Perrot et al., 2016, their Figure B3). Intriguingly, the ring is brighter in scattered light at the opposite side of the disc. ^{13}CO is detected over a considerably larger radial range than the inner edge of the gas disc at 11 au seen in CO rovibrational emission (Goto et al., 2006), than the inner edge of the dust disc of 30 au derived from the

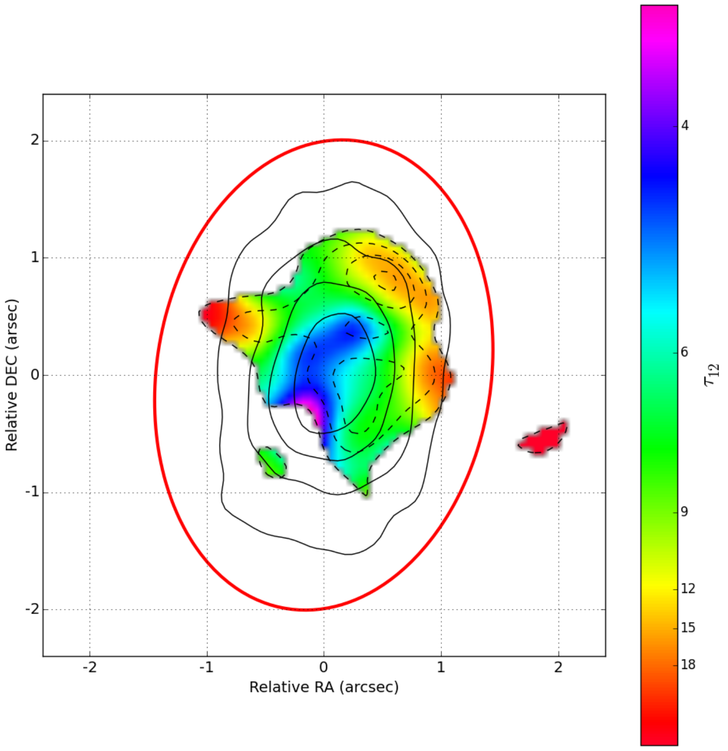

Figure 3.4: Map of the optical depth of ^{12}CO, the colour map is plotted for regions of the disc where $^{13}\mathrm{CO} > 3\sigma_{13}$ is detected. Overlaid in solid black contours of $(10,20,30,40)\times\sigma_{12}$ ($\sigma_{12} = 0.064$ Jy km/s /beam) is the ^{12}CO integrated intensity map convolved with the larger beam and dashed black contours show ^{13}CO as in Figure 3.3.

SED (Marsh et al., 2002), and than the asymmetry seen in ^{12}CO channel maps (White et al., 2016).

The radially brightest ^{13}CO emission is within the same range of stellocentric distances in which the scattered light rings were found, at 45, 61 and 89 au (Perrot et al., 2016), and co-spatial with the HST detection of scattered light between $0\farcs4$ and $1\farcs0$ (Konishi et al., 2016). Through azimuthal averaging (Figure 3.2) the largest radial distance that ^{13}CO is detected to is 220±10 au. This is the same radial separation from the star at which a ring of continuum emission is detected in this data. The first scattered light ring was reported to be at 234 au from the star when using the most recent GAIA distance for HD141569 (Biller et al., 2015).

Such an asymmetry in molecular gas has been seen in the debris disc Beta Pic (Dent et al., 2014), which may have resulted from giant collisions (for example Jackson et al., 2014), but which is more likely to be due to the collisional destruction of planetesimals trapped in resonance with a planet (Matrà et al., 2018; Wyatt, 2003). This scenario would make the gas secondary and so may be different to HD 141569 if the gas in the latter is primordial; the large radial extent of the gas is more typical of a primordial origin, but the nature of the gas in the disc is yet to be confirmed. Kral et al. (2017b) show that a secondary gas model is successful in reproducing the observed gas in the majority of gas bearing debris disc. In fact of their sample, only HD 21997, HD 131835 and HD 138813 appear to be true hybrid discs.

Younger, protoplanetary, discs can also exhibit strong azimuthal asymmetry that is typically strongest in the dust emission, for example, Oph IRS 48, MWC 758 (Boehler et al., 2017; van der Marel et al., 2013). 'Lop-sided' discs form as a result of dust traps that depend upon the surface density and turbulence of the disc (Birnstiel et al., 2013; Pinilla et al., 2012b), making it an unlikely mechanism in the less massive hybrid and debris discs.

To determine the optical depth of ^{12}CO, the spatial distribution of $\tau_{^{12}\mathrm{CO}}$ is calculated by using the ^{12}CO and ^{13}CO images. The more energetic transition ^{12}CO (3-2) emission is converted into the minimum expected ^{12}CO (2-1) emission using a ^{12}CO(2-1)/^{12}CO(3-2) ratio (1.08) obtained from the RADEX online tool for the disc temperature of 50K (van der Tak et al., 2007)[1]. Using lower temperatures does not change this ratio by more than a factor of two and ensures a minimum amount of CO(2-1), therefore calculating the minimum optical depth. The ^{12}CO and ^{13}CO images are convolved with the same synthesised beam of the ^{13}CO image in order to ensure the images have the same effective smoothing. Under the assumption that both lines have the same excitation temperature, the ratio of ^{12}CO(2-1) and ^{13}CO(2-1) emission is then used to compute the optical depths of both lines, following the method used in, e.g. Schwarz et al. (2016).

---

[1] Available at home.strw.leidenuniv.nl/moldata/radex.html

The ratio of optical depths is taken to follow the ISM abundance of 77. The obtained map (Figure 3.4) shows that $\tau_{^{12}\mathrm{CO}}$ ranges from 3 to 45. $\tau_{^{13}\mathrm{CO}}$ is therefore in the range from 0.04 to 0.58.

Figure 3.4 confirms ^{12}CO (2-1), and therefore also (3-2), to be optically thick throughout the disc, while the ^{13}CO is not. In central regions $\tau_{^{12}\mathrm{CO}} \sim 2$ where ^{12}CO is strongest, reaching as high as 25 in outer regions where ^{13}CO is detected strongly. Once ^{12}CO becomes optically thick, it ceases to trace mass in the midplane because emission is coming from upper layers of the disc at greater scale heights.

This may also explain why the asymmetry of the disc is so prominent in the ^{13}CO map, but not in the ^{12}CO; the optically thick ^{12}CO emission is dominated by the temperature of the emitting layer, which increases closer to the star, so a combination of temperature and emitting surface area are responsible for the brightness of emission, rather than the fractional changes in gas density. However the optically thin ^{13}CO traces density more faithfully and provides a better indicator of the spatial distribution of gas in the disc, highlighting any asymmetries which may be hidden by temperature and surface area effects in ^{12}CO. The radial profiles shown in Figure 3.2 illustrate this effect. The azimuthally averaged flux drops sharply after the peak at around ~30 au for ^{12}CO, but the ^{13}CO emission is still >75% of the peak value until after 100 au. This is clearer in the NW/SE slices in Figure 3.2 taken in the direction of the ^{13}CO peak. In green, the ^{12}CO peaks much closer to the star where temperature effects are more prominent (~ 30 au in the NW slice), whilst the ^{13}CO peaks much further out in the disc at a deprojected distance of ~ 120 au. The slices also illustrate the magnitude of the asymmetry in the midplane gas, with a very strong ^{13}CO peak towards the north-west that is considerably stronger than the average flux at that separation. This demonstrates the importance of using CO isotopologues, as done here, to investigate the disc midplane, and the gas density distribution within it.

Having shown that the ^{13}CO emission is optically thin, a lower limit on the mass of the gas disc is derived using

$$M_{gas} = \frac{4\pi}{h\nu_{21}} \frac{F_{21} m d^2}{A_{21} x_2} \left[\frac{\mathrm{H}_2}{^{12}\mathrm{CO}}\right] \left[\frac{^{12}\mathrm{CO}}{^{13}\mathrm{CO}}\right], \tag{3.1}$$

where F_{21} is the integrated line flux from the J=2–1 transition of ^{13}CO, m is the mass of the CO molecule, A_{21} the Einstein coefficient for the transition, ν_{21} is the frequency at which the transition occurs and x_2 is the fractional population of the upper level. The midplane temperature is taken to be 20K and ISM abundances are assumed, $^{12}\mathrm{CO}/^{13}\mathrm{CO} = 77$ and $^{12}\mathrm{CO}/\mathrm{H}_2$=$10^{-4}$ (Wilson and Rood, 1994), to give a total gas disc minimum mass of $(6.0\pm0.9) \times 10^{-4}\mathrm{M}_\odot$. Uncertainties are due to the ALMA 15% flux calibration uncertainty. Like the dust mass, this value depends on disc temperature, for example adopting T=50K would give $(9.0\pm1.0) \times 10^{-4}\mathrm{M}_\odot$. Sequestration of CO into icy bodies or conversion into more complex molecules can reduce gas-phase CO in the disc, decreasing the gas mass calculated by this method. The minimum mass is two orders of magnitude larger than that calculated using the same method but with ^{12}CO as the mass tracer, $\sim 4.5 \times 10^{-6}$ $\mathrm{M}_\odot$ (White et al., 2016). SMA observations of CO(1-0) emission give a gas disc mass $1.05\times10^{-4}\mathrm{M}_\odot$, comparable to the mass derived here, however MCMC modelling of the data gave a slightly lower value of $3.8\times10^{-5}\mathrm{M}_\odot$ (Flaherty et al., 2016). Thi et al. (2014) also find a similar order of magnitude by fitting Herschel gas line observations in the far-IR to simultaneous radiative transfer and chemical modelling, giving a range of 2.5-5 $\times10^{-4}\mathrm{M}_\odot$. Each of these methods assume $^{12}\mathrm{CO}/\mathrm{H}_2 = 10^{-4}$.

^{12}CO therefore appears to be underestimating disc mass, agreeing with the confirmation of the tracer's optical thickness. A similar scenario was found in 30 Myr old hybrid disc HD 21997; Kospal et al. (2013) calculate a CO gas mass in the disc from the optically thin C^{18}O line that was two orders of magnitude larger than that previously calculated assuming optically thin ^{12}CO emission (Moór et al., 2011).

The band 6 ALMA observations did not detect C^{18}O, but from the rms noise in the integrated emission map an upper limit on the C^{18}O gas mass can be derived and a corresponding estimate of the disc gas mass calculated. Rms in the C^{18}O image with natural weighting is 25 mJy/beam, yielding a total gas mass estimate of 1.4×10^{-4} $\mathrm{M}_\odot$ assuming T=20 K, ISM abundances and isotopic ratios. This value is higher than that traced by the optically thick ^{12}CO, but much lower than the estimate based on the ^{13}CO. In fact, the flux ratio between ^{13}CO and the upper limit on C^{18}O flux is 31, significantly higher than the typical ISM abundance of eight (Wilson and Rood, 1994). This implies that $C^{18}O$ is under abundant by at least a factor of 3.8. An explanation for this may be the isotope-selective photo-dissociation, known to deplete the less abundant isotopologues such as $C^{18}O$ in discs (Miotello et al., 2016; Visser et al., 2009). The higher column density of the more abundant isotopologue, in this case ^{13}CO, means that it can self-shield from photodissociation more effectively. It is important to note that isotope-selective photodissociation cannot be the cause of the differences between the gas mass estimates based on ^{12}CO and ^{13}CO, as it would have the opposite effect: the mass based on ^{12}CO should be higher in such case. Only the comparisons between the optically thin isotopologue lines allows us to assess the selective photodissociation effects, again stressing the importance of observing these species.

3.3.3 Nature of the disc

Known hybrid discs generally have disc gas masses derived from CO observations of order Earth mass (e.g. 49 Ceti 6.6×10^{-6} $M_{\odot}$, HD 131835 1.3×10^{-5} $M_{\odot}$, Hughes et al., 2008; Moór et al., 2015).

HD 141569 has a particularly massive gas disc in comparison (see e.g. Figure 6 of Péricaud et al., 2017). All previous estimates were based on optically thick tracers, which explains why in this work the gas mass derived is two orders of magnitude greater than the previous estimate. A more direct comparison can be made with hybrid disc HD 21997, where the disc mass derived from ALMA observations of optically thin $C^{18}O$ giving 0.8-1.8×10^{-4} $M_{\odot}$ (Kospal et al., 2013) a factor of a few less than HD 141569. Hybrid discs in general may be hosting more gas than is traced by CO and its isotopologues, not only due to optical depth but also if CO has been depleted with respect to H_2. ISM abundance of CO, $^{12}CO/H_2=10^{-4}$, is assumed here to convert CO masses to total disc masses in order for ease of comparison disc masses. For individual discs this ratio may be less appropriate than others, particularly in a secondary gas scenario where composition is inherited from the species that were locked into solid bodies during the protoplanetary disc stage, rather than from ISM gas and dust.

The minimum dust mass 1.2±0.2 $M_\oplus$ corresponding to the unresolved component is greater than the dust masses of HD 131835, (0.47 $M_\oplus$ Moór et al., 2015), HD 21997 (0.09 $M_\oplus$ Moor et al., 2013) and 49 Ceti (0.2 $M_\oplus$ Holland et al., 2017).

The millimetre ring at 220 au has a minimum dust mass of 0.13±0.02 $M_\oplus$. This mass and the scattered light ring seen at a slightly larger distance are both comparable to typical debris discs. Debris systems show evidence of rings containing millimetre sized grains at large radii outside an inner debris component like HD 181327 (Marino et al., 2016) and HD 107146 (Marino et al., 2018; Ricci et al., 2015), perhaps the nesting of structure within a larger ring is a more common component than is currently understood; high resolution observations hold the key to confirming this.

3.3.4 Disc evolution

Before ALMA, the distinction between protoplanetary and debris discs was clear-cut: protoplanetary discs are continuous and gas-rich while debris discs are narrow belts with negligible gas content. It is now becoming evident that gaps and rings are ubiquitous features throughout the protoplanetary disc stage at <10Myr (Dullemond et al., 2018; Lodato et al., 2019) and that a number of young debris discs (<50Myr) contain detectable levels of gas (Kral et al., 2017b; Moór et al., 2017).

Figure 3.1 provides initial evidence for HD141569 exhibiting an intermediary stage in disc evolution, plotting the SEDs for three A type stars. The SED of the gas-rich protoplanetary disc around HD 163296 shows strong emission throughout all wavelengths due to its large, bright disc. In stark contrast to the typical protoplanetary disc, the debris disc around 49 Ceti has a more blackbody shaped SED corresponding to one or two belts (characteristic of debris discs Kennedy and Wyatt, 2014). HD141569 contains significantly less material than HD163296, and so has either experienced significant disc depletion in both gas and dust, or started with a significantly less massive protostellar nebula than HD163296. Although the distribution of dust in the HD141569 disc is broadly similar to that of debris disc 49 Ceti (in that it is dominated by two discrete belts/regions), the flux from the HD141569 disc is clearly stronger and requires the inner component to fit the relatively strong signal at ≈10μm. This likely means that 49 Ceti's inner regions have been more successfully cleared of dust, or that grains have grown to larger sizes. At around 10 μm the HD 141569 model diverges from the observed photometry. Grains in the model are assumed to be astrosilicates with a range of grain sizes, a more sophisticated description of the composition of dust grains in different regions of the disc is likely to explain this discrepancy. In order to constrain such parameters, further optically thin observations at new wavelengths are required.

From observations in the last few years a much clearer picture of the HD141569 system has been gained, confirming it to be the only pre-main sequence hybrid disc offering a glimpse into the earliest stages of disc dissipation, and acting as a useful milestone in this transitionary period for the circumstellar material. Figure 3.5 illustrates an up to date description of gas and dust distribution in the disc, including the position of detected scattered light rings.

The gas-poor outer regions shown in Figure 3.5 resemble the belts of a debris disc. However interior to the 220 au belt, the inner regions of the disc host tightly spaced rings and ALMA observations have unveiled significant amounts of ^{12}CO and ^{13}CO emission. Currie et al. (2016) describe the system as a 'matryoshka' disc and the picture presented in Figure 3.5 seems to agree because contained within the wide ('debris'?) belts there is a small gas disc with tight dust rings in the inner regions (Perrot et al., 2016) ('protoplanetary'?).

In Figure 3.6 ALMA images and azimuthally averaged profiles of the gas and dust in HD 141569 are compared with two other A-type systems that display morphologies suggestive of potential pre-cursors, (e.g. HD 163296, Isella et al., 2018), and descendants (e.g. 49 Ceti, Hughes et al., 2017) to HD 141569. Concentric tight rings are observed within 100 au for both HD 141569 and HD 163296, but are absent in both images and SED modelling of 49 Ceti. The radial locations and mutual spacing of rings inward of 100 au is very similar, perhaps signalling that the brighter rings of HD 163295 are likely to dim over time as solid material from the disc is depleted or as grains grow to larger sizes. Future high resolution observations of HD141569 are required to study this hypothesis further through a detailed characterisation of the inner rings. Detection of mm counterparts to the scattered light rings inside of 100 au would also put a useful constraint on the

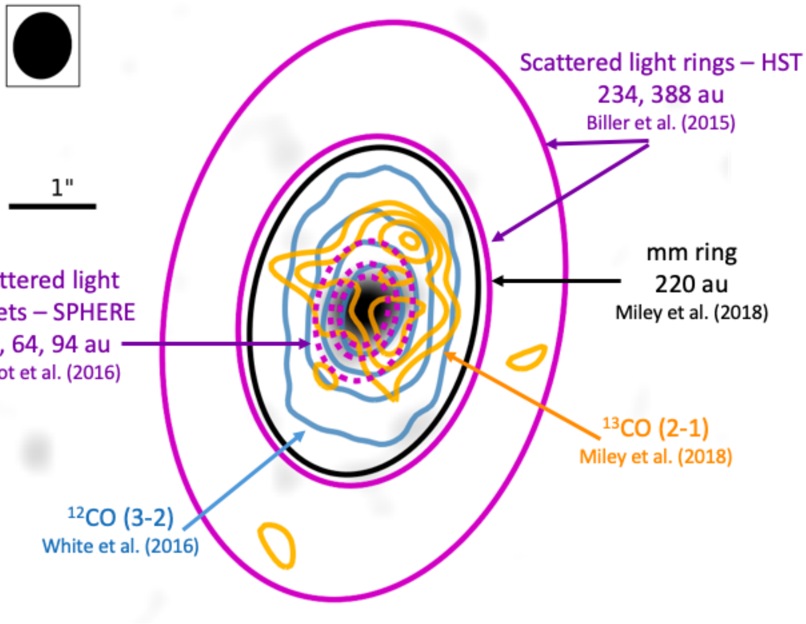

Figure 3.5: Diagram showing observed structure in HD 141569. Greyscale shows the 1.3mm continuum map. Overlaid is the previous detection of ^{13}CO(2-1), with contours at (3,4,5,6)σ_{13}, ^{13}CO(3-2) with contours at (10,20,30,40)σ_{12} and the positions of rings identified by ALMA and in scattered light (Biller et al., 2015; Perrot et al., 2016).

amount of large grains that remain in the disc, confirming whether or not these rings are indeed rings, or simply surface waves on a tenuous inner disc.

49 Ceti shows a radial gas peak inside of its debris-like dust continuum ring and is detected as far as 220±10 au. This draws a striking resemblance to configuration in Figure 3.5, where all gas is contained within the dust ring, and an off-centre ^{13}CO peak detected at a separation of 120 au. The normalised radial flux profiles of HD141569 may come to resemble those of 49 Ceti if the inner regions of HD141569 were to be depleted through the radial drift of solids, photoevaporation of remaining gas or late planet formation

This speculative evolutionary sequence is made on the basis of just three systems with images of varying spatial resolution; nevertheless similarities between the systems are readily apparent and suggestive of physical mechanisms that link

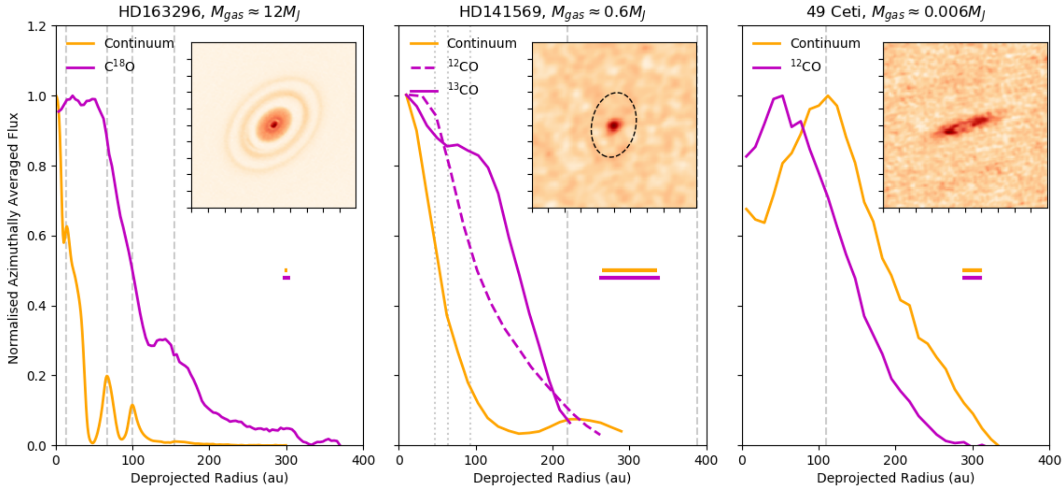

Figure 3.6: Azimuthally averaged profiles of the dust and the most optically thin CO isotopologue observed by ALMA around three A type stars. Dashed grey lines denote the positions of rings detected in the system. For HD 141569 the profile of ALMA detected ^{12}CO is also plotted. Inset are images of the dust continuum at 1.3mm for HD 141569 and 870μm for the other discs . The dashed line in the HD 141569 image denotes position of the mm ring. Horizontal lines represent the FWHM of the synthesising beam for each profile. Total gas mass estimates are taken form the literature and assume ISM abundances.

the stages. Future high sensitivity and high resolution observations of evolved, gas-bearing debris discs are the key to determining how and when multiple rings as seen in a protoplanetary disc are concentrated into debris-like belts, and how the massive gas discs are dissipated.

Full characterisation of the inner regions of HD141569 is an important step in achieving this goal. The inner regions within 100 au are yet to be probed with precision at mm wavelength. The presence (or lack of) mid-plane counterparts to the concentric rings observed in scattered light (Perrot et al., 2016) and confirmation of the spatial distribution of gas will give direct clues as to what mechanisms are driving the disc dispersal. The likely candidates are perturbation by embedded exoplanets, photoevaporation or accretion onto the central star.

3.4 Conclusions

An asymmetric distribution of midplane gas is detected in the young hybrid disc HD 141569, traced by optically thin ^{13}CO emission. In addition, a faint mm ring of emission at 220±10 au is detected through azimuthal averaging of the continuum image, providing a midplane counterpart to the ring detected in scattered light, where these small dust grains originate. The minimum dust mass in the ring is derived to be 0.13 ± 0.02 $M_\oplus$, around 10% of the total flux from the system. The bulk of the millimetre emission, which is known to be variable, coincides with the location of the star and is unresolved placing an upper limit on its radial extension of 72 au. This emission traces a minimum of 1.2 ± 0.2 $M_\oplus$ of dust, but may have a free-free contribution of $\leq$3%. From these observations an upper limit on mass of the outermost ring can be placed at 0.11 ± 0.02 $M_\oplus$.

The gas disc is interior to this ring at 220 au. From the integrated ^{13}CO flux gas mass is derived to be $(6.0\pm0.9)\times10^{-4}M_\odot$; a mass approximately two orders of magnitude greater than that derived using ^{12}CO. The reason for this is the high optical depth of ^{12}CO, rendering any gas mass value derived from its emission a large underestimate. Non-detection of C^{18}O shows that this isotopologue is about four times less abundant than expected, based on the standard isotopic ratio between ^{16}O and ^{18}O. Isotope-selective photodissociation is proposed as the culprit.

New high sensitivity and high resolution images of HD141569 and of other hybrid discs are the key to linking gas-rich, ringed protoplanetary discs with the gas-poor, wide belts in debris discs through an evolutionary path.

Chapter 4

The impact of pre-main sequence stellar evolution on midplane snowline locations and C/O in planet forming discs

4.1 Context

The host star has a major influence on both the evolution of protoplanetary discs and on the properties of the planetary systems that they go on to form. Giant planets occur more frequently around more massive stars, specifically radial velocity surveys find a peak in giant planet occurrence rate for a host stellar mass of 1.9 $M_\odot$ (Johnson et al., 2010; Reffert et al., 2014). ALMA surveys of star forming regions show that the mass of solids in protoplanetary discs also scales with stellar mass (Mulders, 2018; Pascucci et al., 2016). This trend complies with theoretical predictions; the core accretion scenario for planet formation predicts more giant planets to be formed around higher mass stars (Ida and Lin, 2005; Kennedy and Kenyon, 2008a). Furthermore planet population synthesis models by Alibert et al. (2011) show that scaling disc mass with the mass of the stellar host can explain the lack of high mass planets around 0.5 $M_\odot$ hosts and a lack of short separation planets around stars with mass greater than 1.5 $M_\odot$.

The central star determines the temperature structure within the disc it hosts. More massive, more luminous stars result in a warmer disc, which is expected to result in changes in the disc composition. Solids in the disc generally hold a greater relative abundance of oxygen compared to the gas which is instead relatively carbon-rich. Based on observations of gas and dust in discs, Öberg et al. (2011) take the ratio of carbon to oxygen, C/O, in both the gas and solid phase to be dictated by the location of snowlines for key molecular carriers of oxygen and carbon. For example in their model the gas is most carbon-rich between the CO_2 and CO snowlines, because here the gas phase is dominated by CO, leading to C/O$\sim$1.

An exoplanet's overall composition is inherited from the local disc at the time of formation when material is accreted rapidly. Measurements of C/O and of metallicity (e.g. C/H, O/H) in exoplanets can be used to connect the composition of the planet with the location of its formation, and the relative amounts of oxygen-rich solids and carbon-rich gas this would have required. For example Brewer et al. (2017) investigate C/O in hot Jupiters and find that super-stellar C/O and sub-stellar O/H ratios suggest that some hot Jupiters form beyond the

H_2O snowline and migrate inward. The enrichment of the atmospheres of giant exoplanets is aided by radial drift in the disc, which acts to carry solids to shorter radial separations from the star, doing so at a rate faster than depletion due to chemical processes (Booth et al., 2017; Booth and Ilee, 2019; Krijt et al., 2018). The inward drift of pebbles is also an effective mechanism for transporting volatiles that are frozen onto grains towards the inner regions of the disc. This causes a plume of volatile gas to build up at snowline locations, which viscously spreads to enhance gas phase abundances of dominant molecular species within their own snowlines (Booth and Ilee, 2019; Stammler et al., 2017). Exoplanet atmospheric C/O may differ from the exoplanets overall composition due to chemical effects within the atmosphere that are not taken into account by this model (for a detailed description of factors affecting atmospheric chemistry see review by Madhusudhan et al., 2016).

The formation of planets via gravitational instability on the other hand involves the large scale collapse of a mixture of gas and dust. The compositions of objects forming in this manner will likely reflect the stellar value (Madhusudhan et al., 2014). However, thermal history and internal sedimentation in these fragments can form objects with sub-stellar C/O (Ilee et al., 2017).

The temperature in the disc does not necessarily remain constant however, meaning the snowline locations are not fixed to a particular radial distance from the star. Low mass stars decrease in luminosity as they evolve towards the main sequence meaning there is a decreased irradiating flux upon the disc. Intermediate mass stars on the other hand, increase in effective temperature as they evolve towards the main sequence, but do not experience as large a decrease in luminosity as low mass stars, in fact after a few Myr their luminosity begins to increase again. Due to this contrasting evolution of low-mass stars compared to intermediate mass stars, Panić and Min (2017) infer different physical, and therefore chemical, histories in the discs around low- and intermediate-mass stars. So without the need to invoke any internal disc evolution, the temperature structure of the disc can be expected to evolve alongside the luminosity of the host star, introducing a temporal dependence for composition, in addition to the radial dependence from Öberg et al. (2011). Every star must undergo this evolution, therefore every disc must experience the repercussions to some extent.

Furthermore the temperature structure of a disc also influences the mechanisms by which planet formation takes place. Disc temperature is important for the transport of solids in the disc because the speed of radial drift depends on disc temperature, $\mathrm{v_{drift}} \propto \left(\frac{\mathrm{H}}{\mathrm{r}}\right)^2 \propto \mathrm{T}$. It is also important for the composition of solids, as the snowlines dictate the presence of ices on the dust. In inner regions grain size is limited by fragmentation (Birnstiel et al., 2012). The fragmentation velocity is higher for grains possessing an icy mantle in comparison to ice-free grains such as those interior to snowlines from which volatiles have been released into the gas phase. A transition from mainly ice-free to icy grains results in a higher fragmentation velocity and therefore a sharp increase in the grain sizes outside of the $\mathrm{H_2O}$ snowline. Pebble accretion is a mechanism by which planetesimals can grow beyond ∼100s of km in size into cores of ∼10s $\mathrm{M_\oplus}$ (Johansen and Lacerda, 2010; Lambrechts and Johansen, 2012; Ormel and Klahr, 2010). In combination with the streaming instability (Johansen et al., 2007; Youdin and Goodman, 2005), this offers a solution to the metre-sized barrier. It relies on the presence of dust particles of size ≥cm that are accreted as a result of passing through the Hill sphere of large planetesimals. If stellar evolution determines the midplane temperature profile, then there is potential to determine temporal constraints on when and where pebble accretion can operate in a disc, by virtue of whether or not a reservoir of pebble sized dust particles can exist or is limited by fragmentation.

In this chapter the impact that stellar evolution has on midplane conditions is explored in terms of the physical and chemical structure in the midplane of protoplanetary discs. Self consistent temperature profiles calculated using stellar parameters from throughout the pre-main sequence evolution of stars across a range of stellar mass (spectral type) are used. The relative abundance of key C and O carriers are calculated by applying the Öberg et al. (2011) chemistry model and considering the effects of radial drift, viscous evolution, diffusion, and the growth and fragmentation of dust. Gas mass loss from the disc has a significant effect on temperature, resulting in a less flared, cooler disc with a greater degree of dust settling (Panić and Min, 2017). In order to isolate only the effects of stellar evolution, the mass of the disc does not evolve, instead snapshots of a range of disc conditions are provided in which disc mass is high enough to allow giant planet formation. This approach is applied in a case study of the system of HR8799, a F0 type star (Gray et al., 2003) with four directly imaged giant planets between which there are substantial variations in the atmospheric C/O retrieved from their observed spectra (Lavie et al., 2017).

4.2 Methods

4.2.1 Physical Modelling

Three modelling codes are combined to study the impact of stellar evolution on protoplanetary disc midplanes. First, a grid of stellar parameters are calculated using the MESA code (Paxton et al., 2011, 2013) by evolving stars of mass 0.5, 1.0, 2.0, 3.0 $\mathrm{M}_\odot$ for 10 Myrs. These masses were chosen to span the range over which there is a peak in planet occurrence rate measured from radial velocities (Reffert et al., 2014). Figure 4.1 plots this evolution on a Hertzsprung-Russel diagram, alongside MIST[1] isochrones (Dotter, 2016).

The computed stellar parameters are used as input to radiative transfer models. The Monte Carlo radiative transfer code MCMax (Min et al., 2009) is used to iteratively solve for self-consistent temperature and vertical structure throughout the disc. The disc surface density is described by power law with an exponential tail (Andrews et al., 2011) consistent with the self-similar solution for a viscously evolving disc with a viscosity scaling as $\nu \propto R^{\gamma}$ (Hartmann et al., 1998; Lynden-Bell and Pringle, 1974):

$$\Sigma_{\mathrm{gas}} = \Sigma_{\mathrm{c}} \left(\frac{R}{R_{\mathrm{c}}}\right)^{-\gamma} \exp\left[-\left(\frac{\mathrm{R}}{\mathrm{R_c}}\right)^{2-\gamma}\right] , \tag{4.1}$$

where $\mathrm{R_c}$ is the critical radius (outer disc radius) and Σ_{c} the surface density at the critical radius. A disc mass of 0.1 $\mathrm{M}_\odot$ is adopted to ensure the discs that are modelled would be sufficiently massive to form multiple giant planets. This relatively large disc mass is adopted partly to reflect the higher mass expected in the early embedded stages of a disc when the planet formation process begins, and because observational disc masses are expected to be significantly underestimated

---

[1] http://waps.cfa.harvard.edu/MIST/

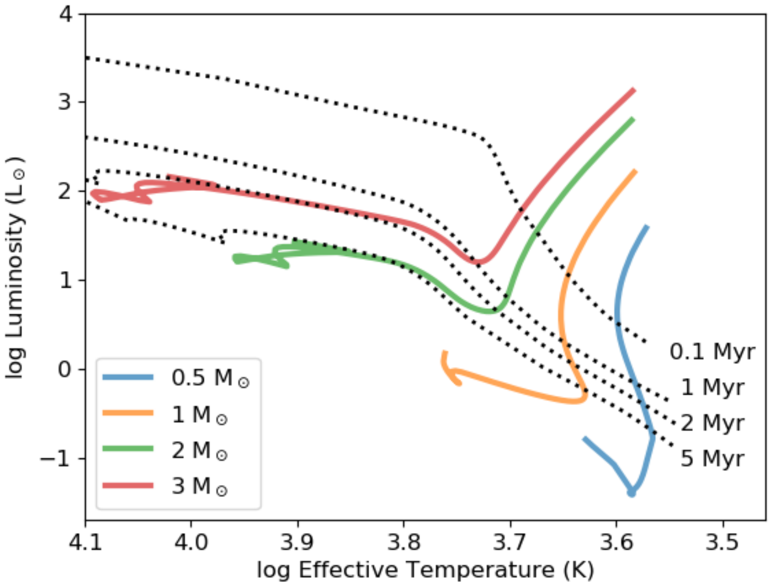

Figure 4.1: Results of the stellar evolution models, following four stellar masses for 10 Myr. Dotted lines mark the isochrones for selected timesteps in the stellar evolution as labelled.

(Booth et al., 2019; Miotello et al., 2018). The dust in the disc model is comprised of astrosilicate grains with an MRN size distribution, $dn/da \propto a^{-3.5}$ (Mathis et al., 1977). Parameters adopted for the MCMax models are summarised in Table 4.1.

Disc evolution is modelled as in Booth et al. (2017) in order to calculate transport within the disc by taking into account a parametric prescription for viscous evolution and diffusion, in conjunction with modelling of the radial drift in solids as a result of the growth and fragmentation of the dust grains following the model of Birnstiel et al. (2012). The midplane dust and gas are allowed to evolve for 10 Myr, the temperature profile is updated throughout this process with the results of the radiative transfer modelling. Radiative transfer models were generated at steps of 0.01, 0.1, 1.0, 2.0, 3.0, 5.0 and 10.0 Myr in stellar evolution, in between these points the temperature profiles for adjacent timesteps are interpolated between, assuming a linear evolution with time. As a result of inward transport of dust and gas, some material is accreted onto the central star.

Table 4.1: Disc parameters adopted in radiative transfer modelling

Parameter		Value(s)
R_{in}	Inner radius	0.1 au
γ	Initial $\Sigma(R)$ slope	1.0
R_c	Critical radius	200 au
a	Grain sizes	0.01 μm - 10 cm
α	Turbulent viscosity	10^{-3}
g/d	Gas-to-dust mass ratio	100
M_d	Dust mass	10^{-3} $M_\odot$

Whilst the viscous evolution of the gas, and the dust evolution in the disc is calculated self-consistently for a given temperature profile, the evolution of disc mass was not included in the radiative transfer calculations. This means that at some points there is a mismatch between the disc mass used to calculate temperature and the remaining mass in the disc following accretion onto the star. The extent to which Σ(R) is altered by drift and viscous evolution depends primarily upon the size of the disc (determined by R_c in the radiative transfer modelling) and on the turbulent viscosity α, and affects inner regions of the disc the most. For R_c=200 au and $\alpha = 10^{-3}$, Σ(R) is not depleted in any model by more than 30% up to 5 Myr, by 10 Myr Σ(<50 au) been depleted by $\sim$ 50%. The removal of gas mass will decrease temperature in the disc as demonstrated in Panić and Min (2017), so these temperature profiles can be taken as warm upper limits.

The dust evolution calculated over a 10 Myr timescale will have implications for the photo-surface of the disc that collects starlight and heats the disc. The most important factors in this regard however are the minimum grain size (as it is the small grains that reside in the upper layers of the disc that absorb the starlight) and the gas mass (Panić and Min, 2017). The choice of a small a_{min} and large gas mass will maximise the heating in the disc models, and so the temperatures calculated offer an upper limit in which heating is the most effective.

The justification for calculating the physical evolution of the midplane separately from the radiative transfer modelling is that a grid of models can be created that represent massive discs such as TW Hydra (Bergin et al., 2013) and HD163296 (Booth et al., 2019), i.e. massive protoplanetary discs with ages beyond that of typical near-IR disc lifetimes.

4.2.2 Chemical model

The simple chemical model of Öberg et al. (2011) is adopted here, as previously implemented as case 2 in Booth et al. (2017); Madhusudhan et al. (2014, 2017) and described in Chapter 1. In summary this model considers the main O- and C- carrying species H_2O, CO, CO_2, silicates, refractory O components, organics and carbon grains. Solar initial abundances are adopted (Asplund et al., 2009), following Konopacky et al. (2013). The abundance of the major C- and O- carriers are then calculated using the model described in Chapter 1 and reproduced in Table 4.2, using the same binding energies as Piso et al. (2016),Booth et al. (2017). The radii of the different snowlines are set by the midplane temperature profiles as calculated by MCMax. Abundances in the gas and ice phase are then calculated for each of the tracers considered.

Different factors can shift snowlines slightly in the disc (Fayolle et al., 2016; Kennedy and Kenyon, 2008b; Lecar et al., 2006). The main purpose of this work however is to investigate global trends with varying stellar mass and age, so for simplicity the binding energies are fixed to the values given in Table 4.2 and the CO, CO_2 and H_2O snowline positions to the characteristic disc temperatures of 20, 47 and 135 K respectively, following Öberg et al. (2011).

As only the most prominent chemistry from these main carriers is of interest here, it is unnecessary to consider the full range of reaction processes present in more sophisticated chemical models of protoplanetary discs (see e.g. Walsh et al., 2014b).

4.3 Results

4.3.1 Midplane temperature

Figure 4.2 shows a selection of midplane temperature profiles resulting from the radiative transfer calculations. Each panel shows the midplane temperature pro-

Species	$T_{\rm bind}$ (K)	X/H
CO	834	$0.65 \times$ C/H
CO_2	2000	$0.15 \times$ C/H
H_2O	5800	O/H - ($3 \times \frac{\rm Si}{\rm H} + \frac{\rm CO}{\rm H} + 2 \times \frac{\rm CO_2}{\rm H}$)
Carbon grains	n/a	$0.2 \times$ C/H
Silicates	n/a	Si/H

Table 4.2: Binding energies, presented as temperatures, and volume mixing ratios of the key chemical species included in the chemical model. Binding energies are from Piso et al. (2016) and volume mixing ratios follow Öberg et al. (2011).

file in the disc that results from the stellar parameters at different timesteps, as labelled in the bottom left corner of each plot. In each panel the results of discs around stars with mass 0.5 - 3 $M_\odot$ are plotted.

In Figure 4.2 the temperature profiles for different M_* are relatively similar to each other in the top left panel for a stellar age of 0.1 Myr, but begin to diverge at later time steps. At 0.1 Myr, at 25 au the disc around the 3.0 $M_\odot$ star is ≈70% hotter than that around the 0.5 $M_\odot$ star. At 5 Myr, the 3.0 $M_\odot$ case is ≈440% hotter than the 0.5 $M_\odot$ one. This divergence of midplane temperatures follows from the differing evolutionary paths taken by the host stars. In Figure 4.1 the difference in luminosity between the 0.5 and 3 $M_\odot$ stars is also significantly larger at 5 Myr than it was at 0.1 Myr.

The effect of this dichotomy in evolution is shown clearly in Figure 4.3, where each panel contains models with the same stellar mass plotting temperature curves for different time steps. Whilst the discs around low-mass/solar-like stars in the top panels cool with age (see the black arrows in Figure 4.3), the discs around intermediate mass stars experience an increase in midplane temperature due to the increasing luminosity of the host star, meaning they are relatively warm at late times. For example, in the 3 $M_\odot$ case (bottom right panel Figure 4.3), at a separation of 25 au the disc is in fact 38 K warmer at 5 Myr than it was at 1 Myr.

These models quantitatively demonstrate that not only are the discs around intermediate mass stars warmer than around their low-mass counterparts, but

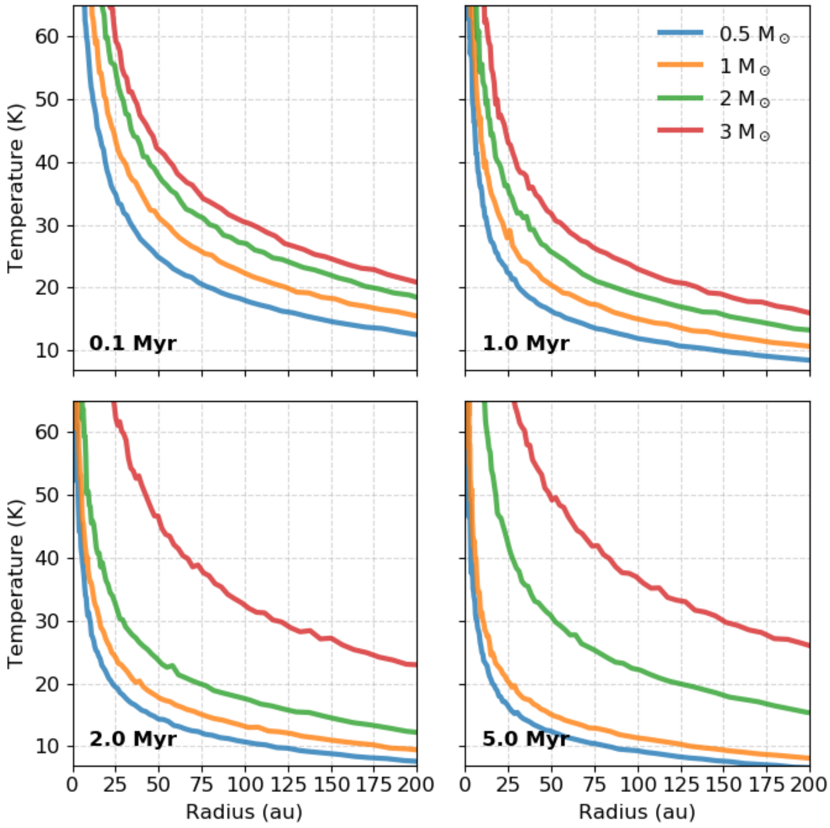

Figure 4.2: Snapshots of the midplane temperature as a function of radius around stars of 0.5, 1, 2 and 3 $M_\odot$ at different stellar ages. Each panel represents a different snapshot in time, each line represents a disc around a different star as labelled in the key.

that they also remain warmer for longer corresponding to the evolution of the host star's luminosity.

4.3.2 Snowline locations

A direct consequence of the variation in midplane temperature profile is variation in the location of snowlines within the disc models. Figure 4.4 shows the CO and CO_2 midplane snowline locations, assumed to be at T=20 K and T=47 K respectively, around different masses of star. Disc temperature at the snowline of a species can vary somewhat depending on the ices that exist on the grain.

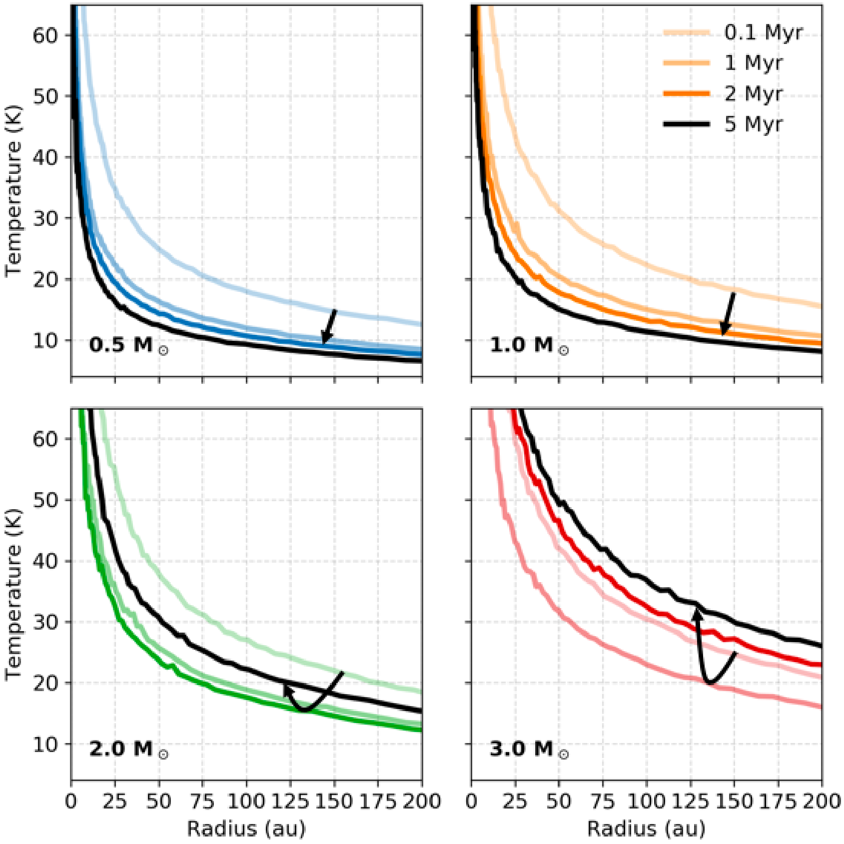

Figure 4.3: Midplane temperature as a function of radius at different times for different M_*. Each panel shows a model with a different central star (labelled in the bottom left corner) and each curve represents a different time step, with the lightest colour representing the earliest time. The arrow on each plot links the 4 curves in chronological order.

Laboratory experiments have shown CO desorption energies to vary by ≥50% depending on the water coverage and structure of the ice in which it is adsorbed (Fayolle et al., 2016). The range in binding energies corresponds to a range in snowline temperatures, for example for an assumed midplane density ($n_H = 10^{10}\mathrm{cm}^{-3}$) and CO abundance relative to $n_H(5 \times 10^{-5})$, Qi et al. (2019) point out that a desorption energy for CO adsorbed to compact H_2O ices (E_{des}=1300 K) corresponds to a CO snowline temperature of ∼ 32 K, whereas considering only pure ices (E_{des}=870 K) corresponds to a snowline temperature of ∼21 K. For this reason fixed values for T are adopted in order to compare global trends across stellar mass and age.

The discs around 0.5 and 1 $M_\odot$ stars are at their coolest at later times, and so the snowlines are at shorter separation from the host star. Figure 4.4 shows that at 2 Myr both discs have CO snowlines that are within 50 au. Conversely the discs around intermediate mass stars begin to warm up at later times, pushing the CO snowline further out into the disc. For example in Figure 4.4 the 3 $M_\odot$ star snowline is found at a distance of over 250 au from the host star after 2 Myr, meaning that CO at large orbital radii will remain in the gas phase for a large proportion of the disc lifetime.

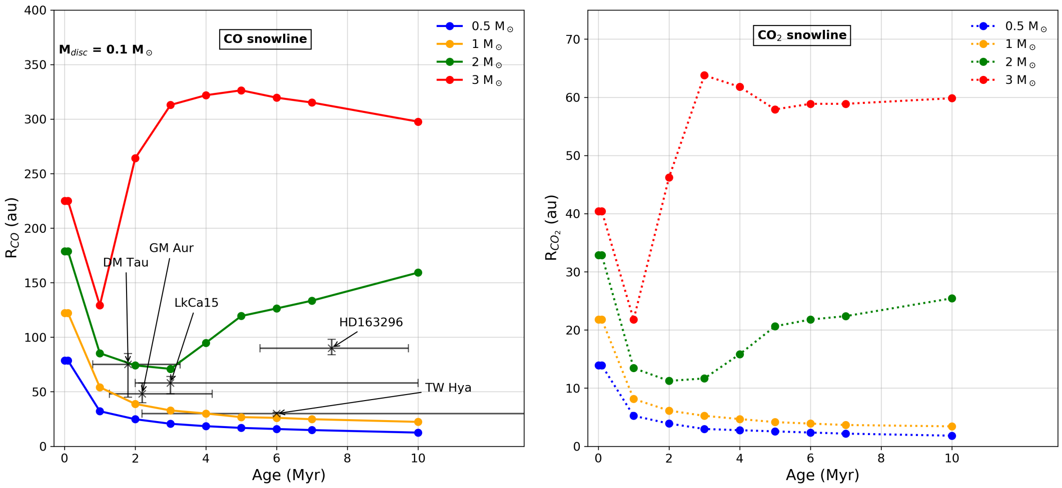

Figure 4.4: Position of the CO (T=20K, left panel) and CO_2 (T=47K, right panel) snowlines in the disc midplane around stars of different mass over a range of time steps. Each model has a total disc mass of 0.1 $M_\odot$. Crosses show the positions of N^2H^+ rings, tracing the CO snowline location of protoplanetary discs GM Aur, LkCa15, DM Tau, HD163296 and TW Hydra. The disc temperatures for each snowline are: GM Aur 24-28 K, LkCa15 21-25 K, DM Tau 13-18 K, HD163296 25 K and TW Hydra 17 K.

In Figure 4.4 snowline locations in real systems have been plotted alongside results from the models, the snowline location in each case has been determined from observations of rings of N_2H^+ by Qi et al. (2015, 2019, 2013). N_2H^+ is a reactive ion abundant where CO is frozen out and therefore a useful CO snowline tracer. These locations give an indication as to current observational results, there is a broad agreement with the expected trends especially in the older systems HD163296 and TW Hydra. HD163296 is a 1.9 $M_\odot$ star that has a midplane CO snowline in its disc at around 90±8 au (Fairlamb et al., 2015; Qi et al., 2015), whereas TW Hydra has a stellar mass of 0.8 $M_\odot$ and a CO snowline much closer in at 21±1 au. Despite both discs being around the same age, the disc of HD163296 is warmer than TW Hydra, supporting the results of the radiative transfer modelling. The CO snowline prediction for a 2 $M_\odot$ star in Figure 4.4 is further out than the location fitted from observations of N_2H^+ in HD163296, in part due to the fact that the observed N_2H^+ ring was found at 25 K rather than 20 K (Qi et al., 2015), and also due to the assumption of a continuous disc, whilst the system famously hosts multiple large gaps. The observed location of the TW Hydra snowline is slightly further out in the disc than the estimate made using models of disc around a host star of a similar mass. Analysis by Schwarz et al. (2019) suggests that N_2H^+ emission from TW Hydra is not originating in the midplane but from higher in the disc, and so is likely to be tracing photodissociation or chemical reprocessing rather than freeze out.

At early times in contrast it is difficult to distinguish midplane temperatures by stellar mass because stellar luminosity is at a minimum and the midplane disc temperatures are at their most similar. The three youngest discs are around stars of lower mass GM Aur (1.3 $M_\odot$), LkCa15 (1.0 $M_\odot$) and DM Tau (0.5 $M_\odot$). In Figure 4.4 the location of the CO snowline in GM Aur agrees with the prediction of the disc models using stars of similar mass. The snowlines in LkCa and DM Tau are slightly further out in the disc by ≈20 au than the models predict. This is likely due to the depleted nature of their inner discs; LkCa 15 has an inner cavity of ∼45 au (Jin et al., 2019; Piétu et al., 2006) and DM Tau has two thin dust rings at 4 au and 25 au with a more extended outer disc from ≈75 au (Kudo et al., 2018). In both these systems, the disc at 10s of au is therefore likely to be much warmer than a similar location in the disc model as described in Table 4.1. Whilst GM Aur has also shown rings in high resolution ALMA observations, its inner disc does not appear to be as efficiently cleared of mm-sized dust (Huang et al., 2020), exhibiting depletion in between the rings rather than gaps.

4.3.3 Disc Composition

Here the effects of the snowline locations on the composition of gas and ice in the disc midplanes are explored. Just as the models place the upper limits on midplane temperatures, so the CO snowline locations represent the furthest possible distance where the CO snowline may be found at the given age/mass.

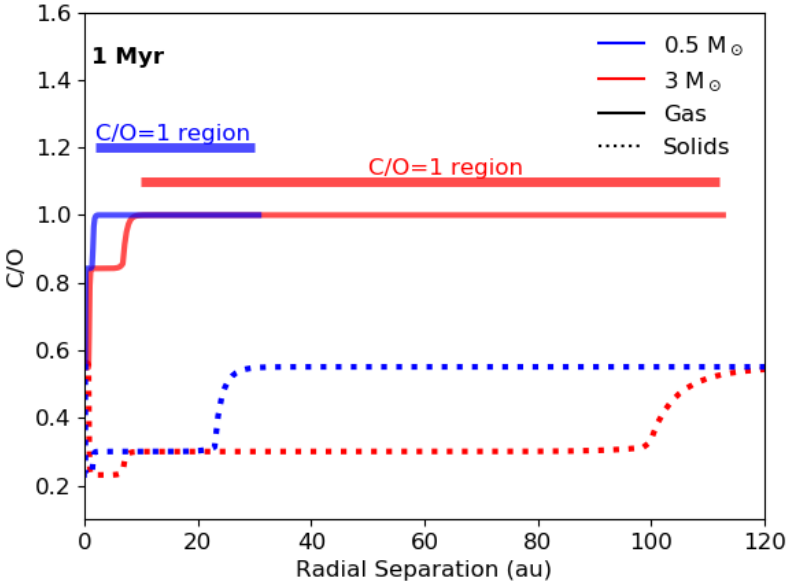

Figure 4.5: C/O in the gas (solid line) and solid phase (dotted line) for models at 1 Myr with blue lines showing the model with a 0.5 $M_\odot$ host star, and red lines showing a 3 $M_\odot$ host star. No drift or transport are included in this instance. The gas phase line is plotted up to the location of the CO snowline in the midplane, taken to be at T=20K. Horizontal lines above the C/O curves denote the region for which gas phase C/O=1 for each of the models and are colour coded accordingly.

Figure 4.5 plots C/O as a function of radius for the two extremes of the stellar mass range, the 0.5 and 3 $M_\odot$ cases, calculated without including any drift or transport within the disc, meaning the only difference should be due to the temperature profile. Each reproduces the same step function as seen in Öberg et al. (2011), presented here on a linear radial scale. The warmer disc around the

3 $M_\odot$ star pushes both the CO and CO_2 snowlines further out in the disc, leading to a more extended region of maximum carbon enrichment in the gas phase (in the model this is where C/O=1) in comparison to the disc around the 0.5 $M_\odot$ star. Outwards of ∼30 au in Figure 4.5, the solids in the 0.5 $M_\odot$ case are much more carbon enriched because all main carbon carriers are frozen out onto the grains. In the warmer 3 $M_\odot$ case, the snowline is at ≈115 au in the disc and so more carbon is in the gas phase, leaving solids with a lower value of C/O ≈ 0.3 .

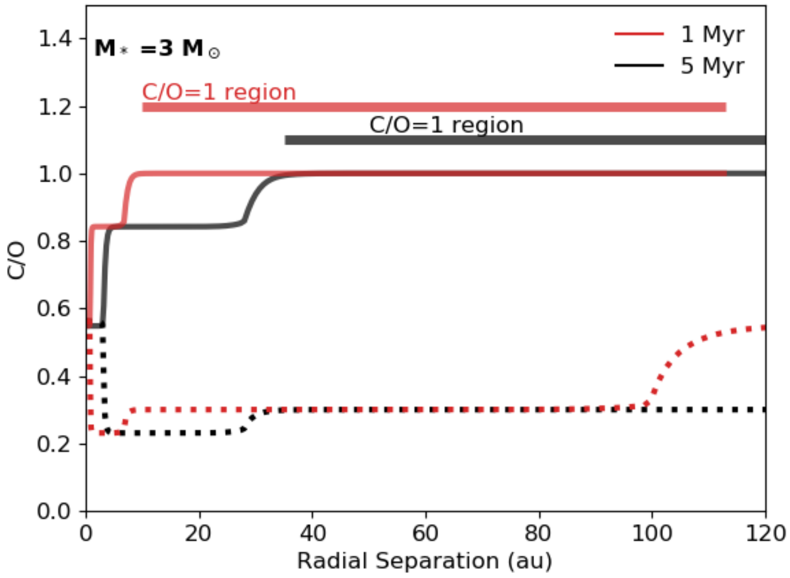

Figure 4.6: C/O in the gas (solid line) and solid phase (dotted line) for models with a 3 $M_\odot$ host star and no drift or transport included. The red lines show the model with stellar parameters at 1 Myr, the black lines show the model at 5 Myr. The gas phase line is plotted until the location of the CO snowline in the midplane, taken to be at T=20 K. Horizontal lines above the curves denote the region for which gas phase C/O=1 for each of the models and are colour coded accordingly.

Heating of the disc depends not only on the mass of the star, but the stage of its evolution as well. In Figure 4.6 the same 1 Myr, 3 $M_\odot$ profile is plotted as in Figure 4.5, but now compared to a model using stellar parameters at 5 Myr when the intermediate mass star's luminosity is greater. In the 5 Myr case the CO_2 snowline is further out than in the 1 Myr case. As shown in Figure 4.6, this results in a lower C/O ratio for the oxygen enriched solids up to 30 au in the 5 Myr case (dotted black line) compared to the 1 Myr case (red dotted line).

CO remains in the gas phase for the vast majority of the disc extent, with the CO snowline found at over 400 au at 5 Myr. Figure 4.6 therefore makes it clear that there is not only a radial dependence to be considered, but also a temporal one. The CO and CO_2 snowline locations will evolve with the disc temperature profile resulting in changes to disc composition. The H_2O snowline is always at shorter separation from the central star, in some discs approaching the inner regions where the disc is viscously heated rather than radiatively, and so it is not necessarily expected that the H_2O snowline will be affected in a similar manner where this is true.

4.4 Discussion

4.4.1 Application to HR8799

The C/O in the gas and solid phases depends on both location within the disc and time. Here the extent to which these results can explain variation in the atmospheric C/O of giant planets within the same system is explored.

HR8799 is an F0 type star (Gray et al., 2003) that hosts four directly imaged giant planets in its system (Marois et al., 2008, 2010). The wide orbits and large masses of the planets have proved difficult to model with current theories of planet formation. Through spectroscopic analysis Sadakane (2006) find the abundances of C and O in HR8799 to be consistent with solar values; $\log_{10}$C/H= -3.57 and $\log_{10}$O/H= -3.31 (Asplund et al., 2009). In this section a disc model is created specific to the stellar mass of HR8799 that includes stellar evolution, disc transport and the chemical model following Öberg et al. (2011). The composition of the model disc is then compared with the C/O determined for each of the four exoplanets from their observed spectra by Lavie et al. (2017) using the atmospheric retrieval code HELIOS. Properties of the four exoplanets are summarised in Table 4.3.

Planet	Mass ^{a}	R_{pl} ^{a,b}	C/H^c	O/H^c	C/O^c
HR8799b	7 M_J	68 au	1.46	1.24	0.92
HR8799c	7 M_J	38 au	0.84	0.84	0.55
HR8799d	7 M_J	24 au	-13.0	0.73	$> 10^{-13}$
HR8799e	5 M_J	15 au	-8.4	0.28	$> 10^{-9}$

Table 4.3: Key properties of the giant exoplanets in the HR8799 system. The retrieved carbon abundance is very low in planets 'd' and 'e', and so the C/O represents a lower limit. C/H and O/H values are given relative to stellar values in the form: $\log_{10}X_{pl}$ - $\log_{10}X_{*}$, where X is the abundance relative to hydrogen. References a) Marois et al. (2010), b) Marois et al. (2008), c) Lavie et al. (2017).

The disc properties as described in Table 4.1 are adopted with a star of mass 1.5 $M_\odot$ and the conditions in the disc models are modelled at ages up to 10 Myr. Figure 4.7 shows snapshots taken from this series of models that illustrate selected key milestones to be discussed in the text. Assuming that the atmospheric C/O listed in Table 4.3 is comprised of a mixture of rapidly accreted local gas and dust, one can analyse whether evolving disc composition as a result of stellar luminosity evolution can put temporal constraints on planet formation in the HR8799 system. Although there will be no speculation on the formation of planets 'd' and 'e', as the C/O values from Lavie et al. (2017) are very low. This is mainly due to the fact that the retrieved probability density functions for C/H in these planets do not constrain the values well. GRAVITY has detected CO in the atmosphere of HR8799e (Lacour et al., 2019), and so carbon bearing molecules are certainly present and it is likely that the C/O values in the atmospheres of planets 'd' and 'e' greater than those in Table 4.3. Future observations will help to determine the composition of these exoplanetary atmospheres.

To aid with this discussion the relative mixing proportions of gas and dust that would be required to achieve the C/O for each exoplanet atmosphere as given in Table 4.3 are calculated. By assuming that the atmospheric C/O is inherited from local disc material, the C/O of a giant planet can be written as a mixture of local gas and dust,

$$\mathrm{C/O_{planet}} = \mathrm{f\ C/O_{gas}} + (1-\mathrm{f})\ \mathrm{C/O_{solid}}, \tag{4.2}$$

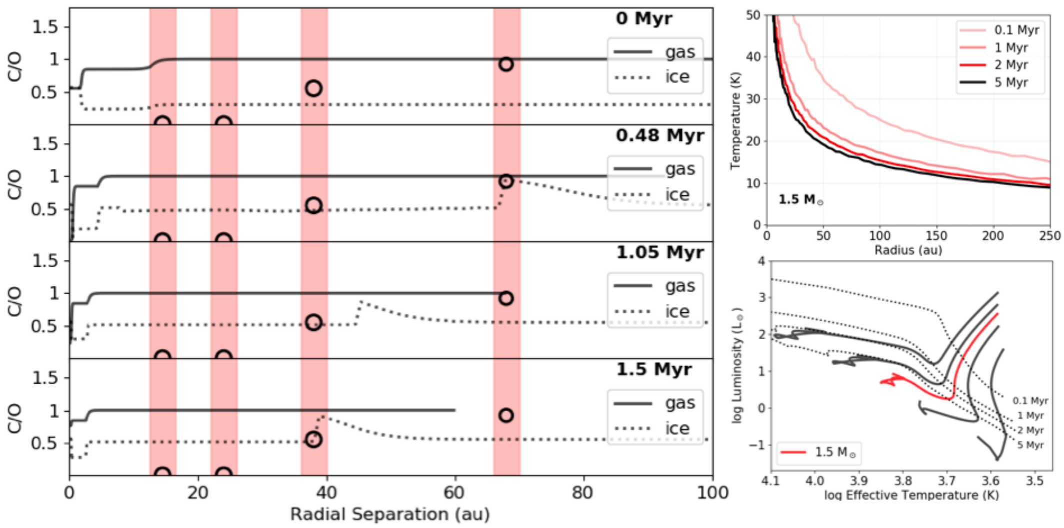

Figure 4.7: The three elements of the HR8799 disc model. **Left hand side:** Ratio of carbon to oxygen abundance in the gas phase (solid line) and solid phase (dotted line) as a function of radius. Shaded areas mark the location of the giant planets in the HR8799 system, black circles are plotted at the corresponding C/O retrieved for their atmosphere. Each panel shows a different time step in the evolution of the model as is labelled in the top right corner of each panel. Timesteps are chosen to reflect key points as referred to in the text. The gas phase C/O line is plotted up until the CO snowline in the midplane, taken to be at 20K. **Right hand side:** On the top is the evolution of T(R) in the model for a 1.5 $M_\odot$ star. On the bottom is an HR diagram comparing the pre-MS evolution of a 1.5 $M_\odot$ star to the evolutionary tracks in Figure 4.1.

where f is the fraction of material that is accreted to the planet that was originally in the gas phase in the disc.

In Figure 4.7 selected snapshots are presented that show key time steps. On the left-hand side are four panels showing C/O radial profiles for the HR8799 system. The black lines give the C/O in the solids and gas as labelled in the legend, the coloured bars give the orbital radii of the 4 known giant planets, with a circle plotted on the y-axis for each planet at the value corresponding to the atmospheric C/O found by (Lavie et al., 2017) for each planet. On the right hand side the midplane temperature profiles are given for different stages of the star's luminosity evolution (which can be compared to those in Figure 4.3). The path of the 1.5 $M_\odot$ star across the HR diagram as calculated by the MESA stellar modelling is shown in the bottom panel on the right hand side, with the tracks of the 0.5, 1, 2 and 3 $M_\odot$ stars also plotted in grey.

In Figure 4.7, after 1.5 Myr, the evolution slows and the radial profile of C/O in gas and dust is well defined. From these key epochs $C/O_{\rm gas}$ and $C/O_{\rm solid}$ can be measured and used in Equation 4.2.

HR8799b

The main constraint that this modelling puts on the formation of carbon-rich exoplanet HR8799b - the outermost planet in Figure 4.7 - is a result of the displacement of the furthest radial location where the CO snowline may be located at different ages. At a radial separation of 68 au HR8799 is interior to the CO snowline position in all models up to the 1.05 Myr one, which is shown in Figure 4.7. Beyond the CO snowline, no major C or O carriers are in the gas phase. This means that rapid gas accretion in this particular region during planet formation will have no affect on the C/O ratio of any forming planet as the gas is mainly H_2, but it will affect the C/H ratio. HR8799b therefore must have accreted the vast majority of its carbon and oxygen while still inside the C/O=1 region (inside the CO snowline).

Using Equation 4.2, the amount of exoplanetary atmosphere that originated in each of the gas and solid phases can be estimated using the relative amounts of carbon and oxygen in the observed atmosphere and in the disc as calculated by the modelling. Figure 4.8 plots f as a function of time through 5 Myr of the disc's evolution. CO dominates the gas phase material at the orbital radius of both planets, and so similar features can be seen in the C/H and O/H profiles. Figure 4.8 shows that most of the carbon and oxygen must originate from the gas phase at all times. f calculated through C/H approached a peak at around 0.5 Myr due to the inward drift of carbon-rich solids shown in Figure 4.7, varying between 0.5 and 0.85. O/H on the other hand remains fairly constant around 0.85, dropping at late times as the CO snowline approaches the planet. The combination of these two curves results in the green C/O line in Figure 4.8. At 0.5 Myr O/H is briefly greater than C/H in the disc model, due to an increase in the density of solids drifting in from the outer disc, resulting in an outlier results where f is very low. Before and after this event f calculated via C/O remains between $\approx$0.75-0.87. This calculation therefore does not support accretion from the inward drifting material that built up at a snowline in the outer disc, as the relative abundances cannot be reconciled with the observed C/O value. The build up of solids in the outer disc depends upon assumptions of disc mass and turbulent α.

The point in time when the CO snowline is located inside the planet's orbital radius depends on gas mass in the disc, as it is the amount of gas which determines the degree of flaring in the disc and the subsequent heating of the disc (Panić and Min, 2017). Disc gas mass will decrease with time as a result of photoevaporation and accretion onto the star, resulting in a lower midplane temperature and a shorter time to form the planet. Furthermore if the planet experienced migration through the disc it would have accreted gas starting at a greater radial separation from the star where there is even less time before the CO snowline is found inside of the planet's orbital radius. The time constraint of $\sim$1 Myr from the modelling therefore represents an upper limit on the accretion of C and O from the disc, pointing towards an early formation time for HR8799b. In certain circumstances runaway migration can also lead to outward motion (Masset and Papaloizou, 2003), for example if a planet is located close to a sharp disc edge on the outside of a disc cavity (Artymowicz, 2004). If this were the case for HR8799b, it would be very difficult to simultaneously explain the planets interior to it. Scattering events between giant planets can theoretically re-order the configuration of a planetary system, similarly to the Nice model for the Solar System (Gomes et al., 2005). This would usually involve a giant planet scattering smaller planets however, and it would be very difficult to produce the tight and seemingly stable orbits of the four giant planets as observed by Marois et al. (2008, 2010) after an event such as this. Fabrycky and Murray-Clay (2010) suggest the stability in the orbits of the system require mean-motion resonance between them, which is more likely to occur through migration into a stable state, rather than a chaotic scattering event.

HR8799c

HR8799c is found at an orbital radius of 38 au and so it remains inside the snowline in all models, meaning it can always accrete gas that will alter its C/O ratio. The 1.5 Myr panel in Figure 4.7 is a good representation of the snowline location up until 10 Myr, as the radial temperature profile is similar at these later stages. Table 4.3 however shows that HR8799c has C/O comparable to that of the central star which has C/O=0.56 (Sadakane, 2006), much lower than the C/O in the gas phase of the disc models.

Using Equation 4.2 to calculate the relative mixing of gas and ice required from the values of C/H and O/H at R=38 au throughout disc evolution, over 90% of C and O must have originated from gas content in the models rather than solids (See Figure 4.9). The solids that are accreted are highly rich in O, and reduce the overall C/O of the atmosphere. Unlike HR8799b, the orbital radius of HR8799c means its enrichment cannot be constrained by snowline location, as it is found inside the CO snowline in all the models and also outside of the CO_2 snowline in all models. This means that local C/O in the gas and solids remains relatively stable as a function of time. This makes it more difficult to pinpoint a specific epoch for formation for a given exoplanetary atmospheric C/O. Formation in the models can be excluded between 1.5 Myr and 3 Myr disc however, where solids are particularly high in C/O due to the inward drift of carbon-rich gas and dust. This carbon-rich material built up at the CO snowline when it was further out in the disc at earlier times. In this case, the build up of material from the snowline is too carbon-rich, and it is impossible to recreate the approximately stellar C/O of HR8799c with this material (See Figure 4.9). The discrepancy may be alerting us to significant chemical effects in the atmosphere, or to planet formation via gravitational instability.

In order to achieve the approximately solar C/O of HR8799c in a region of the disc with carbon-enriched gas, there must have been substantial oxygen enrichment of the atmosphere through the accretion of solids. In our model, radial drift and the subsequent inward transport of volatiles from the outer disc are insufficient to achieve this.

A stellar C/O is seen in a number of hot Jupiters (e.g. 8 out of 9 planets in the sample of Line et al., 2014). But unlike the hot Jupiters, HR8799c is on a relatively wide orbit. Its approximately stellar C/O may be due to the uncertainties in determining C/O of exoplanetary atmospheres from observed spectra. Changes in C/O of an exoplanet's atmosphere can also occur as part of the formation process. If planet formation occurs via gravitational instability, the C/O of a fragment can vary due to the sequestration of volatiles contained within dust that settles towards the fragment core (Ilee et al., 2017) or due to the accretion of planetesimals (Madhusudhan et al., 2014). Kratter et al. (2010) identify a set of criteria to be met in order for any of the planets in HR8799 to have formed via GI. For their proposed scenario, the authors require a formation around the end of the Class I stage and beyond 40-70 au, with temperatures colder than typical discs. These criteria are consistent with the constraints of an early formation in the outer disc for HR8799b and the cooling of disc midplane as a result of stellar evolution.

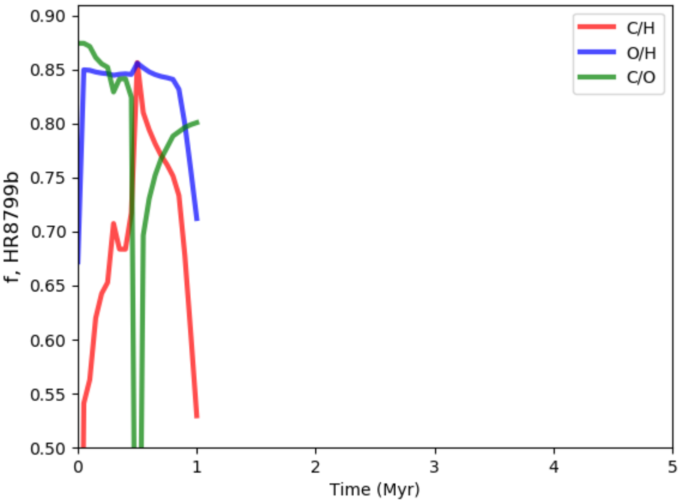

Figure 4.8: The proportion of material in the exoplanetary atmosphere that originated as gas phase disc material, calculated using Equation 2 in order to reproduce the retrieved atmospheric C/H, O/H and C/H for the exoplanet HR8799b. The data is plotted for all times at which the CO snowline is radially exterior to the HR8799b's orbital radius.

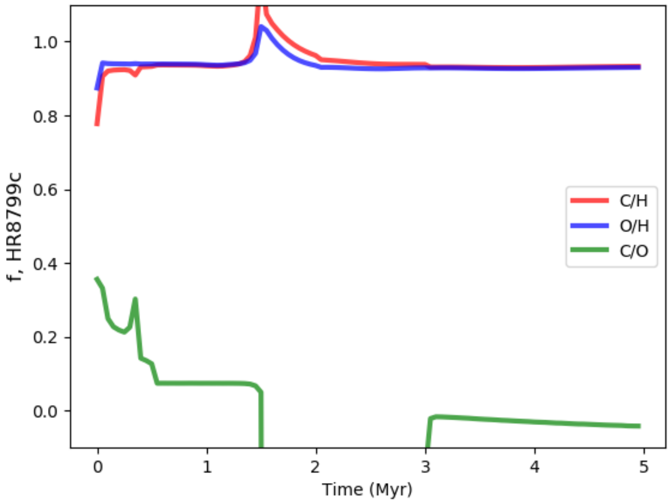

Figure 4.9: Same as Figure 4.8 for the exoplanet HR8799c.

4.4.2 Alternative chemistry model

So far a chemical model has been implemented that uses the temperature profile of the disc to establish the location of key snowlines. Volume mixing ratios and abundances of C and O are based on observations of protoplanetary discs (Draine, 2003; Öberg et al., 2011; Pontoppidan, 2006) and carbon grains are included resulting in a greater amount of solid carbon. In previous studies of disc composition (e.g. Booth et al., 2017; Madhusudhan et al., 2014, 2017) this prescription has been compared to a similar model where volume mixing ratios are based on theoretical computations (Woitke et al., 2009) and CH_4 is included in the species considered. As a result, the predicted disc C/O is altered, particularly in the dust and towards inner regions for the gas.

Table 4.4 gives the mixing ratios used for this model for comparison with Table 4.2. Figure 4.10 shows results when this alternative chemistry model is applied to the disc model for HR8799.

Species	X/H
CO	$0.45\ (1 + f_{CO_2}) \times C/H$
CH_4	$0.45\ (1 - f_{CO_2}) \times C/H$
CO_2	$0.1 \times C/H$
H_2O	$O/H - (3 \times \frac{Si}{H} + \frac{CO}{H} + 2 \times \frac{CO_2}{H})$
Carbon grains	0
Silicates	Si/H

Table 4.4: Binding energies, presented as temperatures, and volume mixing ratios of the key chemical species included in the alternative chemical model.

The key difference in the results from the alternative model comes within the CO_2 snowline, where due to the gas phase CH_4, C/O in the gas phase = 1.5, whereas solid phase material is initially down to 0, due to the lack of carbon grains. As the radial profile of C/O in the disc is changed at short separation from the star, the alternative chemistry model has a negligible effect on the relative mixing ratios of gas and dust in order to reproduce the retrieved exoplanetary atmosphere values.

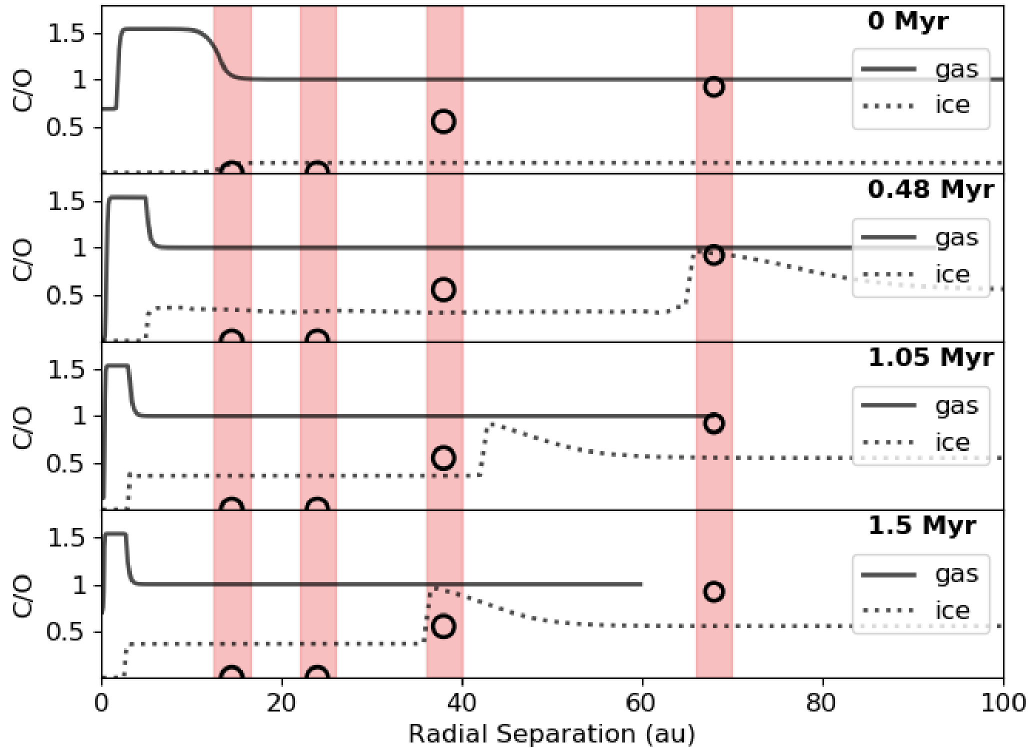

Figure 4.10: Alternative chemical model used as presented in Madhusudhan et al. (2014) and used as 'Case 1' in Booth et al. (2017))

4.4.3 Implications for planet formation

The radiative transfer models quantify the impact of stellar evolution on altering the temperature structure in the midplane of the disc. The discs around intermediate mass stars are warmer and remain at their warmest for later stellar ages as well, meaning key carbon and oxygen carriers remain in the gas phase for a longer time period and for a greater extent of the disc. This dichotomy in disc composition has direct implications for the composition of planets that form in these areas. For example by 2 Myr in the models the CO snowline of discs around stars of 0.5 or 1 $M_\odot$ are within 40 au. Giant planets rich in carbon are not expected to be found at wide separations in the discs around the lower mass stars. On the other hand, the discs around intermediate mass stars are much more likely to host carbon-rich giant planets on wider orbits because CO remains in the gas for a much greater separation in the disc; over 250 au in the case of the 3 $M_\odot$ star at >2 Myr.

By applying this modelling to the HR8799 system, constraints can be placed on the period of time in which the bulk of C- and O- carrying molecules must have been accreted by the two outer planets from the model disc. The position of the CO snowline rules out the formation of HR8799b beyond 1 Myr. This result assumes that atmospheric C/O reflects that of the initial disc material, but chemical processes in the exoplanetary atmosphere will alter the observed ratio. More precise predictions could be made by implementing a more sophisticated chemical network and using species beyond the main C and O carriers as tracers of atmospheric composition.

In this analysis in-situ formation of the giant planets in the system is considered. An evolving temperature structure will also impact upon migration timescales of planets in the disc however, as migrational velocity of a planet increases proportional to temperature. In discs that cool with time as a result of stellar evolution, planets will migrate at a greater velocity at earlier times compared to the velocity of a planet of equal mass at the same radial separation at late times. In discs around intermediate mass stars that are warm at later times, CO is present in the gas phase for a greater proportion of the disc, but any migrating planets within the disc will do so with a greater velocity than at early times in a cooler disc. If planet-driven gaps in the disc begin to overlap, and the planets themselves are in mean-motion resonance then convergent migration can occur (Kley, 2000), potentially helping to achieve mean motion resonances that stabilise the orbits of the planets (Fabrycky and Murray-Clay, 2010).

4.4.4 Implications for dust growth to pebble sizes

In Section 4.4.1 the analysis of HR8799c suggested that significant enrichment by solids could be required to explain the approximately solar C/O of the wide orbit planet. The amount of solids accreted depends on the method of the planet's formation. Here we explore the impact of stellar evolution on the composition of midplane dust, in particular we look to assess to what extent grain size in the disc is limited by the evolution of the star and whether this could prevent pebble accretion in regions of the disc. In order for pebble accretion to be rapid, pebbles have to make up a significant fraction for the gas giant core's solid density (Lambrechts and Johansen, 2012), and so they likely contribute significantly to oxygen enrichment of the forming planet. Here we will define 'pebbles' as dust grains with $a \geq 1$ cm.

In Figure 4.11 results of dust evolution in our models are plotted as coloured lines, the grey lines in the background show the results of modelling where the stellar parameters remain constant but the dust is still allowed to evolve. As expected an increase in grain size in the inner disc occurs due to changes in fragmentation velocity, e.g. the sharp jumps at <2 au for all the models at 0.1 Myr (Figure 4.11).

Maximum grain size as a function of radius is similar among all models at 1 Myr, it is not until the divergence of midplane temperatures that a significant effect is seen in outer regions. The threshold between icy and ice-free fragmentation is pushed further into the disc as a result of the stellar evolution; this is most clearly seen by comparing the red lines showing the 3 $M_{\odot}$ models at different times in Figure 4.11. The extent to which stellar evolution is dictating this location can be seen by comparing to the similar radial features of the grey lines in the background.

In Figure 4.11 there are no pebbles present in the innermost regions of the discs at 0.1 Myr, as the disc midplanes are relatively warm due to the luminous young star. This is a short lived stage however, as stellar luminosity evolves rapidly and the effects of radial drift start to take effect. The models of discs around low mass stars at 1 and 2 Myr (blue and gold lines in Figure 4.11) host pebbles out to 20-30 au. By 5 Myr the 0.5 and 1 $M_{\odot}$ models still host pebbles as far as 10 au. These models show that pebbles reside in the inner disc (<10 au) for at least 5 Myr and will be able to contribute towards core growth in these regions. This is not the case in the discs around intermediate mass stars. The 1 Myr panel in Figure 4.11 shows that fragmentation limit in the 3 $M_{\odot}$ model is found at 1 au, and is at 5 au in the 5 Myr panel. Due to rapid radial drift and fragmentation in collisions any pebbles in these inner regions will be removed from the disc quickly. Pebble sized grains are only efficiently removed from the

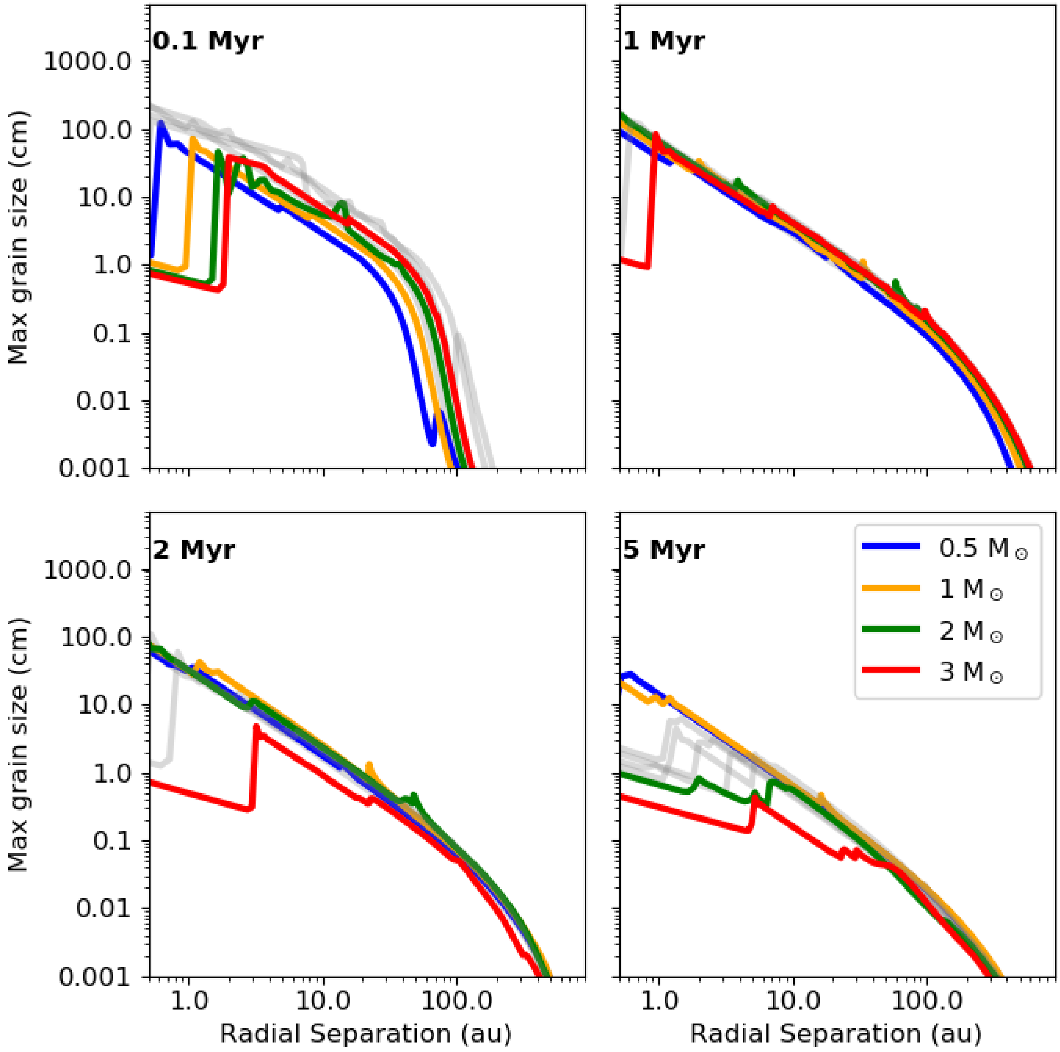

Figure 4.11: In each panel the maximum grain size is plotted as a function of radius for disc models at different time steps. At each time step the results are shown for disc models with different masses of host star plotted as different colours. An indication of the results for a model using stellar parameters that do not evolve, with values adopted from 1 Myr, are plotted in grey.

inner regions of the 2 $M_\odot$ model by around 5 Myr when the effects of radial drift become dominant. This is signalled by the decrease of maximum grain size at all radial locations $\leq$10 au between 2 and 5 Myr, rather than the sharp jump associated with the fragmentation threshold.

The dust modelling presented in Figure 4.11 thereby places some constraints on the ability of discs to host pebble sized grains as a result of the stellar luminosity evolution. Due to the cool discs of low mass stars, their discs remain virtually unaffected. After 1-2 Myr, fragmentation limits grains from growing to pebble sizes in intermediate mass discs as a result of stellar evolution and its subsequent impact on heating of the disc. This only applies within the first 1-5 au however and by $\approx$5 Myr radial drift becomes the dominant factor in removing large grains from the inner disc. Lack of large grains at short radial separation does not affect the formation of the HR8799 planets considered here, as they are on wider orbits. This would, however, affect the formation of giant planets forming at shorter separation, i.e. hot Jupiters, in planet forming discs.

An additional increase in grain size is seen in the models of discs around intermediate mass stars, where the CO_2 snowline creates a similar transition. For example at around 6 au in the 3 $M_\odot$ model at 5 Myr and at 30 au in the 3 $M_\odot$ model in the same panel of Figure 4.11. Unlike at the H_2O snowline there is not a strong effect on the fragmentation threshold. Instead, the dust mass drops as the CO_2 leaves the grains, leading to a decrease in local dust surface density. In Figure 4.12 dust surface density is plotted for models at the extremes of our adopted stellar mass range, for regular time steps. Comparing the 3 $M_\odot$ model at 5 Myr (right hand panel, black line in Figure 4.12) with the corresponding model in Figure 4.11, there is a decrease in dust surface occurring at the same radial separation as the increase in grain size. As discussed in Boneberg et al. (2018), the smaller grains are more closely coupled to the gas, decreasing the speed of inward radial drift. As a result dust surface density rises interior to the H_2O snowline. The discs around lower mass stars do not show the second grain size change. Similarly the 0.5 $M_\odot$ dust surface density profile in Figure 4.12 is not affected in the same way as the higher mass case.

Similar perturbations in grain size can be seen in the outer disc towards the CO snowline, but due to the lower density as greater R, the features do not persist and are smoothed out by transport processes. Additionally much of the CO crossing the snowline is converted in to CO_2 under the assumptions of our chemical model, and so the inward flux of carbon is instead later released at the CO_2 snowline. Three small spikes can be seen on the red line in the 1 Myr panel of Figure 4.11 corresponding to early snowline-induced disturbances. Transport processes and the evolving snowline location in discs mean that there may be some displacement between these radial features and the snowline itself for any given time.

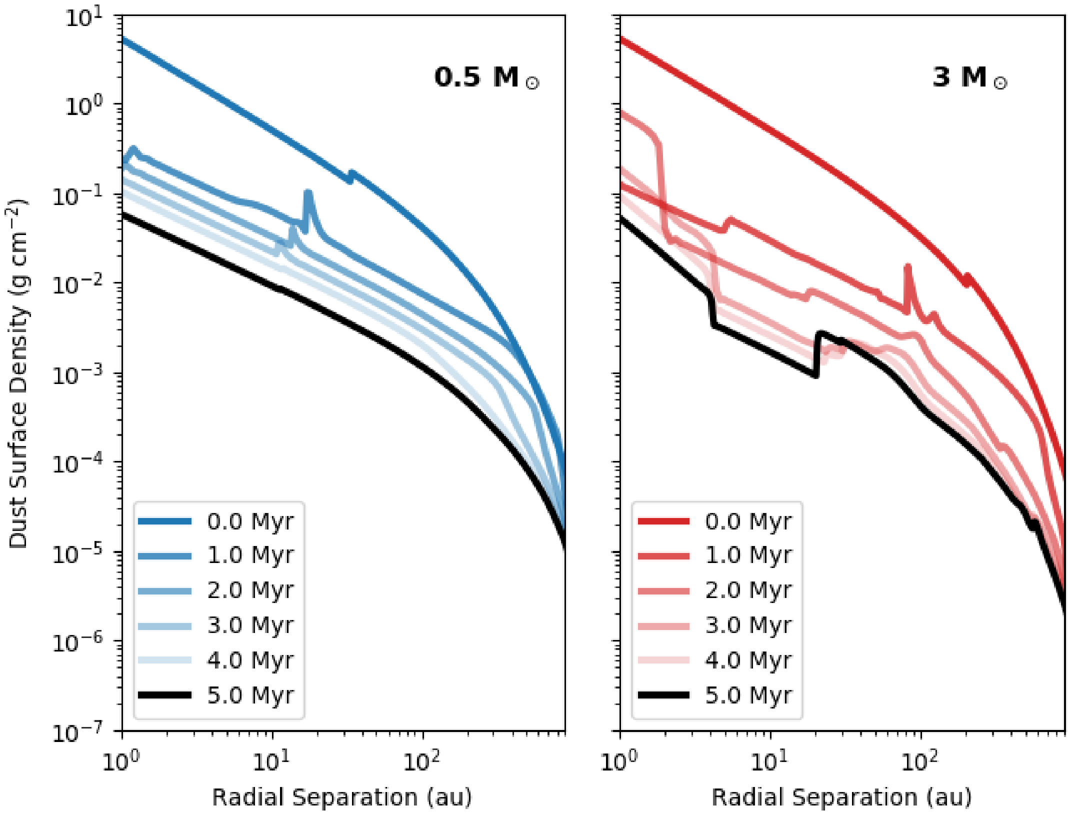

Figure 4.12: Surface density profile as a result of dust evolution in disc models with central stars of mass 0.5 and 3 $M_\odot$ for timesteps of 1 Myr.

We do not include a prescription for dust trapping in our dust model, a mechanism which acts to prevent the rapid removal of pebbles from the disc on short timescales (Pinilla et al., 2012b). Accurate predictions of the timescales for pebble removal in protoplanetary discs will require such considerations. Circular, thin rings of dust that are consistent with dust trapping are common among high resolution observations of bright protoplanetary discs (Dullemond et al., 2018). It therefore seems that dust trapping mechanisms may also be common; further imaging of large samples of discs that are capable of resolving dust rings are necessary to confirm this.

The temporal constraints of our modelling suggest that the pre-main sequence evolution of the host star could be used to identify when key snowline-dependant planet formation mechanisms occur. For example numerical modelling by Schoonenberg and Ormel (2017) shows that planetesimal formation by the streaming instability is aided by the diffusion and condensation at the water snowline. Furthermore snowlines may play an important role in the dust growth leading to self-induced dust traps at the water or even CO snowlines (Vericel and Gonzalez, 2020). For a given proto-planet there will be a window of opportunity for processes such as these to have taken place, the length of which depends upon the spectral type of the star.

4.5 Conclusions

In this paper models of pre-main sequence stellar evolution across a range of masses are combined with radiative transfer modelling of protoplanetary discs to study the impact of stellar evolution on midplane temperature. The grid of radiative transfer models quantify the change in temperature for continuous discs of constant mass when irradiated by stars at different stages of their pre-MS evolution. The consequences of these changes in midplane temperature are discussed with specific attention to the composition of the disc and what this means for the planets that form there. A summary of the main conclusions is listed below.

- At ages >2Myr, stellar evolution of stars with mass $>1.5\mathrm{M}_\odot$ diverges significantly from that of the lower mass stars. The increase in luminosity results in an increase in midplane temperature within the discs they host. Disc models around intermediate mass stars are not only warmer than discs around low- or solar- mass stars, but they also remain at their warmest for a greater duration of the stars' pre-main sequence evolution.

- Applying this modelling procedure to the HR8799 system, it is found that accretion of carbon and oxygen by exoplanet HR8799b must have occurred at early times in the disc's evolution whilst the planet was still inside the CO snowline. A reliable, specific time constraint for any individual disc will however require an accurate disc mass determination and a good estimate of mass loss rate from the disc.
- Stellar evolution can limit growth of dust grains to pebble sizes in the first few au for discs around intermediate mass stars, but only after a 1-2 Myr. Radial drift is the most efficient mechanism at limiting growth to pebble sized in the inner disc.

Chapter 5

Conclusions

5.1 Summary

Protoplanetary discs are the natal environment from which planets are formed, and so the accurate characterisation of disc composition defines the basic building blocks for planet formation. Meanwhile the mechanisms for planet formation disturb this environment and leave imprints behind in the density distribution of the disc. Study of disc structures can therefore give direct clues as to the process by which planet formation occurs and on what drives protoplanetary disc evolution.

This thesis characterises the gas and dust in discs around intermediate mass stars. This was achieved through analysis of new ALMA observations of the discs hosted by stars HD100546 and HD141569. Despite the similarity between the two stars, the discs they host are markedly different because HD141569 demonstrates a more advanced stage of disc evolution. Both discs were found to contain relatively large amounts of gas for their respective evolutionary stages, despite ages approaching what is currently considered to be the ‘typical’ disc lifetime. In addition to analysis of observations, the conditions within long-lived discs were explored further through modelling of protoplanetary disc midplanes and the impact the evolution of the host star has on the properties of this part of the disc. The results found direct implications for planet formation and led to constraints on the radial location and time of the formation of carbon-rich exoplanet HR8799b; a directly imaged wide-orbit planet hosted by another intermediate mass star. The three systems given specific attention in this thesis represent three important epochs of protoplanetary disc evolution. Together, they tell the story of protoplanetary disc evolution around intermediate mass stars. The analysis of imaging and modelling of these systems sets the scene for giant planet formation in their discs.

Observations of the bright, gas-rich, planet forming disc around Herbig star HD100546 proved the power of optically thin tracers in delving into the disc midplane and in tracing the outer regions of the disc where the majority of mass is contained. This method ultimately led to an estimated mass that places HD100546 in the top bracket of the most massive known discs around Herbig stars along with systems such as HD97048 and HD163296. Discs like these must therefore have a way of remaining massive significantly beyond disc lifetimes predicted by IR statistics or photoevaporation models of discs around low mass stars. Examples of massive, long-lived discs exist around some low mass stars as well, for example the disc of TW Hydra. In order to explain giant planets on wide orbits (e.g. the exoplanets of HR8799, Marois et al., 2008), observations of HD100546 and discs similar to it will be the key as they are some of the few systems with sufficient mass in the outer disc to support the formation of giant planets. Quantifying the planet building budget in the outer disc for systems such as HD100546 and others similar to it, is essential for confirming the capability of individual protoplanetary discs to form giant planets on wide orbits, as well as their ability to do so at an age beyond ‘typical’ disc lifetimes.

Studying the outer regions of protoplanetary discs via direct imaging is currently the only way in which to investigate giant planets on wide orbits. Modern exoplanet detection methods are effective for exoplanets at short radial separation (see Figure 5.1) or in systems where discs have dispersed. Identifying signatures of embedded planets can be very difficult, and in the case of HD100546 has involved much debate (Currie et al., 2017; Quanz et al., 2015, 2013; Rameau et al., 2017). Millimetre wavelength observations with facilities such as ALMA are the best way to characterise the coolest parts of the disc pertaining to the wide orbit giants forming in the midplane and in the outer disc. It is here that the massive, wide orbit planets detected by direct imaging originate, shown as blue stars in Figure 5.1.

As well as investigating planet formation the observations analysed in this thesis allow for detailed exploration of disc structures and the disc-embedded mechanisms they could be alerting us to.

HD141569 provides a unique opportunity to study the end of the planet-building phase and the subsequent dispersal of protoplanetary discs as they transition into the debris disc regime. In Chapter 3 observations probing midplane gas and dust reveal a highly asymmetric distribution of ^{13}CO. The ^{13}CO emission in the ALMA observations presented here peaks at 120±10 au away from the stellar position, and the main body of its emission lies in the same position as rings located in scattered light. Analysis of the continuum emission also found

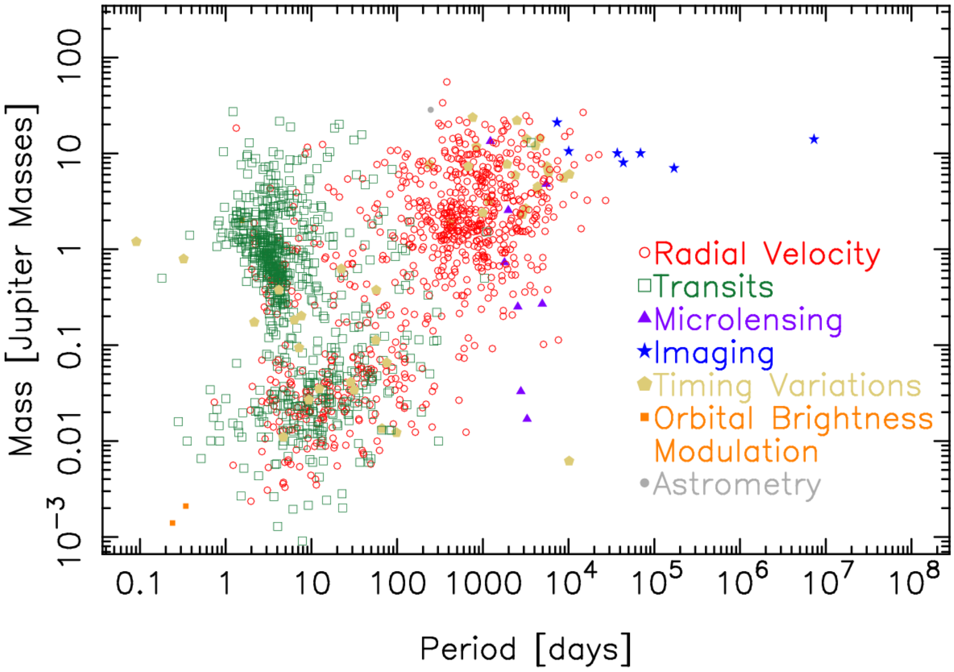

Figure 5.1: Mass of currently detected exoplanets is plotted as a function of the orbital period of the exoplanet. Data points are coloured by the method used to detect the exoplanet as described by the key on the right hand side. Direct imaging detects the exoplanets with the lowest frequency, but is the only method by which planets on wide orbits can be investigated. Data and plot from exoplanetarchive.ipac.caltech.edu, correct as of 19th February 2020.

evidence of a mm counterpart to the wide scattered light ring at 220 au. The structural features identified in the ALMA images add further weight to the view that HD141569 has been caught in the act of its transition towards an evolved exoplanetary system.

A major conclusion from this thesis on methodology is that multi-wavelength analysis is an invaluable tool when describing protoplanetary disc. The millimetre ALMA observations were specifically designed to delve to the cool regions of the discs, yet key results were found for both HD100546 and HD141569 that would not have been possible using data from a single wavelength. In HD100546 grain growth and the composition of the dust population were assessed through calculation of the spectral index between different continuum wavelengths and in

HD141569 the optical depth of gas lines could be calculated to explain the wildly different gas mass estimates made from ALMA observations. Furthermore both studies utilise results from multiple observing techniques by comparing millimetre interferometry to scattered light imaging that traces the surface layers of the disc. Combining tracers of the midplane with those at greater vertical height led to hints of spiral features in the outer disc of HD100546 and evidence for a midplane counterpart to the wide ring at 220 au in HD141569. Throughout all stages of disc evolution, the act of combining alternative observing modes from a range of observational facilities is extremely powerful and adds greater depth and understanding to structural analysis. Proof of this is clear when considering HD141569; multiple data sets have provided the fascinating configuration of disc structure as summarised in Figure 3.5. This has enabled greater scrutiny of the disc's evolutionary state and the nature of the gas it hosts. Circumstantially, the asymmetric ^{13}CO gas emission could be interpreted as the site of secondary gas production originating from a planetesimal belt as seen in Beta Pic (Dent et al., 2014). In this case the morphology of the clump is likely down to a combination of elongation by the synthesising beam and spreading as a result of orbital motion in the disc. On the other hand, gas mass in the disc is an order of magnitude larger compared to that in systems that are consistent with models of secondary gas (Kral et al., 2018). Furthermore HD141569 demonstrates the properties of a hybrid disc as described by (Péricaud et al., 2017). It may be that the gas is primordial, like that in HD100546, but unlike HD100546 the gas and dust in the disc are being actively depleted or dispersed. The peak in ^{13}CO intensity that is separated from the star may in this case be a particularly dense region of gas from a planet-driven spiral wake such as is observed in HD135344B (van der Marel et al., 2016) or V1247 Orionis (Kraus et al., 2017). In the latter scenario new observations that resolve the disc at scales of $\sim$ 10s au would be key in verifying whether the gas asymmetry is linked to spiral arm features detected by scattered light observations such as the arcs on the outer belts (Mawet et al., 2017; Perrot et al., 2016).

Although it no longer holds sufficient mass to form new giant planets, the density distribution in the remaining disc material of HD141569 will be shaped and sculpted by any currently existing planets or by the mechanisms driving disc depletion. As a result we can learn about the architecture of young planetary systems through observations of systems such as this. As the only pre-main sequence hybrid disc, HD141569 is the only known system that can exhibit to observers ‘the beginning of the end’, and so it is also a crucial testing ground for theories on the onset of disc dispersal.

Finally, Herbig stars bridge the gap between the low-mass and high-mass regimes that show differing interior structure and stellar evolutionary paths from each other. The discs hosted by A type stars are unusual in that they are the most likely to host detected giant planets (Johnson et al., 2010; Reffert et al., 2014) and most of the debris discs hosting surprisingly large amounts of gas are also around A type stars (Moór et al., 2017; Péricaud et al., 2017). Furthermore discs around Herbig stars are the brightest, most massive and some of the most well studied protoplanetary discs in planet formation research. In Chapter 4 disc modelling assesses how the variation in pre-main sequence evolution, across the stellar mass range where giant exoplanet detection rates peak, affects the initial conditions for planet formation in a massive protoplanetary disc. A dichotomy emerges between the temperature evolution of discs around low- and intermediate-mass stars in the density profile. As a result not only are discs around intermediate mass star warmer, but they remain at their warmest for longer, and can even heat up at late stages. A direct repercussion of this temperature evolution is the fact that key snowlines can exist at different locations which in turn determine the amount of carbon and oxygen that exists within the gas phase. This provides the perfect opportunity to draw a link between the wide orbit exoplanets around intermediate mass stars and the properties of their natal disc. This thesis demonstrates that modelling of snowlines in discs around intermediate mass stars can be used to determine much tighter radial constraints, and for the first time temporal constraints, on a planet’s formation. With future instruments due to provide a boost to the compositional characterisation of exoplanetary atmospheres (see Section 5.2.4), the wide orbit planets forming in Herbig discs may well provide the best opportunity to zoom in on the initial conditions of giant planet formation, as it is these planets that are most effectively targeted by the modelling procedure presented here. Potential extensions and improvements to this modelling framework are discussed in the following section.

5.2 Future work

5.2.1 Disc masses

Total disc masses still remain uncertain in protoplanetary discs. The largest uncertainty in calculating gas mass with the method adopted in the observational studies in this thesis is the multiplicative factor used to scale the mass of the chosen tracer to the mass of the entire disc. Doing so by abundance ratio in the ISM assumes that no physical or chemical processes have altered this ratio throughout the evolution of the disc, for example it does not take into account the effects of isotope-selective photo dissociation. Physical-chemical modelling by Kama et al. (2016) draws on detections of atomic carbon, a large range of CO transitions and SED fitting to constrain parametric models to precisely estimate mass in HD100546 and TW Hya. However such an approach requires a large amount of observational data for individual discs and so can only be applied in full to the best-studied systems. This application of this approach to large surveys of discs in order to gain statistically significant results for a bulk population is unfeasible for the time being.

Combining the estimates from multiple optically thin tracers is a sensible approach though. The best current candidates for observational mass tracers must continue to be targeted, such as HD (Kama et al., 2016), $C^{18}O$ (Ansdell et al., 2016) and less abundant CO isotopologues (Booth et al., 2019). Corresponding mass estimates should then be made for different tracers within the same disc and compared to establish where trends lie. For example, if in a large sample $C^{18}O$ estimates were to habitually underestimate disc mass compared to estimates with other tracers, it would indicate that isotope selective photo-dissociation, or perhaps high optical depth, is a significant factor in a large proportion of the disc population. Alternatively, HD transitions require relatively warm temperatures and are difficult to observe, it may transpire that it is impossible to accurately correct for the inability to trace the mass reservoirs in the midplane and outer disc. Gas lines require greater sensitivity than continuum observations and so gas in discs can sometimes be neglected in large surveys that require short integration times on each source. The result is that with a few exceptions (e.g. the

Lupus survey, Ansdell et al., 2016), we still do not have statistically significant information on gas mass from across the star forming regions.

5.2.2 Tracing spirals with gas line observations

An interesting link with previously identified spiral structure features is found in Chapter 2. One thing that ALMA observations do not seem to be proficiently uncovering in protoplanetary discs is well defined structure in observations of gas. Elias 2-27 shows two clear spiral arms (Pérez et al., 2016), but it remains a sole example of such a morphology despite the vast amount of disc observations since then. Spirals on smaller scales thought to be driven by planets have been identified through observations of dust in systems such as MWC 758 (Boehler et al., 2017; Grady et al., 2012), HD142527 (Christiaens et al., 2014) and V1247 Orionis (Kraus et al., 2017). When categorising the morphologies identified in scattered light images, Garufi et al. (2018) separate these cases from the wide, asymmetric and relatively faint arms seen in 'giant discs' such as HD100546 and HD34282 however. Imaging of gas density distribution in the outer disc with greater angular resolution would provide important insight into systems such as these. Firstly, structure can be better characterised on smaller length scales. But also because an analogue of spiral structure in gas density would confirm the spiral features as a change in local disc density, whereas a symmetric, structure-free outer disc would suggest that the scattered light features are a surface wave or simply clumps of dust density that might be interpreted as the remnants of a broken ring (e.g. DoAr44, HD141569: Avenhaus et al., 2018; Perrot et al., 2016).

5.2.3 HD141569

As detailed in Chapter 3, the only known pre-main sequence hybrid disc HD141569 is uniquely placed as a case study in disc evolution as it appears to be exhibiting the early stages of transforming from a 'protoplanetary' disc to a 'debris' disc. There are a number of exciting new investigations that can be carried out to clarify the key mechanisms driving this evolution. From an observational perspective, the inner regions of the disc remain unresolved at millimetre wavelengths despite being very well characterised in scattered light observations (e.g. with SPHERE

Perrot et al., 2016). Dispersal processes driven by planet formation or photoevaporation are expected to occur from the inside out, and the inner 10s of au in the disc is crucial to understanding how the disc is evolving. High resolution observations of molecular emission lines and dust continuum at millimetre wavelengths will provide a view of the midplane in the inner regions of the disc, where giant planets leave their detectable signatures. There are already observational campaigns working towards this goal, including an ongoing ALMA large program aiming to map the chemical structure in protoplanetary discs both vertically and radially at 10 au scale, and a survey of hybrid and evolved Herbig discs aiming to determine an inventory of the most important molecules in these evolved systems. In combination with existing observations from SPHERE that trace the surface layers of the disc, new high resolution ALMA observations would finally allow for a comprehensive description of inner regions to be obtained. Continuum emission will confirm whether or not midplane analogues to the broken SPHERE ringlets exist. Concentric rings may be formed through carving by an embedded exoplanet (or exoplanets) however the HD141569 ringlets are also consistent with the structures formed through the photoelectric instability (PEI) (Richert et al., 2018). The inner disc morphology as a result of a gap-opening planet (e.g. Muley et al., 2019) differs from the structures that form through scenarios involving PEI (Castrejon et al., 2019). High resolution ALMA observations will be capable of constraining key structural properties in the disc such as width, eccentricity and mass within dust rings in order to distinguish between these scenarios. Furthermore molecular line observations with angular resolution of ∼10s of au will be capable of unveiling the kinematic signatures of orbiting planets in the disc (e.g. Pinte et al., 2018, 2019) or of a misaligned disc (e.g. Mayama et al., 2018).

In addition to new observational evidence, it must be established whether the system is evolving due to universal mechanisms that would be expected in any disc, or whether it's apparent evolution has been accelerated by an interaction/flyby in the past. Prior to the detection of molecular gas in the system, the flyby scenario was investigated and shown to reproduce the large-scale properties of the disc; namely spiral arms in the disc (Quillen et al., 2005), and since then we have gained a much greater knowledge of the inner disc (within 200 au) and of gas content in terms of mass and spatial distribution. New hydrodynamic modelling can revisit the flyby scenario with these important updated constraints. If such an event can explain the low disc mass, the truncation of the gas disc relative to the dust distribution and the containment of detected gas within the inner dust ring, then triggered evolution is the most likely cause, and HD141569 should be considered a unique case of disc interaction. If not, the system is instead likely to be a unique case study in disc evolution that is actively undergoing the dispersal of gas and concentration of dust into debris-like rings whilst still on the pre-main sequence. In this scenario, the high resolution ALMA observations of optically thin molecular gas lines will be crucial in constraining more precisely the location of gas in the disc. Observations with this level of sensitivity will also be able to detect the presence of giant exoplanets capable of carving gaps, or misalignment in the gas disc, through the kinematic signature in the gas lines (Pinte et al., 2019; Walsh et al., 2017).

5.2.4 Connecting stellar & disc evolution

The modelling methods developed here are applied to the system of HR8799; the only exoplanetary system for which C/O has been constrained for multiple directly imaged giant planets in the outer disc. This is however only one system, and may not be representative of all exoplanetary systems with giant planets. A greater number of wide-separation planets to compare with is sorely needed. Observations in the future with JWST and Ariel will provide spectroscopy of an increased number of exoplanets from which C/O can be retrieved. The determination of composition indicators such as C/O ratios in exoplanetary atmospheres are crucial to confirming the link between disc and planet. Due to the prolific detection rates in radial velocity surveys, it is often hot Jupiters and other planets at short separation that are easily targeted. There would be great value in doing the same for statistically significant numbers of wide orbit planets too, particularly those around intermediate mass stars where snowlines exist at 10s or 100s of au. In Chapter 4 an initial comparison of the calculated temperature profiles with known N_2H^+ rings that trace the CO snowline position is made. At the moment only a small number of these observations exist, and only in the cases where N_2H^+ rings are thin and well-resolved can the snowline position be constrained accurately (Qi et al., 2019). Observations of N_2H^+ across the stellar mass range and for a range of ages would allow for the predictions of snowline movement to be tested and potentially for the models to be calibrated to suit observational data.

The methods presented here decouple radiative transfer calculations and disc evolution in our modelling in order to study discs massive enough to form giant planets up to 10 Myr. An intriguing further development would be to include a prescription for simultaneous and consistent disc evolution alongside the stellar evolution, as this will alter the density distribution within the disc and subsequently the temperature profile. Unfortunately most disc evolution codes result in short disc lifetimes, due to either the efficiency of radial drift or of photoevaporation. These shorter timescales disagree with observed evidence of massive discs with ages $\geq$5 Myr, particularly those around Herbig stars (HD100546, HD163296, TW Hya). Viscous evolution, disc dynamics and icy grain compositions have also been shown to influence snowline positions and subsequently the C/N/O ratios in the disc (Piso et al., 2015, 2016). Disc evolution, particularly at later stages is influenced strongly by photoevaporation and so modelling will require a thorough knowledge of photoevaporative rates across the stellar mass range. Current models including EUV, FUV and X-ray photoevaporation only exist for T Tauri stars and not for their Herbig counterparts. The development of such models for intermediate mass stars will provide an important step in this direction (Kunitomo et al. in prep).

References

Adams, F. C., Lada, C. J., and Shu, F. H. (1987). Spectral Evolution of Young Stellar Objects. *The Astrophysical Journal*, 312:788–806. 23

Alexander, R. D., Clarke, C. J., and Pringle, J. E. (2006). Photoevaporation of protoplanetary discs I. Hydrodynamic models. *Monthly Notices of the Royal Astronomical Society*, 369(1):216–228. 25

Alibert, Y., Mordasini, C., and Benz, W. (2011). Extrasolar planet population synthesis III. Formation of planets around stars of different masses. *Astronomy & Astrophysics*, 526:63. 102

André, P., Men'Shchikov, A., Bontemps, S., Könyves, V., Motte, F., Schneider, N., Didelon, P., Minier, V., Saraceno, P., Ward-Thompson, D., Di Francesco, J., White, G., Molinari, S., Testi, L., Abergel, A., Griffin, M., Henning, T., Royer, P., Merín, B., Vavrek, R., Attard, M., Arzoumanian, D., Wilson, C. D., Ade, P., Aussel, H., Baluteau, J. P., Benedettini, M., Bernard, J. P., Blommaert, J. A., Cambrésy, L., Cox, P., Di Giorgio, A., Hargrave, P., Hennemann, M., Huang, M., Kirk, J., Krause, O., Launhardt, R., Leeks, S., Le Pennec, J., Li, J. Z., Martin, P. G., Maury, A., Olofsson, G., Omont, A., Peretto, N., Pezzuto, S., Prusti, T., Roussel, H., Russeil, D., Sauvage, M., Sibthorpe, B., Sicilia-Aguilar, A., Spinoglio, L., Waelkens, C., Woodcraft, A., and Zavagno, A. (2010). From filamentary clouds to prestellar cores to the stellar IMF: Initial highlights from the Herschel Gould Belt Survey. *Astronomy and Astrophysics*, 518(8):102. 3

Andrews, S. M., Rosenfeld, K. A., Kraus, A. L., and Wilner, D. J. (2013). THE MASS DEPENDENCE BETWEEN PROTOPLANETARY DISKS AND THEIR STELLAR HOSTS. *The Astrophysical Journal*, 771(2):129. 16, 12

REFERENCES

Andrews, S. M., Terrell, M., Tripathi, A., Ansdell, M., Williams, J. P., and Wilner, D. J. (2018). Scaling Relations Associated with Millimeter Continuum Sizes in Protoplanetary Disks. *The Astrophysical Journal*, 865(2):157. 15, 7, 8

Andrews, S. M., Wilner, D. J., Espaillat, C., Hughes, A. M., Dullemond, C. P., McClure, M. K., Qi, C., and Brown, J. M. (2011). Resolved images of large cavities in protoplanetary transition disks. *Astrophysical Journal*, 732(1):42. 10, 27, 105

Ansdell, M., Williams, J. P., Manara, C. F., Miotello, A., Facchini, S., Van Der Marel, N., Testi, L., and Van Dishoeck, E. F. (2017). An ALMA Survey of Protoplanetary Disks in the σ Orionis Cluster. *The Astronomical Journal*, 153:240. 16, 12

Ansdell, M., Williams, J. P., Marel, N. v. d., Carpenter, J. M., Guidi, G., Hogerheijde, M., Mathews, G. S., Manara, C. F., Miotello, A., Natta, A., Oliveira, I., Tazzari, M., Testi, L., van Dishoeck, E. F., and van Terwisga, S. E. (2016). ALMA SURVEY OF LUPUS PROTOPLANETARY DISKS. I. DUST AND GAS MASSES. *ApJ*, 828(1):46. 16, 12, 34, 58, 59, 139, 140

Ansdell, M., Williams, J. P., Trapman, L., van Terwisga, S. E., Facchini, S., Manara, C. F., van der Marel, N., Miotello, A., Tazzari, M., Hogerheijde, M., Guidi, G., Testi, L., and van Dishoeck, E. F. (2018). ALMA Survey of Lupus Protoplanetary Disks II: Gas Disk Radii. *The Astrophysical Journal*, 859(1):21. 12

Ardila, D. R., Golimowski, D. A., Krist, J. E., Clampin, M., Ford, H. C., and Illingworth, G. D. (2007). Hubble Space Telescope Advanced Camera for Surveys Coronagraphic Observations of the Dust Surrounding HD 100546. *ApJ*, 665(1):512–534. 19, 54, 60, 61, 62, 67

Ardila, D. R., Lubow, S. H., Golimowski, D. A., Krist, J. E., Clampin, M., Ford, H. C., Hartig, G. F., Illingworth, G. D., Bartko, F., BenItez, N., Blakeslee, J. P., Bouwens, R. J., Bradley, L. D., Broadhurst, T. J., Brown, R. A., Burrows, C. J., Cheng, E. S., Cross, N. J. G., Feldman, P. D., Franx, M., Goto, T., Gronwall, C., Holden, B., Homeier, N., Infante, L., Kimble, R. A., Lesser, M. P., Martel,

A. R., Menanteau, F., Meurer, G. R., Miley, G. K., Postman, M., Sirianni, M., Sparks, W. B., Tran, H. D., Tsvetanov, Z. I., White, R. L., Zheng, W., and Zirm, A. W. (2005). A Dynamical Simulation of the Debris Disk around HD 141569A. *ApJ*, 627(2):986–1000. 89

Armitage, P. J. (2009). *Astrophysics of Planet Formation.* Cambridge University Press, Cambridge. 16

Artymowicz, P. (2004). Debris disks and the formation of planets: a symposium in memory of Fred Gillet ASP Conference Dynamics of Gaseous Disks with Planets. In *Debris disks and the formation of planets: a symposium in memory of Fred Gillet*, volume 324. 120

Arzoumanian, D., André, P., Peretto, N., and Könyves, V. (2014). Properties of interstellar filaments as derived from herschel observations. In *Astrophysics and Space Science Proceedings*, volume 36, pages 259–263. Springer, Cham. 3

Asplund, M., Grevesse, N., Sauval, A. J., and Scott, P. (2009). The Chemical Composition of the Sun. *Annual Review of Astronomy and Astrophysics*, 47(1):481–522. 108, 116

Augereau, J. C., Lagrange, A. M., Mouillet, D., and Ménard, F. (1999). HST/NICMOS2 observations of the HD 141569 A circumstellar disk. *A&A*, 350:51–54. 4, 82

Augereau, J. C., Lagrange, A. M., Mouillet, D., and Ménard, F. (2001). HST/NICMOS2 coronagraphic observations of the circumstellar environment of three old PMS stars: HD 100546, SAO 206462 and MWC 480. *Astronomy & Astrophysics*, 365(2):78–89. 4

Augereau, J. C. and Papaloizou, J. C. B. (2004). Structuring the HD 141569 A circumstellar dust disk. *A&A*, 414(3):1153–1164. 89

Avenhaus, H., Quanz, S. P., Garufi, A., Perez, S., Casassus, S., Pinte, C., H-M Bertrang, G., Caceres, C., Benisty, M., and Dominik, C. (2018). Disks around T Tauri Stars with SPHERE (DARTTS-S). I. SPHERE/IRDIS Polarimetric Imaging of Eight Prominent T Tauri Disks *. *ApJ*, 863(44). 140

REFERENCES

Avenhaus, H., Quanz, S. P., Meyer, M. R., Brittain, S. D., Carr, J. S., and Najita, J. R. (2014). HD100546 MULTI-EPOCH SCATTERED LIGHT OBSERVATIONS. *ApJ*, 790(1):56. 18, 47, 48, 54, 63

Bally, J., Langer, W. D., Stark, A. A., and Wilson, R. W. (1987). Filamentary Structure in the Orion Molecular Cloud. *The Astrophysical Journal*, 45:45–49. 3

Banzatti, A., Testi, L., Isella, A., Natta, A., Neri, R., and Wilner, D. J. (2011). Astronomy & Astrophysics New constraints on dust grain size and distribution in CQ Tauri. *A&A*, 525. 78

Barenfeld, S. A., Carpenter, J. M., Ricci, L., and Isella, A. (2016). ALMA OBSERVATIONS OF CIRCUMSTELLAR DISKS IN THE UPPER SCORPIUS OB ASSOCIATION. *The Astrophysical Journal*, 827(2):142. 16, 12

Barenfeld, S. A., Carpenter, J. M., Sargent, A. I., Isella, A., and Ricci, L. (2017). Measurement of Circumstellar Disk Sizes in the Upper Scorpius OB Association with ALMA. *The Astrophysical Journal*, 851:85. 12

Baruteau, C., Crida, A., Paardekooper, S.-J., Guilet, J., Bitsch, B., Nelson, R., Kley, W., and Papaloizou, J. (2014). Planet-Disc Interactions and Early Evolution of Planetary Systems. In Henrik Beuther, Ralf S. Klessen, Cornelis P. Dullemond, and Thomas Henning, editors, *PPVI*, pages 667–689. Univ.of Arizona Press, Tucson. 60, 71

Bate, M. R. (2000). Predicting the properties of binary stellar systems: The evolution of accreting protobinary systems. *Monthly Notices of the Royal Astronomical Society*, 314(1):33–53. 3

Beckwith, S. V. W. and Sargent, A. I. (1991). Particle emissivity in circumstellar disks. *The Astrophysical Journal*, 381:250. 21

Bell, K. R., Cassen, P. M., Klahr, H. H., and Henning, T. (1997). THE STRUCTURE AND APPEARANCE OF PROTOSTELLAR ACCRETION DISKS : LIMITS ON DISK FLARING. *The Astrophysical Journal*, 486:372–387. 4

Bergin, E. A., Cleeves, L. I., Gorti, U., Zhang, K., Blake, G. A., Green, J. D., Andrews, S. M., Evans II, N. J., Henning, T., Öberg, K., Pontoppidan, K., Qi, C., Salyk, C., and van Dishoeck, E. F. (2013). An old disk still capable of forming a planetary system. *Nature*, 493(7434):644–646. 16, 108

Biller, B. A., Liu, M. C., Rice, K., Wahhaj, Z., Nielsen, E., Hayward, T., Kuchner, M. J., Close, L. M., Chun, M., Ftaclas, C., and Toomey, D. W. (2015). The Gemini NICI Planet-Finding Campaign: asymmetries in the HD 141569 disc. *MNRAS*, 450(4):4446–4457. 21, 22, 82, 83, 87, 88, 90, 97

Birnstiel, T. and Andrews, S. M. (2013). ON THE OUTER EDGES OF PROTOPLANETARY DUST DISKS. *ApJ*, 780(2):153. 16

Birnstiel, T., Dullemond, C. P., and Pinilla, P. (2013). Lopsided dust rings in transition disks. *A&A*, 550:L8. 91

Birnstiel, T., Klahr, H., and Ercolano, B. (2012). A simple model for the evolution of the dust population in protoplanetary disks. *Astronomy and Astrophysics*, 539:A148. 18, 43, 104, 106

Birnstiel, T., Ormel, C. W., and Dullemond, C. P. (2011). Dust size distributions in coagulation/fragmentation equilibrium: numerical solutions and analytical fits. *A&A*, 525:A11. 18, 79

Birnstiel, T., Ricci, L., Trotta, F., Dullemond, C. P., Natta, A., Testi, L., Dominik, C., Henning, T., Ormel, C. W., and Zsom, A. (2010). Testing the theory of grain growth and fragmentation by millimeter observations of protoplanetary disks. *A&A*, 516:L14. 78

Bjorkman, J. E. and Wood, K. (2001). Radiative Equilibrium and Temperature Correction in Monte Carlo Radiation Transfer. *The Astrophysical Journal*, 554(1):615–623. 42

Boccaletti, A., Di Folco, E., Pantin, E., Dutrey, A., Guilloteau, S., Tang, Y. W., Piétu, V., Habart, E., Milli, J., Beck, T. L., and Maire, A. L. (2020). Possible evidence of ongoing planet formation in AB Aurigae. A showcase of the SPHERE/ALMA synergy. 15, 6

Boehler, Y., Ricci, L., Weaver, E., Isella, A., Benisty, M., Carpenter, J., Grady, C., Shen, B.-T., Tang, Y.-W., and Perez, L. (2017). The complex morphology of the young disk MWC 758: Spirals and dust clumps around a large cavity. *ApJ*, 853(2):162. 91, 140

Boneberg, D. M., Facchini, S., Clarke, C. J., Ilee, J. D., Booth, R. A., and Bruderer, S. (2018). The extremely truncated circumstellar disc of V410 X-ray 1: A precursor to TRAPPIST-1? *Monthly Notices of the Royal Astronomical Society*, 477(1):325–334. 129

Boneberg, D. M., Panić, O., Haworth, T. J., Clarke, C. J., and Min, M. (2016). Determining the mid-plane conditions of circumstellar discs using gas and dust modelling: a study of HD 163296. *MNRAS*, 461:385–401. 30, 59

Booth, A. S., Walsh, C., Ilee, J. D., Notsu, S., Qi, C., Nomura, H., and Akiyama, E. (2019). The First Detection of 13 C 17 O in a Protoplanetary Disk: A Robust Tracer of Disk Gas Mass. *Astrophysical Journal Letters*, 882:L31. 106, 108, 139

Booth, R. A., Clarke, C. J., Madhusudhan, N., and Ilee, J. D. (2017). Chemical enrichment of giant planets and discs due to pebble drift. *Monthly Notices of the Royal Astronomical Society*, 469(4):3994–4011. 24, 43, 44, 103, 106, 108, 124, 125

Booth, R. A. and Ilee, J. D. (2019). Planet-forming material in a protoplanetary disc : the interplay between chemical evolution and pebble drift. *Monthly Notices of the Royal Astronomical Society*, 487(3):3998–4011. 103

Bouvier, J., Alencar, S. H. P., Harries, T. J., Johns-Krull, C. M., and Romanova, M. M. (2007). Magnetospheric Accretion in Classical T Tauri Stars. In Reipurth, B., Jewitt, D., and Keil, K., editors, *Protostars and Planets V*, pages 479–494. 33

Brauer, F., Dullemond, C. P., and Henning, T. (2008). Coagulation, fragmentation and radial motion of solid particles in protoplanetary disks. *A&A*, 480(3):859–877. 78

Bressan, A., Marigo, P., Girardi, L., Salasnich, B., Cero, C. D., Rubele, S., and Nanni, A. (2012). PARSEC: stellar tracks and isochrones with the PAdova and TRieste Stellar Evolution Code. *MNRAS*, 427:127–145. 46

Brewer, J. M., Fischer, D. A., and Madhusudhan, N. (2017). C/O AND O/H RATIOS SUGGEST SOME HOT JUPITERS ORIGINATE BEYOND THE SNOW LINE. *The Astronomical Journal*, 153(2):83. 102

Brittain, S. D., Carr, J. S., Najita, J. R., Quanz, S. P., and Meyer, M. R. (2014). NIR SPECTROSCOPY OF THE HAeBe STAR HD 100546. III. FURTHER EVIDENCE OF AN ORBITING COMPANION? *ApJ*, 791(2):136. 47

Brittain, S. D., Najita, J. R., Carr, J. S., Liskowsky, J., Troutman, M. R., and Doppmann, G. W. (2013). HIGH-RESOLUTION NEAR-INFRARED SPECTROSCOPY OF HD 100546. II. ANALYSIS OF VARIABLE ROVIBRATIONAL CO EMISSION LINES. *ApJ*, 767:159. 47

Brown, J. M., Blake, G. A., Qi, C., Dullemond, C. P., Wilner, D. J., and Williams, J. P. (2009). EVIDENCE FOR DUST CLEARING THROUGH RESOLVED SUBMILLIMETER IMAGING. *ApJ*, 704(1):496–502. 27

Carmona, A., Thi, W. F., Kamp, I., Baruteau, C., Matter, A., Van Den Ancker, M., Pinte, C., Kóspál, A., Audard, M., Liebhart, A., Sicilia-Aguilar, A., Pinilla, P., Regály, Z., Güdel, M., Henning, T., Cieza, L. A., Baldovin-Saavedra, C., Meeus, G., and Eiroa, C. (2017). Astrophysics A gas density drop in the inner 6 AU of the transition disk around the Herbig Ae star HD 139614 Further evidence for a giant planet inside the disk? *A&A*, 598:118. 27

Castrejon, A., Lyra, W., Richert, A. J. W., and Kuchner, M. (2019). Disentangling Planets from Photoelectric Instability in Gas-rich Optically Thin Dusty Disks. *The Astrophysical Journal*, 887(1):6. 141

Cazzoletti, P., van Dishoeck, E. F., Pinilla, P., Tazzari, M., Facchini, S., van der Marel, N., Benisty, M., Garufi, A., and Pérez, L. (2018). Evidence for a massive dust-trapping vortex connected to spirals: a multi-wavelength analysis of the HD˜135344B protoplanetary disk. *Astronomy & Astrophysics*, 619:A161. 17, 23, 67

Chen, P., Shan, H., and Zhang, P. (2016). A new photometric study of Herbig Ae/Be stars in the infrared. *New Astronomy*, 44:1–11. 33

Chiang, E. I. and Goldreich, P. (1997). Spectral Energy Distributions of T Tauri Stars with Passive Circumstellar Disks. *The Astrophysical Journal*, 490(1):368–376. 11

Choi, J., Dotter, A., Conroy, C., Cantiello, M., Paxton, B., and Johnson, B. D. (2016). MESA ISOCHRONES AND STELLAR TRACKS (MIST). I. SOLAR-SCALED MODELS. *The Astrophysical Journal*, 823(2):102. 17, 34

Christiaens, V., Casassus, S., Perez, S., van der Plas, G., and Ménard, F. (2014). SPIRAL ARMS IN THE DISK OF HD 142527 FROM CO EMISSION LINES WITH ALMA. *The Astrophysical Journal*, 785(1):L12. 140

Condon, J. J. and Ransom, S. M. (2016). *Essential Radio Astronomy*. Princeton University Press. 87

Currie, T., Brittain, S., Grady, C. A., Kenyon, S. J., and Muto, T. (2017). Clarifying the Status of HD 100546 as Observed by the Gemini Planet Imager. *Research Notes of the AAS*, 1(1):40. 135

Currie, T., Cloutier, R., Brittain, S., Grady, C., Burrows, A., Muto, T., Kenyon, S. J., and Kuchner, M. J. (2015). RESOLVING THE HD 100546 PROTOPLANETARY SYSTEM WITH THE GEMINI PLANET IMAGER: EVIDENCE FOR MULTIPLE FORMING, ACCRETING PLANETS. *ApJ*, 814(2):L27. 47

Currie, T., Grady, C. A., Cloutier, R., Konishi, M., Stassun, K., Debes, J., Marel, N. v. d., Muto, T., Jayawardhana, R., and Ratzka, T. (2016). THE MATRYOSHKA DISK: KECK/NIRC2 DISCOVERY OF A SOLAR-SYSTEM-SCALE, RADIALLY SEGREGATED RESIDUAL PROTOPLANETARY DISK AROUND HD 141569A. *The Astrophysical Journal*, 819(2):L26. 96

d 'Alessio, P., Merín, B., Calvet, N., Hartmann, L., and Montesinos, B. (2005). WWW DATABASE OF MODELS OF ACCRETION DISKS IRRADIATED BY THE CENTRAL STAR. *RMxAA*, 41:61–67. 56, 79

de Muizon, M., Strom, R. G., Oort, M. J. A., Claas, J. J., and Braun, R. (1988). G70.7+1.2: Supernova, nova, or stellar shell? *A&A*, 193(248-264). 87

Dent, W. R. F., Greaves, J. S., and Coulson, I. M. (2005). CO emission from discs around isolated HAeBe and Vega-excess stars. *MNRAS*, 359(2):663–676. 82

Dent, W. R. F., Wyatt, M. C., Roberge, A., Augereau, J.-C., Casassus, S., Corder, S., Greaves, J. S., de Gregorio-Monsalvo, I., Hales, A., Jackson, A. P., Hughes, A. M., Lagrange, A.-M., Matthews, B., and Wilner, D. (2014). Molecular gas clumps from the destruction of icy bodies in the \$$\beta$\$ Pictoris debris disk. *Science (80-.).*, 343(6178):1490–1492. 17, 31, 91, 137

Dominik, C. and Dullemond, C. P. (2002). From Protoplanetary to Debris Disks. In *The Origin of Stars and Planets: The VLT View*, pages 439–444. Springer-Verlag, Berlin/Heidelberg. 82

Donaldson, J. K., Weinberger, A. J., Gagné, J., Faherty, J. K., Boss, A. P., and Keiser, S. A. (2016). NEW PARALLAXES AND A CONVERGENCE ANALYSIS FOR THE TW Hya ASSOCIATION. *The Astrophysical Journal*, 833. 30

Dong, R., Li, S., Chiang, E., and Li, H. (2017). Multiple Disk Gaps and Rings Generated by a Single Super-Earth. *The Astrophysical Journal*, 843(2):127. 28

Dong, R., Rafikov, R., Zhu, Z., Hartmann, L., Whitney, B., Brandt, T., Muto, T., Hashimoto, J., Grady, C., Follette, K., Kuzuhara, M., Tanii, R., Knapp, R., Kudo, T., Kusakabe, N., Matsuo, T., Mcelwain, M. W., Miyama, S., Morino, J.-I., Moro-Martin, A., Nishimura, T., Pyo, T.-S., Suto, H., Suzuki, R., Takami, M., Takato, N., Terada, H., Tomono, D., Turner, E. L., Watanabe, M., Yamada, T., Takami, H., Usuda, T., and Tamura, M. (2012). THE MISSING CAVITIES

IN THE SEEDS POLARIZED SCATTERED LIGHT IMAGES OF TRANSITIONAL PROTOPLANETARY DISKS: A GENERIC DISK MODEL. *The Astrophysical Journal*, 750(16pp):161. 5

Dotter, A. (2016). MESA ISOCHRONES AND STELLAR TRACKS (MIST) 0: METHODS FOR THE CONSTRUCTION OF STELLAR ISOCHRONES. *The Astrophysical Journal Supplement Series*, 222:8. 105

Draine, B. (2003). Interstellar Dust Grains. *Annual Review of Astronomy and Astrophysics*, 41(1):241–289. 20, 124

Draine, B. T. (2006). On the Submillimeter Opacity of Protoplanetary Disks. *ApJ*, 636:1114–1120. 16, 20, 9, 18, 21, 56, 75, 76, 77, 79, 86

Du, F., Bergin, E. A., and Hogerheijde, M. R. (2015). VOLATILE DEPLETION IN THE TW HYDRAE DISK ATMOSPHERE. *ApJL*, 807:L32. 16

Dullemond, C. P., Birnstiel, T., Huang, J., Kurtovic, N. T., Andrews, S. M., Guzmán, V. V., Pérez, L. M., Isella, A., Zhu, Z., Benisty, M., Wilner, D. J., Bai, X.-N., Carpenter, J. M., Zhang, S., and Ricci, L. (2018). The Disk Substructures at High Angular Resolution Project (DSHARP). VI. Dust Trapping in Thin-ringed Protoplanetary Disks. *ApJL*, 869:L46. 17, 95, 131

Dullemond, C. P. and Dominik, C. (2004a). Flaring vs. self-shadowed disks: The SEDs of Herbig Ae/Be stars. *Astronomy and Astrophysics*, 417(1):159–168. 6

Dullemond, C. P. and Dominik, C. (2004b). The effect of dust settling on the appearance of protoplanetary disks. *Astronomy and Astrophysics*, 421(3):1075–1086. 11

Dullemond, C. P., Hollenbach, D., Kamp, I., and D'Alessio, P. (2007). Models of the Structure and Evolution of Protoplanetary Disks. In *Protostars and Planets V*, page 555. 16, 19

Dutrey, A., Di Folco, E., Guilloteau, S., Boehler, Y., Bary, J., Beck, T., Beust, H., Chapillon, E., Gueth, F., Huré, J.-M., Pierens, A., Piétu, V., Simon, M., and Tang, Y.-W. (2014). Possible planet formation in the young, low-mass, multiple stellar system GG Tau A. *Nature*, 514(7524):600–602. 63

Dzyurkevich, N., Flock, M., Turner, N. J., Klahr, H., and Henning, T. (2010). Trapping solids at the inner edge of the dead zone: 3-D global MHD simulations. *A&A*, 515:A70. 17

Eisner, J. A., Arce, H. G., Ballering, N. P., Bally, J., Andrews, S. M., Boyden, R. D., Francesco, J. D., Fang, M., Johnstone, D., Kim, J. S., Mann, R. K., Matthews, B., Pascucci, I., Ricci, L., Sheehan, P. D., and Williams, J. P. (2018). Protoplanetary Disk Properties in the Orion Nebula Cluster: Initial Results from Deep, High-resolution ALMA Observations. *The Astrophysical Journal*, 860(1):77. 16, 12

Eistrup, C., Walsh, C., and Van Dishoeck, E. F. (2016). Setting the volatile composition of (exo)planet-building material: Does chemical evolution in disk midplanes matter? *Astronomy and Astrophysics*, 595:A83. 16

Espaillat, C., Calvet, N., D'alessio, P., Hernández, J., Qi, C., Hartmann, L., Furlan, E., and Watson, D. M. (2007). ON THE DIVERSITY OF THE TAURUS TRANSITIONAL DISKS: UX TAU A & LK CA 15. Technical report. 27

Fabrycky, D. C. and Murray-Clay, R. A. (2010). Stability of the directly imaged multiplanet system HR 8799: Resonance and masses. *Astrophysical Journal*, 710(2):1408–1421. 121, 126

Facchini, S., Birnstiel, T., Bruderer, S., and Van Dishoeck, E. F. (2017). Different dust and gas radial extents in protoplanetary disks: consistent models of grain growth and CO emission. *A&A*, 605:16. 73

Fairlamb, J. R., Oudmaijer, R. D., Mendigutía, I., Ilee, J. D., and van den Ancker, M. E. (2015). A spectroscopic survey of Herbig Ae/Be stars with X-shooter I. Stellar parameters and accretion rates. *Monthly Notices of the Royal Astronomical Society*, 453(1):976–1001. 46, 113

Favre, C., Cleeves, L. I., Bergin, E. A., Qi, C., and Blake, G. A. (2013). A SIGNIFICANTLY LOW CO ABUNDANCE TOWARD THE TW Hya PROTOPLANETARY DISK: A PATH TO ACTIVE CARBON CHEMISTRY? *The Astrophysical Journal*, 776(2):L38. 16

Fayolle, E. C., Balfe, J., Loomis, R., Bergner, J., Graninger, D., Rajappan, M., and Öberg, K. I. (2016). N2 and CO desorption energies from water ice. *The Astrophysical Journal*, 816(2):L28. 108, 111

Fedele, D., Tazzari, M., Booth, R., Testi, L., Clarke, C. J., Pascucci, I., Kospal, A., Semenov, D., Bruderer, S., Henning, T., and Teague, R. (2018). ALMA continuum observations of the protoplanetary disk AS 209 Evidence of multiple gaps opened by a single planet. *A&A*, 610:A24. 27

Fedele, D., Van Den Ancker, M. E., Henning, T., Jayawardhana, R., and Oliveira, J. M. (2010). Timescale of mass accretion in pre-main-sequence stars. *A&A*, 510:72. 30

Finkbeiner, D. P., Davis, M., and Schlegel, D. J. (1999). EXTRAPOLATION OF GALACTIC DUST EMISSION AT 100 MICRONS TO COSMIC MICROWAVE BACKGROUND RADIATION FREQUENCIES USING FIRAS. *THE ASTROPHYSICAL JOURNAL*, 524:867–886. 21

Flaherty, K. M., Hughes, A. M., Andrews, S. M., Qi, C., Wilner, D. J., Boley, A. C., White, J. A., Harney, W., and Zachary, J. (2016). RESOLVED CO GAS INTERIOR TO THE DUST RINGS OF THE HD 141569 DISK. *ApJ*, 818(1):97. 82, 85, 93

Fleck, J. and Canfield, E. (1984). A random walk procedure for improving the computational efficiency of the implicit Monte Carlo method for nonlinear radiation transport. *Journal of Computational Physics*, 54(3):508–523. 43

Follette, K. B., Rameau, J., Dong, R., Pueyo, L., Close, L. M., Duchêne, G., Fung, J., Leonard, C., Macintosh, B., Males, J. R., Marois, C., Millar-Blanchaer, M. A., Morzinski, K. M., Mullen, W., Perrin, M., Spiro, E., Wang, J., Ammons, S. M., Bailey, V. P., Barman, T., Bulger, J., Chilcote, J., Cotten, T., De Rosa, R. J., Doyon, R., Fitzgerald, M. P., Goodsell, S. J., Graham, J. R., Greenbaum, A. Z., Hibon, P., Hung, L.-W., Ingraham, P., Kalas, P., Konopacky, Q., Larkin, J. E., Maire, J., Marchis, F., Metchev, S., Nielsen, E. L., Oppenheimer, R., Palmer, D., Patience, J., Poyneer, L., Rajan, A., Rantakyrö, F. T., Savransky, D., Schneider, A. C., Sivaramakrishnan, A., Song, I., Soummer, R., Thomas, S., Vega, D., Wallace, J. K., Ward-Duong, K., Wiktorowicz, S., and Wolff, S. (2017). Complex Spiral Structure in the HD 100546 Transitional Disk as Revealed by GPI and MagAO. *AJ*, 153(6):264. 18, 5, 47, 48, 54, 60

Garufi, A., Benisty, M., Pinilla, P., Tazzari, M., Dominik, C., Ginski, C., Henning, T., Kral, Q., Langlois, M., Ménard, F., Stolker, T., Szulagyi, J., Villenave, M., and Van Der Plas, G. (2018). Evolution of protoplanetary disks from their taxonomy in scattered light: Spirals, rings, cavities, and shadows. *Astronomy and Astrophysics*, 620:94. 140

Garufi, A., Quanz, S. P., Avenhaus, H., Buenzli, E., Dominik, C., Meru, F., Meyer, M. R., Pinilla, P., Schmid, H. M., and Wolf, S. (2013). Small vs. large dust grains in transitional disks: do different cavity sizes indicate a planet? *Astronomy & Astrophysics*, 560:A105. 15, 6

Garufi, A., Quanz, S. P., Schmid, H. M., Mulders, G. D., Avenhaus, H., Boccaletti, A., Ginski, C., Langlois, M., Stolker, T., Augereau, J.-C., Benisty, M., Lopez, B., Dominik, C., Gratton, R., Henning, T., Janson, M., Ménard, F., Meyer, M. R., Pinte, C., Sissa, E., Vigan, A., Zurlo, A., Bazzon, A., Buenzli, E., Bonnefoy, M., Brandner, W., Chauvin, G., Cheetham, A., Cudel, M., Desidera, S., Feldt, M., Galicher, R., Kasper, M., Lagrange, A.-M., Lannier, J., Maire, A. L., Mesa, D., Mouillet, D., Peretti, S., Perrot, C., Salter, G., and Wildi, F. (2016). The SPHERE view of the planet-forming disk around HD 100546. *A&A*, 588:A8. 18, 47, 48, 54, 60, 63

Ginski, C., Stolker, T., Pinilla, P., Dominik, C., Boccaletti, A., De Boer, J., Benisty, M., Biller, B., Feldt, M., Garufi, A., Keller, C. U., Kenworthy, M., Maire, A. L., Ménard, F., Mesa, D., Milli, J., Min, M., Pinte, C., Quanz, S. P., Van Boekel, R., Bonnefoy, M., Chauvin, G., Desidera, S., Gratton, R., Girard, J. H., Keppler, M., Kopytova, T., Lagrange, A. M., Langlois, M., Rouan, D., and Vigan, A. (2016). Direct detection of scattered light gaps in the transitional disk around HD 97048 with VLT/SPHERE. *Astronomy and Astrophysics*, 595. 15, 6

Gomes, R., Levison, H. F., Tsiganis, K., and Morbidelli, A. (2005). Origin of the cataclysmic Late Heavy Bombardment period of the terrestrial planets. *Nature*, 435(7041):466–469. 121

Gonzalez, J.-F., Laibe, G., Maddison, S. T., Pinte, C., and Ménard, F. (2015). ALMA images of discs: are all gaps carved by planets? *MNRAS*, 454:36–40. 28

Gorti, U., Dullemond, C. P., and Hollenbach, D. (2009). TIME EVOLUTION OF VISCOUS CIRCUMSTELLAR DISKS DUE TO PHOTOEVAPORATION BY FAR-ULTRAVIOLET, EXTREME-ULTRAVIOLET, AND X-RAY RADIATION FROM THE CENTRAL STAR. *The Astrophysical Journal*, 705(2):1237–1251. 28

Goto, M., Usuda, T., Dullemond, C. P., Henning, T., Linz, H., Stecklum, B., and Suto, H. (2006). Inner Rim of a Molecular Disk Spatially Resolved in Infrared CO Emission Lines. *ApJ*, 652(1):758–762. 83, 89

Grady, C. A., Muto, T., Hashimoto, J., Fukagawa, M., Currie, T., and Biller, B. (2012). SPIRAL ARMS IN THE ASYMMETRICALLY ILLUMINATED DISK OF MWC 758 AND CONSTRAINTS ON GIANT PLANETS. *The Astrophysical Journal*, 762(13pp). 140

Grady, C. A., Polomski, E. F., Henning, T., Stecklum, B., Woodgate, B. E., Telesco, C. M., Piña, R. K., Gull, T. R., Boggess, A., Bowers, C. W., Bruhweiler, F. C., Clampin, M., Danks, A. C., Green, R. F., Heap, S. R., Hutchings, J. B., Jenkins, E. B., Joseph, C., Kaiser, M. E., Kimble, R. A., Kraemer, S., Lindler, D., Linsky, J. L., Maran, S. P., Moos, H. W., Plait, P., Roesler, F., Timothy, J. G., and Weistrop, D. (2001). The Disk and Environment of the Herbig B[CLC]e[/CLC] Star HD 100546. *AJ*, 122(6):3396–3406. 54

Gray, R. O., Corbally, C. J., Garrison, R. F., Mcfadden, M. T., and Robinson, P. E. (2003). CONTRIBUTIONS TO THE NEARBY STARS (NSTARS) PROJECT: SPECTROSCOPY OF STARS EARLIER THAN M0 WITHIN 40 PARSECS: THE NORTHERN SAMPLE. I. *Astronomical Journal*, 126:2048–2059. 105, 116

Guidi, G., Tazzari, M., Testi, L., de Gregorio-Monsalvo, I., Chandler, C. J., Pérez, L., Isella, A., Natta, A., Ortolani, S., Hennings, T., Corder, S., Linz, H., Andrews, S., Wilner, D., Ricci, L., Carpenter, J., Sargent, A., Mundy, L., Storm, S., Calvet, N., Dullemond, C., Greaves, J., Lazio, J., Deller, A., and Kwon, W. (2016). Dust properties across the CO snowline in the HD 163296 disk from ALMA and VLA observations. *A&A*, 588:A112. 21, 23, 76, 78

Haffert, S. Y., Bohn, A. J., de Boer, J., Snellen, I. A., Brinchmann, J., Girard, J. H., Keller, C. U., and Bacon, R. (2019). Two accreting protoplanets around the young star PDS 70. 5, 28

Haisch, K. E., Lada, E. A., and Lada, C. J. (2001). Disk Frequencies and Lifetimes in Young Clusters. *The Astrophysical Journal, Volume 553, Issue 2, pp. L153-L156.*, 553:L153–L156. 30

Hammer, M., Pinilla, P., Kratter, K. M., and Lin, M.-K. (2019). Observational diagnostics of elongated planet-induced vortices with realistic planet formation time-scales. *MNRAS*, 482:3609–3621. 23

Hartmann, L., Calvet, N., Gullbring, E., and D'Alessio, P. (1998). Accretion and the Evolution of T Tauri Disks. *The Astrophysical Journal*, 495(1):385–400. 9, 105

Henning, T., Launhardt, R., Steinacker, J., and Thamm, E. (1994). Cold dust around southern Herbig Ae/Be stars. *A&A*, 291:546. 78

Herbig, G. H. (1960). The Spectra of Be- and Ae-TYPE Stars Associated with Nebulosity. *The Astrophysical Journal Supplement Series*, 4:337. 32

Hillenbrand, L. A., Strom, S. E., Vrba, F. J., and Keene, J. (1992). Herbig Ae/Be stars - Intermediate-mass stars surrounded by massive circumstellar accretion disks. *The Astrophysical Journal*, 397:613. 6, 32

Högbom, J. A. (1974). Aperture Synthesis with a Non-Regular Distribution of Interferometer Baselines. *Astronomy and Astrophysics Supplement Series*, 15:417. 39

Holland, W. S., Matthews, B. C., Kennedy, G. M., Greaves, J. S., Wyatt, M. C., Booth, M., Bastien, P., Bryden, G., Butner, H., Chen, C. H., Chrysostomou, A., Jenness, T., Kavelaars, . J., Lawler, S., Lestrade, J.-F., Marshall, J. P., Pani, O., Phillips, N., Serjeant, S., Schieven, G. H., Sibthorpe, B., Vican, L., Ward-Thompson, D., and Van Der Werf, P. (2017). SONS: The JCMT legacy survey of debris discs in the submillimetre. *MNRAS*, 470:3606–3663. 95

Huang, J., Andrews, S. M., Dullemond, C. P., Isella, A., Pérez, L. M., Guzmán, V. V., Oberg, K. I. ., Zhu, Z., Zhang, S., Bai, X.-N., Benisty, M., Birnstiel, T., Carpenter, J. M., Hughes, A. M., Ricci, L., Weaver, E., and Wilner, D. J. (2018). The Disk Substructures at High Angular Resolution Project (DSHARP): II. Characteristics of Annular Substructures. *ApJL*, 869:L42. 28

Huang, J., Andrews, S. M., Dullemond, C. P., Öberg, K. I., Qi, C., Zhu, Z., Birnstiel, T., Carpenter, J. M., Isella, A., Macías, E., McClure, M. K., Pérez, L. M., Teague, R., Wilner, D. J., and Zhang, S. (2020). A Multifrequency ALMA Characterization of Substructures in the GM Aur Protoplanetary Disk. *The Astrophysical Journal*, 891(1):48. 113

Hughes, A. M., Lieman-Sifry, J., Flaherty, K. M., Daley, C. M., Roberge, A., Kóspál, ., Moór, A., Kamp, I., Wilner, D. J., Andrews, S. M., Kastner, J. H., and Ábrahám, P. (2017). Radial Surface Density Profiles of Gas and Dust in the Debris Disk around 49 Ceti. *The Astrophysical Journal*, 839:86. 96

Hughes, A. M., Wilner, D. J., Kamp, I., and Hogerheijde, M. R. (2008). A Resolved Molecular Gas Disk around the Nearby A Star 49 Ceti. *ApJ*, 681(1):626–635. 10, 57, 94

Ida, S. and Lin, D. N. C. (2005). Toward a Deterministic Model of Planetary Formation. III. Mass Distribution of ShortPeriod Planets around Stars of Various Masses. *The Astrophysical Journal*, 626(2):1045–1060. 102

Ilee, J. D., Forgan, D. H., Evans, M. G., Hall, C., Booth, R., Clarke, C. J., Rice, W. K., Boley, A. C., Caselli, P., Hartquist, T. W., and Rawlings, J. M. (2017). The chemistry of protoplanetary fragments formed via gravitational instabilities. *Monthly Notices of the Royal Astronomical Society*, 472(1):189–204. 103, 122

Ireland, M. J. and Kraus, A. L. (2008). THE DISK AROUND CoKu TAURI/4: CIRCUMBINARY, NOT TRANSITIONAL. *The Astrophysical Journal*, 678:59–62. 28

Isella, A., Carpenter, J. M., and Sargent, A. I. (2010). INVESTIGATING PLANET FORMATION IN CIRCUMSTELLAR DISKS: CARMA OBSERVATIONS OF RY Tau AND DG Tau. *The Astrophysical Journal*, 714:1746–1761. 9

Isella, A., Guidi, G., Testi, L., Liu, S., Li, H., Li, S., Weaver, E., Boehler, Y., Carperter, J. M., De Gregorio-Monsalvo, I., Manara, C. F., Natta, A., Pérez, L. M., Ricci, L., Sargent, A., Tazzari, M., and Turner 11, N. (2016). Ringed Structures of the HD 163296 Protoplanetary Disk Revealed by ALMA. *PRL*, 117:251101. 78

Isella, A., Huang, J., Andrews, S. M., Dullemond, C. P., Birnstiel, T., Zhang, S., Zhu, Z., Guzmán, V. V., Pérez, L. M., Bai, X.-N., Benisty, M., Carpenter, J. M., Ricci, L., and Wilner, D. J. (2018). The Disk Substructures at High Angular Resolution Project (DSHARP). IX. A High-definition Study of the HD 163296 Planet-forming Disk. *The Astrophysical Journal Letters*, 869:L49. 96

Jackson, A. P., Wyatt, M. C., Bonsor, A., and Veras, D. (2014). Debris froms giant impacts between planetary embryos at large orbital radii. *MNRAS*, 440(4):3757–3777. 91

Jäger, C., Mutschke, H., and Henning, T. (1998). Optical properties of carbonaceous dust analogues. *A&A*, 332:291–299. 20

Jin, S., Isella, A., Huang, P., Li, S., Li, H., and Ji, J. (2019). New Constraints on the Dust and Gas Distribution in the LkCa 15 Disk from ALMA. *The Astrophysical Journal*, 881:108. 113

Johansen, A. and Lacerda, P. (2010). Prograde rotation of protoplanets by accretion of pebbles in a gaseous environment. *Monthly Notices of the Royal Astronomical Society*, 404(1):475–485. 104

Johansen, A., Oishi, J. S., Low, M. M. M., Klahr, H., Henning, T., and Youdin, A. (2007). Rapid planetesimal formation in turbulent circumstellar disks. *Nature*, 448(7157):1022–1025. 104

Johnson, J. A., Aller, K. M., Howard, A. W., and Crepp, J. R. (2010). Giant Planet Occurrence in the Stellar Mass-Metallicity Plane. *Publications of the Astronomical Society of the Pacific*, 122(894):905–915. 35, 102, 138

Johnston, K. G., Robitaille, T. P., Beuther, H., Linz, H., Boley, P., Kuiper, R., Keto, E., Hoare, M. G., and Boekel, R. V. (2015). A KEPLERIAN-LIKE DISK AROUND the FORMING O-TYPE STAR AFGL 4176. *Astrophysical Journal Letters*, 813(1). 35

Johnstone, D., Hollenbach, D., and Bally, J. (1998). Photoevaporation of Disks and Clumps by Nearby Massive Stars: Application to Disk Destruction in the Orion Nebula. *The Astrophysical Journal*, 499(2):758–776. 4

Juhász, A. and Rosotti, G. P. (2018). Spiral arms in thermally stratified protoplanetary discs. *MNRASL*, 474(1):L32–L36. 66

Kama, M., Bruderer, S., Van Dishoeck, E. F., Hogerheijde, M., Folsom, C. P., Miotello, A., Fedele, D., Belloche, A., Güsten, R., and Wyrowski, F. (2016). Volatile-carbon locking and release in protoplanetary disks A study of TW Hya and HD 100546. *A&A*, 592:A83. 16, 59, 139

Kamp, I. and Dullemond, C. P. (2004). The gas temperature in the surface layers of protoplanetary disks. *ApJ*, 615:991–999. 42

Kemper, F., Vriend, W. J., and Tielens, A. G. G. M. (2004). The Absence of Crystalline Silicates in the Diffuse Interstellar Medium. *The Astrophysical Journal*, 609(2):826–837. 9

Kennedy, G. M. and Kenyon, S. J. (2008a). Planet Formation around Stars of Various Masses: Hot SuperEarths. *The Astrophysical Journal*, 682(2):1264–1276. 102

Kennedy, G. M. and Kenyon, S. J. (2008b). Planet Formation around Stars of Various Masses: The Snow Line and the Frequency of Giant Planets. *The Astrophysical Journal*, 673(1):502–512. 108

Kennedy, G. M. and Wyatt, M. C. (2014). Do two-temperature debris discs have multiple belts? *MNRAS*, 444(4):3164–3182. 26, 82, 95

Keppler, M., Benisty, M., Müller, A., Henning, T., Van Boekel, R., Cantalloube, F., Ginski, C., Van Holstein, R. G., Maire, A. L., Pohl, A., Samland, M., Avenhaus, H., Baudino, J. L., Boccaletti, A., De Boer, J., Bonnefoy, M., Chauvin, G., Desidera, S., Langlois, M., Lazzoni, C., Marleau, G. D., Mordasini, C., Pawellek, N., Stolker, T., Vigan, A., Zurlo, A., Birnstiel, T., Brandner, W., Feldt, M., Flock, M., Girard, J., Gratton, R., Hagelberg, J., Isella, A., Janson, M., Juhasz, A., Kemmer, J., Kral, Q., Lagrange, A. M., Launhardt, R., Matter, A., Ménard, F., Milli, J., Mollière, P., Olofsson, J., Pérez, L., Pinilla, P., Pinte, C., Quanz, S. P., Schmidt, T., Udry, S., Wahhaj, Z., Williams, J. P., Buenzli, E., Cudel, M., Dominik, C., Galicher, R., Kasper, M., Lannier, J., Mesa, D., Mouillet, D., Peretti, S., Perrot, C., Salter, G., Sissa, E., Wildi, F., Abe, L., Antichi, J., Augereau, J. C., Baruffolo, A., Baudoz, P., Bazzon, A., Beuzit, J. L., Blanchard, P., Brems, S. S., Buey, T., De Caprio, V., Carbillet, M., Carle, M., Cascone, E., Cheetham, A., Claudi, R., Costille, A., Delboulbé, A., Dohlen, K., Fantinel, D., Feautrier, P., Fusco, T., Giro, E., Gluck, L., Gry, C., Hubin, N., Hugot, E., Jaquet, M., Le Mignant, D., Llored, M., Madec, F., Magnard, Y., Martinez, P., Maurel, D., Meyer, M., Möller-Nilsson, O., Moulin, T., Mugnier, L., Origné, A., Pavlov, A., Perret, D., Petit, C., Pragt, J., Puget, P., Rabou, P., Ramos, J., Rigal, F., Rochat, S., Roelfsema, R., Rousset, G., Roux, A., Salasnich, B., Sauvage, J. F., Sevin, A., Soenke, C., Stadler, E., Suarez, M., Turatto, M., and Weber, L. (2018). Discovery of a planetary-mass companion within the gap of the transition disk around PDS 70. *Astronomy and Astrophysics*, 617. 28

Klahr, H. and Bodenheimer, P. (2006). Formation of Giant Planets by Concurrent Accretion of Solids and Gas inside an Anticyclonic Vortex. *ApJ*, 639(1):432–440. 16

Kley, W. (2000). On the migration of a system of protoplanets. *Monthly Notices of the Royal Astronomical Society*, 313(4):47–51. 126

Konishi, M., Grady, C. A., Schneider, G., Shibai, H., McElwain, M. W., Nesvold, E. R., Kuchner, M. J., Carson, J., Debes, J. H., Gaspar, A., Henning, T. K., Hines, D. C., Hinz, P. M., Jang-Condell, H., Moro-Martin, A., Perrin, M., Rodigas, T. J., Serabyn, E., Silverstone, M. D., Stark, C. C., Tamura, M., Weinberger, A. J., and Wisniewski, J. P. (2016). DISCOVERY OF AN INNER DISK COMPONENT AROUND HD 141569 A. *ApJ*, 818(2):L23. 90

Konopacky, Q. M., Barman, T. S., Macintosh, B. A., and Marois, C. (2013). Detection of Carbon Monoxide and Water Absorption Lines in an Exoplanet Atmosphere. *Science*, 339(6126):1398–1401. 108

Kospal, A., Moor, A., Juhasz, A., Abraham, P., Apai, D., Csengeri, T., Grady, C. A., Henning, T., Hughes, A. M., Kiss, C., Pascucci, I., and Schmalzl, M. (2013). ALMA OBSERVATIONS OF THE MOLECULAR GAS IN THE DEBRIS DISK OF THE 30 Myr OLD STAR HD 21997. *Astrophysical Journal*, 776(2):77. 49, 93, 94

Kral, Q., Marino, S., Wyatt, M. C., Kama, M., and Matra, L. (2018). Imaging [CI] around HD 131835: reinterpreting young debris discs with protoplanetary disc levels of CO gas as shielded secondary discs. *Monthly Notices of the Royal Astronomical Society*, 000:1–23. 137

Kral, Q., Marino, S., Wyatt, M. C., Kama, M., and Matrá, L. (2019). Imaging [CI] around HD 131835: reinterpreting young debris discs with protoplanetary disc levels of CO gas as shielded secondary discs. *Monthly Notices of the Royal Astronomical Society*, 489(3):3670–3691. 30

Kral, Q., Matrà, L., Wyatt, M. C., and Kennedy, G. M. (2017a). Predictions for the secondary CO, C and O gas content of debris discs from the destruction of volatile-rich planetesimals. *Monthly Notices of the Royal Astronomical Society*, 469(1):521–550. 31

Kral, Q., Matrà, L., Wyatt, M. C., and Kennedy, G. M. (2017b). Predictions for the secondary CO, C and O gas content of debris discs from the destruction of volatile-rich planetesimals. *Monthly Notices of the Royal Astronomical Society*, 469(1):521–550. 91, 95

Kratter, K. M., Murray-Clay, R. A., and Youdin, A. N. (2010). The runts of the litter: Why planets formed through gravitational instability can only be failed binary stars. *Astrophysical Journal*, 710(2):1375–1386. 122

Kraus, S., Kreplin, A., Fukagawa, M., Muto, T., Sitko, M. L., Young, A. K., Bate, M. R., Harries, T., Monnier, J. D., Willson, M., and Wisniewski, J. (2017). Dust-trapping vortices and a potentially planet-triggered spiral wake in the pre-transitional disk of V1247 Orionis. *ApJL*, 848:L11. 17, 137, 140

Krijt, S., Schwarz, K. R., Bergin, E. A., and Ciesla, F. J. (2018). Transport of CO in Protoplanetary Disks: Consequences of Pebble Formation, Settling, and Radial Drift. *The Astrophysical Journal*, 864(1):78. 103

Kudo, T., Hashimoto, J., Muto, T., Liu, H. B., Dong, R., Hasegawa, Y., Tsukagoshi, T., and Konishi, M. (2018). A Spatially Resolved au-scale Inner Disk around DM Tau. *The Astrophysical Journal Letters*, 868:L5. 113

Lacour, S., Nowak, M., Wang, J., Pfuhl, O., Eisenhauer, F., Abuter, R., Amorim, A., Anugu, N., Benisty, M., Berger, J. P., Beust, H., Blind, N., Bonnefoy, M., Bonnet, H., Bourget, P., Brandner, W., Buron, A., Collin, C., Charnay, B., Chapron, F., Clénet, Y., Coudé Du Foresto, V., De Zeeuw, P. T., Deen, C., Dembet, R., Dexter, J., Duvert, G., Eckart, A., Förster Schreiber, N. M., Fédou, P., Garcia, P., Garcia Lopez, R., Gao, F., Gendron, E., Genzel, R., Gillessen, S., Gordo, P., Greenbaum, A., Habibi, M., Haubois, X., Haußmann, F., Henning, T., Hippler, S., Horrobin, M., Hubert, Z., Jimenez Rosales, A., Jocou, L., Kendrew, S., Kervella, P., Kolb, J., Lagrange, A. M., Lapeyrère, V., Le Bouquin, J. B., Léna, P., Lippa, M., Lenzen, R., Maire, A. L., Mollière, P., Ott, T., Paumard, T., Perraut, K., Perrin, G., Pueyo, L., Rabien, S., Ramírez, A., Rau, C., Rodríguez-Coira, G., Rousset, G., Sanchez-Bermudez, J., Scheithauer, S., Schuhler, N., Straub, O., Straubmeier, C., Sturm, E., Tacconi, L. J., Vincent, F., Van Dishoeck, E. F., Von Fellenberg, S., Wank, I., Waisberg, I., Widmann, F., Wieprecht, E., Wiest, M., Wiezorrek, E., Woillez, J., Yazici, S., Ziegler, D., and Zins, G. (2019). First direct detection of an exoplanet by optical interferometry: Astrometry and K -band spectroscopy of HR 8799 e. *Astronomy and Astrophysics*, 623. 117

Lada, C. J. (1987). Proceedings of the International Astronomical Union: Preface. In *IAU Symposium*, volume 115, page 1. Cambridge University Press. 23

Lambrechts, M. and Johansen, A. (2012). Rapid growth of gas-giant cores by pebble accretion. *Astronomy and Astrophysics*, 544:32. 104, 127

Lavie, B., Mendonça, J. M., Mordasini, C., Malik, M., Bonnefoy, M., Demory, B.-O., Oreshenko, M., Grimm, S. L., Ehrenreich, D., and Heng, K. (2017). HELIOS-RETRIEVAL: An Open-source, Nested Sampling Atmospheric Retrieval Code; Application to the HR 8799 Exoplanets and Inferred Constraints for Planet Formation. *The Astronomical Journal*, 154:91. 105, 116, 117, 119

Lecar, M., Podolak, M., Sasselov, D., and Chiang, E. (2006). On the Location of the Snow Line in a Protoplanetary Disk. *The Astrophysical Journal*, 640(2):1115–1118. 108

Li, A. and Draine, B. T. (2001). Infrared Emission from Interstellar Dust. II. The Diffuse Interstellar Medium. *The Astrophysical Journal*, 554(2):778–802. 21

Lieman-Sifry, J., Hughes, A. M., Carpenter, J. M., Gorti, U., Hales, A., and Flaherty, K. M. (2016). DEBRIS DISKS IN THE SCORPIUSCENTAURUS OB ASSOCIATION RESOLVED BY ALMA. *ApJ*, 828(1):25. 32

Lindegren, L., Hernández, J., Bombrun, A., Klioner, S., Bastian, U., Ramos-Lerate, M., de Torres, A., Steidelmüller, H., Stephenson, C., Hobbs, D., Lammers, U., Biermann, M., Geyer, R., Hilger, T., Michalik, D., Stampa, U., McMillan, P., Castañeda, J., Clotet, M., Comoretto, G., Davidson, M., Fabricius, C., Gracia, G., Hambly, N., Hutton, A., Mora, A., Portell, J., van Leeuwen, F., Abbas, U., Abreu, A., Altmann, M., Andrei, A., Anglada, E., Balaguer-Núñez, L., Barache, C., Becciani, U., Bertone, S., Bianchi, L., Bouquillon, S., Bourda, G., Brüsemeister, T., Bucciarelli, B., Busonero, D., Buzzi, R., Cancelliere, R., Carlucci, T., Charlot, P., Cheek, N., Crosta, M., Crowley, C., de Bruijne, J., de Felice, F., Drimmel, R., Esquej, P., Fienga, A., Fraile, E., Gai, M., Garralda, N., González-Vidal, J., Guerra, R., Hauser, M., Hofmann, W., Holl, B., Jordan, S., Lattanzi, M., Lenhardt, H., Liao, S., Licata, E., Lister, T., Löffler, W., Marchant, J., Martin-Fleitas, J.-M., Messineo, R., Mignard, F., Morbidelli, R., Poggio, E., Riva, A., Rowell, N., Salguero, E., Sarasso, M., Sciacca, E., Siddiqui, H., Smart, R., Spagna, A., Steele, I., Taris, F., Torra, J., van Elteren, A., van Reeven, W., and Vecchiato, A. (2018). Gaia Data Release 2. *A&A*, 616:A2. 46, 54

Lindegren, L., Lammers, U., Bastian, U., Hernández, J., Klioner, S., Hobbs, D., Bombrun, A., Michalik, D., Ramos-Lerate, M., Butkevich, A., Comoretto, G., Joliet, E., Holl, B., Hutton, A., Parsons, P., Steidelmüller, H., Abbas, U., Altmann, M., Andrei, A., Anton, S., Bach, N., Barache, C., Becciani, U., Berthier, J., Bianchi, L., Biermann, M., Bouquillon, S., Bourda, G., Brüsemeister, T., Bucciarelli, B., Busonero, D., Carlucci, T., Castañeda, J., Charlot, P., Clotet, M., Crosta, M., Davidson, M., de Felice, F., Drimmel, R., Fabricius, C., Fienga, A., Figueras, F., Fraile, E., Gai, M., Garralda, N., Geyer, R., González-Vidal, J. J., Guerra, R., Hambly, N. C., Hauser, M., Jordan, S., Lattanzi, M. G., Lenhardt, H., Liao, S., Löffler, W., McMillan, P. J., Mignard, F., Mora, A., Morbidelli, R., Portell, J., Riva, A., Sarasso, M., Serraller, I., Siddiqui, H., Smart, R., Spagna, A., Stampa, U., Steele, I., Taris, F., Torra, J., van Reeven, W., Vecchiato, A., Zschocke, S., de Bruijne, J., Gracia, G., Raison, F., Lister, T., Marchant, J., Messineo, R., Soffel, M., Osorio, J., de Torres, A., and OMullane, W. (2016). Gaia Data Release 1. *A&A*, 595:A4. 82

Line, M. R., Knutson, H., Wolf, A. S., and Yung, Y. L. (2014). A systematic retrieval analysis of secondary eclipse spectra. II. A uniform analysis of nine planets and their C to O ratios. *Astrophysical Journal*, 783(2):70. 122

Lodato, G., Dipierro, G., Ragusa, E., Long, F., Herczeg, G. J., Pascucci, I., Pinilla, P., Manara, C. F., Tazzari, M., Liu, Y., Mulders, G. D., Harsono, D., Boehler, Y., Ménard, F., Johnstone, D., Salyk, C., Van Der Plas, G., Cabrit, S., Edwards, S., Fischer, W. J., Hendler, N., Nisini, B., Rigliaco, E., Avenhaus, H., Banzatti, A., and Gully-Santiago, M. (2019). The newborn planet population emerging from ring-like structures in discs. *MNRAS*, 486:453–461. 95

Long, F., Herczeg, G. J., Pascucci, I., Drabek-Maunder, E., Mohanty, S., Testi, L., Apai, D., Hendler, N., Henning, T., Manara, C. F., and Mulders, G. D. (2017). An ALMA Survey of CO Isotopologue Emission from Protoplanetary Disks in Chamaeleon I. *ApJ*, 844(2):99. 59

Loomis, R. A., Öberg, K. I., Andrews, S. M., and MacGregor, M. A. (2017). A Multi-ringed, Modestly Inclined Protoplanetary Disk around AA Tau. *ApJ*, 840(1):23. 63

Lynden-Bell, D. and Pringle, J. E. (1974). The Evolution of Viscous Discs and the Origin of the Nebular Variables. *Monthly Notices of the Royal Astronomical Society*, 168(3):603–637. 9, 105

Macgregor, M. A., Matrà, L., Kalas, P., Wilner, D. J., Pan, M., Kennedy, G. M., Wyatt, M. C., Duchene, G., Hughes, A. M., Rieke, G. H., Clampin, M., Fitzgerald, M. P., Graham, J. R., Holland, W. S., Panić, O., Shannon, A., and Su, K. (2017). A Complete ALMA Map of the Fomalhaut Debris Disk. 16, 26

MacGregor, M. A., Wilner, D. J., Chandler, C., Ricci, L., Maddison, S. T., Cranmer, S. R., Andrews, S. M., Hughes, A. M., and Steele, A. (2016). CONSTRAINTS ON PLANETESIMAL COLLISION MODELS IN DEBRIS DISKS. *ApJ*, 823:79. 26, 87

Madhusudhan, N., Agúndez, M., Moses, J. I., Hu, Y., Agúndez, M., Moses, J. I., Org, J., and Hu, Y. (2016). Exoplanetary Atmospheres-Chemistry, Formation Conditions, and Habitability. *Space Sci Rev*, 205:285–348. 103

Madhusudhan, N., Amin, M. A., and Kennedy, G. M. (2014). Towards Chemical Constraints on Hot Jupiter Migration. *Astrophysical Journal Letters*, 794(1):L12. 24, 44, 103, 108, 122, 124, 125

Madhusudhan, N., Bitsch, B., Johansen, A., and Eriksson, L. (2017). Atmospheric signatures of giant exoplanet formation by pebble accretion. *Monthly Notices of the Royal Astronomical Society*, 469(4):4102–4115. 44, 108, 124

Malfait, K., Waelkens, C., Waters, L. B. F. M., Vandenbussche, B., Huygen, E., and De Graauw, M. S. (1998). The spectrum of the young star HD 100546 observed with the Infrared Space Observatory. *Astron. Astrophys*, 332:25–28. 9

Manara, C. F., Morbidelli, A., and Guillot, T. (2018). Why do protoplanetary disks appear not massive enough to form the known exoplanet population? *Astronomy and Astrophysics*, 618:L3. 19, 20, 57

Marino, S., Carpenter, J., Wyatt, M. C., Booth, M., Casassus, S., Faramaz, V., Guzman, V., Hughes, A. M., Isella, A., Kennedy, G. M., Matra, L., Ricci, L., and Corder, S. (2018). A gap in the planetesimal disc around HD 107146 and asymmetric warm dust emission revealed by ALMA. *Monthly Notices of the Royal Astronomical Society*, 479(4):5423–5439. 95

Marino, S., Matrà, L., Stark, C., Wyatt, M. C., Casassus, S., Kennedy, G., Rodriguez, D., Zuckerman, B., Perez, S., Dent, W. R. F., Kuchner, M., Hughes, A. M., Schneider, G., Steele, A., Roberge, A., Donaldson, J., and Nesvold, E. (2016). Exocometary gas in the HD 181327 debris ring. *MNRAS*, 460:2933–2944. 95

Marois, C., Macintosh, B., Barman, T., Zuckerman, B., Song, I., Patience, J., Lafrenière, D., and Doyon, R. (2008). Direct imaging of multiple planets orbiting the star HR 8799. *Science*, 322(5906):1348–1352. 5, 116, 117, 121, 135

Marois, C., Zuckerman, B., Konopacky, Q. M., Macintosh, B., and Barman, T. (2010). Images of a fourth planet orbiting HR 8799. *Nature*, 468(7327):1080–1083. 116, 117, 121

Marsh, K. A., Silverstone, M. D., Becklin, E. E., Koerner, D. W., Werner, M. W., Weinberger, A. J., and Ressler, M. E. (2002). MID-INFRARED IMAGES OF THE DEBRIS DISK AROUND HD 141569. *ApJ*, 573:425–430. 83, 84, 90

REFERENCES

Masset, F. S. and Papaloizou, J. C. B. (2003). Runaway Migration and the Formation of Hot Jupiters. *The Astrophysical Journal*, 588(1):494–508. 120

Mathis, J. S., Rumpl, W., and Nordsieck, K. H. (1977). THE SIZE DISTRIBUTION OF INTERSTELLAR GRAINS. *Astrophysical Journal*, 217:425–433. 17, 56, 79, 106

Matrà, L., Marino, S., Kennedy, G. M., Wyatt, M. C., Öberg, K. I., and Wilner, D. J. (2018). An Empirical Planetesimal Belt Radius-Stellar Luminosity Relation. *ApJ*, 859:72. 91

Matrà, L., Panić, O., Wyatt, M. C., and Dent, W. R. F. (2015). CO mass upper limits in the Fomalhaut ring - the importance of NLTE excitation in debris discs and future prospects with ALMA. *MNRAS*, 447:3936–3947. 57

Mawet, D., Choquet, ., Absil, O., Huby, E., Bottom, M., Serabyn, E., Femenia, B., Lebreton, J., Matthews, K., Gomez Gonzalez, C. A., Wertz, O., Carlomagno, B., Christiaens, V., Defrère, D., Delacroix, C., Forsberg, P., Habraken, S., Jolivet, A., Karlsson, M., Milli, J., Pinte, C., Piron, P., Reggiani, M., Surdej, J., and Vargas Catalan, E. (2017). CHARACTERIZATION OF THE INNER DISK AROUND HD 141569 A FROM KECK/NIRC2 L-BAND VORTEX CORONAGRAPHY. *The Astronomical Journal*, 153. 137

Mayama, S., Akiyama, E., Panić, O., Miley, J., Tsukagoshi, T., Muto, T., Dong, R., de Leon, J., Mizuki, T., Oh, D., Hashimoto, J., Sai, J., Currie, T., Takami, M., Grady, C. A., Hayashi, M., Tamura, M., and Inutsuka, S.-i. (2018). ALMA Reveals a Misaligned Inner Gas Disk inside the Large Cavity of a Transitional Disk. *ApJ*, 868(1):L3. 141

Meeus, G., Pinte, C., Woitke, P., Montesinos, B., Mendigutía, I., Riviere-Marichalar, P., Eiroa, C., Mathews, G. S., Vandenbussche, B., Howard, C. D., Roberge, A., Sandell, G., Duchêne, G., Ménard, F., Grady, C. A., Dent, W. R. F., Kamp, I., Augereau, J. C., Thi, W. F., Tilling, I., Alacid, J. M., Andrews, S., Ardila, D. R., Aresu, G., Barrado, D., Brittain, S., Ciardi, D. R., Danchi, W., Fedele, D., de Gregorio-Monsalvo, I., Heras, A., Huelamo, N., Krivov, A., Lebreton, J., Liseau, R., Martin-Zaidi, C., Mora, A., Morales-Calderon, M., Nomura, H., Pantin, E., Pascucci, I., Phillips, N., Podio, L., Poelman, D. R., Ramsay, S., Riaz, B., Rice, K., Solano, E., Walker, H., White, G. J., Williams, J. P., Wright, G., and Collaboration, t. G. (2010). Gas in the protoplanetary disc of HD 169142: Herschel's view. *A&A*, 518(L124). 59

Mendigutía, I., Oudmaijer, R. D., Garufi, A., Lumsden, S. L., Huélamo, N., Cheetham, A., De Wit, W. J., Norris, B., Olguin, F. A., and Tuthill, P. (2017). The protoplanetary system HD 100546 in Hα polarized light from SPHERE/ZIMPOL A bar-like structure across the disk gap? *A&A*, 608:A104. 47

Miley, J. M., Panić, O., Haworth, T. J., Pascucci, I., Wyatt, M., Clarke, C., Richards, A. M. S., and Ratzka, T. (2019). Asymmetric mid-plane gas in ALMA images of HD 100546. *Monthly Notices of the Royal Astronomical Society*, 485(1):739–752. 30

MillanGabet, R., Schloerb, F. P., and Traub, W. A. (2001). Spatially Resolved Circumstellar Structure of Herbig Ae/Be Stars in the NearInfrared. *The Astrophysical Journal*, 546(1):358–381. 4

Min, M., Dullemond, C. P., Dominik, C., De Koter, A., and Hovenier, J. W. (2009). Radiative transfer in very optically thick circumstellar disks. *Astronomy and Astrophysics*, 497(1):155–166. 41, 105

Miotello, A. (2018). *THE PUZZLE OF PROTOPLANETARY DISK MASSES*. PhD thesis. 16, 15

Miotello, A., Bruderer, S., and van Dishoeck, E. F. (2014). Protoplanetary disk masses from CO isotopologue line emission. *A&A*, 572:A96. 15, 58

Miotello, A., Facchini, S., van Dishoeck, E. F., and Bruderer, S. (2018). Probing the protoplanetary disk gas surface density distribution with 13 CO emission. *Astronomy & Astrophysics*, 619:A113. 106

Miotello, A., van Dishoeck, E. F., Kama, M., and Bruderer, S. (2016). Determining protoplanetary disk gas masses from CO isotopologues line observations. *A&A*, 594:A85. 58, 94

Miotello, A., van Dishoeck, E. F., Williams, J. P., Ansdell, M., Guidi, G., Hogerheijde, M., Manara, C. F., Tazzari, M., Testi, L., van der Marel, N., and van Terwisga, S. (2017). Lupus disks with faint CO isotopologues: low gas/dust or high carbon depletion? *A&A*, 599:A113. 11

Monnier, J. D., Berger, J.-P., MillanGabet, R., Traub, W. A., Schloerb, F. P., Pedretti, E., Benisty, M., Carleton, N. P., Haguenauer, P., Kern, P., Labeye, P., Lacasse, M. G., Malbet, F., Perraut, K., Pearlman, M., and Zhao, M. (2006). Few Skewed Disks Found in First ClosurePhase Survey of Herbig Ae/Be Stars. *The Astrophysical Journal*, 647(1):444–463. 4

Moór, A., Abrahám, P., Juhász, A., Kiss, C., Pascucci, I., Kóspál, ., Apai, D., Henning, T., Csengeri, T., and Grady, C. (2011). MOLECULAR GAS IN YOUNG DEBRIS DISKS. *ApJ*, 740(1):L7. 93

Moor, A., Abraham, P., Kospal, A., Szabo, G. M., Apai, D., Balog, Z., Csengeri, T., Grady, C., Henning, T., Juhász, A., Kiss, C., Pascucci, I., Szulágyi, J., and Vavrek, R. (2013). A RESOLVED DEBRIS DISK AROUND THE CANDIDATE PLANET-HOSTING STAR HD 95086. *ApJ*, 775(2):L51. 95

Moór, A., Curé, M., Kóspál, A., Abrahám, P., Csengeri, T., Eiroa, C., Gunawan, D., Henning, T., Hughes, A. M., Juhász, A., Pawellek, N., and Wyatt, M. (2017). Molecular Gas in Debris Disks around Young A-type Stars. *The Astrophysical Journal*, 849:123. 30, 35, 95, 138

Moór, A., Henning, T., Juhász, A., Ábrahám, P., Balog, Z., Kóspál, ., Pascucci, I., Szabó, G. M., Vavrek, R., Curé, M., Csengeri, T., Grady, C., Güsten, R., and Kiss, C. (2015). DISCOVERY OF MOLECULAR GAS AROUND HD 131835 IN AN APEX MOLECULAR LINE SURVEY OF BRIGHT DEBRIS DISKS. *ApJ*, 814(1):42. 82, 94, 95

Mordasini, C. (2018). Planetary Population Synthesis. In Deeg, H. J. and Belmonte, J. A., editors, *Handbook of Exoplanets*, pages 1–50. Springer International Publishing, Cham. 71

Mordasini, C., Alibert, Y., Benz, W., Klahr, H., and Henning, T. (2012). Extrasolar planet population synthesis IV. Correlations with disk metallicity, mass, and lifetime. *Astronomy & Astrophysics*, 541:A97. 71

Mulders, G. D. (2013). *Radiative transfer models of protoplanetary disks : theory vs. observations*. PhD thesis, Anton Pannekoek Institute for Astronomy (API). 16, 24

Mulders, G. D. (2018). Planet Populations as a Function of Stellar Properties. In Deeg, H. J. and Belmonte, J. A., editors, *Handbook of Exoplanets*, pages 2009–2034. Springer, Cham. 102

Mulders, G. D., Paardekooper, S.-J., Panić, O., Dominik, C., van Boekel, R., and Ratzka, T. (2013). Planet or Brown Dwarf? Inferring the Companion Mass in HD 100546 from the Wall Shape using Mid-Infrared Interferometry. *A&A*, 557:A68. 47

Muley, D., Fung, J., and Van Der Marel, N. (2019). PDS 70: A Transition Disk Sculpted by a Single Planet. *The Astrophysical Journal Letters*, 879:L2. 141

Natta, A., Prusti, T., Neri, R., Wooden, D., Grinin, V. P., and Mannings, V. (2001). A reconsideration of disk properties in Herbig Ae stars. *Astronomy and Astrophysics*, 371(1):186–197. 6

Natta, A., Testi, L., Calvet, N., Henning, T., Waters, R., and Wilner, D. (2006). *Dust in Proto-Planetary Disks: Properties and Evolution*. University of Arizona Press, Tucson. 9

Ndugu, N., Bitsch, B., and Jurua, E. (2019). Are the observed gaps in protoplanetary discs caused by growing planets? *Monthly Notices of the Royal Astronomical Society*, 488(3):3625–3633. 28

Öberg, K. I., Murray-Clay, R., and Bergin, E. A. (2011). The effects of snowlines on C/O in planetary atmospheres. *Astrophysical Journal Letters*, 743(1):16. 14, 43, 102, 103, 104, 108, 109, 114, 116, 124

Ormel, C. W. and Klahr, H. H. (2010). The effect of gas drag on the growth of protoplanets: Analytical expressions for the accretion of small bodies in laminar disks. *Astronomy and Astrophysics*, 520(5):43. 104

Panić, O. and Hogerheijde, M. R. (2009). Characterising discs around Herbig Ae/Be stars through modelling of low-J 12CO lines. *Astronomy and Astrophysics*, 508(2):707–716. 54, 60

Panić, O., Holland, W. S., Wyatt, M. C., Kennedy, G. M., Matthews, B. C., Lestrade, J. F., Sibthorpe, B., Greaves, J. S., Marshall, J. P., Phillips, N. M., and Tottle, J. (2013). First results of the SONS survey: submillimetre detections of debris discs. *Monthly Notices of the Royal Astronomical Society*, 435:1037–1046. 16, 29, 82

Panić, O. and Min, M. (2017). Effects of disc mid-plane evolution on CO snowline location. *Monthly Notices of the Royal Astronomical Society*, 467:1175–1185. 56, 58, 68, 103, 104, 107, 120

Panić, O., Ratzka, T., Mulders, G. D., Dominik, C., van Boekel, R., Henning, T., Jaffe, W., and Min, M. (2014). Resolving HD 100546 disc in the mid-infrared: Small inner disc and asymmetry near the gap. *Astronomy & Astrophysics*, 562:A101. 27, 47, 53, 63

Panić, O., Van Dishoeck, E. F., Hogerheijde, M. R., Belloche, A., Güsten, R., Boland, W., and Baryshev, A. (2010). Observations of warm molecular gas and kinematics in the disc around HD 100546. *Astronomy and Astrophysics*, 519(12). 54

Pascucci, I. and Sterzik, M. (2009). Evidence for disk photoevaporation driven by the central star. *Astrophysical Journal*, 702(1):724–732. 4

Pascucci, I., Testi, L., Herczeg, G. J., Long, F., Manara, C. F., Hendler, N., Mulders, G. D., Krijt, S., Ciesla, F., Henning, T., Mohanty, S., Drabek-Maunder, E., Apai, D., Szűcs, L., Sacco, G., and Olofsson, J. (2016). A STEEPER THAN LINEAR DISK MASS-STELLAR MASS SCALING RELATION. *The Astrophysical Journal*, 831. 16, 12, 102

Paxton, B., Bildsten, L., Dotter, A., Herwig, F., Lesaffre, P., and Timmes, F. (2010). Modules for Experiments in Stellar Astrophysics (MESA). *The Astrophysical Journal Supplement Series*, 192(1):3. 17, 34

Paxton, B., Bildsten, L., Dotter, A., Herwig, F., Lesaffre, P., and Timmes, F. (2011). Modules for Experiments in Stellar Astrophysics (MESA). *Astrophysical Journal, Supplement Series*, 192(1):3. 105

Paxton, B., Cantiello, M., Arras, P., Bildsten, L., Brown, E. F., Dotter, A., Mankovich, C., Montgomery, M. H., Stello, D., Timmes, F. X., and Townsend, R. (2013). Modules for Experiments in Stellar Astrophysics (MESA): Giant Planets, Oscillations, Rotation, and Massive Stars. *The Astrophysical Journal Supplement Series*, 208(1):4. 105

Pearson, T. J. and Readhead, A. C. S. (1984). Image Formation by Self-Calibration in Radio Astronomy. *Annual Review of Astronomy and Astrophysics*, 22(1):97–130. 40

Pérez, L. M., Carpenter, J. M., Andrews, S. M., Ricci, L., Isella, A., Linz, H., Sargent, A. I., Wilner, D. J., Henning, T., Deller, A. T., Chandler, C. J., Dullemond, C. P., Lazio, J., Menten, K. M., Corder, S. A., Storm, S., Testi, L., Tazzari, M., Kwon, W., Calvet, N., Greaves, J. S., Harris, R. J., and Mundy, L. G. (2016). Spiral density waves in a young protoplanetary disk. *Science*, 353(6307):1519–1521. 140

Pérez, L. M., Carpenter, J. M., Chandler, C. J., Isella, A., Andrews, S. M., Ricci, L., Calvet, N., Corder, S. A., Deller, A. T., Dullemond, C. P., Greaves, J. S., Harris, R. J., Henning, T., Kwon, W., Lazio, J., Linz, H., Mundy, L. G., Sargent, A. I., Storm, S., Testi, L., and Wilner, D. J. (2012). CONSTRAINTS ON THE RADIAL VARIATION OF GRAIN GROWTH IN THE AS 209 CIRCUMSTELLAR DISK. *ApJ*, 760(1):L17. 78

Pérez, S., Casassus, S., Hales, A., Marino, S., Cheetham, A., Zurlo, A., Cieza, L., Dong, R., Alarcón, F., Benítez-Llambay, P., and Fomalont, E. (2019). Long baseline observations of HD100546 with ALMA: a possible circumplanetary disk detected in dust continuum and gas kinematics. 60

Péricaud, J., Di Folco, E., Dutrey, A., Guilloteau, S., and Piétu, V. (2017). The hybrid disks: a search and study to better understand evolution of disks. *Astronomy & Astrophysics*, 600:A62. 17, 31, 32, 35, 82, 83, 94, 137, 138

Perrot, C., Boccaletti, A., Pantin, E., Augereau, J.-C., Lagrange, A.-M., Galicher, R., Maire, A.-L., Mazoyer, J., Milli, J., Rousset, G., Gratton, R., Bonnefoy, M., Brandner, W., Buenzli, E., Langlois, M., Lannier, J., Mesa, D., Peretti, S., Salter, G., Sissa, E., Chauvin, G., Desidera, S., Feldt, M., Vigan, A., Di Folco, E., Dutrey, A., Péricaud, J., Baudoz, P., Benisty, M., De Boer, J., Garufi, A., Girard, J. H., Menard, F., Olofsson, J., Quanz, S. P., Mouillet, D., Christiaens, V., Casassus, S., Beuzit, J.-L., Blanchard, P., Carle, M., Fusco, T., Giro, E., Hubin, N., Maurel, D., Moeller-Nilsson, O., Sevin, A., and Weber, L. (2016). Discovery of concentric broken rings at sub-arcsec separations in the HD 141569A gas-rich, debris disk with VLT/SPHERE. *A&A*, 590:L7. 22, 84, 85, 89, 90, 96, 97, 98, 137, 140, 141

Piétu, V., Dutrey, A., Guilloteau, S., Chapillon, E., and Pety, J. (2006). Resolving the inner dust disks surrounding LkCa 15 and MWC 480 at mm wavelengths. *Astronomy and Astrophysics*, 460(3). 113

Pineda, J. E., Quanz, S. P., Meru, F., Mulders, G. D., Meyer, M. R., Panić, O., and Avenhaus, H. (2014). Resolved images of the protoplanetary disk around HD 100546 with ALMA. *ApJL*, 788. 47, 53, 54, 62

Pineda, J. E., Szulágyi, J., Quanz, S. P., van Dishoeck, E. F., Garufi, A., Meru, F., Mulders, G. D., Testi, L., Meyer, M. R., and Reggiani, M. (2019). High-resolution ALMA Observations of HD 100546: Asymmetric Circumstellar Ring and Circumplanetary Disk Upper Limits. *The Astrophysical Journal*, 871(1):48. 63

Pinilla, P., Benisty, M., and Birnstiel, T. (2012a). Ring shaped dust accumulation in transition disks. *Astronomy & Astrophysics*, 545:A81. 17

Pinilla, P., Benisty, M., Birnstiel, T., Ricci, L., Isella, A., Natta, A., Dullemond, C. P., Quiroga-Nuñez, L. H., Henning, T., and Testi, L. (2014). Millimetre spectral indices of transition disks and their relation to the cavity radius. *Astronomy & Astrophysics*, 564:A51. 22, 74, 87

Pinilla, P., Birnstiel, T., Ricci, L., Dullemond, C. P., Uribe, A. L., Testi, L., and Natta, A. (2012b). Trapping dust particles in the outer regions of protoplanetary disks. *A&A*, 538:A114. 17, 66, 67, 91, 130

Pinte, C., Price, D. J., Ménard, F., Duchêne, G., Dent, W. R. F., Hill, T., De Gregorio-Monsalvo, I., Hales, A., and Mentiplay, D. (2018). Kinematic Evidence for an Embedded Protoplanet in a Circumstellar Disk. *The Astrophysical Journal Letters*, 860:L13. 141

Pinte, C., van der Plas, G., Ménard, F., Price, D. J., Christiaens, V., Hill, T., Mentiplay, D., Ginski, C., Choquet, E., Boehler, Y., Duchêne, G., Perez, S., and Casassus, S. (2019). Kinematic detection of a planet carving a gap in a protoplanetary disk. 141, 142

Piso, A. M. A., Öberg, K. I., Birnstiel, T., and Murray-Clay, R. A. (2015). C/O and snowline locations in protoplanetary disks: The effect of radial drift and viscous gas accretion. *Astrophysical Journal*, 815(2). 143

Piso, A.-M. A., Pegues, J., and Öberg, K. I. (2016). The role of ice compositions for snowlines and the C/N/O ratios in active disks. *The Astrophysical Journal*, 833(2):203. 44, 108, 109, 143

Pontoppidan, K. M. (2006). Spatial mapping of ices in the Ophiuchus-F core A direct measurement of CO depletion and the formation of CO2. *Astronomy and Astrophysics*, 453(3):47–50. 124

Price, D. J., Cuello, N., Pinte, C., Mentiplay, D., Casassus, S., Christiaens, V., Kennedy, G. M., Cuadra, J., Sebastian Perez, M., Marino, S., Armitage, P. J., Zurlo, A., Juhasz, A., Ragusa, E., Laibe, G., and Lodato, G. (2018). Circumbinary, not transitional: on the spiral arms, cavity, shadows, fast radial flows, streamers, and horseshoe in the HD 142527 disc. *MNRAS*, 477:1270–1284. 28, 60, 63

Qi, C., Öberg, K. I., Andrews, S. M., Wilner, D. J., Bergin, E. A., Hughes, A. M., Hogherheijde, M., and D'alessio, P. (2015). CHEMICAL IMAGING OF THE CO SNOW LINE IN THE HD 163296 DISK. *The Astrophysical Journal*, 813:128. 59, 112, 113

Qi, C., Öberg, K. I., Espaillat, C. C., Robinson, C. E., Andrews, S. M., Wilner, D. J., Blake, G. A., Bergin, E. A., and Cleeves, L. I. (2019). Probing CO and N 2 Snow Surfaces in Protoplanetary Disks with N 2 H + Emission. *The Astrophysical Journal*, 882:160. 111, 112, 143

Qi, C., Öberg, K. I., and Wilner, D. J. (2013). H2CO and N2H+ in protoplanetary disks: EVIDENCE for a CO-ice regulated chemistry. *Astrophysical Journal*, 765(1):34. 59, 112

Quanz, S. P., Amara, A., Meyer, M. R., Girard, J. H., Kenworthy, M. A., and Kasper, M. (2015). CONFIRMATION AND CHARACTERIZATION OF THE PROTOPLANET HD 100546 b - DIRECT EVIDENCE FOR GAS GIANT PLANET FORMATION AT 50 AU. *ApJ*, 807(1):64. 46, 58, 71, 135

Quanz, S. P., Amara, A., Meyer, M. R., Kenworthy, M. A., Kasper, M., and Girard, J. H. (2013). A young protoplanet candidate embedded in the circumstellar disk of HD100546. *ApJL*, 766(1):5. 135

Quillen, A. C. (2006). The Warped Circumstellar Disk of HD 100546. *ApJ*, 640(2):1078–1085. 54

Quillen, A. C., Varnière, P., Minchev, I., and Frank, A. (2005). DRIVING SPIRAL ARMS IN THE CIRCUMSTELLAR DISKS OF HD 100546 AND HD 141569A. *The Astronomical Journal*, 129:2481–2495. 141

Raghavan, D., Mcalister, H. A., Henry, T. J., Latham, D. W., Marcy, G. W., Mason, B. D., Gies, D. R., White, R. J., and Ten Brummelaar, T. A. (2010). A SURVEY OF STELLAR FAMILIES: MULTIPLICITY OF SOLAR-TYPE STARS. *The Astrophysical Journal Supplement Series*, 190:1–42. 3

Rameau, J., Follette, K. B., Pueyo, L., Marois, C., Macintosh, B., Millar-Blanchaer, M., Wang, J. J., Vega, D., Doyon, R., Lafrenière, D., Nielsen, E. L., Bailey, V., Chilcote, J. K., Close, L. M., Esposito, T. M., Males, J. R., Metchev, S., Morzinski, K. M., Ruffio, J.-B., Wolff, S. G., Ammons, S. M., Barman, T. S., Bulger, J., Cotten, T., De Rosa, R. J., Duchene, G., Fitzgerald, M. P., Goodsell, S., Graham, J. R., Greenbaum, A. Z., Hibon, P., Hung, L.-W., Ingraham, P., Kalas, P., Konopacky, Q., Larkin, J. E., Maire, J., Marchis, F., Oppenheimer, R., Palmer, D., Patience, J., Perrin, M. D., Poyneer, L., Rajan, A., Rantakyrö, F. T., Marley, M. S., Savransky, D., Schneider, A. C., Sivaramakrishnan, A., Song, I., Soummer, R., Thomas, S., Wallace, J. K., Ward-Duong, K., and Wiktorowicz, S. (2017). An Optical/Near-infrared Investigation of HD 100546 b with the Gemini Planet Imager and MagAO. *The Astronomical Journal*, 153:244–9. 135

Rau, U. and Cornwell, T. J. (2011). A multi-scale multi-frequency deconvolution algorithm for synthesis imaging in radio interferometry. *A&A*, 532:A71. 39, 49, 84

Reche, R., Beust, H., and Augereau, J.-C. (2009). Investigating the flyby scenario for the HD 141569 system. *A&A*, 493(2):661–669. 84, 89

Reffert, S., Bergmann, C., Quirrenbach, A., Trifonov, T., and Künstler, A. (2014). Precise Radial Velocities of Giant Stars VII. Occurrence Rate of Giant Extrasolar Planets as a Function of Mass and Metallicity. *Astronomy & Astrophysics*, 574:116. 35, 102, 105, 138

Remijan, A., Biggs, A., Cortes, P., A., Dent, B., Di Francesco, J., Fomalont, E., Hales, A., Kameno, S., Mason, B., Philips, N., Saini, K., Stoehr, F., Vilaro, V. B., and Villard, E. (2019). *ALMA Technical Handbook*. Alma doc. edition. 39

Ricci, L., Carpenter, J. M., Fu, B., Hughes, A. M., Corder, S., and Isella, A. (2015). ALMA OBSERVATIONS OF THE DEBRIS DISK AROUND THE YOUNG SOLAR ANALOG HD 107146. *ApJ*, 798(2):124. 95

Ricci, L., Trotta, F., Testi, L., Natta, A., Isella, A., and Wilner, D. J. (2012). The effect of local optically thick regions in the long-wave emission of young circumstellar disks. *A&A*, 540:A6. 22, 74

Richert, A. J. W., Lyra, W., and Kuchner, M. (2018). The interplay between radiation pressure and the photoelectric instability in optically thin disks of gas and dust. *The Astrophysical Journal*, 856:41. 141

Roberge, A., Kamp, I., Montesinos, B., Dent, W. R. F., Meeus, G., Donaldson, J. K., Olofsson, J., Moór, A., Augereau, J.-C., Howard, C., Eiroa, C., Thi, W.-F., Ardila, D. R., Sandell, G., and Woitke, P. (2013). HERSCHEL OBSERVATIONS OF GAS AND DUST IN THE UNUSUAL 49 Ceti DEBRIS DISK. *ApJ*, 771(1):69. 82

Rodríguez, L. F., Curiel, S., Moran, J. M., Mirabel, I. F., Roth, M., and Garay, G. (1989). LARGE PROPER MOTIONS IN THE REMARKABLE TRIPLE RADIO SOURCE IN SERPENS. Technical report. 87

Sadakane, K. (2006). λ Bootis-like abundances in the vega-like, γ doradus type-pulsator HD 218396. *Publications of the Astronomical Society of Japan*, 58(6):1023–1032. 116, 121

Sana, H., De Mink, S. E., De Koter, A., Langer, N., Evans, C. J., Gieles, M., Gosset, E., Izzard, R. G., Le Bouquin, J. B., and Schneider, F. R. (2012). Binary interaction dominates the evolution of massive stars. *Science*, 337(6093):444–446. 4

Sandell, G., Weintraub, D. A., and Hamidouche, M. (2011). A SUBMILLIMETER MAPPING SURVEY OF HERBIG AeBe STARS. *ApJ*, 727(1):26. 82

Schoonenberg, D. and Ormel, C. W. (2017). Planetesimal formation near the snowline: In or out? *Astronomy and Astrophysics*, 602:A21. 131

Schwarz, K. R., Bergin, E. A., Cleeves, L. I., Blake, G. A., Zhang, K., Öberg, K. I., van Dishoeck, E. F., and Qi, C. (2016). THE RADIAL DISTRIBUTION OF H 2 AND CO IN TW HYA AS REVEALED BY RESOLVED ALMA OBSERVATIONS OF CO ISOTOPOLOGUES. *ApJ*, 823(2):91. 58, 73, 91

Schwarz, K. R., Teague, R., and Bergin, E. A. (2019). Line Ratios Reveal N2H+ Emission Originates Above the Midplane in TW Hydrae. *The Astrophysical Journal*, 881(2):L44. 113

Shakura, N. I. and Sunyaev, R. A. (1973). Astronomy and Astrophysics. *Astronomy and Astrophysics*, 24:337–355. 9

Skrutskie, M. F., Dutkevitch, D., Strom, S. E., Edwards, S., Strom, K. M., and Shure, M. A. (1990). A sensitive 10-micron search for emission arising from circumstellar dust associated with solar-type pre-main-sequence stars. *The Astronomical Journal*, 99(4):1187. 26

Stammler, S. M., Birnstiel, T., Panić, O., Dullemond, C. P., and Dominik, C. (2017). Redistribution of CO at the location of the CO ice line in evolving gas and dust disks. *Astronomy and Astrophysics*, 600:140. 103

Strom, K. M., Strom, S. E., Edwards, S., Cabrit, S., and Skrutskie, M. F. (1989). Circumstellar material associated with solar-type pre-main-sequence stars - A possible constraint on the timescale for planet building. *The Astronomical Journal*, 97:1451. 26

Sylvester, R. J., Skinner, C. J., Barlow, M. J., and Mannings, V. (1996). Optical, infrared and millimetre-wave properties of Vega-like systems. *MNRAS*, 279(3):915–939. 82

Takeuchi, T. and Artymowicz, P. (2001). DUST MIGRATION AND MORPHOLOGY IN OPTICALLY THIN CIRCUMSTELLAR GAS DISKS. *ApJ*, 557:990–1006. 89

Takeuchi, T. and Lin, D. N. C. (2005). Attenuation of Millimeter Emission from Circumstellar Disks Induced by the Rapid Dust Accretion. *ApJ*, 623(1):482–492. 18, 89

Tazzari, M., Testi, L., Ercolano, B., Natta, A., Isella, A., Chandler, C. J., Pérez, L. M., Andrews, S., Wilner, D. J., Ricci, L., Henning, T., Linz, H., Kwon, W., Corder, S. A., Dullemond, C. P., Carpenter, J. M., Sargent, A. I., Mundy, L., Storm, S., Calvet, N., Greaves, J. A., Lazio, J., and Deller, A. T. (2016).

Multiwavelength analysis for interferometric (sub-)mm observations of protoplanetary disks. *A&A*, 588:A53. 78

Tazzari, M., Testi, L., Natta, A., Ansdell, M., Carpenter, J., Guidi, G., Hogerheijde, M., Manara, C. F., Miotello, A., Van Der Marel, N., Van Dishoeck, E. F., and Williams, J. P. (2017). Physical properties of dusty protoplanetary disks in Lupus: evidence for viscous evolution? *A&A*, 606:88. 28

Testi, L., Birnstiel, T., Ricci, L., Andrews, S., Blum, J., Carpenter, J., Dominik, C., Isella, A., Natta, A., Williams, J., and Wilner, D. (2014). Dust Evolution in Protoplanetary Disks. *Protostars and Planets VI, Henrik Beuther, Ralf S. Klessen, Cornelis P. Dullemond, and Thomas Henning (eds.), University of Arizona Press, Tucson, 914 pp., p.339-361*, pages 339–361. 17

The, P. S., de Winter, D., and Perez, M. R. (1994). A new catalogue of members and candidate members of the Herbig Ae/Be (HAEBE) stellar group. *Astronomy & Astrophysics Supplement Series*, 104:315–339. 33

Thi, W. F., Pinte, C., Pantin, E., Augereau, J. C., Meeus, G., Ménard, F., Martin-Zaïdi, C., Woitke, P., Riviere-Marichalar, P., Kamp, I., Carmona, A., Sandell, G., Eiroa, C., Dent, W., Montesinos, B., Aresu, G., Meijerink, R., Spaans, M., White, G., Ardila, D., Lebreton, J., Mendigutía, I., and Brittain, S. (2014). Gas lines from the 5-Myr old optically thin disk around HD 141569A Herschel observations and modeling. *A&A*, 561:A50. 83, 93

Thompson, A. R., Moran, J. M., and Swenson, G. W. (2017). Van CittertZernike Theorem, Spatial Coherence, and Scattering. In *Interferometry and Synthesis in Radio Astronomy*, pages 767–786. Springer, Cham. 36

Tobin, J. J., Sheehan, P. D., Megeath, S. T., Díaz-Rodríguez, A. K., Offner, S. S. R., Murillo, N. M., van t Hoff, M. L. R., van Dishoeck, E. F., Osorio, M., Anglada, G., Furlan, E., Stutz, A. M., Reynolds, N., Karnath, N., Fischer, W. J., Persson, M., Looney, L. W., Li, Z.-Y., Stephens, I., Chandler, C. J., Cox, E., Dunham, M. M., Tychoniec, ., Kama, M., Kratter, K., Kounkel, M., Mazur, B., Maud, L., Patel, L., Perez, L., Sadavoy, S. I., Segura-Cox, D., Sharma, R., Stephenson, B., Watson, D. M., and Wyrowski, F. (2020). The VLA/ALMA

Nascent Disk and Multiplicity (VANDAM) Survey of Orion Protostars. II. A Statistical Characterization of Class 0 and Class I Protostellar Disks. *The Astrophysical Journal*, 890(2):130. 25

Toomre, A. (1964). On The Gravitational Stability of a Disk of Stars. *ApJ*, 139:1217–1238. 66

Trapman, L., Facchini, S., Hogerheijde, M. R., van Dishoeck, E. F., and Bruderer, S. (2019). Gas versus dust sizes of protoplanetary discs: effects of dust evolution. *Astronomy & Astrophysics*, 629:A79. 12

Trotta, F., Testi, L., Natta, A., Isella, A., and Ricci, L. (2013). Constraints on the radial distribution of the dust properties in the CQ Tauri protoplanetary disk. *A&A*, 558:A64. 78

van den Ancker, M. E., Thé, P. S., Tjin, H. R. E., Djie, A., Catala, C., De Winter, D., Blondel, P. F. C., and Waters, L. B. F. M. (1997). Hipparcos data on Herbig Ae/Be stars: an evolutionary scenario. *A&A*, 324:33–36. 46

Van Der Marel, N., Cazzoletti, P., Pinilla, P., and Garufi, A. (2016). VORTICES AND SPIRALS IN THE HD 135344B TRANSITION DISK. *ApJ*, 823:178. 60

van der Marel, N., Pinilla, P., Tobin, J., Kempen, T. v., Andrews, S., Ricci, L., Birnstiel, T., Ataiee S., Pinilla P., Z. A. e. a., J., B. P., Sommeria, Baryshev A. M., Hesper R., M. F. P. e. a., Birnstiel T., D. C. P., F., B., Birnstiel T., D. C. P., P., P., Brauer F., D. C. P., T., H., Brown J. M., Rosenfeld K. A., A. S. M. W. D. J., van Dishoeck E. F., Bruderer S., van der Marel N., v. D. E. F., van Kempen T. A., Casassus S., van der Plas G., M. S. P. e. a., T., D. B., Espaillat C., Muzerolle J., N. J. e. a. e. B. H. e. a., Flock M., Ruge J. P., D. N. e. a., Follette K. B., Grady C. A., S. J. R. e. a., Fukagawa M., Tsukagoshi T., M. M. e. a., Fung J., S. J.-M., E., C., Geers V. C., Pontoppidan K. M., v. D. E. F. e. a., Johansen A., Y. A., H., K., T., K. H. H., Henning, M.-K., L. W., Lin, Marino S., P. S., S., C., Pérez L. M., Isella A., C. J. M., J., C. C., Perez S., Casassus S., M. F. e. a., Pinilla P., Birnstiel T., R. L. e. a., Pinilla P., de Juan Ovelar M., A. S. e. a., Raettig N., L. W., H., K., Rodmann J., Henning T., C. C. J. M. L. G., J., W. D., Ubach C., Maddison S. T., W. C. M. e. a., van der

Marel N., van Dishoeck E., B. S. e. a., van der Marel N., van Dishoeck E., B. S. P. L. M., A., I., van der Marel N., van Dishoeck E. F., B. S. e. a., J., W. S., A., W. F. L. e. E., Windmark F., Birnstiel T., G. C. e. a., Zhang K., Isella A., C. J. M., A., B. G., M., Z. Z., and J., S. (2015). A CONCENTRATION OF CENTIMETER-SIZED GRAINS IN THE OPHIUCHUS IRS 48 DUST TRAP. *Astrophysical Journal*, 810(1):L7. 17, 23

van der Marel, N., van Dishoeck, E. F., Bruderer, S., Andrews, S. M., Pontoppidan, K. M., Herczeg, G. J., van Kempen, T., and Miotello, A. (2016). Resolved gas cavities in transitional disks inferred from CO isotopologs with ALMA. *A&A*, 585:A58. 27, 137

van der Marel, N., van Dishoeck, E. F., Bruderer, S., Birnstiel, T., Pinilla, P., Dullemond, C. P., van Kempen, T. A., Schmalzl, M., Brown, J. M., Herczeg, G. J., Mathews, G. S., and Geers, V. (2013). A Major Asymmetric Dust Trap in a Transition Disk. *Science*, 340(6137):1199–1202. 60, 91

van der Marel, N., Williams, J. P., Ansdell, M., Manara, C. F., Miotello, A., Tazzari, M., Testi, L., Hogerheijde, M., Bruderer, S., van Terwisga, S., and van Dishoeck, E. F. (2018). New insights into the nature of transition disks from a complete disk survey of the Lupus star forming region. *The Astrophysical Journal*, 854(2):177. 28

van der Plas, G., Ménard, F., Gonzalez, J. F., Perez, S., Rodet, L., Pinte, C., Cieza, L., Casassus, S., and Benisty, M. (2019). ALMA study of the HD 100453 AB system and the tidal interaction of the companion with the disk. *Astronomy & Astrophysics*, 624:A33. 27

van der Tak, F. F. S., Black, J. H., Schöier, F. L., Jansen, D. J., and van Dishoeck, E. F. (2007). A computer program for fast non-LTE analysis of interstellar line spectra. *A&A*, 468(2):627–635. 91

van Dishoeck, E. F. and Black, J. H. (1988). The Photodissociation and Chemistry of Interstellar CO. *The Astrophysical Journal*, 334:771–802. 14

Verhoeff, A. P., Min, M., Pantin, E., Waters, L. B., Tielens, A. G., Honda, M., Fujiwara, H., Bouwman, J., Van Boekel, R., Dougherty, S. M., De Koter, A., Dominik, C., and Mulders, G. D. (2011). The complex circumstellar environment of HD142527. *Astronomy and Astrophysics*, 528:91. 4

Vericel, A. and Gonzalez, J. F. (2020). Self-induced dust traps around snow lines in protoplanetary discs. *Monthly Notices of the Royal Astronomical Society*, 492(1):210–222. 131

Vioque, M., Oudmaijer, R. D., Baines, D., Mendigutía, I., and Pérez-Martínez, R. (2018). Gaia DR2 study of Herbig Ae/Be stars. *A&A*, 620:128. 33, 46

Visser, R., van Dishoeck, E. F., and Black, J. H. (2009). The photodissociation and chemistry of CO isotopologues: applications to interstellar clouds and circumstellar disks. *A&A*, 503(2):323–343. 15, 94

Wagner, K., Follete, K. B., Close, L. M., Apai, D., Gibbs, A., Keppler, M., Müller, A., Henning, T., Kasper, M., Wu, Y.-L., Long, J., Males, J., Morzinski, K., and Mcclure, M. (2018). Magellan Adaptive Optics Imaging of PDS 70: Measuring the Mass Accretion Rate of a Young Giant Planet within a Gapped Disk. *The Astrophysical Journal Letters*, 863:L8. 28

Walsh, C., Daley, C., Facchini, S., and Juhász, A. (2017). Astronomy & Astrophysics CO emission tracing a warp or radial flow within 100 au in the HD 100546 protoplanetary disk. *Astronomy & Astrophysics*, 607:A114. 54, 63, 142

Walsh, C., Juhász, A., Meeus, G., Dent, W. R. F., Maud, L. T., Aikawa, Y., Millar, T. J., and Nomura, H. (2016). ALMA REVEALS THE ANATOMY OF THE mm-SIZED DUST AND MOLECULAR GAS IN THE HD 97048 DISK. *Astrophysical Journal*, 831:200. 34

Walsh, C., Juhasz, A., Pinilla, P., Harsono, D., Mathews, G. S., Dent, W. R. F., Hogerheijde, M. R., Birnstiel, T., Meeus, G., Nomura, H., Aikawa, Y., Millar, T. J., and Sandell, G. (2014a). ALMA hints at the presence of two companions in the disk around HD 100546. *ApJL*, 791:L6. 20, 35, 47, 49, 50, 52, 53, 54, 57, 62, 71, 74, 75, 76, 77, 78

Walsh, C., Millar, T. J., Nomura, H., Herbst, E., Weaver, S. W., Aikawa, Y., Laas, J. C., and Vasyunin, A. I. (2014b). Complex organic molecules in protoplanetary disks. *Astronomy & Astrophysics*, 563:33. 108

Wehrse, R., Baschek, B., and Von Waldenfels, W. (2000). The diffusion of radiation in moving media I. Basic assumptions and formulae. *Astron. Astrophys*, 359:780–787. 43

Weidenschilling, S. J. (1977). Aerodynamics of solid bodies in the solar nebula. *Monthly Notices of the Royal Astronomical Society*, 180:57–70. 16, 17

Weinberger, A. J., Becklin, E. E., Schneider, G., Smith, B. A., Lowrance, P. J., Silverstone, M. D., Zuckerman, B., and Terrile, R. J. (1999). THE CIRCUMSTELLAR DISK OF HD 141569 IMAGED WITH NICMOS. *ApJ*, 525:53–56. 82

Weinberger, A. J., Rich, R. M., Becklin, E. E., Zuckerman, B., and Matthews, K. (2000). Stellar Companions and the Age of HD 141569 and Its Circumstellar Disk. *ApJ*, 544(2):937–943. 82

Whipple, F. L. (1972). On Certain Aerodynamic Processed for Asteroids and Comets. In Elvius, A., editor, *From Plasma to Planet*, page 211, Saltsjöbaden. Wiley Interscience Division. 17

White, J. A., Boley, A. C., Hughes, A. M., Flaherty, K. M., Ford, E., Wilner, D., Corder, S., and Payne, M. (2016). ALMA OBSERVATIONS OF HD 141569s CIRCUMSTELLAR DISK. *Astrophysical Journal*, 829(1):6. 57, 59, 82, 83, 84, 85, 90, 93

White, J. A., Boley, A. C., MacGregor, M. A., Hughes, A. M., and Wilner, D. J. (2018). ALMA and VLA Observations of the HD 141569 System. *MNRAS*, 474:4500–4506. 22, 84, 87

Williams, J. P., Blitz, L., and Mckee, C. F. (2000). THE STRUCTURE AND EVOLUTION OF MOLECULAR CLOUDS: FROM CLUMPS TO CORES TO THE IMF. In Mannings, V., Boss, A. P., and Russell, S. S., editors, *PPIV*. University of Arizona Press. 3

Wilner, D. J., Bourke, T. L., Wright, C. M., Jørgensen, J. K., Van Dishoeck, E. F., and Wong, T. (2003). DISKS AROUND THE YOUNG STARS TW HYDRAE AND HD 100546 IMAGED AT 3.4 MILLIMETERS WITH THE AUSTRALIA TELESCOPE COMPACT ARRAY. *ApJ*, 596:597. 78

Wilson, T. L. (1999). Isotopes in the interstellar medium and circumstellar envelopes. *RPPh*, 62(2):143–185. 73

Wilson, T. L. and Rood, R. T. (1994). Abundances in the Interstellar Medium. *ARA&A*, 32(1):191–226. 15, 58, 93, 94

Woitke, P., Kamp, I., and F. Thi, W. (2009). Radiation thermo-chemical models of protoplanetary disks: I. Hydrostatic disk structure and inner rim. *Astronomy and Astrophysics*, 501(1):383–406. 124

Wright, C. M., Maddison, S. T., Wilner, D. J., Burton, M. G., Lommen, D., van Dishoeck, E. F., Pinilla, P., Bourke, T. L., Menard, F., and Walsh, C. (2015). Resolving structure of the disc around HD100546 at 7 mm with ATCA. *MNRAS*, 453(1):414–438. 18, 19, 47, 48, 56, 60, 63, 78, 79, 87

Wyatt, M. C. (2003). Resonant Trapping of Planetesimals by Planet Migration: Debris Disk Clumps and Vegas Similarity to the Solar System. *ApJ*, 598(2):1321–1340. 91

Wyatt, M. C. (2005). Spiral structure when setting up pericentre glow: possible giant planets at hundreds of AU in the HD 141569 disk. *A&A*, 440(3):937–948. 84

Wyatt, M. C., Panić, O., Kennedy, G. M., and Matrà, L. (2015). Five steps in the evolution from protoplanetary to debris disk. *ApASS*, 357(2):103. 16, 29, 30, 82

Youdin, A. N. and Goodman, J. (2005). Streaming Instabilities in Protoplanetary Disks. *The Astrophysical Journal*, 620(1):459–469. 104

Yu, M., Willacy, K., Dodson-Robinson, S. E., Turner, N. J., and Evans Ii, N. J. (2016). PROBING PLANET FORMING ZONES WITH RARE CO ISOTOPOLOGUES. *ApJ*, 822:53. 16